Ordered Transparent Conductive Oxides (TCOs) for Applications to Photoelectrochemistry

Menglong Zhang

Doctor of Philosophy

University of York

Chemistry

May 2016

Abstract

A method for fabricating high quality photonic TCO (transparent conductive oxide) films of macroporous FTO (fluorine doped tin oxide) (mac-FTO) and hollow sphere AZO (aluminum doped zinc oxide) (hs-AZO) is described. The films were used as electrodes to support photoelectrochemical reactions relevant to energy research. Methods have been developed for conformal coating the TCO electrodes with photoactive materials including CdS, Fe_2O_3 and C_3N_4. Previous literature describing photonic mac-FTO films generally show poor conductivity and optical properties, which limit the performance of structured TCOs in supporting photoelectrochemistry. Optimizing the synthesis and processing conditions gives high quality optical and conductive films of mac-FTO. Coating films with dispersed nanoparticles of CdS shows that the mac-FTO supports charge carrier transport to the contact and is not just a structural support for continuous conductive films of photoactive materials. Coating to maximise photocurrent gives over 9 mA cm^{-2} for conformally coated CdS@mac-FTO under visible light (> 420 nm) through a simple approach, showing an improvement in comparison to previous CdS literature work on structured electrodes. The new hs-AZO TCO also supports photocurrents up to 7.8 mA cm^{-2} after CdS coating. Both FTO and AZO show significant photocurrent enhancement in comparison to planar FTO analogues.

In addition to CdS, methods were developed to conformally coat the organic photocatalyst C_3N_4 and the metal oxide Fe_2O_3 onto mac-FTO which showed enhanced photocurrent compared to planar analogues. Enhancements were typically in the range x (CdS), y (C_3N_4), and z (Fe_2O_3) which reflect the increase in surface area and greater loading of photoactive material. Potential photonic enhancements were not determined, however there is clearly scope for increasing the photocurrent per illuminated surface area using structured TCO electrodes.

Table of Contents

Table of Figures

Table of Tables

List of Accompanying Material

A digital copy of this thesis is included on a CD in the back of this volume.

Acknowledgements

There are many people I wish to thank for their support and help, without which this work would not have been possible. Firstly, I would like to thank all my family, especially my wife Xinyu Tang, for being supportive throughout my studies, and always being there when I needed her. And I am extremely grateful for everything my parents have done for me.

I would like to thank my supervisor Richard Douthwaite for his academic support and guidance, and always being approachable with any problems no matter how busy he is. He taught me how to be a good scientist, how to arrange my research. I am grateful to my IPM Martin Cockett, for the useful discussions and advice in TAP meetings. I am also grateful to the Wild Funding for funding my research.

In terms of instruments, numerous people provided me with training which was invaluable to my research. For all of their assistance, I would like to thank Ian Wright, Adrian Whitwood and Stephen Cowling. I would like to thank all the admin and technical staff in the department.

Around the lab and the office, the first one I would like to thank is Dr Robert Mitchell, he is always nice and friendly, and make the lab a comfortable and funny place. I would like to thank Rob again for showing me how to use the experimental instruments in the lab and sharing me with interesting literature reports, especially for helping me with the TEM. Thank you Natalie, who is always kind to me and always keep the lab a tidy place. Thank you also to Danielle, who helped me a lot in photoelectrochemistry and the useful discussions. Thanks also to Haowei and Xuan, who provides my useful discussions and chatting with them is always a good time for me in the lab. Outside of the RED group, I am especially grateful to VC group, in

particular Zhou, for loading chemicals when I needed and sharing with me the experience about the study and daily life in this country. I am grateful to Prof Paul Walton, for his encouragement after my first presentation here, he made me confident about what I am doing.

Declaration

The work presented in this thesis is to the best of my knowledge original. This work has not previously been presented for an award at this, or any other, University. All sources are acknowledged as References. The work contained within is entirely my own, with the following exceptions:

- TEM of hs-AZO and CdS@hs-AZO were performed by Dr Robert Mitchell
- Solid state NMR was performed by Dr Pedro Aguilar
- The CV, capacitance and IPCE were performed by PhD student Danielle Jowett

Chapter 1: Introduction

1.1: Overview

Nanoparticles have been loaded onto suitable supports for fabricating functional composite materials. These composite materials are of great interest in fields including catalysis,[1] solar energy,[2,3] photoelectrochemistry,[4,5] and sensors.[6] In this thesis, in-situ and particle deposition approaches to composite materials were designed. Highly ordered porous transparent supports were fabricated independently, and then coated with crystallized photocatalyst nanoparticles or films. The aim of this work is to investigate the synthesis and properties of a highly ordered porous photonic transparent conducting support, which have influence on the photocatalytic activity of the loaded photocatalyst materials. This chapter will present a brief review of semiconductor photocatalysts, improving their efficiency and relevant photonic behaviour.

1.2: Solar energy

Sunlight is the most abundant and sustainable source of energy. Approximately 120 thousand TW (1TW = 10^{12}W) of solar energy is received annually by earth and the annual worldwide energy consumption rate is around 15 TW. [7] However, hydrocarbon fuel is still the most common energy source at present. Hydrocarbon fuels (petroleum, natural gas and coal) are currently the most important source of energy, because of their kinetic stability, being freely provided by nature, high energy content, easy for transportation and storage. They are currently cheap and have a high energy density (33 GJ/m^3 for gasoline).[8] In 2008, United States, hydrocarbon fuels account for 80% of the energy usage.[9] In terms of worldwide,

according to the intergovernmental Panel on Climate Change (IPCC), the major energy sources consist of oil (34.6%), coal (28.4%), gas (22.1%) and nuclear energy (2.0%) in 2008.[10] The renewable energy account for 12.9% of total consumption, which even including burning of biomass (6.3%). However, the prolonged use of hydrocarbon fuels has resulted in air and water pollution, climate change and the rise of sea levels because of carbon dioxide emissions. It is indispensable to build a clean energy system in order to solve energy and environmental issues. Solar energy products such as hydrogen and carbon monoxide will play a critical role in the green energy system because it is an ultimate clean energy which can be used in fuel cells. Through photocatalysis or electrolysis, solar energy can be stored in chemical bonds (solar fuels). Photoactivated semiconductor photocatalysts have been used as strong oxidizing and reducing agents (n-type and p-type semiconductors) due to their band structures, and the photoexited state are capable of redox transformations to form solar fuels.

Since Fujishima and Honda first reported the TiO_2 electrode for hydrogen production through photoelectrochemical water splitting under UV light in 1972,[11] photocatalytic water splitting has attracted more and more attention. Materials with photocatalytic properties have been used to convert solar energy into chemical energy through reducing or oxidizing to acquire suitable products including hydrogen,[12-14] carbon monoxide,[15,16] hydrogen peroxide,[17] and formic acid.[18].

1.3: Semiconductor Photocatalysis

Splitting water into hydrogen and oxygen is a typical “uphill reaction”, involving a large positive change in the Gibbs free energy (ΔG=238kJ mol^{-1})[13] The role of semiconductor such as the TiO_2 (rutile) photoanode electrode in Fujishima-Honda solar cell is a light absorber. TiO_2 anode is an n-type semiconductor and when it was

illuminated by light whose energy is greater than the band gap energy of TiO_2, electrons in valence band was excited. The electron and hole pairs were therefore generated. The photogenerated electrons and holes will take part into the redox reactions as shown in Equation 1.

Equation 1: $2H_2O \rightarrow 2H_2 + O_2$

The half reactions are described as follows:

$$2H^+ + 2e^- \rightarrow H_2$$

$$2H_2O + 4h^+ \rightarrow O_2 + 4H^+$$

For the solar to chemical conversions, there are 3 common processes as shown in Figure 1: (i) absorption of photons by the semiconductors. When the energy of the incident light is greater than the band gap, electrons and holes are generated in the conduction and valence band, respectively; (ii) charge separation and migration to the surface reaction sites, the particle size, crystal structure and crystallinity have influence on the charge migration. Defects operate as trapping centres, the recombination between electrons and holes tend to occur in these trapping centres and the higher crystalline quality generally has less defects. The size of particles largely determines the distance for the electrons and holes have to travel to reaction sites on the surface.[19] Decreasing the distance and the trapping centres can improve the photocatalyic activity; (iii) redox catalysis and construction of the surface reaction sites for O_2 or H_2 evolution. The photogenerated electrons and holes will recombine with each other if the active sites for redox reactions do not exist on the surface, even if sufficient potential for water splitting is available.

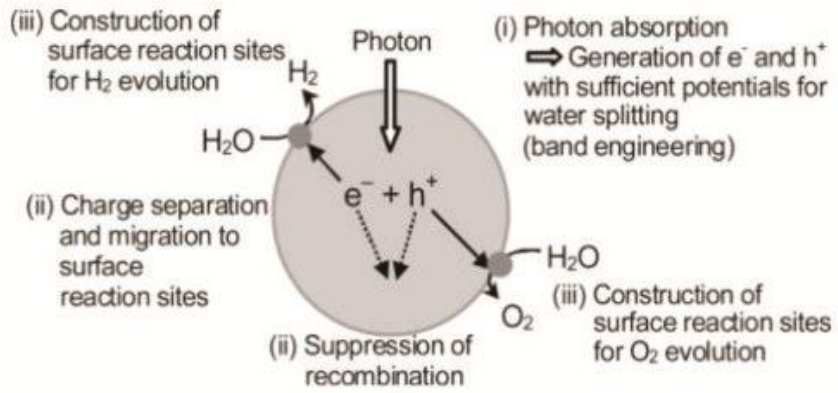

Figure 1: Main processes in semiconductor photocatalytic during water splitting.[12]

1.4: Preferred energy resource

The energy of sunlight is composed of 50% infrared light, 40% visible light and 10 % ultraviolet light (100nm to 420nm) at the top of Earth's atmosphere.[20] But the atmosphere blocks about 77 % of the ultraviolet light from sunlight, therefore, the light energy at ground level of Earth consists of 53 % infrared light, 44 % visible light and 3 % ultraviolet light.[21] This means the visible light contains much more energy than ultraviolet light.

The conduction band and valence band of semiconductors are separated by a band gap (also called band gap energy) typically expressed in eV. When the energy of incident light is greater than the band gap, the energy of light is absorbed by the semiconductor and the photoexcited electrons are therefore generated, which result in electrons and holes in the conduction band and valence band, respectively. For water splitting the free energy of activation is 238 kJ mol^{-1}. This equates to 1.23 eV or 976 nm and therefore all visible light (420 - 800 nm) can potentially be used to

split water. Of course there will be activation energies for charge transport and catalytic processes and in reality ca. 1.6 eV (< 750 nm) will be required.

Common semiconductor materials including TiO_2 (3.0 eV), WO_3 (2.8 eV), CdS (2.4 eV), CdSe (1.7 eV) and MoS_2 (1.75 eV) exhibit various band gap energies. According to Equation 2, semiconductor materials with a band gap smaller than 2.95 eV can absorb the visible light (> 420 nm).

Equation 2: Band gap (eV) = 1240/λ (nm)

Suitable band engineering techniques had been studied in order to develop new semiconductor photocalysts for water splitting under visible light irradiation. In terms of metal oxide materials, the conduction bands of stable oxide semiconductor photocatalysts are consisted of empty orbitals (LUMOs) of metal cations with d^0 and d^{10} configurations, such as Ti^{4+}, Ta^{5+} and Ga^{3+}.[22,23] The position of the valence band is basically determined by crystal structure and the bond character between metal and oxygen (O 2p orbital). Through doping some elements into conventional photocatalysts with wide band gaps such as TiO_2 and $SrTiO_3$,[24,25] an extra electron donor level was created above the original valence band, this will lead to narrower energy gap as shown in Figure 2. However it was found that the dopant tends to introduce defects in the band gap which act as a surface for electron/hole pair recombination. For example, nitrogen doped TiO_2 can photodegrade methyl orange under visible light, but lower photoactivity was obtained when increasing nitrogen doping level.[26] More information on band structures will be discussed in the next section.

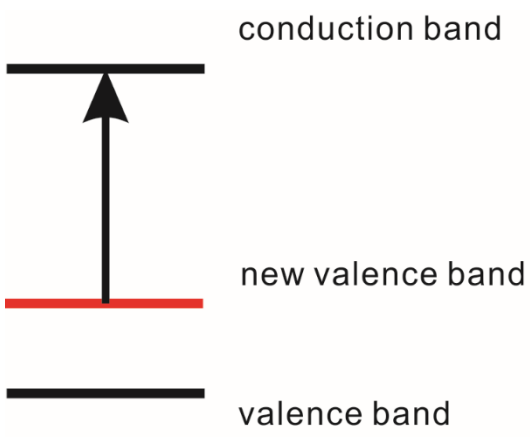

Figure 2: Band engineering for design visible light active photocatalysts.

1.5: Band position

In addition to the band gap energy, the position of the conduction and valence bands is critical when the semiconductor is in direct contact with the electrolyte (such as water). The lowest level of the conduction band has to be more negative than the reduction potential of the reactants. In terms of water splitting, the conduction band of photocatalyst should been more negative than reduction potential of H^+/H_2 (0 V *vs.* NHE); and the highest level of the valence band must be more positive than the oxidation potential of O_2/H_2O (1.23 eV *vs*. NHE). Therefore, the theoretical narrowest band gap of a semiconductor for overall water splitting is 1.23 eV.

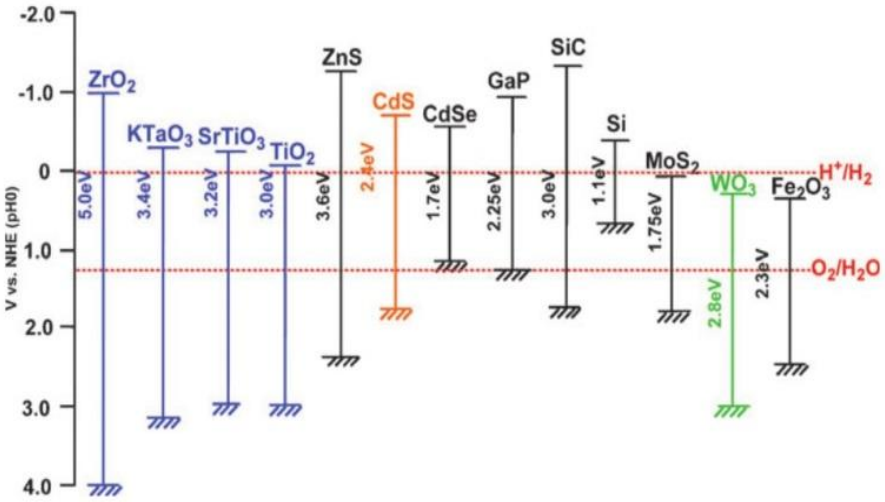

Figure 3: Band levels of semiconductor and redox potentials of water splitting at pH=0.[27]

As shown in Figure 3, the materials exhibit various band positions and band gap energy. In terms of the semiconductor materials, the redox potential of water will shift with a change of pH (-0.059 V/pH). By studying the band structures, ZrO_2, $KTaO_3$, $SrTiO_3$, TiO_2, ZnS, CdS and SiC are potential options for overall water splitting under suitable conditions or modified with co-catalysts due to their band structures. The band gap of these semiconductors determines the necessary energy for generation of electron/hole pairs. As mentioned above, solution pH and orbitals of elements of photocatalysts are important for defining the relative position of bands and redox potentials. In terms of typical metal oxide photocatalysts, the top of the valence band is composed of O 2p orbitals, and the conduction band consist of d, s or p orbitals from metal cations. The incomplete d shells of metal cations normally behave as recombination centres for electron/hole pairs, in addition, metal ions with partially filled d subshells tend to have poor photocatalytic activities due to the isolated d electrons in metal centres.

It can be seen from Figure 3 that although a material may have a suitable band gap, the band positions must span the redox potentials of the oxidation and reduction half

reactions. In addition, although CdS has a suitable band level and a band gap which can response to visible light, it is not sufficient for splitting water into both H_2 and O_2 due to corrosion. In CdS, sulfide rather than H_2O is oxidized by h^+ in valence band giving sulfur according to Equation 3. This photocorrosion reaction is often a problem of metal sulfide photocatalysts. However, CdS is still an excellent photocatalyst for H_2 evolution under visible lightin the presence of sacrificial reagent (Na_2S/Na_2SO_3, cysteine, ethanol, etc.).[28,29]. WO_3 photocatalyst is not able to reduce water to H_2 because its low conduction band level, but it is a good photocatalyst for producing O_2 under visible light when electron acceptor such as Ag^+ in present.[30]

Equation 3: $CdS + 2h^+ \rightarrow Cd^{2+} + S$

In addition, the band structure of photocatalysts can be affected by the synthesis conditions. For example, anatase and rutile TiO_2 can be obtained by varying the calcination temperature of its precursor. The band gap of anatase is 3.2 eV and rutile is 3.0 eV, and the conduction band of anatase is more negative than that of rutile[12] suggesting that the crystal structure has influence on the band position.

The smallest band gap achieved so far in a functional catalyst is 2.3 eV in NiO/RuO_2-Ni:$InTaO_4$.[31] But the improvement of light absorbing does not always end with high efficiency water splitting. At present, NiO-modified La/KTaO3 (QE = 56%, pure water, under UV),[32] ZnS (QE = 90%, aqueous, Na_2S/Na_2SO_3, $\lambda > 300$ nm) are the records in terms of quantum efficiencies (the incident photon to converted electron ratio of a photosensitive device).

1.6: Visible light active photocatalysts

Visible light active photocatalysts have drawn more and more attention recently due to the high light energy contained in the visible region. As mentioned above, WO_3 is a typical visible light active semiconductor photocatalyst for oxygen evolution in the presence of sacrificial reagent such as Ag^+ or Fe^{3+}.[33] It was found that Pt/WO_3 can be used for the degradation of CH_3CHO and acetic acid.[34] Bi_2WO_6 and Bi_2MoO_6 with Aurivillius structure also do oxygen evolution under visible light irradiation, but all of these three sorts of photocatalysts are not active for hydrogen evolution because their conduction bands are not negative enough.[22] However, most of metal oxide semiconductors for both hydrogen and oxygen evolution have wide band gap with energies only corresponding to UV light, such as TiO_2 (anatase, 3.2 eV), [35] ZrO_2 (5.0 eV)[36] and Ta_2O_5 (4.0 eV).[37] Therefore, elemental doping has often been attempted for the synthesis of visible light active photocatalysts. The idea is replacing some crystal lattice points of the host material with foreign elements. For example, when nitrogen was doped in Ta_2O_5 at high temperature (1123 K) under a flow of NH_3, the band gap was reduced from 3.9 eV to 2.4 eV in TaON and 2.1 eV when Ta_3N_5 formed, this depends on the doping level and is controlled by adjusting the experimental conditions (flow rate, heating time, etc.).[38] The bottom of conduction band is fixed (5d orbitals in Ta), the top of valence band was raised due to contributions N 2p orbitals after N^{3-} replacing O^{2-} in the crystal lattice as shown in Figure 4. The doped products of Ta_2O_5 (TaON and Ta_3N_5) exhibit high efficiency of oxygen evolution under visible light in presence of sacrificial $AgNO_3$.[39] Although the idea of doping is an excellent strategy to prepare visible light responsive materials, the activities of photocatalysts sometimes decrease drastically after doping because the doping tends to introduce recombination centres between photogenerated electrons and holes. But the activities of photocatalysts can be improved with suitable dopants.

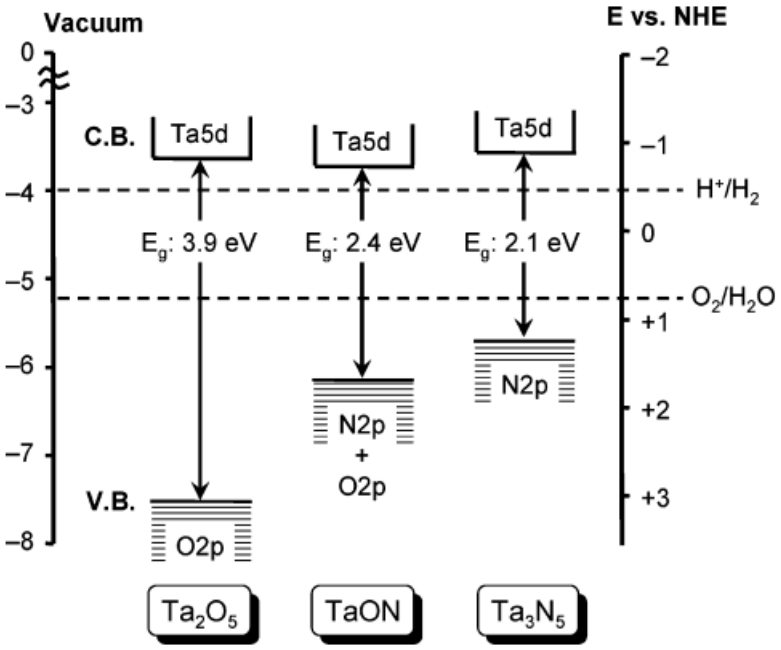

Figure 4: Schematic illustration of band structures of Ta_2O_5, TaON and Ta_3N_5 in literature.[40]

$SrTiO_3$ (3.2 eV) was doped with Rh to give visible light driven photocatalyst with a band gap of 2.3 eV.[41] The $SrTiO_3$: Rh shows an efficiency for hydrogen evolution under visible light. Although GaN and ZnO are only active under UV light, GaN: ZnO solid solutions can respond to visible light by heat treatment of a mixture of Ga_2O_3 and ZnO at 1123K for 30 h under NH_3 flow.[42] As shown in Figure 5, the compositions between GaN and ZnO play an important role in visible light absorption.

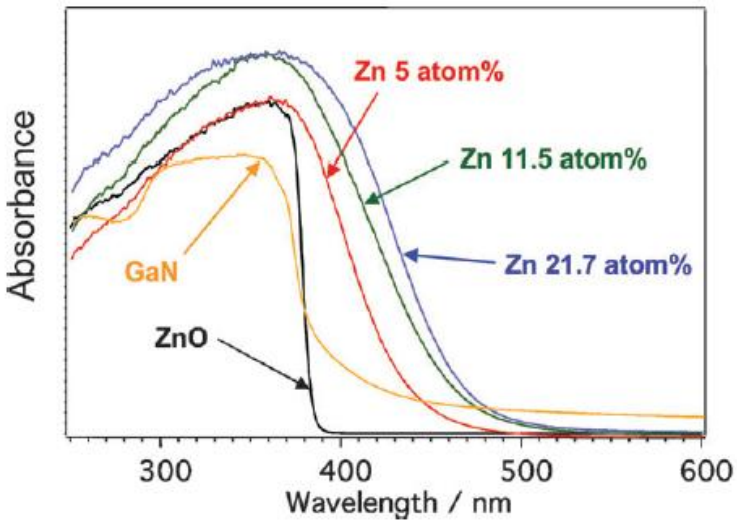

Figure 5: UV-vis absorbance spectra of GaN:ZnO photocatalysts in various Zn ratio.[43]

In addition to CdS, the CdS:ZnS solid solution can be used for hydrogen evolution under visible light irradiation due to their shared crystal structure.[44]

1.7: Photocatalytic efficiency

Quantum yield (the rate at which material undergo a given event per photons absorbed per unit time) is a common way to express the efficiency of a photocatalyst. The output of a photocatalyst such as photocurrent or chemical products has a relationship with the amount of photons absorbed by the photocatalyst. The quantum yield of a photocatalyst material can be expressed by Equation 4.[45] The quantum yield of a photocatalyst material is normally valid for a specific range of wavelength gives the quantum yield varies with the changing of light wavelength absorbed. In terms of the calculation of quantum yield, not all of the incident photons are considered since the possibilities of reflected photons.

Equation 4: $$\text{Quantum yield}\ (\%) = 100 \times \frac{\mathrm{N_{product}(mol\ s^{-1})transformed}}{\mathrm{N_{photons}(mol\ s^{-1})absorbed}}$$

In addition, when a photocatalyst is irradiated by light with greater energy than its band gap, the redox reaction should proceed. Quantum efficiency (QE) is used when the action spectrum of the irradiation source in unknown, especially for visible light driven photocatalysts. For photoelectrochemical processes, the efficiency of photocatalysts is commonly described by the incident photons to current conversion efficiency (IPCE). This efficiency can be defined by Equation 5 below.

Equation 5: $$\text{IPCE}\ (\%) = 100\ \times \frac{\text{Number of moles charge carriers collected}}{\text{Number of moles photons absorbed}}$$

1.8: Electrochemistry

Electrochemical methods are commonly used to evaluate potential semiconductor materials as photocatalysts. By supporting the material of interest on a conductive substrate (such as FTO or ITO glass), a voltage can be applied to provide energy for chemical reactions in the absence of light irradiation. Redox catalysts are often required to increase the reaction kinetics. In addition to the electrical properties of materials, electrochemistry has been used for study the roughness of metal oxides such as TiO_2 thin film.[46]

1.9: Photoelectrochemistry

Photoelectrochemistry is a common method used to evaluate photocatalyst materials under various light and electrical bias conditions. Photocatalysts can be supported on a conductive substrate, and illuminated under a bias voltage and

current or chemical products monitored. Comparison of dark and illuminated responses allows for investigation of photochemical processes.

In terms of a photocatalyst semiconductor, there is a group of the semiconductors acting as both light harvester and catalyst: the hydrogen formed by photoexited electrons can occur on the surface of the semiconductor and the holes perform oxidation at an external electrode. Alternatively, the semiconductor harvest photons and transfer the photogenerated electrons to external electrode and catalytic oxidation occurs with holes at the surface. In the process of transferring charge carriers, there is a possibility of recombination between electrons and holes. Structured transparent conductive oxides can be applied to reduce the recombination, by increasing the rate of charge carrier separation and improve the efficiency. Unfortunately, many photoelectrodes are not the best catalysts and it is usually necessary to add a co-catalyst to the surface to increase the efficiency.

1.10: Photocatalytic redox of water in sacrificial system

Sacrificial reagents are often used in photocatalysis of water since the redox of water is kinetically slow. When the photocatalytic reactions for water redox undergo in a system with sacrificial reducing reagents (such as methanol and S^{2-}), the photogenerated holes tend to oxidize the sacrificial reagent irreversibly instead of water.[47,48] This process can enrich electrons in the photocatalytic system, therefore enhance the hydrogen evolution on the photocatalyst or at a counter electrode such as Pt wire or Pt nanoparticles. In practical hydrogen production, this reaction will be economic when biomass and abundant compounds in nature or industries can be used as reducing reagent.[49] Alternatively, the photogenerated electrons on conduction band can be used to reduce the oxidizing sacrificial reagents such as Ag^{+} and Fe^{3+} irreversibly which will end up with an h^{+} dominant

system with enhanced oxygen evolution efficiency. In this case, the reaction is considered as half reactions of water splitting and can be employed for testing reactions of photocatalytic hydrogen and oxygen evolution.

1.11: Improvement of photocatalytic activity

1.11.1: Surface area

The surface area in contact with the solution or electrolyte is an important property of photocatalyst materials. A material with high surface area normally means more active sites per gram of material for reactive species to be attached to. For example, mesoporous carbon doped TiO_2 for rhodamine B degradation exhibits higher activity with increasing surface.[50] TiO_2 (P25)-graphene nanocomposite photocatalyst possessed greater absorptivity with increasing surface area, hence a significant improvement in photodegradation of methylene blue has been achieved. [51] In addition to modify the morphologies of photocatalyst materials, high surface area photoactive materials can be prepared by loading of catalyst species onto structured support which will be discussed in the next section.

1.11.2: Defects, crystallinity, morphologies of photocatalysts

In terms of the photocatalyst materials on the nano-scale, smaller nanoparticles tend to be more active in photocatalytic reactions than larger nanoparticles. This is because of the smaller nanoparticles have greater surface area and shorter distance between the photogenerated e^-/h^+ pairs and the surface. The photocatalytic activity of $NiO/NaTaO_3$ was enhanced significantly with the doping of La ions.[32,52] After doping, it was observed that the particle size of La doped $NaTaO_3$ crystal (0.1

to 0.7 μm) is smaller than the pure $NaTaO_3$ (2 to 3 μm). In addition, a step shape ordered nanostructure was also observed after the La doping. According to this study, the hydrogen evolution sites on the edge of the nano-step was separated from the oxygen evolution sites on the groove of the nano-step in surface as shown in Figure 6. This separation of electrons and holes can improve the efficiency of water splitting by prevent it from back reaction to water. It was also found that doping of Ca, Sr or Ba show same effect as La doping in terms of the formation of characteristic morphology of $NaTaO_3$ which result in an improvement of photocatalytic efficiency.[53] It was found that the La doping in $NaTaO_3$ prolonged the lifetime of photogenerated electrons in conduction band through time-resolved IR measurements.[54]

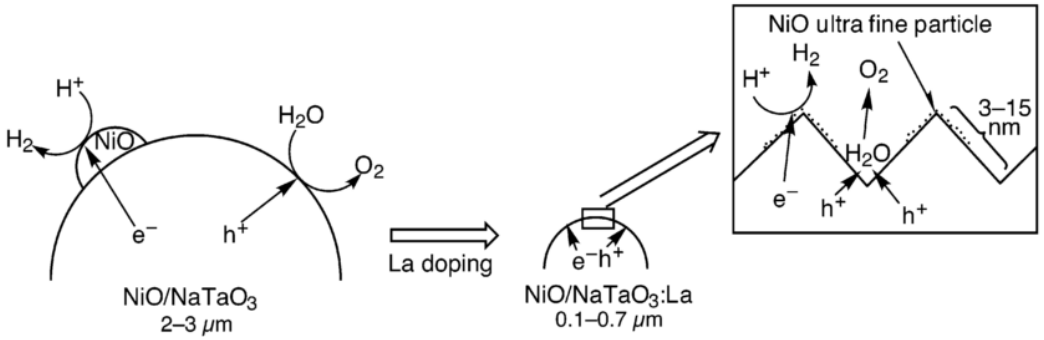

Figure 6: Mechanism of highly efficient photocatalytic water splitting over $NiO/NaTaO_3$: La photocatalysts.[32]

1.11.3: Co-catalysts

Co-catalysts such as Pt was first loaded to TiO_2 for H_2 evolution in 1982,[55] because although the photogenerated electron/hole pairs possess thermodynamically sufficient potentials for redox reactions, the recombination will occur if there are no active sites on the surface of photocatalysts. The most common co-catalysts for

hydrogen evolution had been used in previous works are NiO, RuO_2 and Pt. In a water splitting system, the back reaction to form water can hardly proceeds in the presence of NiO and RuO_2. It was reported that powdered $SrTiO_3$ can split water into hydrogen and oxygen efficiently when loaded with NiO.[56] In the presence of NiO co-catalyst, a NiO/Ni double layer structure was usually formed after water redox reaction and this double layer structure can improve the migration of electron from photocatalyst substrate to co-catalyst.[57]. In addition, the $PbWO_4$ exhibits efficiency in hydrogen evolution under UV light irradiation when RuO_2 co-catalyst was employed.

In terms of the co-catalyst for oxygen evolution, it was reported that the oxygen generation rate of $Sm_2Ti_2S_2O_5$ was improved by over 5 times when loaded with 0.25 wt. % of IrO_2 colloid.[58]

1.12: Structured materials for application to photoelectrochemistry

For further enhancement of photocatalytic activity, efforts had been made to improve the light absorption and collection in solar devices. More products can be formed by increasing exciton formation. Reflective silver back contacts and deposition of Al_2O_3 nanoparticles for light scattering have been employed on silicon nanowire photoelectrodes, and it was applied in a photoelectrochemical cell which shows 90 % internal quantum efficiency (IQE) in wavelength range from 400 to 900 nm.[59] Gold nanoparticles were also employed to enhance the light absorption. Gold nanoparticles were dispersed on the surface of photocatalyst, and Surface Plasmon Resonance (SPR) effects caused by the dispersion have influence on light absorption.[60] However, noble metals such as gold and silver are never the first choice for chemical experiments. Cheaper and more efficient ways are necessary for light collection and absorption.

In addition to the noble metals, it was found that the morphology of materials can affect light absorption. Periodic 1D, 2D and 3D structured materials were found to have influence on the propagation and group velocity of electromagnetic radiation. Theoretical studies suggested that as the diameter of a silicon nanowire became smaller than 20 nm, the photon dispersion relation can be modified (as a result of photon confinement) such that the group velocities of photons would reduce significantly relative to the bulk value resulting in greater light absorption.[61] Based on this, structured material, as a support can potentially enhance the photocatalytic activity of the photocatalyst within it. The structured materials that have influence on photons are also called photonic crystals.

1.12.1: Photonic crystals

Photonic crystals (PCs) are designed to affect the propagation of electromagnetic waves and increase the probability of light absorption. The photoactivities of materials structured into photonic crystals can give an increase in the efficiency of photocatalytic reactions. In photonic crystals, when compared to the materials without photonic structure, modular variation in refractive index of the nanostructure can be exploited to trap photons and increase the possibility of light absorption to enhance the photocatalytic efficiency.[62] Besides, the nano-structuring involved bestows an inherent increased surface area when compared to a bulk material. Literature reports had already proved that the photonic crystal can enhance the efficiency of solid dye-sensitive solar cells (DSSCs).[63,64]

1.12.2: Photonic effects

Within the photonic crystal materials, reflection of light as shown by Bragg diffraction of certain wavelengths is observed.[65,66] As shown in Figure 7, which can be considered as a 2D photonic crystal, when the photonic crystal material has greater refractive index than the external media, the internally emitted light will reflect back and back again between the top and the bottom of surfaces until it is finally reabsorbed.[67]

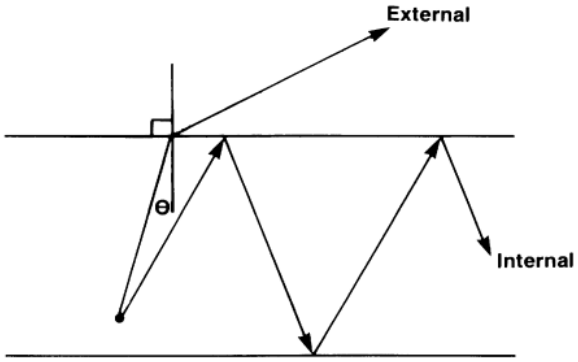

Figure 7: The internal spontaneous emission can be trapped and eventually reabsorbed in a solar cell with plane parallel geometry.

Photonic crystal materials normally consist of an ordered periodic structure, comprising a regular array of objects of similar dimension to the wavelength of light of interest. The structures of photonic crystals are composed of periodic materials with highly ordered 2D (nanorods) or 3D (nanospheres) array, or the inversed nanostructures of them. To achieve the photonic behaviour, there must be a difference in refractive index between the photonic crystal material and the external media (air, water or electrolyte). These photonic structured materials can prevent the light from traveling in certain directions over a certain wavelength range, which is reflected if the source of illumination is external or the emission can be suppressed if the source of illumination is internal. This wavelength region is known as the

photonic band gap and is characterized by a photonic stop band in UV-vis reflection spectrum (DRUVS).[68]

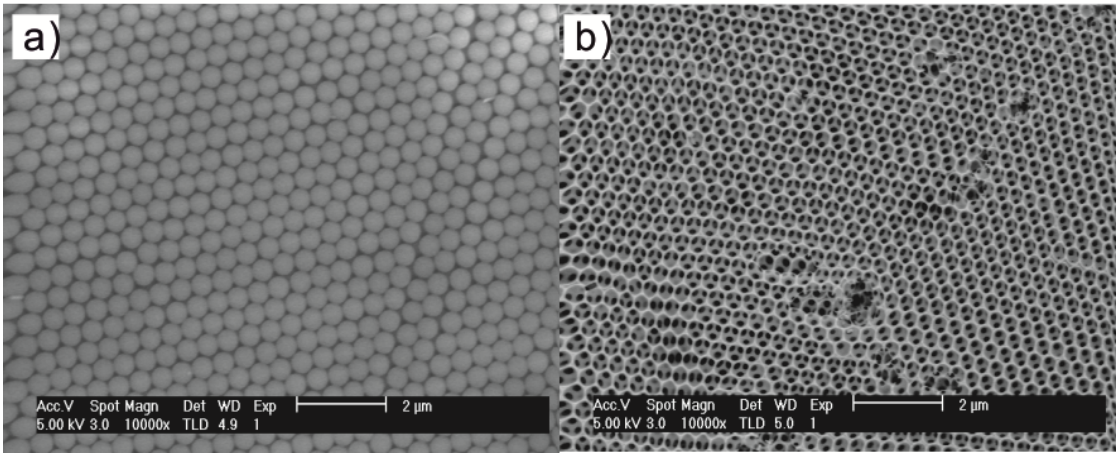

Figure 8: SEM images of 3 dimensional opal and inverse opal photonic crystal materials. a): close packed opal structure polystyrene (111) planes and b): inverse opal structure FTO (111) planes.

As shown in Figure 8, the ordered periodic structure of both opal and inverse structured materials, with difference of refractive index between polystyrene (1.6) and voids (air, 1.0) in Figure 8a, and between FTO (2.5) and voids (air, 1.0) in Figure 8b should show photonic effects.

Compared with the opal structured materials, inverse opal materials such as three dimensional ordered macroporous (3DOM) semiconductors supply more pore surface. Therefore, nanoparticles or films photocatalysts with suitable band gap can be loaded onto the walls of 3DOM semiconductors homogeneously, the absorption and emission of photocatalyst can be improved if the band gap of photocatalysts overlapping with the photonic stop band. Besides, when the energy of band gap of the semiconductor coincides with the position of photonic (energy eV = 1240/λ) stop band, the recombination between electrons and holes can be suppressed.[69] Figure

9 shows a photonic stop band of three dimensional ordered macroporous FTO (mac-FTO) electrode, the propagation of light of energy around 2.38 eV (equals to 520 nm) is forbidden within the photonic FTO crystal.

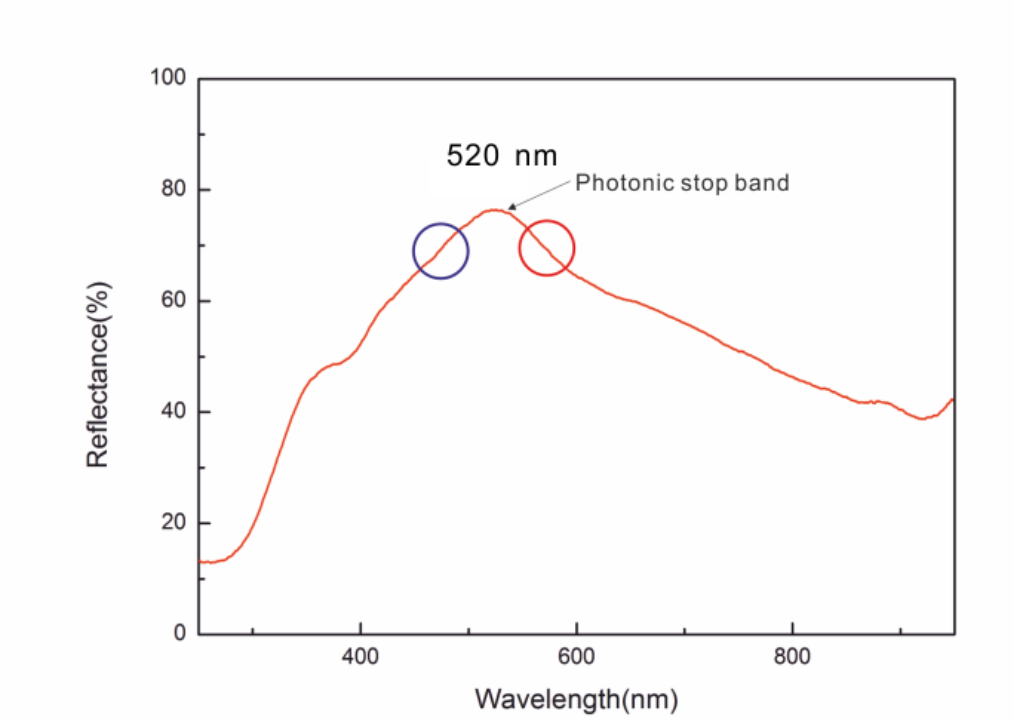

Figure 9: DRUVS spectra of a photonic stop band of mac-FTO film which centred at 520 nm, the slow photons were normally observed in the red and blue circle.

When the energy of photons absorbed is greater than the band gap of the photocatalyst, the electron will be excited to a more negative energy level than the bottom of conduction band. After relaxation to the bottom of the conduction band, further radiative relaxation by band gap emission will be suppressed by the photonic semiconductor as shown in Figure 10. In a literature report, $TbLaF_3$ nanoparticles were deposited on 3DOM SiO_2 photonic crystal and the emission band gap and photonic stop band overlapped, resulting an enhancement of the excited state lifetime from 2.8 ms to 4.0 ms being observed.[70] And it was also found InAs quantum dots (QDs) loaded on GaAs photonic crystal showing much longer lifetime (86 ps) than the lifetime (4.38 ps) of InAs QDs in bulk GaAs.[71]

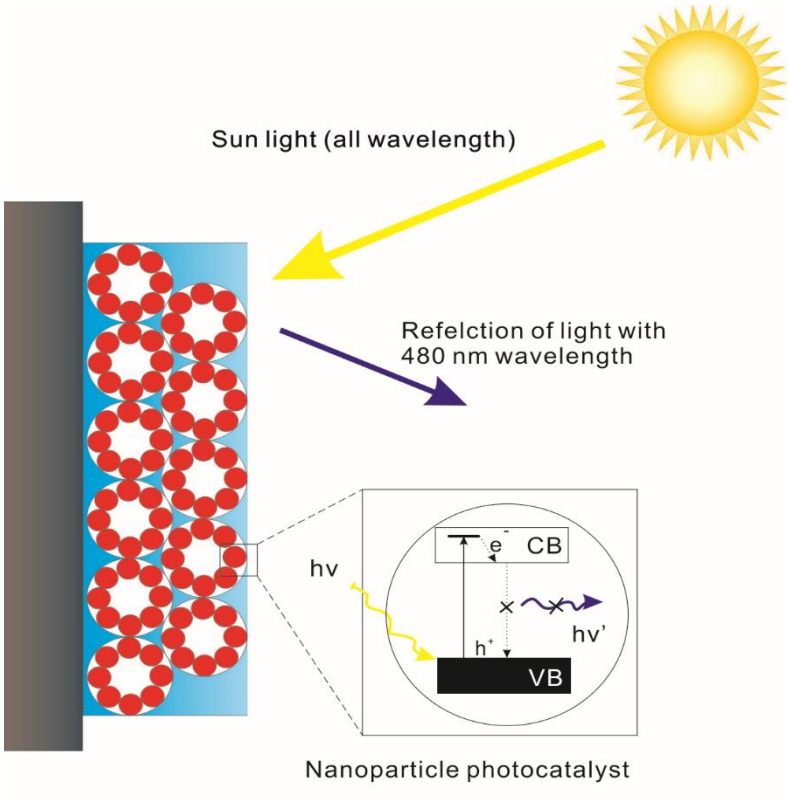

Figure 10: Schematic of the inhibition of spontaneous electron/hole recombination for nanoparticle photocatalyst embedded mac-FTO film with a stop band at 480 nm.

In addition to suppression of recombination, it has been reported that multiple light scattering effects can increase the effective light absorption in comparison to bulk materials was observed.[72] Another important effect of photonic crystal is known as slow light phenomena, similarly, this photonic effect can increase the light absorption efficiency of photocatalysts within photonic crystals as well. Photons with energy directly below and above the photonic stop band position (the position of red and blue circle in Figure 9) have a slower group velocity within the photonic crystal.[73] The wavelengths affected are known as slow photons. In terms of theoretical research, it was predicted that a semiconductor material with band gap energy on the red or blue edge of the photonic stop band has a longer effective path length of slow photons, hence the light absorption was improved.[74-76] Generally, broader stop

bands tend to be advantageous for slowing light with larger range of wavelength. It was found that the slow photons in photonic TiO_2 increases the photodegradation rate of methylene blue by a factor of 1.7 in comparison to that without slow photons.[77]

1.12.3: Definition and modification of photonic stop band

By a similar principle to that of X-ray diffraction from an atom lattice, Bragg diffraction of electromagnetic radiation was caused by photonic crystal lattice (express as photonic stop bands) as a result of diffraction from different lattice planes.

In terms of an oriented photonic material, singular photonic stop band is observed due to the one specific crystal plane. An approximate expression for the stop bands position of photonic crystals on UV-vis spectra can be calculated by a modified version of Bragg's and Snell's law. The position of photonic stop band with an angular dependence can be expressed in Equation 6:

Equation 6[78]*:* $\lambda_{max} = \frac{2d_{hkl}}{m}\left[n_{avg}^2 - \sin^2\theta\right]^{1/2}$

Where λ_{max} is the wavelength of stop band maximum (wavelength with maximum intensity in DRUVS spectra or minimum intensity in UV-vis transmission spectra), m is the order of Bragg diffraction, d_{hkl} is the separation distance of the lattice planes, n_{avg} is the average refractive index of the walls materials and voids and θ is the angle of incident light irradiation. Then h, k and l are employed to define the crystal planes within the photonic crystal lattice. The value of $\sin^2\theta$ increases with larger θ (form 0 to 90^o) resulting in a decrease value of λ_{max}, which was known as blue shift of stop band position. It was proved that an ordered polystyrene film exhibits a blue

shift of stop band position from 570 nm to 450 nm when θ is changed from 0 to 75°.[79]

For a photonic crystal material with random orientation, such as powdered macroporous photonic crystals, multiple photonic stop bands are normally observed if the light was reflected from multiple crystal planes. To do the calculations in this situation, the angular dependence of the stop band is relaxed due to the random orientation of the crystal planes. The calculation of the stop band position in this case is expressed in Equation 7, where φ and *n* present the filling factor and the refractive index of the solid wall materials, respectively, and n_{void} is the refractive index of the voids.

Equation 7[78]: $\lambda_{max} = \frac{2d_{hkl}}{m}[\varphi n + (1-\varphi)n_{void}]$

Different from the powder macroporous photonic materials, there is no random orientation in film materials such as mac-FTO and 3DOM silicon film.[80,81] For example, in the UV-vis transmission study of 3DOM silicon film and polystyrene (PS) template film as shown in Figure 11.[80] The PS crystal film showed the existence of a photonic stop band centred at 1390 nm due to Bragg's diffraction. For the 3DOM silicon film, a broad photonic stop band and a diffraction peak were observed at around 1350 nm and 440 nm, respectively. The appearance of the quite broad peak at 1350 nm (compared with the photonic stop band of PS templates) was caused by several factors, including the imperfect replication or multiple orientation of the PS template. The 3DOM structure tends to be considered as a defect-free structure in theory, however, in this 3DOM silicon case, the imperfects from replication of the templates and the surface oxidation of 3DOM silicon (refractive index of Si and SiO_2 equals to 1.95 and 1.12, respectively) will lead to deviations from theory.

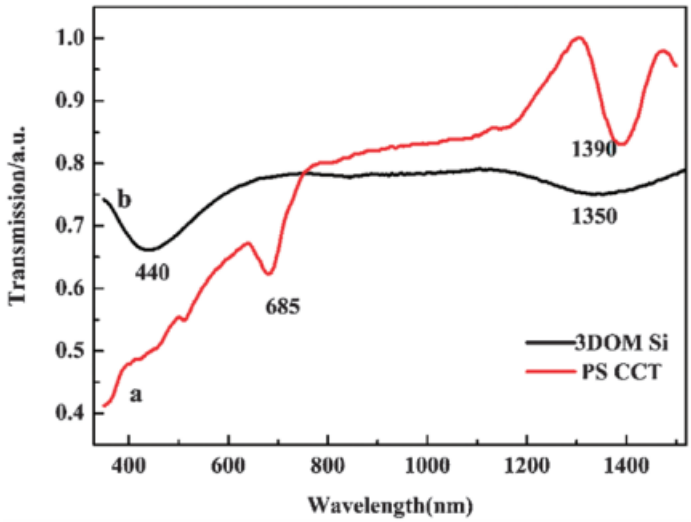

Figure 11: UV-vis transmission spectra of PS colloidal crystals (582 nm) and 3DOM silicon.

The photonic stop band position of a certain structured material is size and angular dependent, as concluded from a combination of Bragg's and Snell's law.[82] In terms of mac-FTO film, where n is the refractive index of the FTO crystal, n_0 is the refractive index of voids, D is the periodicity order of photonic crystal film and φ is the filling factor, therefore the photonic stop band position (λ_{max}) can be calculated by Equation 8. In terms of the 3DOM photonic crystals, the periodicity order is determined by the pore size and the thickness of walls. But in practice, the pore size rather than wall thickness is commonly modified to control the position of photonic stop band due to the ease in methodologies. For an ideal mac-FTO film with face centred cubic structure, the maximum filling factor φ is 26 %. Changing the periodicity order D by using template sphere of various diameters can adjust the position of the photonic stop band. It was found that for FCC opal or inverse opal structured photonic crystals, the most effective planes in the Bragg reflection are those with Miller indices all odd or all even such as (111) plane.[78] Diffuse Reflectance UV Visible Spectroscopy (DRUVS) is the most common technique for stop band position measurement.

Equation 8[83]: $\lambda max = \frac{2d_{hkl}}{m}[\varphi n^2 + (1-\varphi)n_0^2 - \sin^2\theta]^{1/2}$

$$d_{hkl} = \frac{D\sqrt{2}}{[h^2 + k^2 + l^2]^{1/2}}$$

1.13: 3DOM Transparent Conductive Oxides (TCOs)

1.13.1: Applications of TCOs

Transparent conductive oxides (TCOs) have multiple applications for solar energy utilization and energy savings.[84,85] Relying on the electrical conductivity, TCOs can be very useful as a current collector and transporter in solar cells. The TCOs for solar energy utilization is normally coated on a transparent or non-transparent substrate as thin films with a thickness from 10 nm to 1000 nm through sputter deposition, sol-gel deposition, or chemical vapour deposition (more details about the methodologies are discussed in section 2.1.1). The most common materials used in recent days for fabrication of conductive transparent substrate are aluminium doped zinc oxide (AZO) films, fluorine doped tin oxide (FTO) film and indium doped tin oxide (ITO) film, made into conductive substrates with electrical resistivity of 1.5×10^{-4} Ω cm^{-1} by planar magnetron sputtering deposition,[86] 3.8×10^{-4} Ω cm^{-1} spray pyrolysis technique,[87] and 9.5×10^{-4} Ω cm^{-1} by sol-gel process,[88] respectively.

In addition to planar transparent conductive thin film coatings, TCOs can also be structured into non-planar morphologies including photonic crystals. TCO photonic structures do not absorb in the visible spectrum but can appear brightly coloured due to the photonic properties of the structures. As a result of optical diffraction from

the crystal lattice planes, the macroporous photonic materials exhibit colourful reflections similar to those observed in natural opals[78]

Inverse opal is an attractive structure among several types of 3DOM photonic crystal structures because it can be easily fabricated, it is stable, and offers larger void fractions.[89] Since the photonic crystals with inverse opal structure can be fabricated from readily available polystyrene spheres suspension in variety of sizes, the porosity and the stop band position of the photonic crystals can be easily controlled. Besides, the thickness of the 3DOM photonic crystals (number of the porous layers) can be easily tuned by changing concentrations of the polystyrene sphere suspension or the conditions for the deposition of PS templates.

1.13.2: Techniques for fabrication of 3DOM photonic films

In terms of the preparation of these periodic porous structures, the void spaces among spheres in the colloidal crystal template can be infiltrated with different kinds of precursor solutions that penetrate the sphere template and are transformed into a crystal solid by heat treatments. By removing the template sphere, a solid skeleton that surrounds the air pores is left in the original locations of the template spheres. Generally, hydrofluoric acid is employed to remove template silica spheres by an etching method; as for the polymer spheres, these can be removed by dissolution in appropriate solvent such as acetone or by calcination. This processes can not only create the macropore voids, but also control the skeleton formation.

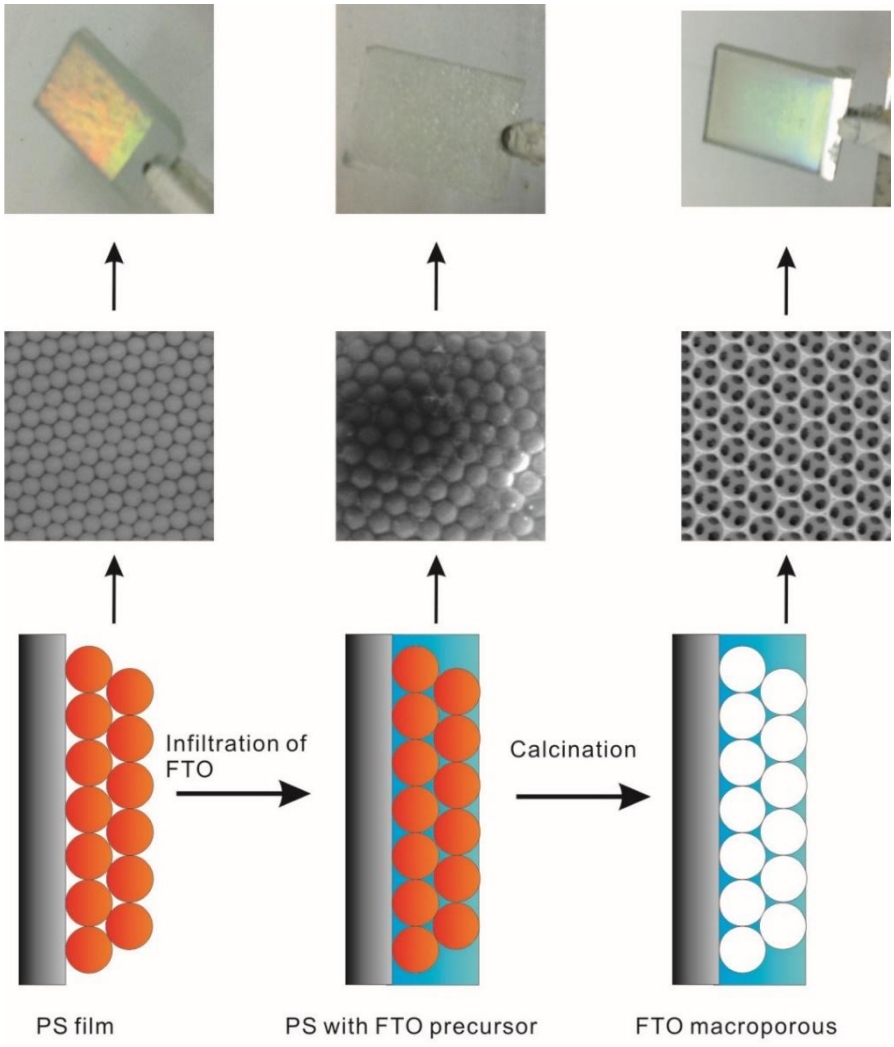

Figure 12: Schematic diagrams, SEM images and photographs of the template polystyrene sphere film deposited on a FTO glass substrate (left); template polystyrene film infiltrated with FTO precursor (middle) and the mac-FTO obtained by removal of template polystyrene sphere film with calcination in this work.

Figure 12 shows an example of a mac-FTO film fabricated in this thesis. The processes consists of three simple steps: deposition, infiltration and removal. In the first step, a clean FTO glass substrate was stood in a glass vial with polystyrene sphere suspension in certain concentrations and the polymer film was achieved after few hours under certain temperatures; in the next step, polystyrene sphere film was soaked in FTO precursor solution with a vacuum being applied; in the last, the polystyrene sphere template was burned off under high temperature in air and the

FTO crystal solid skeleton formed. The photographs in the left and right in Figure 12 exhibit opalescence, these visual appeal can be considered as a result of the photonic properties of 3DOM structure as mentioned in section 1.5.2. Other methods including sol-gel chemistry, in situ polymerization, chemical bath deposition, chemical vapour deposition, atomic layer deposition and co-deposition of template spheres with nanoparticles have also been applied for the fabrication of 3DOM structure materials.[90]

As the inverse opal structure is a replication of the typically face cantered cubic opal structure, the wall materials can be considered as surrounding by face cantered cubic air spheres. And this air spheres are interconnected through nano-windows at where the template spheres touched. For a face cantered cubic template, each air sphere is connected to 12 nano-windows. But this 3DOM structure are always obtained with imperfections, for the colloidal spheres with diameter in submicrometer range, a decrease of diameters by 10-30% due to shrinkage of the precursor solution or/and the template was observed in many cases.[90]

1.13.3: Techniques for the synthesis of photocatalysts

The methods for synthesis of photocatalysts are usually depend on the preferred crystal structure and types of starting materials.

Some metal oxide photocatalysts are commonly synthesized by a solid state reaction, of which the starting materials are calcined at high temperature under air to achieve the products such as the synthesis of TiO_2 (1273K , 2 hr),[91] $LiTaO_3$, $KTaO_3$ (1420K , 10 hr)[92] and $BaCeO_3$ (673K, 6 hr).[93] The starting materials in solid state reaction are mostly metal oxide and/or alkali and alkaline earth carbonates.

Compared with solid state method, relatively low calcination temperature and short calcination time are employed in polymerization complex method. Photocatalysts such as $K_2La_2Ti_3O_{10}$ was prepared by both polymerization complex method and solid state reaction method.[94] In terms of the polymerization method, the product was obtained with a heat treatment at 1173 K for 2 h; as for the solid state method, the same product was obtained with a calcination at 1173 K for 72 h and at 1323 K for 48 h. Comparing the products prepared at same calcination temperature by polymerization complex method (1173 K, 2 h) and solid state reaction method (1173K, 5 h), the former showed better crystallinity. This indicates the polymerization complex method can relatively increase the crystallization rate.

Another common method used for the synthesis of photocatalysts is the hydrothermal method. For example, TiO_2 prepared by hydrothermal treatment under different conditions was attempted, brookite (pH 10, 473 K for 24 h), rutile (pH 6, 473 K for 24 h) and a mixture of rutile and anatase (pH 6, 433 K for 24 h) were obtained under these conditions.[95] In the presence of sodium, potassium or calcium cation in basic solutions, $Na_2Ta_2O_6$ (383 K for 4.5 h), $K_2Ta_2O_6$ (443 K for 6 h) and $Ca_2Ta_2O_7$ (373 K for 120 h) were also prepared by hydrothermal methods.[95]

1.13.4: Techniques for the decoration of 3DOM photonic film with nanoparticles

The most straightforward and common method used for deposition of nanoparticles on photonic films is the chemical bath method. The photonic substrate is immersed in a precursor solution, allowing the adsorption of metal ions on its surface, after that, the substrate is separated from the solution by transfer or heating the precursor solution to evaporation. Depending on the material of interest, the substrate is transferred to a second precursor solution (this process can be repeated for multiple

cycles to obtain the desire loading or number of layers) or a furnace oven for a heat treatment.

Planar films are often deposited on oxide substrates by chemical bath method, for example the CdSe films on mesoscopic TiO_2 substrate,[96] ZnO thin films on microscope glass[97] and CdS films on glass substrate.[98] Chemical bath method was also employed for the deposition of CoO and Co_3O_4 on nitride material such as Ta_3N_5.[99]

In terms of porous structured materials, metal nanoparticles such as silver[100] and gold[101] in 5-10 nm had been loaded into 3DOM TiO_2 films by chemical bath deposition of $AgNO_3$ and $HAuCl_3$, respectively. Photocatalysts such as CdS had been loaded into 3DOM TiO_2 by chemical bath deposition as well.[102] The size of particle can be tuned by the chemical composition and concentration of the precursor solution, but it seems that other conditions can affect the size of particles. Even although the nanoparticles size is difficult to control by the chemical bath deposition method, it still has been employed to decorate a wide variety of materials on particulate, planar and porous substrates because the chemical bath deposition is simple, effective and tends to give a homogeneous deposition.

Many other methods have been used for the films and nanoparticles deposition such as chemical vapour deposition, electrochemical deposition and photodeposition.

1.14: Project aims

As discussed in this chapter, there are many factors that have influence on the efficiency of photocatalytic reactions. The efficiency of semiconductor

photocatalysts can be improved by controlling the size because the smaller particles can supply larger surface area and the recombination of photogenerated electron/hole pairs can be reduced by decreased distance to the surface for taking part in chemical reactions, in comparison to larger particles. The photonic crystal structured materials will be applied as a support for the nanoparticles due to the benefits of the photonic properties. To achieve that, a composition of nanoparticle photocatalyst loaded homogeneously in transparent photonic crystal film will be fabricated, and the photocatalytic activity will be evaluated by comparison of the nanoparticle photocatalyst on varied structure substrates.

The mac-FTO film and hollow sphere AZO film on FTO glass substrates with stop bands in visible light region will be fabricated by replica from a polystyrene sphere templates. CdS nanoparticle will be synthesized, and a general method will be applied for the deposition of CdS nanoparticles in mac-FTO films. Chemical bath technique will also be applied for the CdS decoration in mac-FTO as a comparison to the nanoparticle deposited CdS/mac-FTO samples. Hollow sphere AZO films will be decorated with CdS by chemical bath technique to evaluate the influences of photonic crystal with different structures.

The fabrication of mac-FTO and hollow sphere AZO will be described in chapter 2, and the subsequent decoration of CdS nanoparticles within the photonic crystals will be presented in Chapter 3 and other catalysts such as iron oxide and carbon nitride will be synthesized and deposited on mac-FTO which will be presented in chapter 4.

Chapter 2: Synthesis of highly orderd photonic TCO films

2.1: Introduction

2.1.1: Techniques for the synthesis of planar TCO films

In the solar energy field, TCOs are commonly used for the synthesis of thin films on various substrates due to the good optical and electrical properties of TCOs. Sputter deposition[103] had been widely used for uniform TCOs thin film coatings on glass, polymers and metals. Essentially, a plasma is filled with inert and/or reactive gases under low pressure, and energetic ions in the plasma dislodge material from a solid plate or cylinder of raw material of film and deposit these atoms on the substrates as a uniform film. Sol-gel deposition are also commonly used for TCOs coating without employing a vacuum. Typically, sol-gel deposition[85] involves immersion of substrate in precursor solution, and then withdrawal at a controlled rate. Subsequent calcination is normally employed for crystallization and removal of ligands. Alternatively, chemical vapour deposition (CVD) is also a popular method, a substrate is exposed to a vapour of precursor by heating to achieve the desired thin film.[104] A spray pyrolysis can be considered as branch of chemical vapour deposition: a fluid or mist containing the precursor solution commonly is sprayed onto a hot substrate by an air brush. Spray pyrolysis is a quite common method used for deposition of metal oxide thin films on hot glass.[105] Besides, some electrochemical techniques including cathodic electrodeposition from a chemical precursor solution[106] and anodic conversion[107] of a metallic surface are used in TCOs film deposition on glass as well.

2.1.2: Substrates for the synthesis of planar TCO films

To optimize the coating of TCOs, the substrate materials for TCOs coating must be considered. The most widely used material as a substrate for TCOs coatings is glass. Float glass is a highly standardized product and the most common glass. It is characterized by uniformity and flatness almost on atomic scale.[108] Figure 12 shows the UV-vis transmission spectra of standard float glass with varied amount of iron oxide doping. The low content of iron oxide in float glass enhanced the transmittance, especially in the UV range.[109] For a conductive glass loaded with photocatalysts, the transmittance is an important property for the loaded glass substrate used in photoelectrochemistry experiments, because the light irradiation normally come from the back of the glass substrate. In addition, the melting point of the substrate must be considered when the heat treatment temperature for the coated materials is very high.

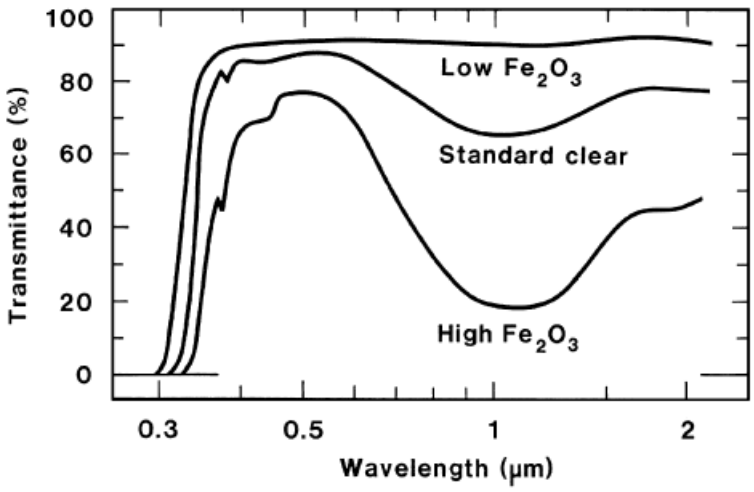

Figure 12: UV-vis transmission spectra of standard float glass with three different amount of Fe_2O_3.

2.1.3: Common materials for the synthesis of planar TCO films

For the purpose of supporting photocatalytic reactions, the ideal materials for the synthesis of either flat or nanostructured thin films should be cheap, non-toxic, transparent and conductive, and ideally a well-established technology. The TCOs thin films studied in this thesis were coated on borosilicate glass and quartz to make transparent conductive substrates with high transparency in visible and near infrared spectra rage and high electrical conductivities. Thin films made from metal oxides such as indium, zinc, titanium and tin oxide crystals[110] are widely used for fabrication of transparent conductive substrate in solar cells devices. Up to now, the transparent substrate with lowest resistance around $10^{-4}\ \Omega\ cm^{-1}$ was synthesis from indium doped tin oxide (ITO).[111] Indium doped tin oxide is an n-type semiconductor with a band gap between 3.5 and 4.3 eV and a maximum charge carrier concentration in the order of $10^{21}\ cm^{-3}$.[112] ITO thin films have great light transparency in visible and near infrared range, good electrical conductivity, excellent substrate adherence, hardness and chemical inertness. The ITO films are widely used as coatings in photoelectronic devices[113] due to these properties. The optical and electrical properties of ITO films are found to be sensitive to conditions during preparation.[114]

Similarly, fluorine doped tin oxide (FTO) also has good optical and electrical properties which is suitable for the fabrication of transparent films but with much cheaper cost, when compared to ITO. In a literature report,[115] the solar cell performances with regard to ITO and FTO transparent conductive substrates were investigated. TiO_2 nanoparticles (9 nm size, anatase phase) were deposited on FTO and ITO conductive transparent substrates, respectively. It was found that the solar cells manufactured from FTO exhibited a slightly higher conductivity than that from ITO. In addition, according to a previous literature report[116], aluminium doped zinc

oxide thin (AZO) film exhibits a resistivity of 3.8×10^{-4} Ω cm^{-1} with optical transmittance of 91 % and it had been used for organic light-emitting device.[116]

2.1.4: Structured metal oxides

The most common strategy to increase the surface area of photo electrode is to modify the morphology of photoactive semiconductor which had been deposited on a planar conductive substrate. Macroporous, mesoporous, hollow sphere etc. structured photoelectrode had been found that can supply large surface area to support high photocurrent.[102,117,118]

Up to now, many structured metal oxides fabricated on planar TCO films have been reported. In terms of the 1D structured metal oxides, multiple layer SiO_2/TiO_2[119] and SiO_2/ITO[120] photonic crystal have been fabricated on FTO glass substrate through spin-coating and magnetron sputtering. Also, TiO_2 nanotube arrays as a 1D nanostructure, have been developed to couple to the DSSC photoanode.[121] As for 2D structured metal oxides, TiO_2 slabs with cylindrical columns with/without walls filled with acetonitrile have been proposed by Matsushita *et al*.[122]

3D structured metal oxides have been widely studied because they can manipulate light from all directions.[123] 3DOM (3 dimensional ordered macroporous) structures are normally made from uniform and spherical templates, colloidal particles assembled into crystalline arrays that resemble natural opals. Silica and polymer spheres are most commonly used for colloidal crystal templating. Different from the natural templates such as bioskeletons or plant components, the silica and polymer sphere template boast a highly periodicity in three dimensions, and this periodicity can be translated into the replica 3DOM structures.[90]

The most common method to synthesize photonic structures is to impregnate metal alkoxide precursors into these polystyrene sphere templates. Since the polystyrene tends to self-assemble into a face centred structure, photonic structure in powder or orientated photonic structure on a substrate can be achieved from impregnating materials into the voids among polystyrene spheres and remove polystyrene by heating or etching. Example oxides include those of Si, Ti, Zr, Al, W, Sn, Fe, Sb, Zr/Y mixture etc.[124] For example, 3DOM SnO_2 on FTO glass,[125] 3DOM ZnO on ITO glass[126] and 3DOM TiO_2 on FTO glass[100] had been successfully fabricated in previous literature reports. However, these metal oxides generally exhibit low electrical conductivity.

2.1.5: Structured TCOs

Relevant to the materials for synthesis of the photonic crystal film in this study, indium-doped Tin Oxide (ITO) is an excellent option for forming photonic structures due to its good optical and electrical properties. It is possible to get ITO macroporous structure film with relatively high transmittance in visible light range and also with low resistance through many methods.[127] However, indium is a rare element which makes it more expensive than other metals. Because of this, a replacement for ITO is desirable. It was found that enhancement in electric conductivity of tin oxide can be achieved through fluorine doping, the so-called fluorine-doped tin oxide (FTO). FTO has good transparency in visible light range and electric conductivity.[128] Antimony can also be doped into tin oxide. The introduction of antimony sharply increases the material's conductivity, which reaches a peak at 4 wt. % antimony, being more than 2 orders of magnitude higher than that of the pristine SnO_2.[129] When compared to ITO, antimony doped-Tin Oxide (ATO) is more thermally stable and lower cost.[130]

ZnO is also stable and abundant and aluminium doped zinc oxide (AZO) exhibits a similar resistivity to FTO. In addition, TCOs such as ATO with disordered macroporous structure have been synthesised on FTO glass exhibited efficient high surface area support for the electrochemical splitting of water using hematite.[131] AZO inverse opal film fabricated on FTO glass was decorated with $BiVO_4$ for water oxidation, it exhibited an efficiency 2 times larger in comparison to that on planar FTO glass.[132]

Ordered macroporous FTO film was also fabricated on FTO glass.[133] But due to the poor coverage and small thickness (0.5 to 3.5 μm), the mac-FTO films exhibit a transmittance over 40 % in visible light region as shown in Figure 13. The mac-FTO in this literature report shows lower transmission than planar FTO, this is due to scattering within the mac-FTO film which will increase the path length of photons and hence the transmission was decreased. The optical properties of structured TCOs can be characterized by transmission or reflectance spectra, and high quality structured TCOs commonly exhibit low transmission or high reflectance, which means the incident photons can not easily penetrate the electrode.

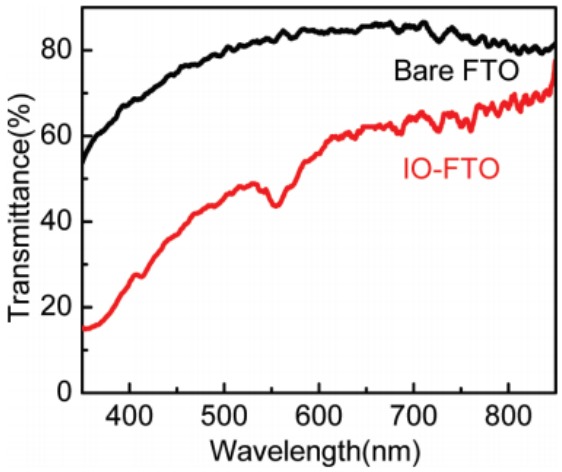

Figure 13: UV-vis transmittance spectra of mac-FTO film and planar commercial FTO film in a previous literature report.[133]

The photocurrent generation of TiO_2@mac-FTO and TiO_2@mac-TiO_2 films in various thickness under full wavelength light irradiation was investigated in a previous literature report.[134] The thickest mac-FTO (5.6 μm) and mac-TiO_2 film (6.2 μm) synthesised exhibit the highest efficiency for supporting TiO_2 when compared with that of thinner 3DOM films. In addition, TiO_2@mac-FTO electrode show a photocurrent density around twice larger than TiO_2@mac-TiO_2 electrode due to the better conductivity of FTO when loaded with same amount of photocatalyst. Therefore, synthesis of conductive mac-FTO with low transmission can be expected to exhibit high efficiency for supporting photocatalysts.

2.2: Chapter aims

As mentioned in last section, structured TCO films for supporting photocatalysts had been widely studied in the past, but they have not shown high conductivity or quality optical structures which limit the performance of them for supporting photocatalysts in photoelectrochemistry. The aim of this chapter is making structured conductive films of FTO and AZO with high optical quality that are mechanical robust.

To achieve this goal, planar conductive FTO film on borosilicate glass and quartz were synthesised as a substrate for the fabrication of mac-FTO and hs-AZO films. Polystyrene (PS) spheres of 450 nm in diameter were synthesised to make highly ordered PS photonic crystal films on planar FTO films. Various conditions to optimize the quality of planar FTO films and PS photonic crystal films were investigated and are presented. 3 dimensional ordered macroporous FTO (mac-FTO) films and hollow sphere AZO (hs-AZO) films will be synthesised from these PS templates. In addition, attempts will be made to optimize the quality of these structured TCO films.

A range of structural and spectroscopic techniques including PXRD, SEM, TEM, EDX, DRUVS and electrochemistry were employed to study the structural and optical properties of these samples.

2.3: Result and discussion

2.3.1: Coating of the transparent substrate with planar FTO film

In the study, it was found that the macroporous FTO film is stable to 800 ^{o}C but the commercial conductive substrates melt at 650 ^{o}C. The deposition of macporous FTO film on quartz substrate can increase the temperature range available for synthesis of photoelectrodes. Photonic electrode with higher tolerant temperature normally means more options for the photocatalyst decorated into the photonic electrode, since some of the photocatalysts such as GaN must be synthesized at over 800 ^{o}C through in-situ method. Based on this, a mixture solution of $SnCl_4$ and NH_4F was used as source for making the conductive film on quartz.

FTO planar films were synthesized on glass and quartz substrates by spray pyrolysis with different concentrations or fluorine content of precursor solutions and various experimental conditions to optimize the quality of FTO planar films. The FTO precursor solutions used for the coating were modified from a literature report[133] and the substrates used were borosilicate glass and quartz of 1 $\times$1.5 cm size and 0.2 cm in thickness. FTO films with sheet resistance ranging from 7 Ω □ to over 10^4 Ω □ and transparency over 85 % in the visible light range were synthesized by spray pyrolysis method.

The experimental conditions were modified to evaluate the effects of various experimental conditions on the quality of FTO planar film achieved. Four points probe technique was used to determine the sheet resistance of FTO planar film.

Sheet resistance is an important value to present the electrical conductivity of a sample. To obtain a relatively accurate value of the sheet resistance of these samples, a result was recorded by averaging the sheet resistance of three samples with same experiment conditions. SEM imaging was used to evaluate the defects, thickness and morphology of the FTO planar films. UV-vis transmission spectra was employed to determine the transparency of FTO planar films which is as an expression of optical property of the FTO film. PXRD was used to determine the crystalline quality of the FTO planar films and EDX was applied to analyse the composition of the FTO planar film. During the spray pyrolysis the following endothermic reaction occurs as shown in equation 9:

Equation 9: $\mathrm{SnCl_4 + 2H_2O = SnO_2 + 4HCl}$

The post-heat treatment temperature, F/Sn ratio in the precursor solution, the concentration of precursor solution, the distance between the substrate and the nozzle and the amount of precursor solution used for the spray pyrolysis were varied in few series of experiments. It has been reported that the concentration in the precursor solution, gas flow rate, substrate to nozzle distance, substrate temperature and doping level in the precursor solution had influence on the quality of the films.[135] According to the above study, the process parameters such as gas flow rate, nozzle distance and substrate temperature were fixed as: 10 mL/min, 13 cm and 430 ^{o}C (at which FTO was well crystalized) to get high transparent and low electrical sheet resistant FTO films. The spray operation was temporarily stopped and resumed after the surface temperature of the glass substrate returned to 430 ^{o}C. The average interval between the spray was around 10 s. The F/Sn atomic ratio has been varied from 0.25 to 1.00 in the FTO precursor solution. For each ratio the period of the spray operation was changed from 5 min to 11 min and optimized to get films of minimum sheet resistance.

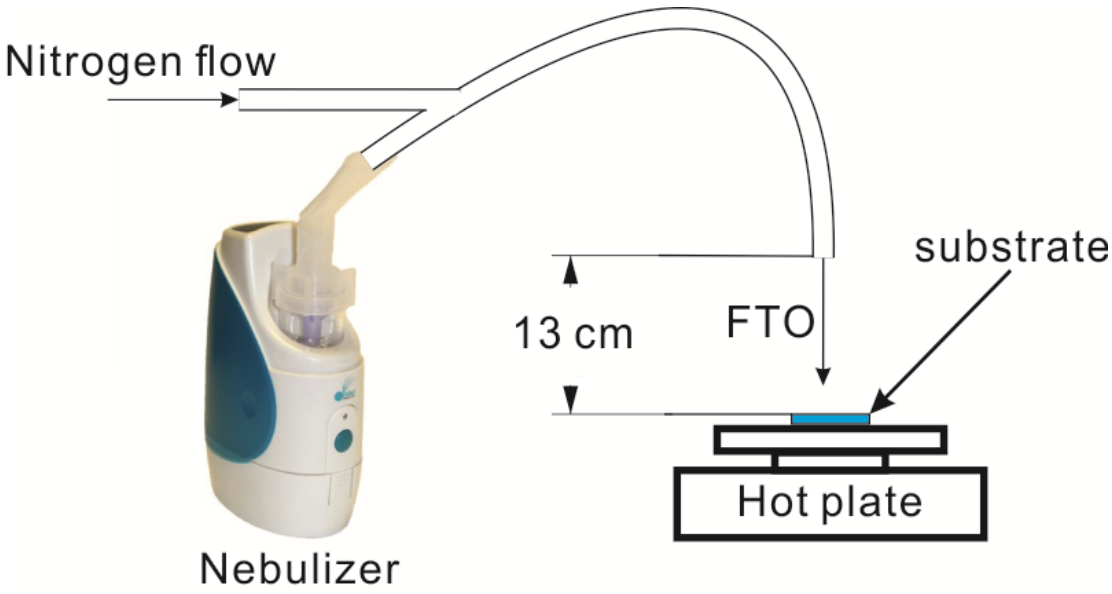

Figure 14: Schematic diagram of the spray pyrolysis setup in this work.

By using air brush spray pyrolysis, the lowest sheet resistance of FTO planar film obtained is 7.6 Ω □, but the reproducibility is poor since the spray operation depends on the operator. Therefore, a nebulizer was employed instead of the air brush to do the spray pyrolysis as shown in Figure 14. The borosilicate glass/quartz substrate was pre-heated on a hot plate set at 510 ^{o}C for a period of time until the top surface temperature of the substrates reached 430 ^{o}C. The nebulizer was filled with 5 mL of FTO precursor solutions with varied F/Sn atomic ratios and concentrations. A mist of FTO precursor was formed when the nebulizer turned on and then the FTO mist was pushed to the hot substrate through a tunnel by a nitrogen flow with certain period of time. The substrate was then cooled down to room temperature. Typically, the electrical properties of continuous films are determined via the four point probe van der Pauw method and Hall measurements.[136] In this case, the sheet resistance of the achieved FTO planar films was measured by four point probe method directly when it is cool and after a heat treatment at certain temperature.

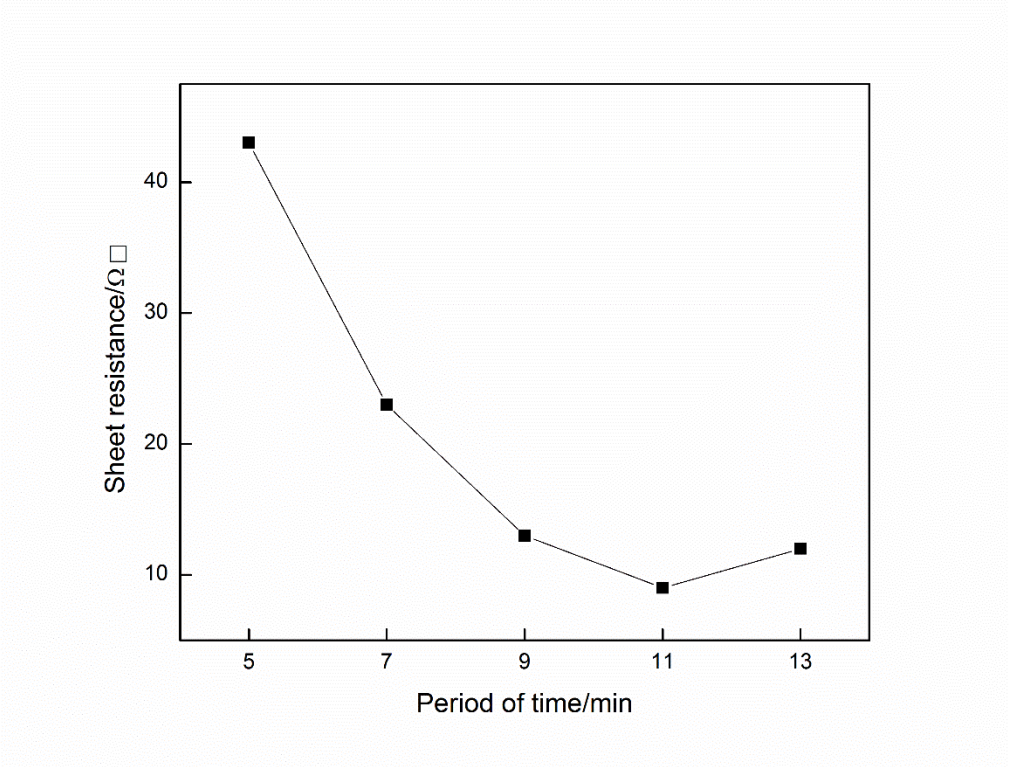

Figure 15: Variation of sheet resistance by different period of time of spray pyrolysis with F/Sn atomic ratio = 0.5 in precursor solution.

To optimize the quality of FTO planar film, the sheet resistance of samples with varied period time of spray pyrolysis was measured directly after cooled down to room temperature as shown in Figure 15. In this experiment, the F/Sn atomic ratio is constant at 0.5 which tend to give the best result as previous literature reports claimed.[137,138] The sheet resistance decreased with increasing spray period of time, and the lowest sheet resistance of 7.6 Ω □ was achieved at 11 min of spray period. However, the sheet resistance increased when the spray period time is over 13 min, this is because the sheet resistance saturates after a certain value of thickness as reported in previous studies. However, the saturated value of thickness for the lowest resistance is quite different in literature reports, ～1.2 μm,[139] ～1.4 μm[140] and 180 nm[141] were reported to be the most effective thickness for FTO film showing lowest sheet resistance. The duration of spray generally imply the amount of precursor material put onto the hot substrate and an insufficient coating material

tend to form a film without full coverage. On the substrate coated with insufficient materials, crystal particles in some area were not continuous, Figure 16 shows the SEM images of the FTO planar films with 0.5 F/Sn atomic ratio in precursor solution and a spray period time of 5 min and 7 min, respectively. The voids among FTO particles observed by SEM imaging suggest a poor pathway for current which will lead to high sheet resistance.

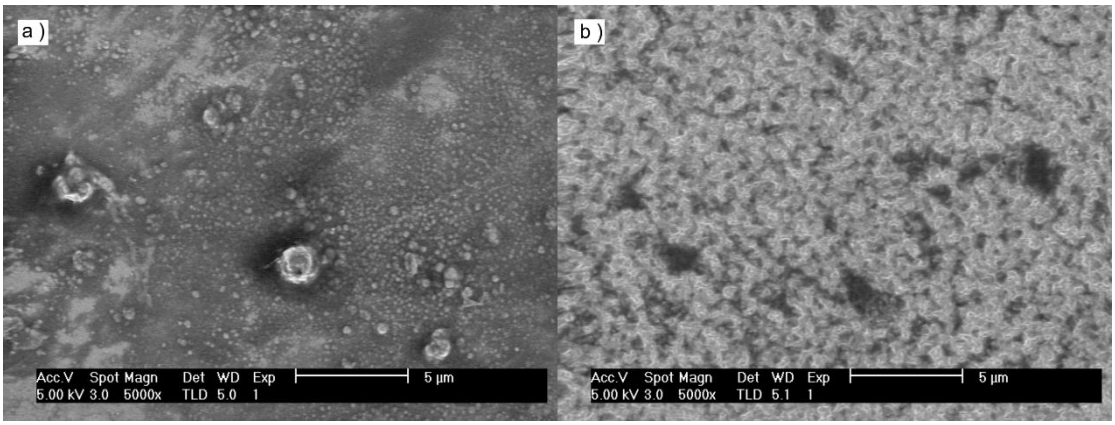

Figure 16: SEM images of the FTO films made with 0.5 F/Sn atomic ratio in precursor solution and a spray period for a): 5 min and b) 7 min.

The Sheet resistance is available in which the thin films (the thickness of film can be ignored when compared with the length and width) can be considered as two-dimensional entities. It means the current flow going across the thin film but not moving perpendicular to it. Since the majority electrical current tend to flow through the pathways with the lowest resistance, some defects such as cracks and insolation of FTO nanoparticle in the FTO planar films may not lead to distinct resistance. The high sheet resistance (52.7 Ω □ for 5 min and 23.3 Ω □ for 7 min) was measured from these two FTO film samples may also due to the poor contact between the FTO film and the point probes of device. The substrate coated with sufficient precursor material was also imaged by SEM for comparison as shown in Figure 17. The FTO film was coated on the substrate uniformly with a full coverage

due to the sufficient material, and no cracks or blank are observed during SEM operation, hence the electrical current going through the film with least resistance and allowing better contact between the film sample and point probe of device.

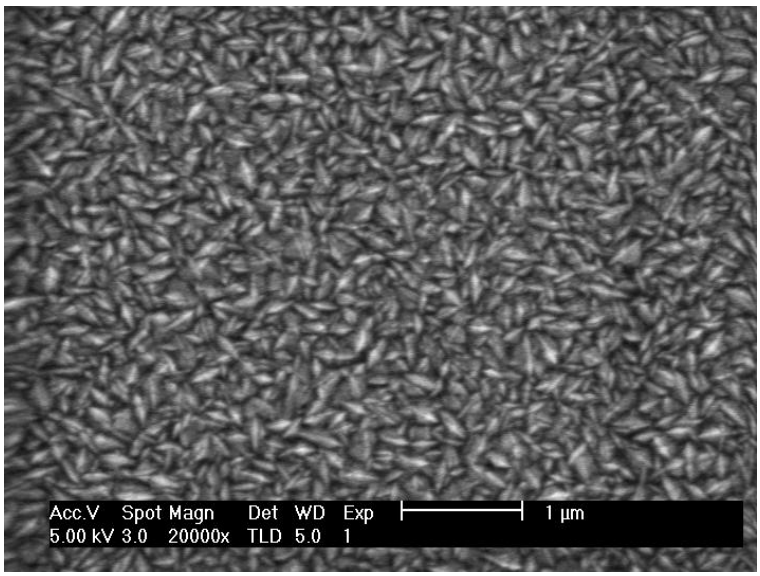

Figure 17: SEM image of the FTO films made with 0.5 F/Sn atomic ratio in precursor solution and a spray period for 11 min.

The different F/Sn atomic ratios in precursor solution were studied to optimize the sheet resistance of FTO planar film with a fixed spray period of time for 11 min. The plots of sheet resistance of FTO vs. F/Sn atomic ratio in FTO precursor solution are shown in Figure 18. The sheet resistance of FTO films decrease with F/Sn atomic ratio initially reaches a minimum and then increases beyond this particular atomic ratio (0.5), and this ratio can correspond to previous literature reports.[135,142] To be more specific, although the lowest sheet resistance (7.6 Ω □) was obtained at F/Sn atomic ratio = 0.5, there is no obvious change in the electrical conductivity when the doping level was slightly tuned which give a sheet resistance of 10.2 and 9.4 Ω □ for ratio 0.25 and 0.75, respectively. However, the sheet resistance of FTO increases dramatically with a F/Sn ratio over 1.0 and reaches 62.4 Ω □ at ratio = 1.5.

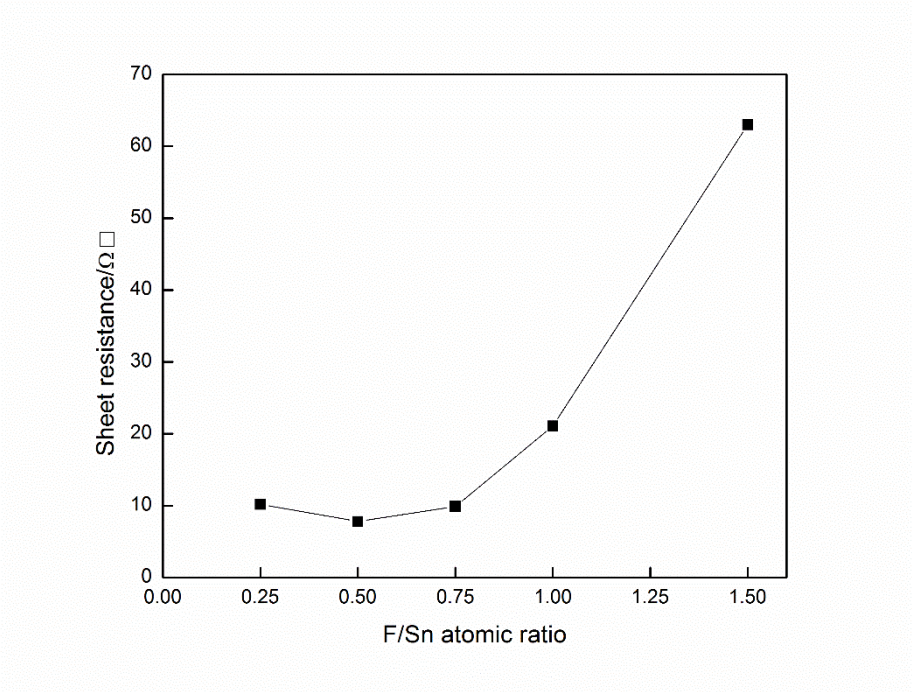

Figure 18: Variation of sheet resistance by different F/Sn atomic ratio in precursor solution with a pyrolysis period for 11 min.

In the fluorine doped tin oxide materials, the F^- anion tends to substitute for an O^{2-} anion in the SnO_2 lattice which creates more free electrons and therefore leads to a decrease of sheet resistance. But the excess F atoms cannot occupy the proper lattice points to contribute extra free carriers and the increasing disorder leads to an increase of the sheet resistance.[137] It confirms that the free carriers in FTO films come from oxygen vacancies and the F doping. When the fluorine content in the precursor is very high, there is an incorporation of fluorine atoms in the oxygen vacancies and to the formation of Sn-F complexes lead to the crystalline structure of the FTO films deteriorates and tends to become amorphous which result a decrease in electrical conductivity of FTO films.[135,143]

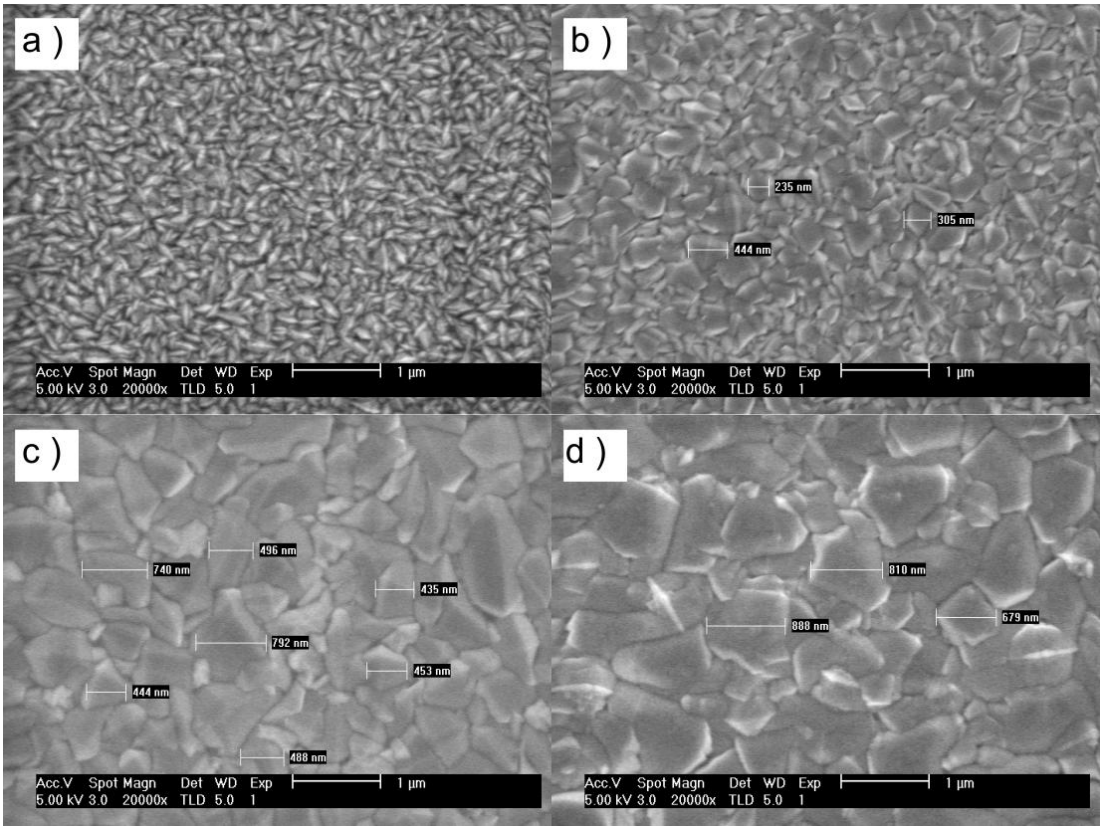

Figure 19: SEM images of FTO planar films synthesized with varied F/Sn atomic ratios in precursor solution: a) 0.5, b) 0.75, c) 1.0 and d) 1.5.

The SEM images obtained on the surface of FTO planar films are shown in Figure 19 for different F/Sn atomic ratios in precursor solution. The SEM images indicated that the crystallites are well formed and densely packed for all these four film samples. The film made from a low fluorine content precursor solution (0.5) comprise of largely distributed needle shaped crystallites (～150 nm) which is similar to the grain size observed in a literature report[144] by using the same precursor. The distribution of needle shaped crystals is random in FTO films, but such needle shaped grains are seen less in the samples with higher fluorine content. The SEM images express a grain size around 300 nm, 500 nm and 700 nm for the FTO films synthesized by Sn/ratio at 0.75, 1.0 and 1.5 in precursor solution, respectively. The grain size is larger for the FTO films with higher F doped tin oxide.[145] The size distribution is also getting larger with increasing F content in precursor solutions. The similar trend of grain size changing with increasing F ratio

in precursor solution was observed in a literature report,[87] Beyond F/Sn ratio at 0.5 the grain size increased with smaller grains among larger grains and compact structures. The FTO grain crystal size has influence on the surface area of the FTO film, and the deposition of nanoparticle photocatalysts can benefit from a substrate with larger surface..

As discussed above, the FTO film exhibit lowest sheet resistance at ~7.6 Ω □ was synthesized on borosilicate glass/quartz substrate with Sn/F atomic ratio in precursor solution and spray time for 11 min. The achieved FTO with low sheet resistance was applied a post-heat treatment from at 450 ^{o}C to 850 ^{o}C for 2 h after spray pyrolysis operation to study the stability. The post-heat treatment over 650 ^{o}C can only be applied on planar-FTO@quartz sample, since the borosilicate glass substrate start melting at 650 ^{o}C and break into pieces at 750 ^{o}C. In terms of the sheet resistance, there is no differences being found when different substrate (borosilicate glass/quartz) was used for the FTO film coating.

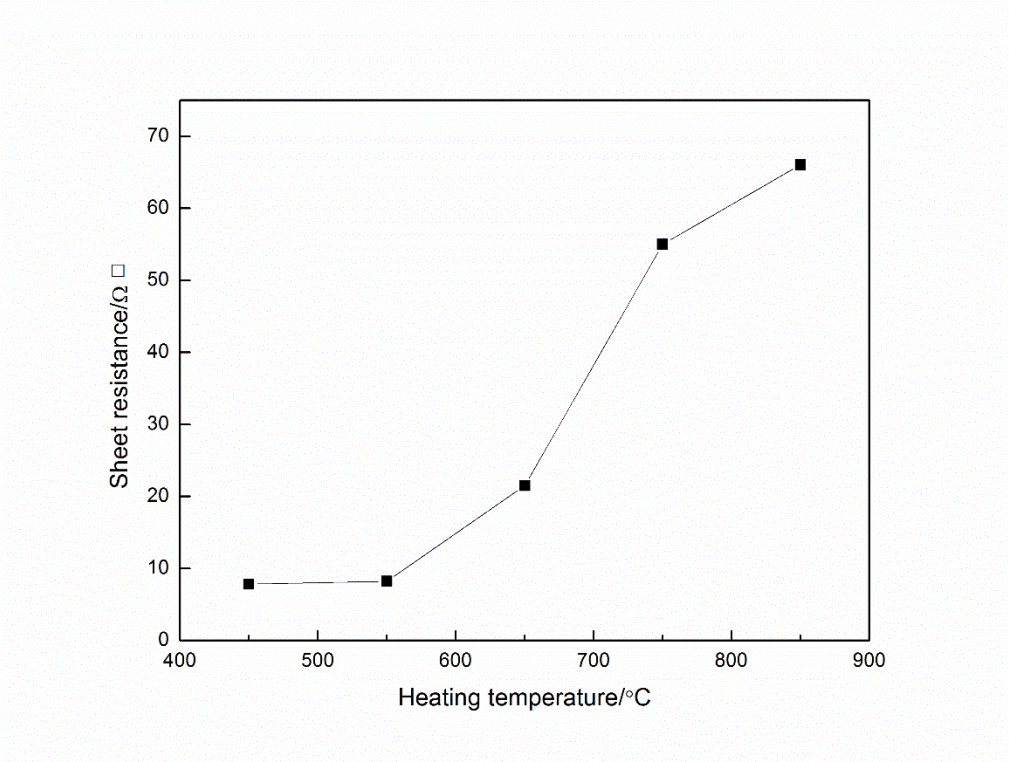

Figure 20: Variation of post-heat treatment temperatures applied on FTO films with 0.5 F/Sn atonic ratio and 11 min spray time.

As shown in Figure 20, almost no influence on the sheet resistance of FTO film was observed with a varied calcination temperature below 550 ^{o}C, but a dramatical increase of the sheet resistance was observed when calcined for 2 h at 750 ^{o}C and 850 ^{o}C, respectively. Cracks crossing the FTO film was observed in the samples calcined at 750 ^{o}C and 850 ^{o}C by SEM as shown in Figure 21, for the FTO film calcined at 850 ^{o}C, more extensive cracks were observed.

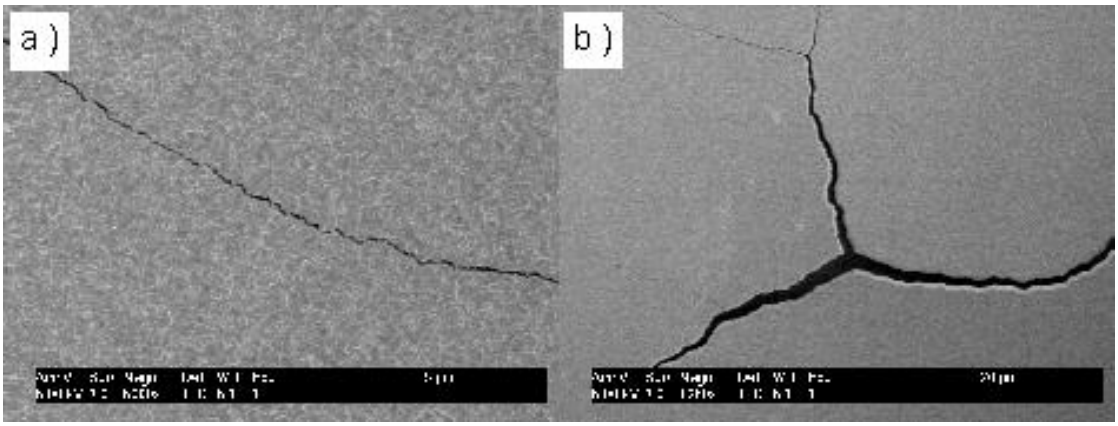

Figure 21: SEM images of defects observed in FTO films treated with calcination at a): 750 ^{o}C, b) 850 ^{o}C.

In addition to the defects introduced by the high temperature, there may be other factors causing an increase in the sheet resistance of the FTO film since the resistivity of circular pellet of FTO powder was increase from 3.7 to 4.61 $\times$ 10^{-4} Ω cm^{-1} with calcination temperature at 600 and 700 ^{o}C, respectively,[146] even though no such defects were found in these samples.

Beyond a spray time for 11 min, the FTO films synthesized by various F/Sn atomic ratios in precursor and varied post-heat treatment temperatures were measured by

UV-vis transmission spectra as shown in Figure 20. The transmission in range 400 to 900 nm of FTO film is around 87 %, which is similar to a previous study,[147] showing no obvious dependency on these experiment conditions. In a previous literature report, it was also found that the average transmission of FTO films is around 85 % as the substrate temperature increase; and with increase fluorine doping level at 425 ^{o}C, a very slight decrease in the percentage of transmission has been observed from FTO films.[135] But in this work, no obvious transmission change of the planar FTO film was observed by DRUVS when varying the fluorine doping.

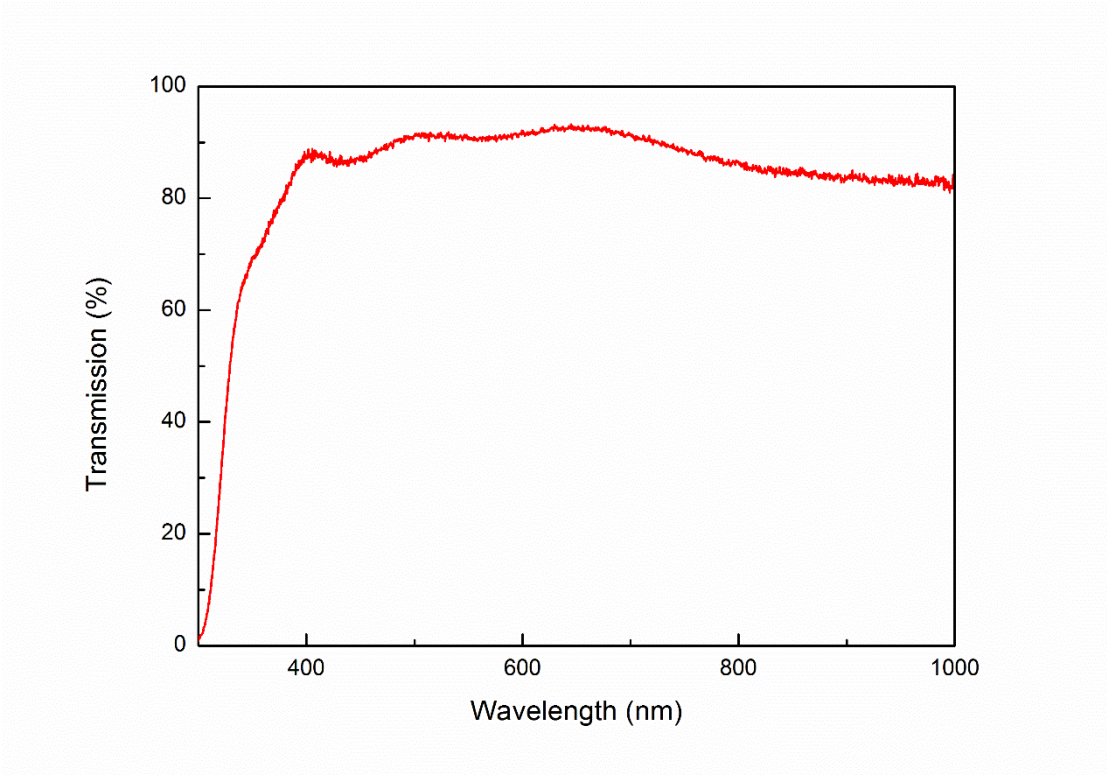

Figure 21: UV-vis transmission spectra of the FTO film coated on transparent substrate.

FTO films synthesized in this thesis, the borosilicate glass substrate and a commercial FTO film were measured by PXRD for comparison in an aluminum holder. In addition to the patterns of glass substrate and Al holder, typical diffraction

peaks of SnO_2 JCPDS 41-1445 were observed from both commercial and lab made FTO as shown in Figure 22. Besides, the X-ray diffraction peaks of synthesised planar FTO films can correspond to the commercial FTO film. The EDX spectra (Figure 23) provides the elements composition in FTO film, the atomic ratio in the FTO film product is 0.78 at % made from a precursor solution of F/Sn atomic ratio = 0.5. A commercial FTO film was also measured by EDX as comparison and 0.60 at. % of fluorine was observed. Although there is different content of fluorine observed, the lab-made FTO films shown a similar sheet resistance in comparison with the commercial ones (~7 Ω □). In terms of the sheet resistance of FTO film coated heated to 850 ^{o}C, even though the sheet resistance (~65 Ω □) is not great, it still offer a way for the synthesis of metal nitride such as GaN through in situ techniques because the metal nitride are generally made at very high temperature over 850 ^{o}C.

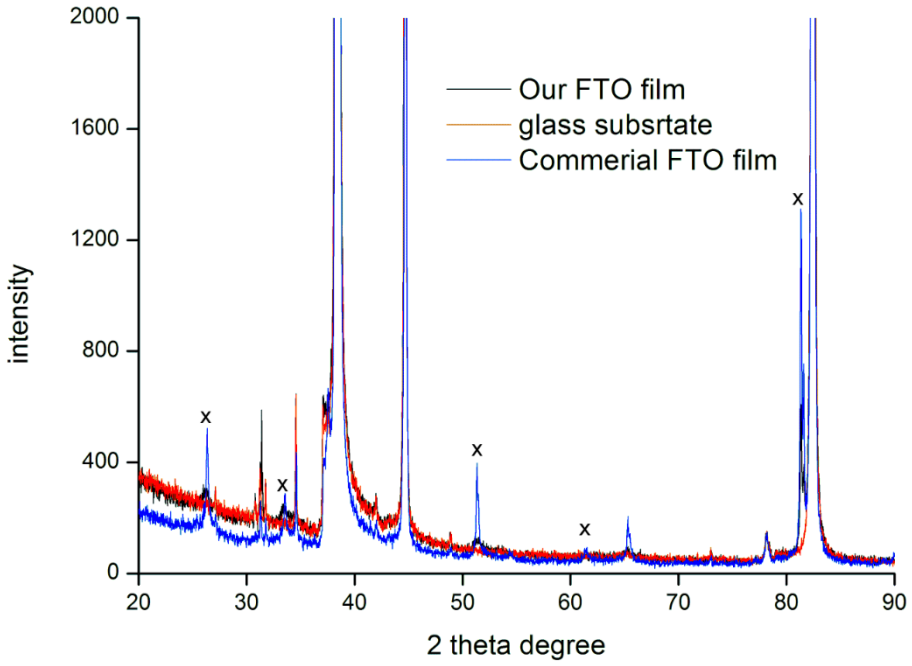

Figure 22: PXRD of FTO film synthesized in lab, commercial FTO films and borosilicate glass substrate the samples measured within aluminum holder (x = SnO_2 JCPDS 41-1445).

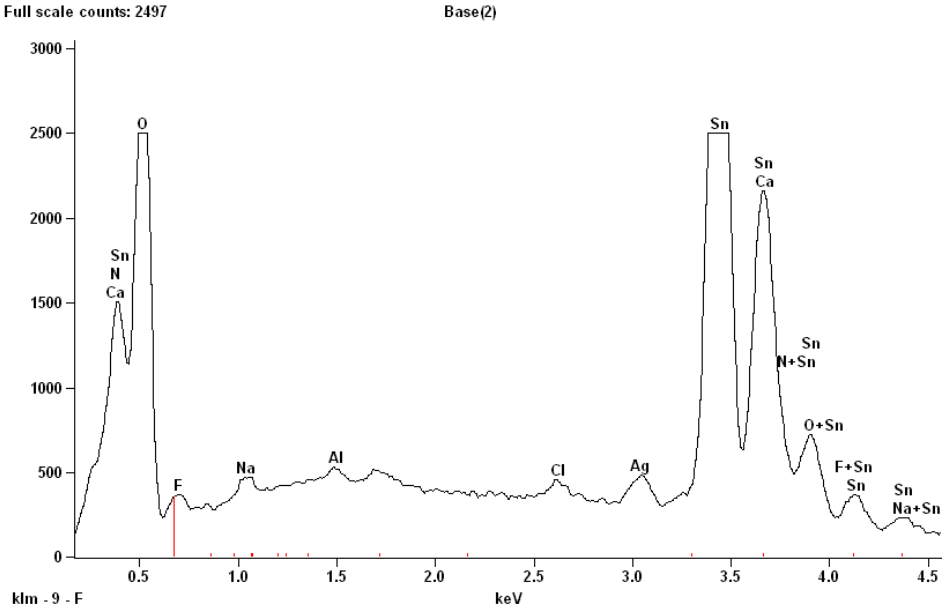

Figure 23: EDX spectra of FTO film made with 0.5 F/Sn atomic ratio in precursor solution.

2.3.2: Deposition of close packed colloidal spheres on FTO film

Polystyrene spheres of different sizes were used as templates on FTO film substrate to form 3DOM photonic crystal films. It was found that polymer spheres often organize themselves into a highly ordered 3D structure under certain conditions.[148] Template spheres can be packed to form cubic close-packed (CCP) arrays of spheres by self-assembly or vertical capillary deposition on planar substrate to form the photonic films.[79]

By a simple vertical evaporation deposition method with optimized conditions such as polystyrene suspension concentration, composition of solvent, evaporation time and temperature, close-packed photonic crystal PS films in face centred cubic were obtained. Different ratios between water and ethanol and deposition temperatures were investigated and it was found that a mixture of water and ethanol in ratio 8:82

at 60 ^{o}C were found to be the optimum conditions to give the highest quality PS opal structure films. With the suitable conditions, as the solvent evaporate, the meniscus region travels down the surface of substrate, depositing the polymer spheres by a capillary force as shown in Figure 24. Capillary forces are directly employed to drive the polystyrene spheres to assemble themselves and the lateral capillary immersion force between the spheres contribute to the formation of hexagonal sphere arrays.[149]

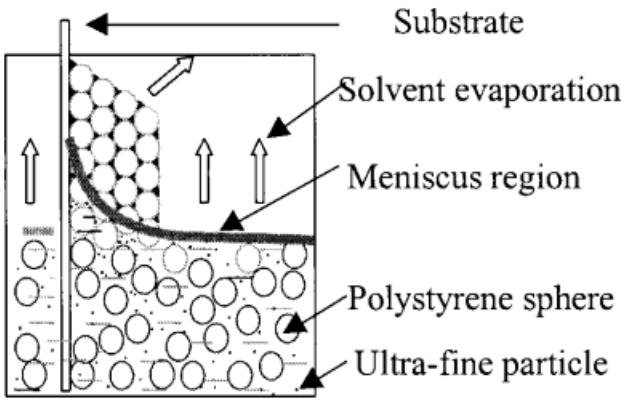

Figure 24: Schematic image of vertical vapour deposition.[150]

The concentration of the polystyrene sphere suspension has an influence on the thickness (number of layers) of PS photonic films. Lower concentration PS suspension normally leads to thinner PS films and if the PS film is too thin, the PS film cannot exhibit photonic properties in all three dimensions. As a template for fabrication of 3DOM photonic films, not only the poor photonic properties of thin PS films will be replicated by 3DOM photonic crystal film after remove the PS template, but also the surface area of the thin photonic crystal will be limited. Alternatively, the PS suspension with higher concentration generally forms thicker PS films and if it is too thick, the PS films tend to be less mechanically robust leading to poor photonic properties (less intense photonic stop band). In addition, the thicker films lead to a problem for the infiltration step for the fabrication of 3DOM photonic crystals, as it is increasingly difficult for the FTO solution to get into entire voids among PS spheres

by capillary forces in a structure with more layers. Furthermore, because the PS film is not perfectly flat, every part of the PS films may not have the same thickness. When the average thickness is too high, some area can be infiltrated completely but some may not.

Furthermore, thick films tend to flake off as they become too heavy due to the gravity. As a template for 3DOM films, even if a stop-band of the 3DOM films can be achieved from a too thick PS film, the 3DOM film is quite weak because of the thinner wall thickness due to insufficient infiltration of precursors. More mechanically robust and homogeneous films are therefore achieved with a thinner PS film and therefore the film thickness needs to be optimised to obtain a sufficient number of layers to obtain a stop band with high filling. Besides, the cracks in the PS films are generated during the drying of the samples.[151] In this work, the evaporation temperatures of the PS solvent was investigated and it was adjusted to 60 ^{o}C for a lower percentage of cracks in PS films. Typically, a FTO coated substrate was stood vertically in a glass vial containing a suspension of certain amount of polystyrene spheres dispersed in ethanol and water (x:82:8 = PS:ethanol:water in mL) to a level just above the top of the electrode. Here x means the volume of stock PS dispersion for dilution, typically, 4 g of powder PS spheres can be obtained from 50 mL of PS dispersion. In this experiment, 1, 1.2 and 2 mL of stock PS dispersion was diluted by 90 mL of mixture of water and ethanol. The volatiles were evaporated over 15 h at 60 ˚C until 10 mm of film has been deposited. The electrode was then removed and the remaining 5 mm cleaned with acetone giving an electrode coated in a continuous opalescent polystyrene film 10 x 10 mm and *ca*. 7 -10 μm thick.

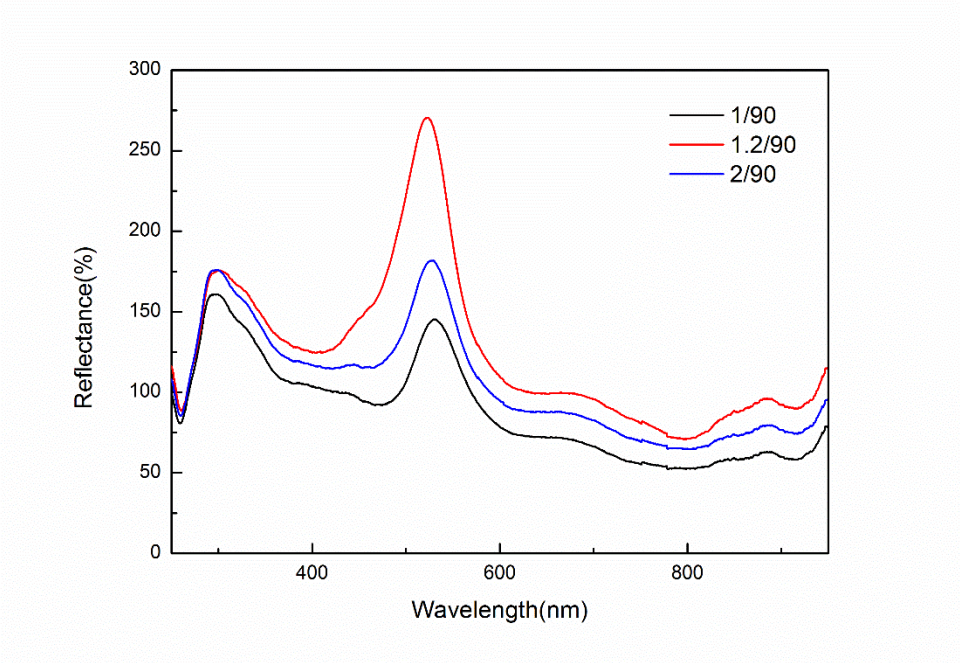

Figure 25: DRUVS spectra of PS opal film deposited on FTO coated substrates. The intensity of photonic stop bands was controlled by varying the concentration of PS suspension, in this case, 1.0 mL (black line), 1.2 mL (red line) and 2 mL (blue line) of PS suspension were dispersed in 90 mL (ethanol:water = 82:8) solvent.

As shown in Figure 25, the position of photonic stop band (reflectance peaks) for all these samples are the same, which means the filling factor and the crystal structure will not be affected by the variation of PS latex concentration (according to Equation 8). However the intensity of photonic stop band of PS films enhanced dramatically when the PS content in 90 mL solvent increased from 1.0 to 1.2 mL. The increased intensity of the stop band at 540 nm occurs from the long range periodic structure introduced by higher concentration PS suspension. The intensity of PS film stop band then decreased when the concentration of PS suspension increased to 2/90 mL due to a less mechanically robust film. These mechanical defects were replicated when this PS film was used as template for the fabrication of mac-FTO film as shown in Figure 26. Some area of the PS thicker (left) film fall off during the soaking for FTO precursor infiltration resulting in incomplete coverage of the final mac-FTO film.

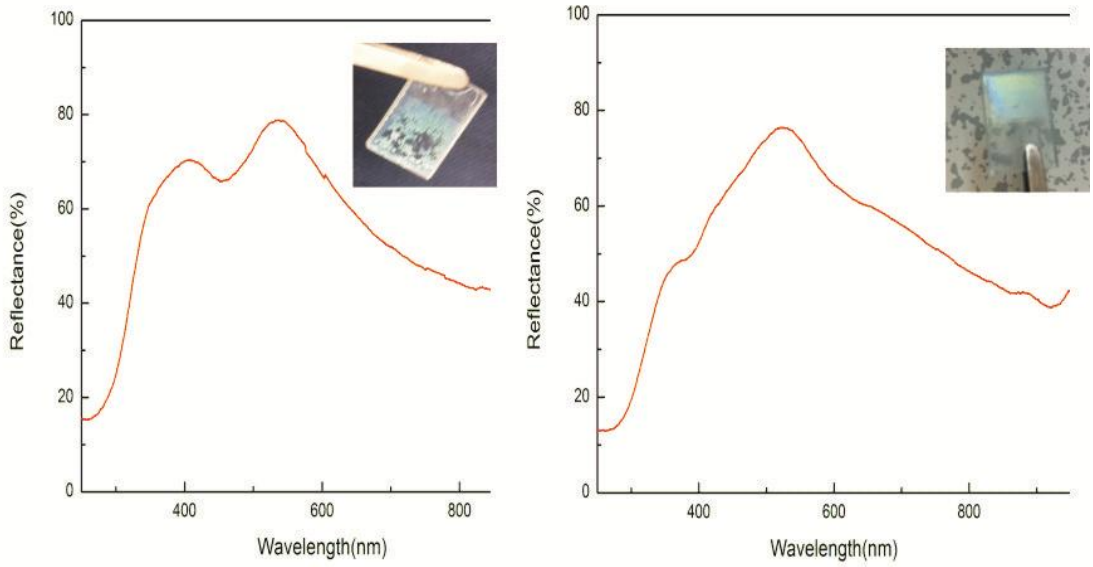

Figure 26: DRUVS spectra of FTO films made from thicker PS film (Left) and thinner PS film (Right) and corresponded photograph of samples.

According to Bragg-Snell equation (Equation 8), varying the parameters in the equation will affect the position of the photonic stop bands. When soaking the PS film in water, a red shift from 620 to ca. 720 nm was observed (Figure 27a) since the water has higher refractive index than air (increased n_0). In addition, different sizes of polystyrene spheres were used for the fabrication of PS opal films. The position of photonic stop bands as shown in figure 27b. The major peaks observed at 480 nm and 620 nm of the photonic PS films were synthesize with polystyrene sphere size of 350 nm and 450 nm (as shown in Figure 28) respectively.

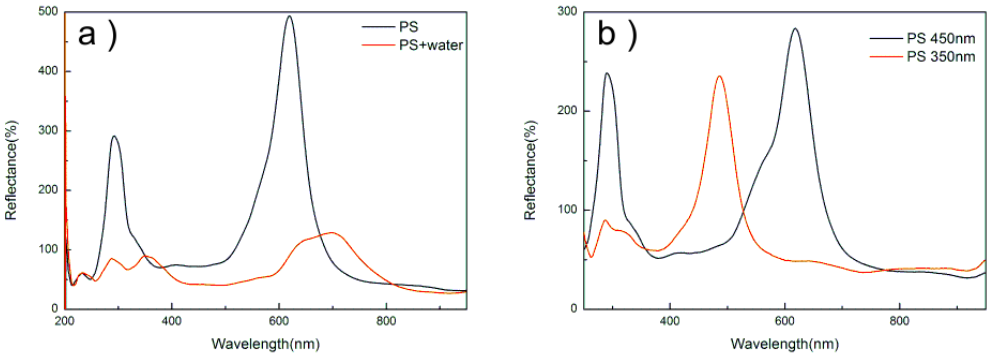

Figure 27: DRUVS spectra of PS films a): filled with/without water b): different size of polystyrene spheres.

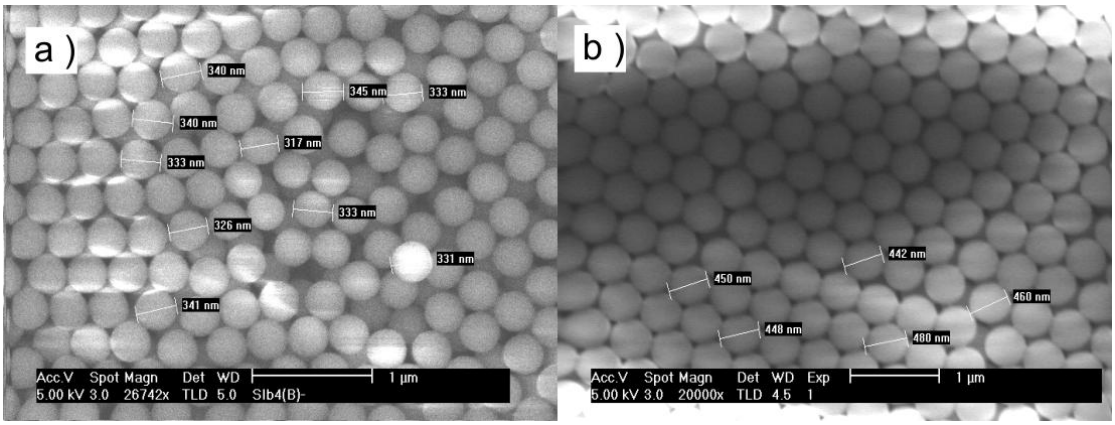

Figure 28: SEM images of polystyrene sphere with diameters of a): ca. 350 nm and b): ca. 450 nm.

The photonic stop bands of the PS opal films have an incident light angular dependence and exhibit opalescence due to the photonic properties and the transparency as shown in Figure 29. The varied colours we saw from the photographs indicate the photonic stop band position changing on the PS films. The colour from blue to red in Figure 29 is likely to correspond to a stop band position at around 450 nm, 500 nm, 550 nm, 600 nm and 650 nm, respectively. Based on Bragg-Snell equation, larger incident light angle indicates greater value of sin θ

which lead to a blue shift of the stop band position. Alternatively, smaller incident angle tend to result in a blue shift as shown in Figure 30.

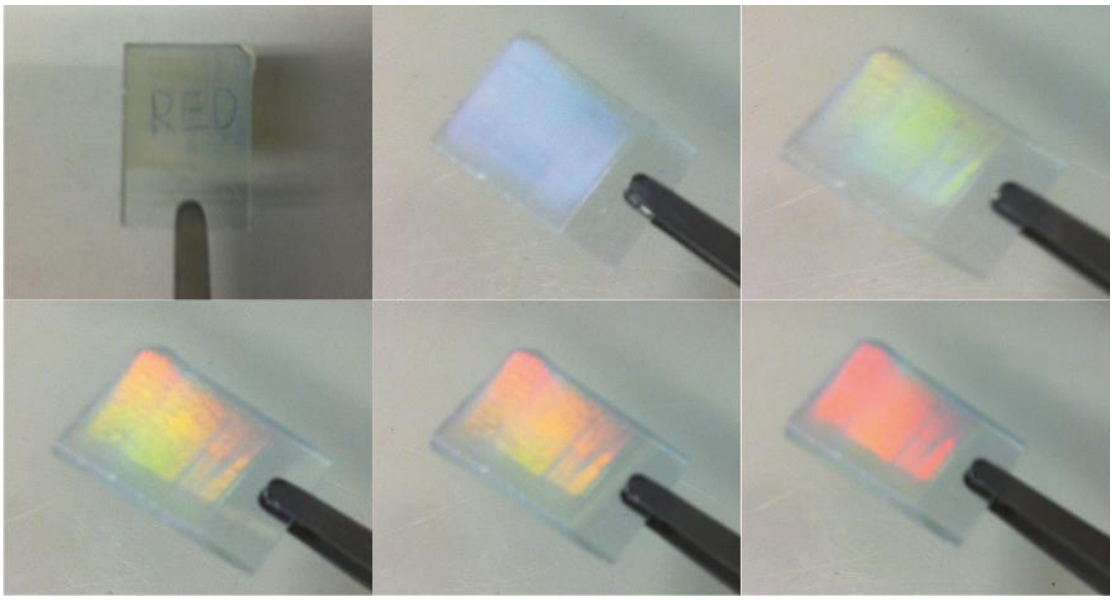

Figure 29: Digital photographs of PS photonic film on FTO substrate exhibit varied colours with changing the light incident angles.

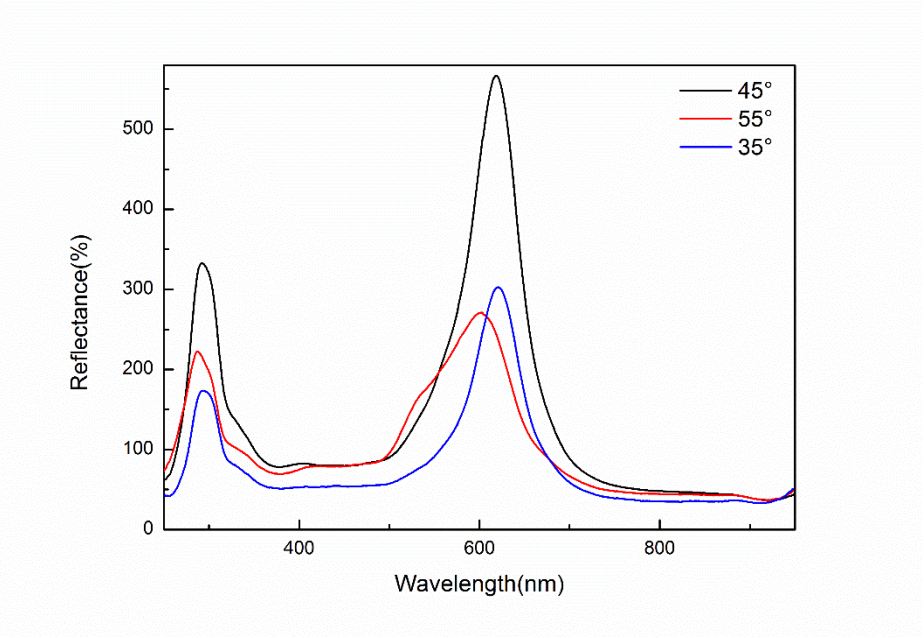

Figure 30: DRUVS spectra of PS photonic film with various incident light angle.

A reproducibility problem was faced due to the variability in temperature and vibration present in the laboratory. Using a more impermeable oven and moving the oven for deposition of PS films to a room with relatively constant temperature and less vibration gave much better PS film. This suggests that the deposition of PS sphere template on FTO coated substrates is very sensitive to the environment and experimental conditions. More details of PS film are shown in Figure 31 using SEM imaging. The polystyrene spheres were self assemblied on FTO substrate homogeneous and the ordered periodic array has long range order. In most areas of the PS film, the hexagonally packed plane is parallel to the substrate surface. A few cracks were sometimes observed on the PS film, which may be due to the vibration, air flow or temperature fluctuations during the deposition process. These defects are often reported.[150]

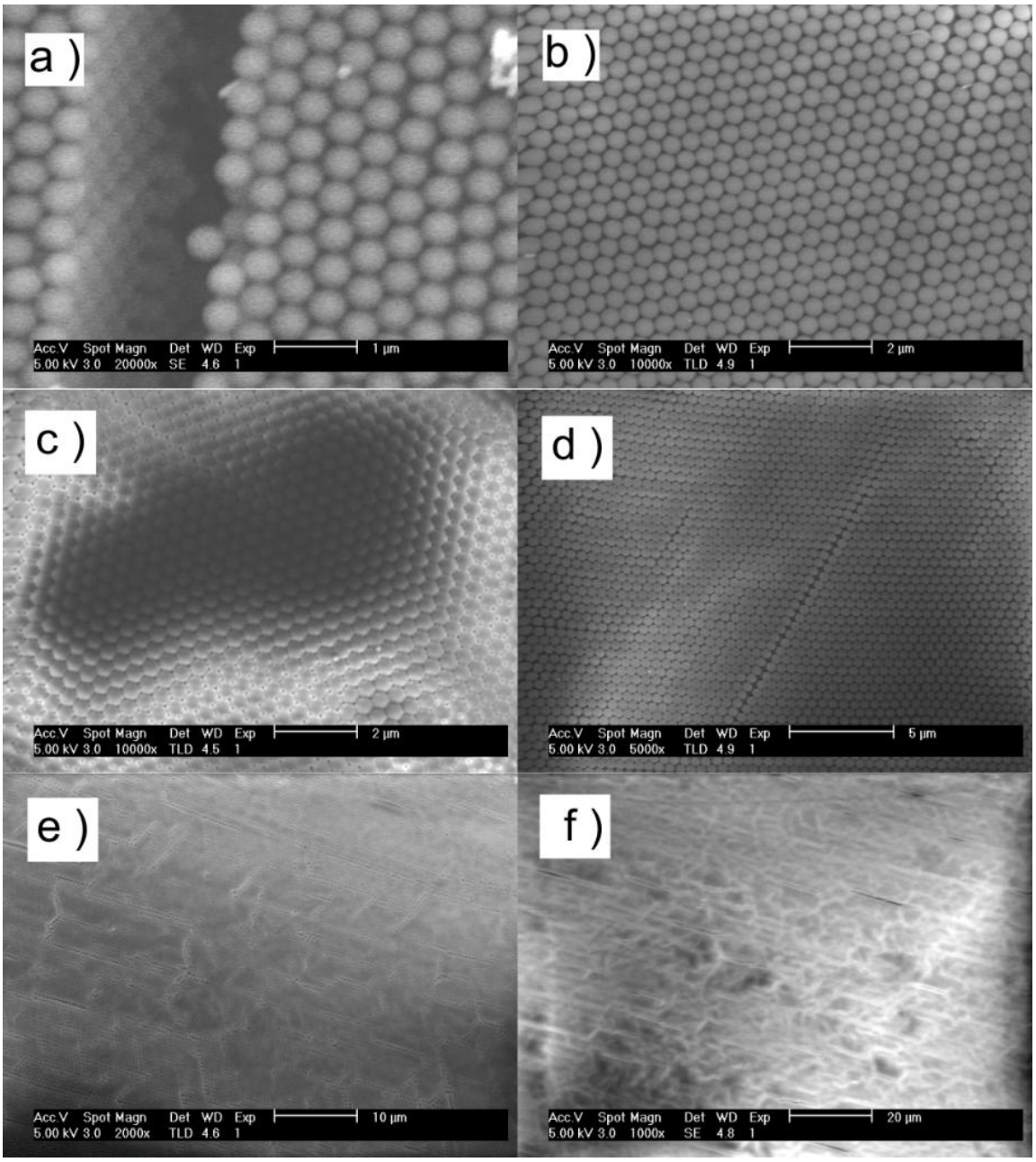

Figure 31: SEM images of PS (ca. 450 nm) photonic film deposited on planar-FTO film in varied magnification.

2.3.3: Synthesis of mac-FTO film from PS template

For all the experiments in this section, the substrates used for fabrication of mac-FTO films were FTO conductive glass deposited with highly ordered photonic PS film (PS sphere size = ca. 450 nm) with a thickness from 7 to 10 μm. A planar FTO substrate is required because the mac-FTO films exhibit perpendicular cracks which would prevent current extraction parallel to the substrate. The presence of a conductive substrate beneath the mac-FTO film should allow charge to travel from the mac-FTO to the planar FTO beneath and onto the external contact.

The FTO precursor solution was prepared through a typical preparation process,[152] where 1.40 g (4 mmol) of $SnCl_4.5H_2O$ was dissolved in 20 mL of absolute ethanol followed by sonication, and then saturated (45 g in 100 mL) 0.12 to 0.72 g (1 to 6 mmol) of NH_4F solution was added, and the result mixture was sonicated until optically clear and colourless. The varied amount of NH_4F in the FTO precursor solution is for the investigation of the influence of F content on the quality of mac-FTO films.

The initial attempts for fabrication of mac-FTO films were attempted by following a literature report.[133] For these attempts, the as-prepared FTO precursor solutions were used immediately after sonication, a total amount of FTO precursor solution from 50 to 150 μL was homogeneously spread on the PS photonic template films. 50 μL of FTO precursor solution infiltrated the PS photonic films through the voids among polystyrene sphere by capillary force. The FTO infiltrated samples were then dried at room temperature for 10 min, and the films were then heat to 100 ^oC to remove any residual solvent. This process was repeated for 1 or 2 more times intend to obtain a sufficient filling of the voids by FTO precursor. The resulting samples were then heated to 450 ^oC. This heating temperature is optimised from

350 to 550 ^{o}C. It should be noticed that, by eye, the obtained mac-FTO film has reduced opalescence. During the experimental process, after drying the infiltrated films at 100 ^{o}C, some area of the film flake off or curl up presumably caused by shrinkage of the FTO and PS mixture material at 100 ^{o}C. Figure 32 shows an example of the common defects in the mac-FTO film fabricated through this method.

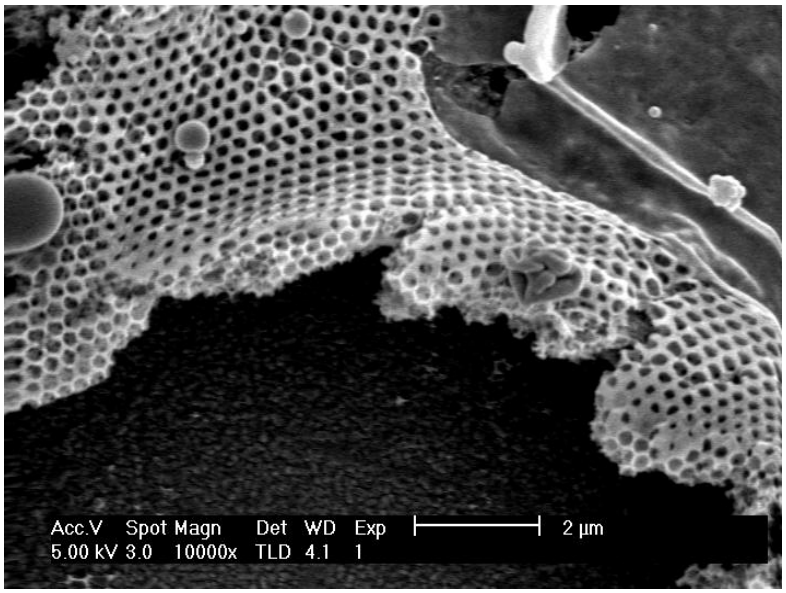

Figure 32: SEM image of a common defect observed in mac-FTO films fabricated by dropwise infiltration.

In terms of the PS film infiltrated with 50 µL, it is obvious that there is insufficient precursor material which leads to poor coverage of a mac-FTO film with a high percentage of defects (Figure 32) and large cracks (Figure 33 a). Therefore, a quite poor photonic stop band was observed by DRUVS as shown in Figure 33b. The stop band position can be predicted by Bragg-Snell equation (Equation 8). The detailed analyse on the stop band by Bragg-Snell equation will be presented for high quality mac-FTO films in the next section.

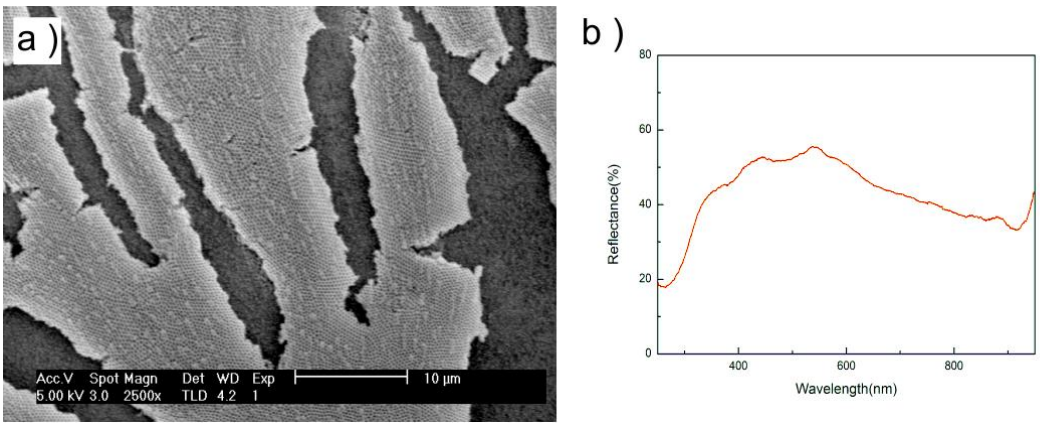

Figure 33: SEM image (a) and DRUVS spectra (b) of the mac-FTO films made with 50 µL precursor solution through the method above.

The infiltration of FTO precursor solution was repeated for multiple times to offer sufficient material form the 3DOM structures. SEM imaging was employed to investigate the process of multiple infiltration. Figure 34 shows a film sample imaged directly after the first (Figure 34a) and second (Figure 34b) time infiltration of FTO precursor.

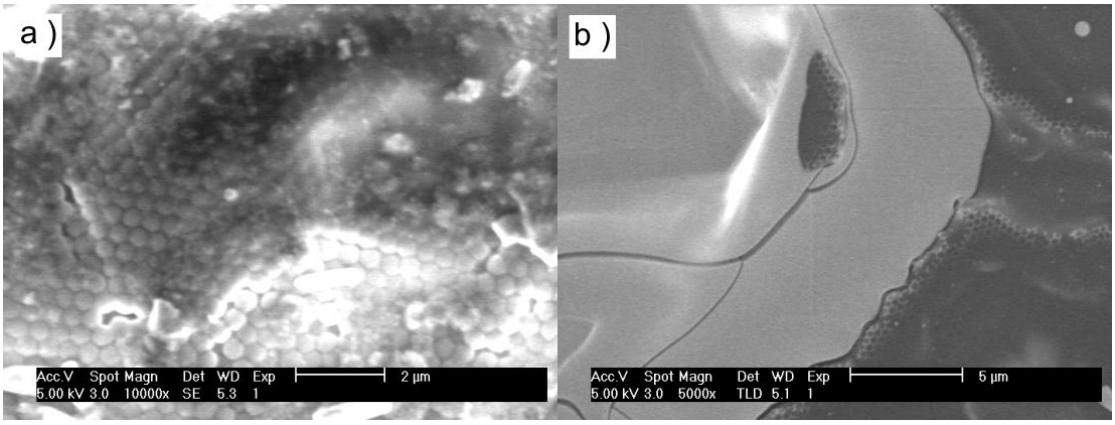

Figure 34: SEM images of PS photonic films imaged directly after a): the first time and b): the second time infiltration of FTO precursor before the calcination.

As shown in Figure 34a, FTO precursor material was observed among the voids and on top of the PS photonic films. The FTO precursor solution composed of $SnCl_4$ and

NH_4F was cast into the voids of the PS opal matrix, although there was over-loaded material found on the top of PS films. Upon the evaporation of the ethanol, the deposited $SnCl_4$ was hydrolysed to SnO_2 at 100 ^oC under a humid environment. The Figure 34b shows a PS film deposited with a mixture of $SnCl_4$ (light area) and SnO_2 (Dark area), due to the hydrolysed $SnCl_4$ at 100 ^oC.

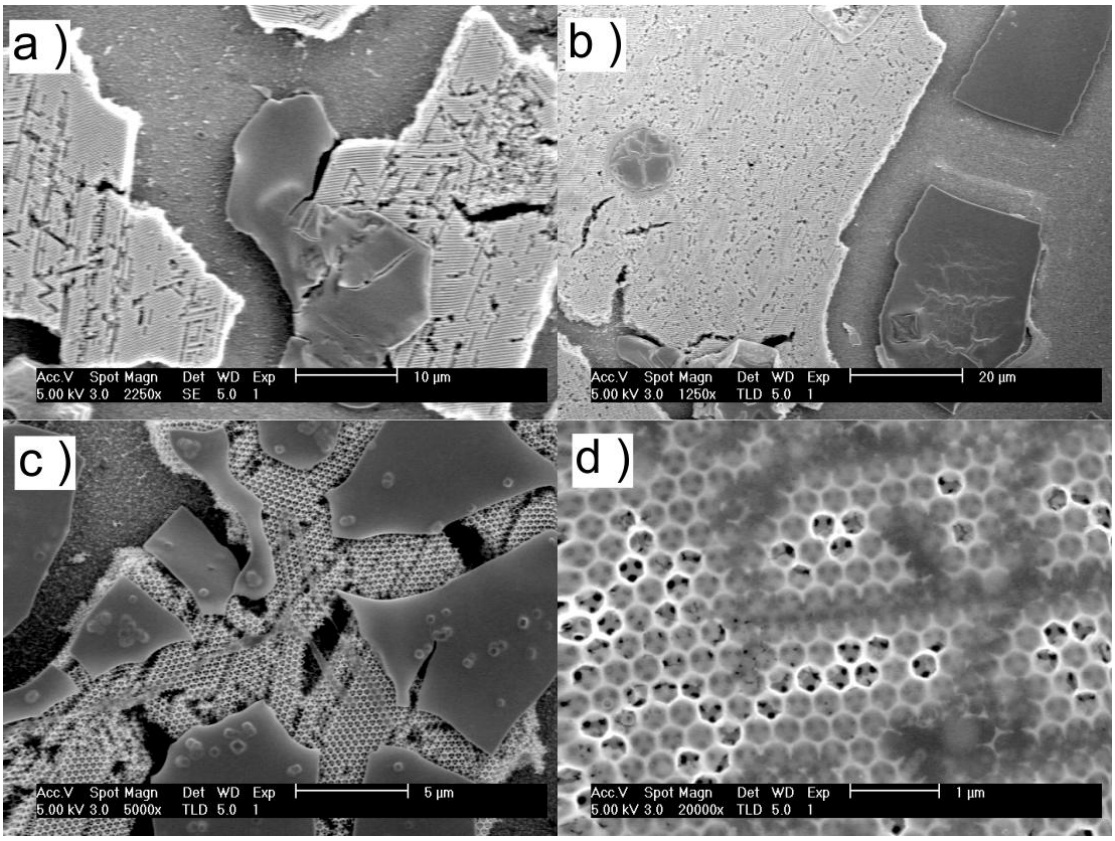

Figure 35: SEM images of the mac-FTO fabricated with multiple infiltration of FTO precursor solution after calcination.

After the calcination at 450 ^oC, PS sphere templates were removed and mac-FTO was hence achieved. Although the larger mac-FTO gives continuous 'islands' over 40 µm as shown Figure 35b (compared to ca.15 µm for a single infiltration) suggesting the infiltration is more sufficient, the obtained 3DOM is still of poor quality. As shown in Figure 35a-b, most of the precursor material refilled into the cracks formed large FTO solid pieces rather than forming the 3DOM structure. In addition,

the overloaded precursor material (Figure 35c) on the top of macroporous film blocked the pores which will have a negative influence on the decoration of photocatalysts into the mac-FTO. Not surprisingly, these samples also exhibit quite poor photonic properties.

These attempts above suggest that the sufficient precursor material is an important factor for fabrication of high quality mac-FTO films. Repeating the infiltration of precursor material process after the $SnCl_4$ hydrolysed to SnO_2 is not a reliable way to offer enough material for forming the 3DOM structure as shown in Figure 35. Multiple filling of FTO precursor will be required, because shrinkage will occur due to the loss of liquid volume of the precursor solution and densification of the FTO structure.

2.3.4: Method development for the synthesis of mac-FTO film

To improve the quality of the mac-FTO films, a modified soaking method was employed and the conditions were optimized. The FTO precursor solution was used immediately after preparation to avoid formation of particles from oxidized $SnCl_4$ blocking infiltration of precursor. A PS template coated FTO slide was pre-soaked in ethanol for 30 min before being stood vertically and submerged in the FTO precursor solution (3.5 mL) in a glass vial for another 30 min under a partial vacuum in a vacuum desiccator. The wet slide was removed from the glass vial and fresh stock FTO precursor solution (0, 20 µL and 40 µL) was carefully dropped onto the wet film with a Gilson pipette. The FTO infiltrated slides were then transferred to a furnace oven immediately for calcination at 450 ^{o}C under air. Figure 36 shows the main process of the fabrication of mac-FTO films.

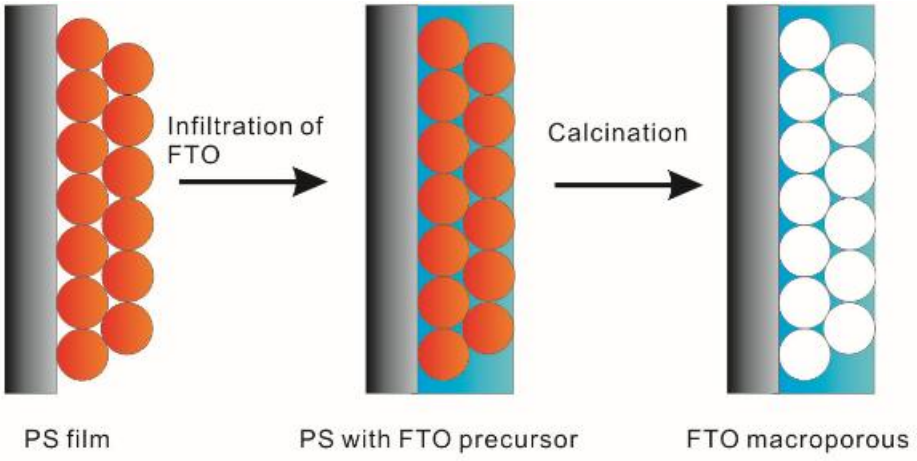

Figure 36: Schematic image of the fabrication of mac-FTO films.

The benefits of this method are to remove any air bubbles present in the PS film, which could prevent the infiltration of FTO precursor, and bubbles were observed when the vacuum was applied. In addition, pre-soaking the PS film in ethanol promotes infiltration of the ethanolic FTO precursor, by reducing surface tension and increasing miscibility within the PS film. Infiltration using more concentrated ethanolic solutions is limited by an increase in the viscosity of the precursor solution. Previous work on 3DOM materials has shown similar problems with poor infiltration of the precursor solution with high viscosity.[153] However, the more diluted precursor solution, will lead to insufficient infiltration of precursor materials for complete filling leading to thinner walls and larger windows between adjacent voids of the 3DOM structure which is not mechanically robust.[154,155] In this section, conditions such as F/Sn atomic ratio in precursor solution, vacuum and the volume of added stock FTO precursor after soaking were investigated to optimise the quality of mac-FTO films. Instead of making powder 3DOM materials,[153] vacuum was not commonly used for making film 3DOM materials in previous study. Hence the mac-FTO films were also synthesised without applied vacuum to study the effect of reducing pressure on making 3DOM films.

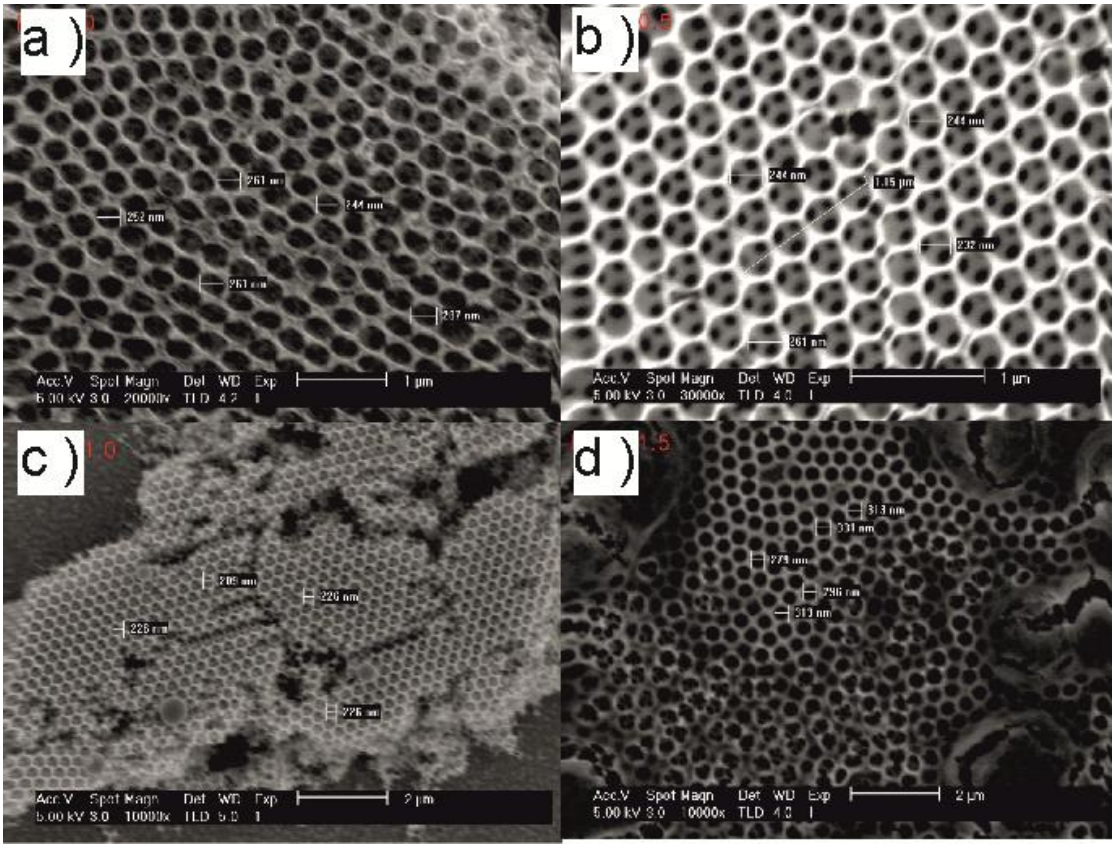

Figure 37: SEM images of mac-FTO film synthesized of varied F/Sn atomic ratio in the precursor solution without vacuum. a): 0, b): 0.5, c): 1.0 and d): 1.5.

By using the modified soaking method without vacuum, the effectsF/Sn atomic ratio in precursor solution was firstly studied. The SEM images in Figure 37 show four mac-FTO films synthesize with a F/Sn atomic ratio = 0, 0.5, 1.0 and 1.5 which exhibit a pore size around 250 nm, 240 nm, 230 nm and 290 nm in the mac-FTO films, respectively. The size of pores in mac-FTO film show a dependency on the fluorine content in precursor solution. This phenomena was also observed in reported antimony doped tin oxide, the larger pores were fabricated from a precursor solution with higher Sb/Sn atomic ratio.[130] In addition, the shrinkage of the pore size which is also material dependent. For example, for a PS opal film with sphere diameter of 450 nm, the spherical pore sizes of 3DOM TiO_2, Nb_2O_5, Ta_2O_5 and ZrO_2 are around 250±10 nm, 300±5 nm, 305±5 nm and 300±15 nm, respectively. In comparison with the PS template sphere size, the shrinkage of the

3DOM materials is 44 %, 33 %, 32 % and 33 %, respectively.[153] And this shrinkage is due to the melting of polystyrene spheres during the calcination and varying infiltration.[156] Furthermore, in terms of the pore size of NiO 3DOM films, it was also observed that the pore diameter has a dependency on the calcination temperature and the grain size: the pore size of NiO 3DOM films slightly decreased with the increasing calcination temperature and grain size.[156]

The ordered periodic structure of these macroporous films above are expected to exhibit photonic behaviour due to the regular modulation of the refractive index difference between walls and voids. DRUVS spectra of these mac-FTO films are shown in Figure 38 and sample (F/Sn = 0.5) exhibits greater reflectance than other three samples suggesting precursor solution in this ratio is more likely to give a high quality mac-FTO film. In addition, the overall reflectance decreased with increasing F/Sn atomic ratio in precursor solution.

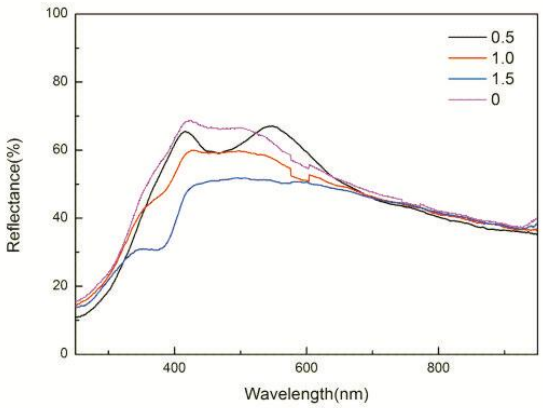

Figure 38: DRUVS spectra of mac-FTO films synthesized with varied F/Sn atomic ratio in precursor solution by soaking the PS template slides in FTO precursor solution without any other treatments.

The mac-FTO film sample (F/Sn = 0.5) imaged by SEM with various areas and magnification is shown in Figure 39. Ordered porous regions are observed, within

islands of around 10 to 20 μm in size. Such islands are often observed in 3DOM films caused by contraction of the film during heat treatment. Typically, the distance between the islands is around 5 to 7 μm. The distance between islands and the size of islands can give a rough idea of coverage of a mac-FTO film. In terms of use as a device, although the mac-FTO film is not continuous in long range, the conductive substrate attached to the bottom of the 3DOM film can still allow the transfer of charges across the electrode. However, it is still necessary to improve the coverage of mac-FTO to offer greater surface area and quality optical properties.

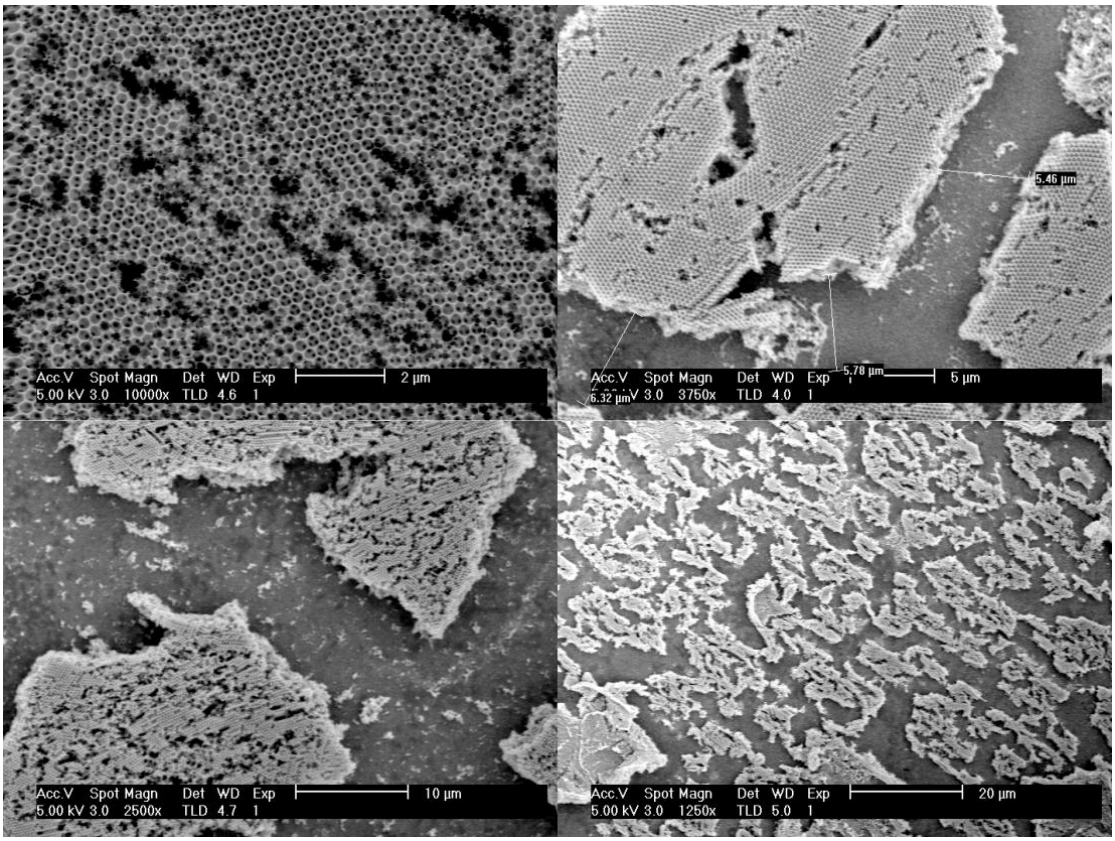

Figure 39: SEM images in different magnification of mac-FTO film (F/Sn = 0.5) synthesised in the absence of vacuum.

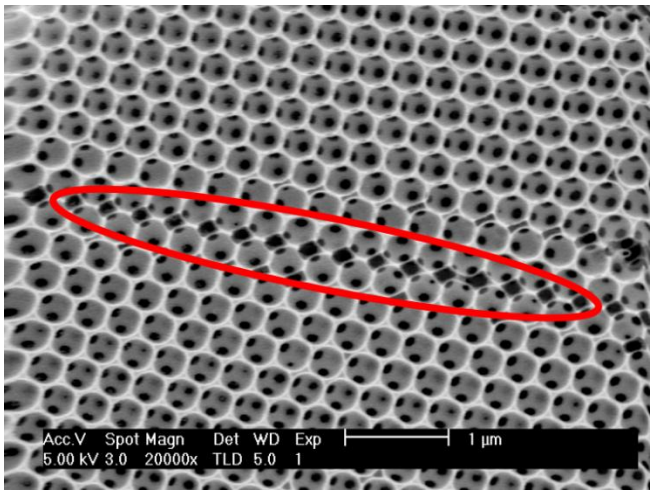

Figure 40: SEM image of the defect observed in mac-FTO, this defect is a combine of insufficient infiltration and dislocation.

Here Figure 40 shows an example of the defects observed in mac-FTO film which will exhibit a wide photonic stop band in DURVS spectra. The light regions in this SEM image represent the mac-FTO, and the dark regions the voids (air spheres) which were previously occupied by polystyrene spheres. Former contact points between neighbouring polystyrene spheres appear as windows between the pores (the small black holes). As is shown in the red ellipse, the body centred cubic structure (due to the bcc region in PS template) with defects in the 3DOM structure was observed. This is essentially a dislocation on the nm scale that is commonly observed at the atomic scale in condensed solid materials such as metals.

An obvious improvement of the quality of mac-FTO films were observed by reducing the pressure during the infiltration of FTO precursor solution. The improved mac-FTO films were synthesized by FTO precursor solution with F/Sn atomic ratio = 0.5, 1.0 and 1.5, respectively.

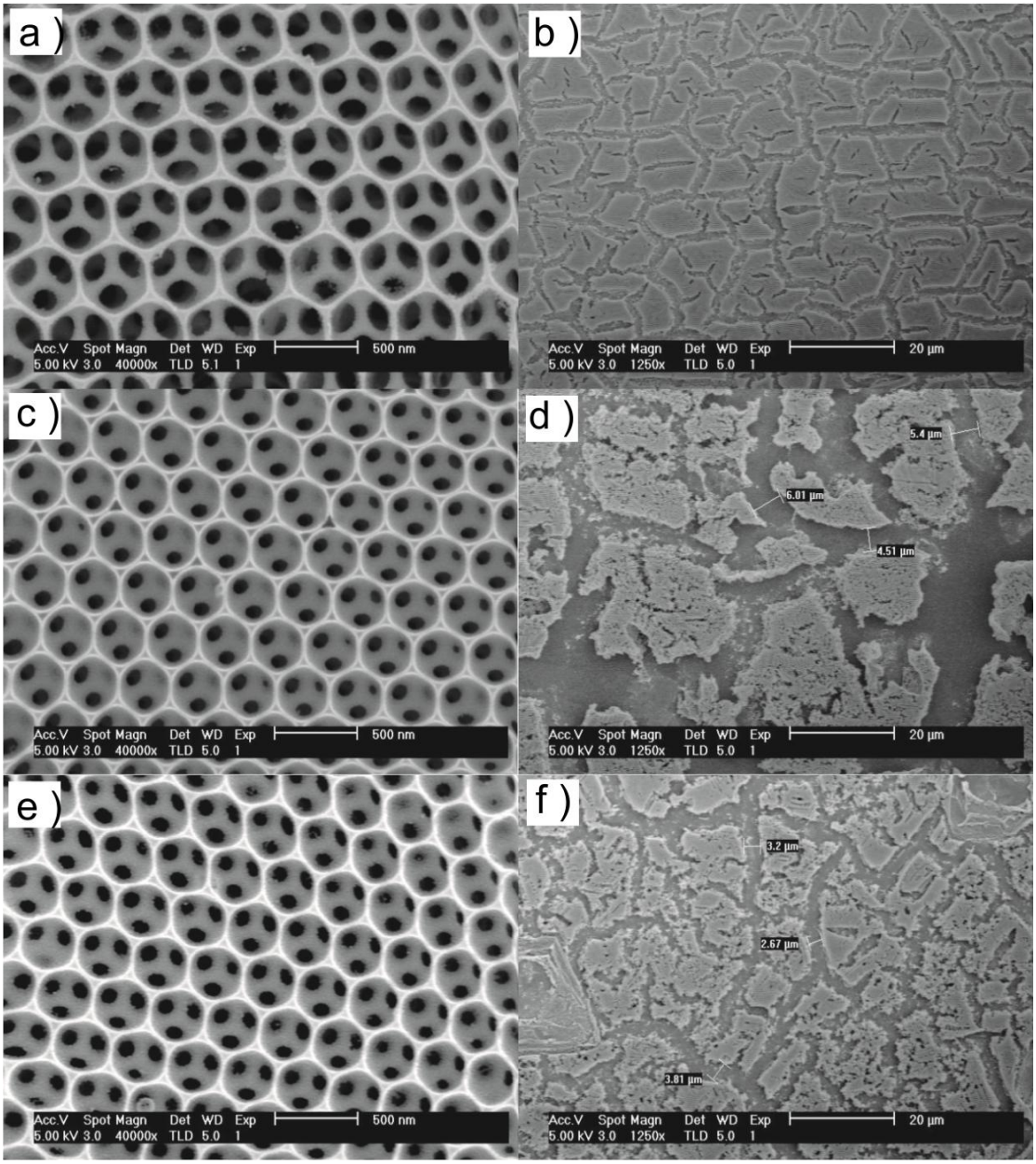

Figure 41: SEM images of mac-FTO films prepared by vacuum infiltration with various F/Sn atomic ratio in precursor solution. a) and b): 0.5; c) and d): 1.0; e) and f): 1.5.

Figure 41 shows the SEM images of the mac-FTO film prepared by soaking the PS template film in precursor solution under an applied house vacuum. The time for vacuum was optimized by vacuum infiltration experiments with varied periods. The mac-FTO films exhibit ordered and uniform pores in all three ratios and much less defects in the structures were observed in comparison to samples where soaking without vacuum or dropping is used to infiltrate the precursor solutions. The surface

coverage in terms of the size and distance between mac-FTO islands was also improved. Especially for the sample shown in Figure 41 (a,b) , where the size of islands in this sample is around 8 to 10 μm and the separation distance between islands is below 1 μm. The sample shown in Figure 41 (c,d) exhibited an island size around 15 to 20 μm and separation distance around 4 to 5 μm. As for the sample shown in Figure 41 (e,f), a small islands size around 5 to 10 μm and a separation distance around 3 to 4 μm was observed. By measuring the area of the islands in multiple SEM images, the percentage of surface covered with mac-FTO film was estimated to be ca. 75%, ca. 65 % and ca. 55 % for the sample prepared with F/Sn ratio in precursor solution of 0.5, 1.0 and 1.5, respectively. The coverage of mac-FTO film is similar to the percentage (67 %) reported in previous literature and the F/Sn =0.5 (ca. 75% coverage) sample even exhibits an improvement in comparison to the literature report.[157] In addition, the periodic ordered (D) of these mac-FTO films was measured to be ca. 310 nm from the SEM images. The morphology and photonic properties of these mac-FTO films mentioned above were also reflected in the DRUVS spectra as shown in Figure 42.

Optical Bragg reflections, manifest as photonic stop bands (A photonic stop band of structured TCO film is expressed as a peak in reflectance spectrum or a dip in transmission spectra. In the DRUVS spectra, the position of the stop band (λ_{max}) is dependent on the structure, periodicity (D), refractive index difference of the walls and voids (n and n_0), and the fraction of the volume of the film (φ) which it comprises (the symbol D, n, n_0 and φ are refer to equation 8). For example, the 3DOM film with smaller periodicity tend to exhibit a photonic stop band position at smaller wavelength. Alternatively, larger periodicity generally present a photonic stop band at larger wavelength.

Furthermore, the reflectance of 3DOM materials expressed by DRUVS spectra contains lots of information complementary to SEM imaging. The stop band intensity and width are reflective of the homogeneity and coverage of the macroporous

structure. A sharp photonic stop band with high intensity generally suggest that the filling factor and the pore size across the 3DOM film is quite homogeneous, the coverage of the 3DOM film is in a high percentage and the crystal structure of the spherical pores is or nearly monodispersed.

Alternatively, a wide photonic stop band generally suggest a less homogeneous 3DOM film. The wide photonic stop band can be visualized as a combination of multiple photonic stop bands distributed in a wavelength range, these stop bands are slightly different in filling factors (wall thickness), periodic orders (pore size) or crystal structures (such as bcc structure due to the dislocations). The photonic stop bands with low reflectance intensity in the spectra normally imply a weak photonic properties which will caused by very thin 3DOM film (short periodic structure in perpendicular direction) or a film with low coverage (insufficient infiltration and less mechanical robust).

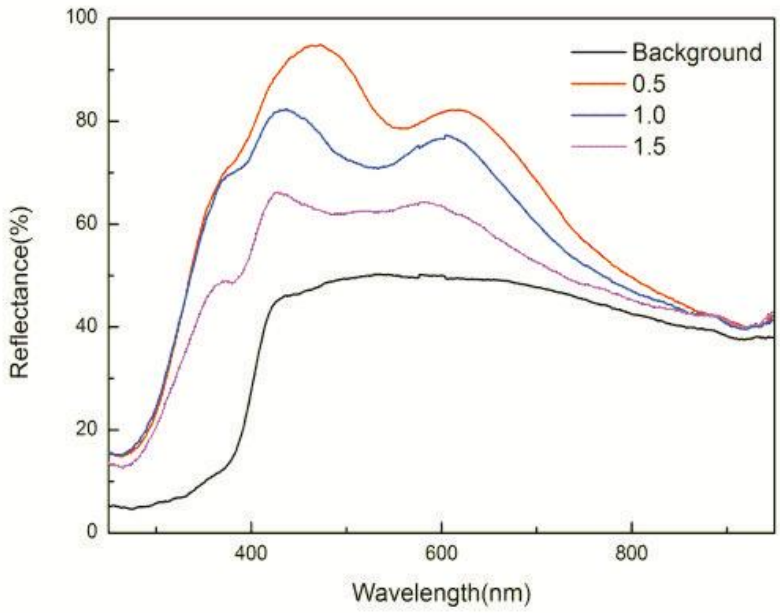

Figure 42: DRUVS spectra of the mac-FTO films prepared by soaking infiltration under vacuum with F/Sn ratio in precursor solution of 0.5 (red), 1.0 (blue) and 1.5 (purple). A planar FTO (black) substrate was also measured for comparison.

The mac-FTO film with F/Sn atomic ratio at 0.5 exhibited the most intense photonic stop band in DRUVS spectra shown in Figure 42 which can correspond to the greater coverage of it shown in Figure 41b. The photonic stop band of sample (F/Sn atomic ratio = 0.5) is located at a slightly longer wavelength (ca. 610 nm) in comparison to the other two samples which may be due to the slightly larger filling factor (φ) induced by a more sufficient infiltration of FTO precursor solution. By using Equation 8, the filling factor (φ) of these samples can be calculated as shown in Table 1 where D = 310, n = 2.5, n_0 = 1.0, θ = 45^o. Here n and n_0 mean the refractive index of FTO and air, respectively. The mac-FTO films exhibit decreasing filling factor with increased F/Sn ratio in precursor solution.

F/Sn ratio	λ_{max}	hkl	φ
0.5	610	111	0.181
1.0	600	111	0.172
1.5	590	111	0.164

Table 1: Stop band positions (as shown in Figure 42), Bragg reflection assignments of mac-FTO prepared with vacuum infiltration and calculated filling factors.

In addition, the photonic stop band position (ca. 610 nm) of sample (F/Sn = 0.5) made under vacuum shown in Figure 42 have a red-shift when compared with the stop band position of sample (F/Sn = 0.5) made without vacuum shown in Figure 38 (ca. 570 nm). This is because the more sufficient infiltration of FTO precursor solution by applying vacuum lead to enhancement of filling factor.

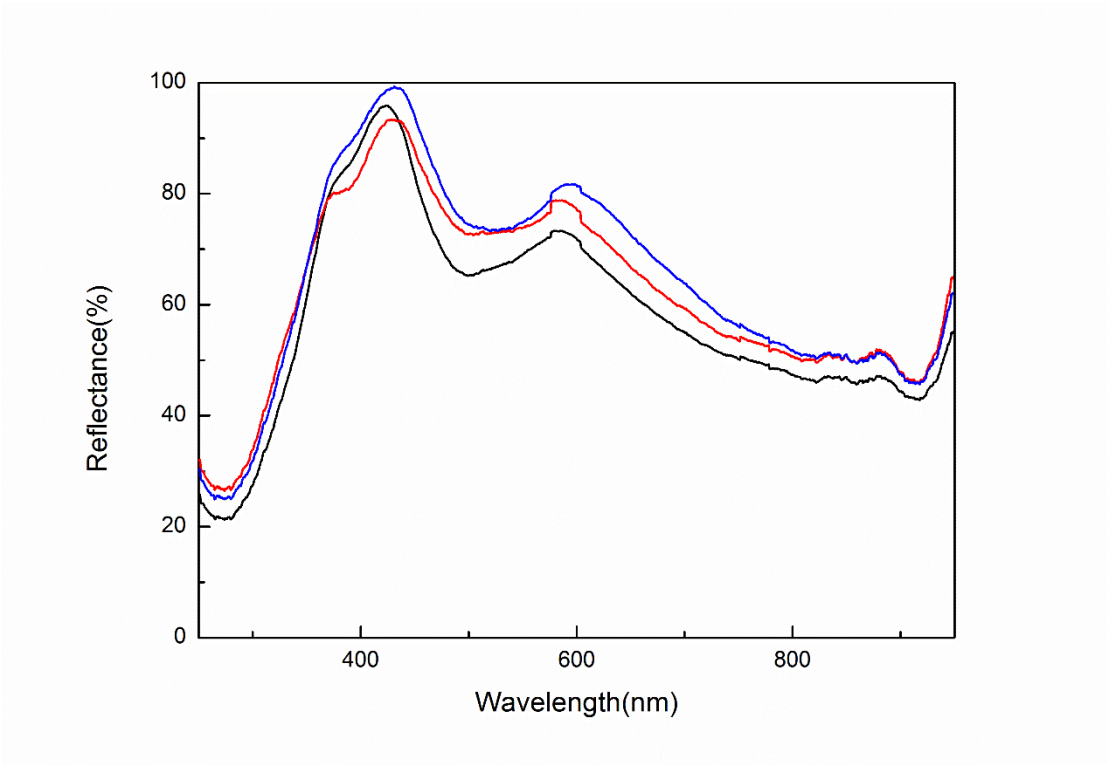

Figure 43: DRUVS spectra of three mac-FTO films on planar FTO glass, showing reproducibility of the stop band position. This three samples were prepared by vacuum infiltration in the same batch with Sn/F = 0.5 in precursor solution.

Figure 43 shows the DRUVS spectra of three mac-FTO films prepared in the same batch through vacuum infiltration. The photonic stop band position and intensity is reproducible between samples in a small distribution range. All these discussions and experiments above suggest that the sufficient infiltration is a key factor to enhance the quality of mac-FTO films and it can be optimized effectively by modifying the infiltration process.

To further improve the quality of mac-FTO films, 20 or 40 µL of fresh FTO precursor solution was carefully added to the wet film samples by Gilson pipette after the vacuum infiltration, to refill the pores. This process is intended to supply more precursor material for the fabrication of mac-FTO films.

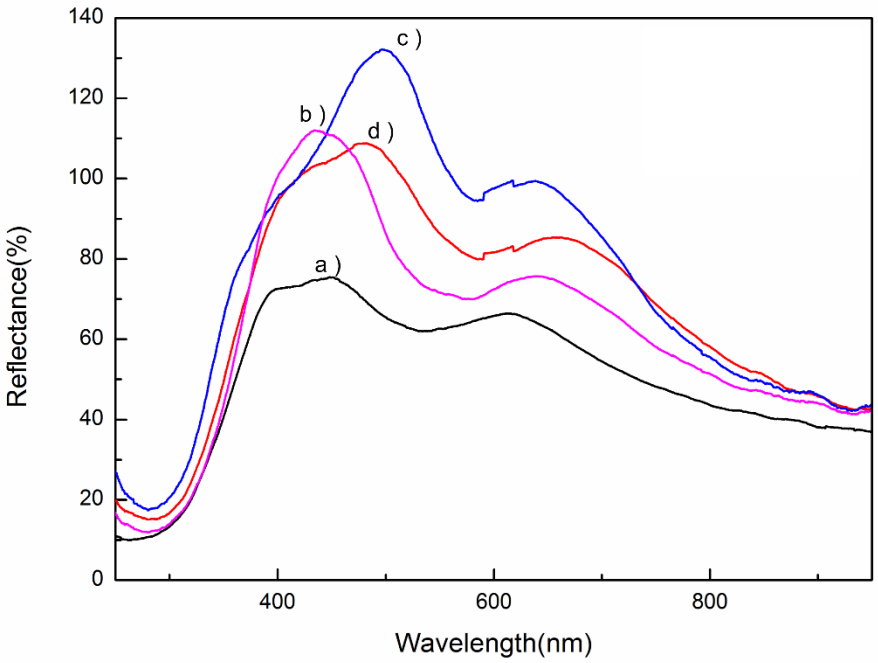

Figure 44: DRUVS spectra of four mac-FTO films on FTO glass substrate prepared by F/Sn ratio= 0.5 in precursor solution with different conditions of infiltration. a): simply soaking in FTO precursor solution; b): vacuum infiltration; c): refill of 20 μL of fresh FTO precursor solution after the vacuum infiltration; d): refill of 40 μL of fresh FTO precursor solution after the vacuum infiltration.

Here Figure 44 shows a DRUVS spectra of four mac-FTO films prepared by the same precursor solution, but the varied conditions of infiltration lead to samples with different photonic properties. The photonic stop band intensity enhanced after 20 μL of FTO precursor solution was added to the vacuum infiltration sample in comparison to vacuum infiltration without adding material. The improvement of the intensity of photonic stop band suggest a mac-FTO film with greater coverage or thickness was obtained. Another peak (such as the peak located at ca. 490 nm in Figure 44c and other DRUVS spectra of mac-FTO shown in this section) appears due to multiple scattering of the incident light. This effect is known as the Renninger effects and can cause additional peaks to appear when there should be none and is

based solely on Bragg diffraction.[158,159] This additional reflectance peak can also suppress the photons travelling within the mac-FTO film, hence improve the light absorption.

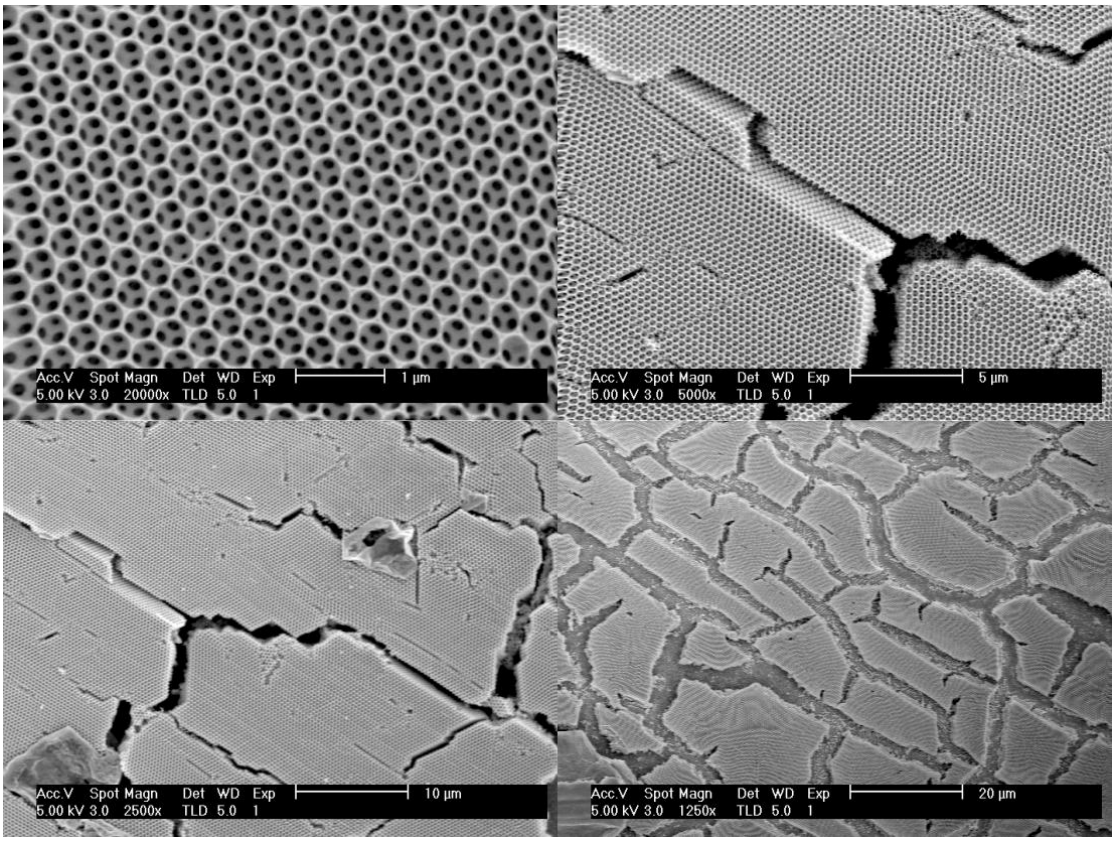

Figure 45: SEM images in varied magnifications of the mac-FTO film prepared by FTO precursor solution (F/Sn = 0.5) through vacuum infiltration with 20 µL of refilled precursor material.

Corresponding to the reflectance spectra shown in Figure 44c, a high quality mac-FTO film (with vacuum, F/Sn = 0.5 and 20 µL of refilled material) with a thickness around 5 to 7 µm was presented by SEM imaging in different regions and magnifications (Figure 43). Highly ordered FCC lattice structure with a long periodic range was expressed in the SEM images, and only a few defects were observed in the structure of the mac-FTO film. The majority of the islands size are around 20 to

25 μm and the separation distance between the islands is around 500 to 800 nm. The estimated coverage of this high quality mac-FTO film is around 80 %.

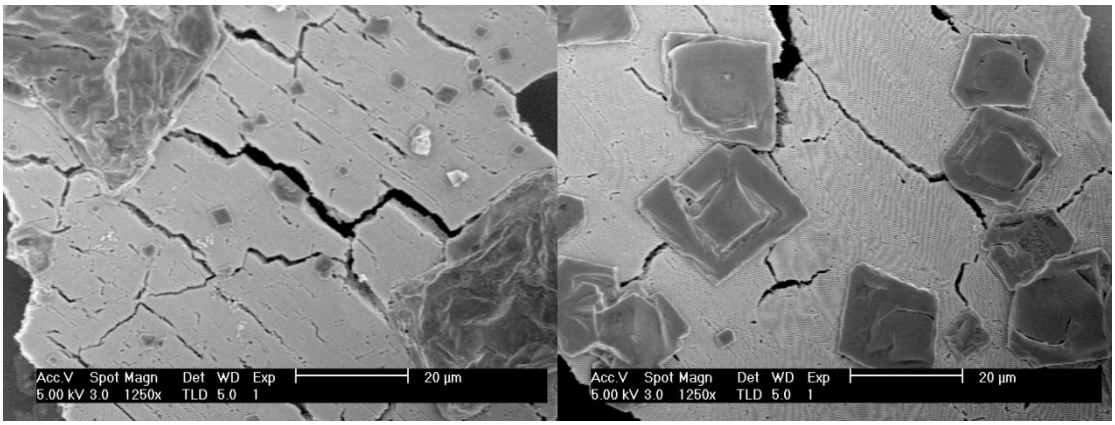

Figure 46: SEM images of the mac-FTO film prepared by FTO precursor solution (F/Sn = 0.5) through vacuum infiltration with 40 μL of refilled precursor material.

The sample with a 40 μL refill of precursor material exhibits less intense photonic stop band than that with 20μL refill. This can be explained by the SEM images shown in Figure 46. Although the mac-FTO sample present a great coverage and a stop band position in longer wavelength (greater filling factor), the bulk FTO on top of the 3DOM film will block reflected light during DRUVS measurement. In addition, it will also block the decoration of photocatalysts within the structure. Furthermore, mac-FTO films prepared with varied F content in precursor solution through this improved method were investigated. F/Sn ratio = 0.5 in precursor solution exhibited best photonic properties by this approach in comparison to other samples as shown in Figure 45. Samples made with other ratios exhibit less intense and broader stop band reflective of greater film heterogeneity and poor film coverage. In addition, the extinguish reflectance peak from Renninger effects (Such as the peak shown in Figure 47c, at 450 nm) seems to be proportional to the intensity of photonic stop band. Further study is worth doing to utilize Renninger effects for light harvesting.

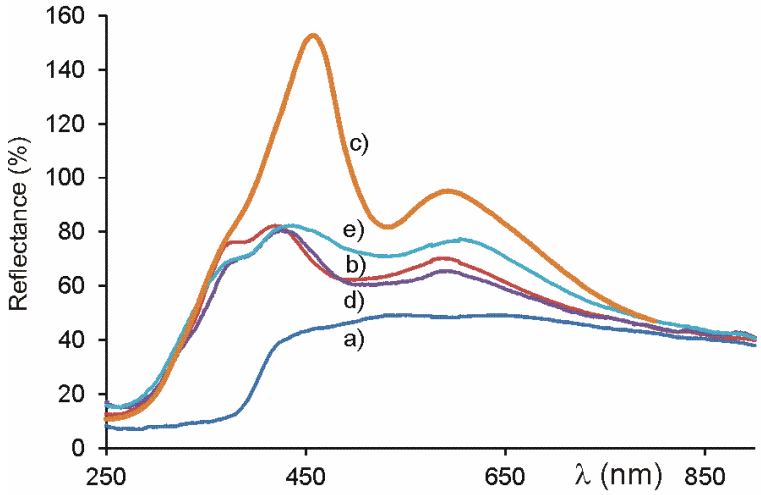

Figure 47: DRUVS spectra of mac-FTO films prepared through vacuum infiltration with 20 µL of refilled precursor material by F/Sn atomic ratios in precursor solution of a): blank FTO substrate; b): 0.25; c): 0.5; d): 0.75 and e): 1.0.

Corresponding to the DRUVS result of the four samples prepared with various F/Sn atomic ratio in precursor solution (Figure 47), calculation of the filling factors of them is presented in Table 2. Sample (F/Sn = 1.0) shows a slightly higher filling factor but much lower intensity in reflectance than Sample (F/Sn = 0.5) suggesting the filling factor is not necessarily corresponding to the optical quality of mac-FTO films.

F/Sn ratio	λ_{max}	hkl	ϕ
0.25	595	111	0.168
0.5	615	111	0.186
0.75	600	111	0.172
1.0	620	111	0.191

Table 2: Stop band positions (as shown in Figure 47), Bragg reflection assignments of mac-FTO films prepared with the improved method under vacuum and calculated filling factors.

2.4: Additional Characterization of mac-FTO

2.4.1: Powder X-ray Diffraction

Powder XRD was used to characterize the crystal phases of FTO films. For both the planar FTO films and the mac-FTO films, the crystalline peaks are observed. PXRD spectra of aluminum holder used for PXRD analysis on mac-FTO and planar FTO is presented in Figure 49 as a background. Figure 50 shows the PXRD spectra of mac-FTO film with cassiterite crystal structure (SnO_2 JCPDS 41-1445), which is commonly seen in previous literature reports and commercial planar FTO glass.

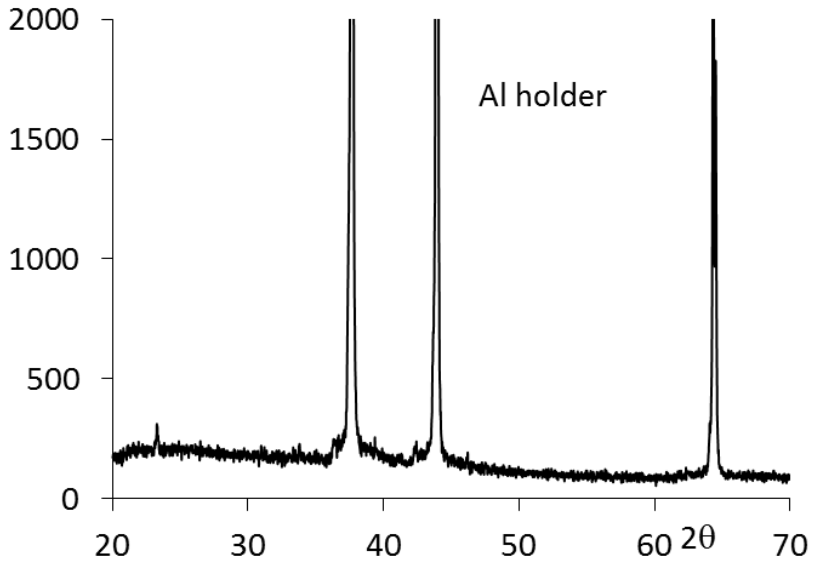

Figure 49: Diffractogram of blank aluminium holder used for surface electrode PXRD

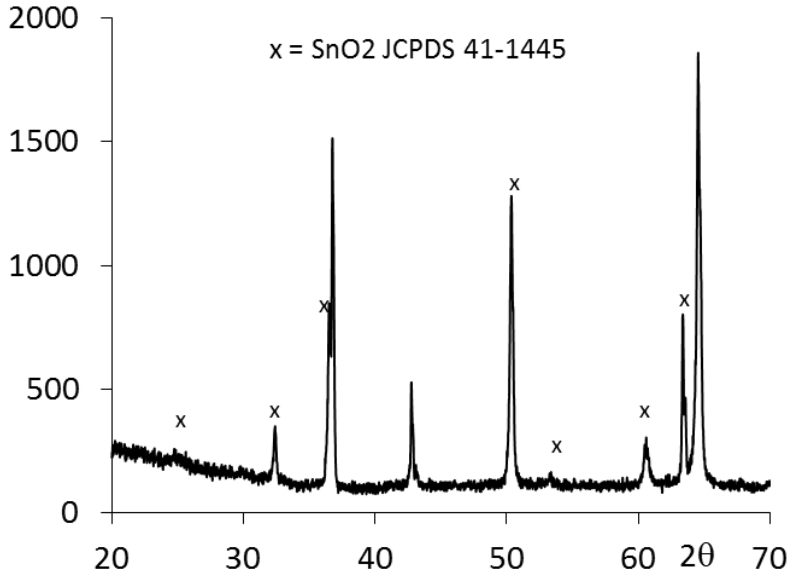

Figure 50: PXRD spectra of a mac-FTO electrode, x = SnO_2 JCPDS 41-1445.

2.4.2: Electron Microscopy

The cross section SEM images in Figure 51 and Figure 52 exhibit the approximately thickness of planar and mac-FTO film, respectively. For the planar FTO films with the lowest sheet resistance (7.6 Ω □) obtained in this work, a thickness around 850 nm was observed. According to a literature report,[160] the sheet resistance of FTO thin film decreases with increasing thickness until thicker than 800 nm, an almost constant value in sheet resistance was observed. In addition, the planar FTO film exhibits roughness as shown in SEM image, this may due to the unstable surface temperature of substrate during spray pyrolysis.

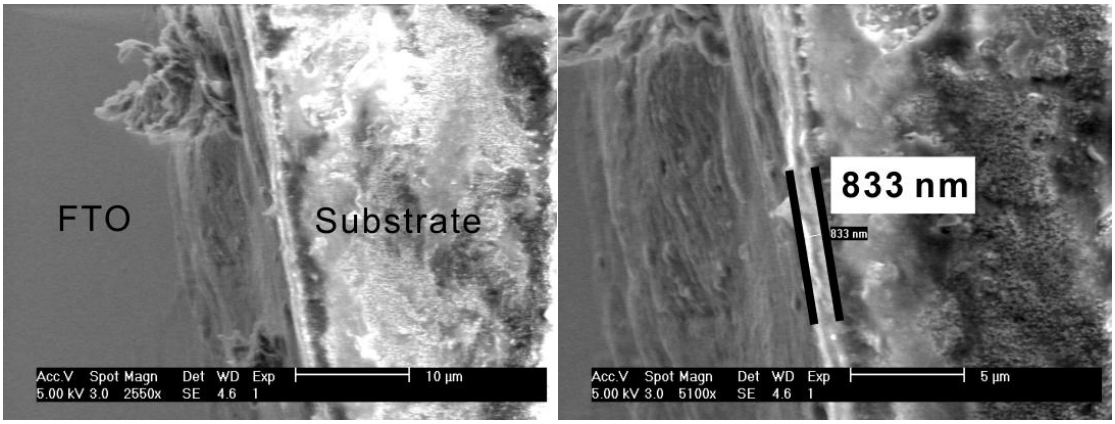

Figure 51: SEM images of a cut edge of FTO planar film on glass substrate.

As shown in Figure 52, the thickness of mac-FTO films obtained in this work in around 5 to 7 µm (15 to 20 layers) which is slightly thicker in comparison to a literature mac-FTO film (～5 µm).[133] As mentioned in the introduction in this chapter, mac-FTO film with a thickness from 1.4 to 5.6 µm and mac-TiO_2 film with a thickness of 1.6 to 6.2 µm were investigated, it was found that both of these 3DOM films exhibit the highest efficiency when with greatest thickness. [134] However, the thickness of 3DOM films are limited by the PS sphere templates, since too thick PS film tend to show poor mechanical strength.

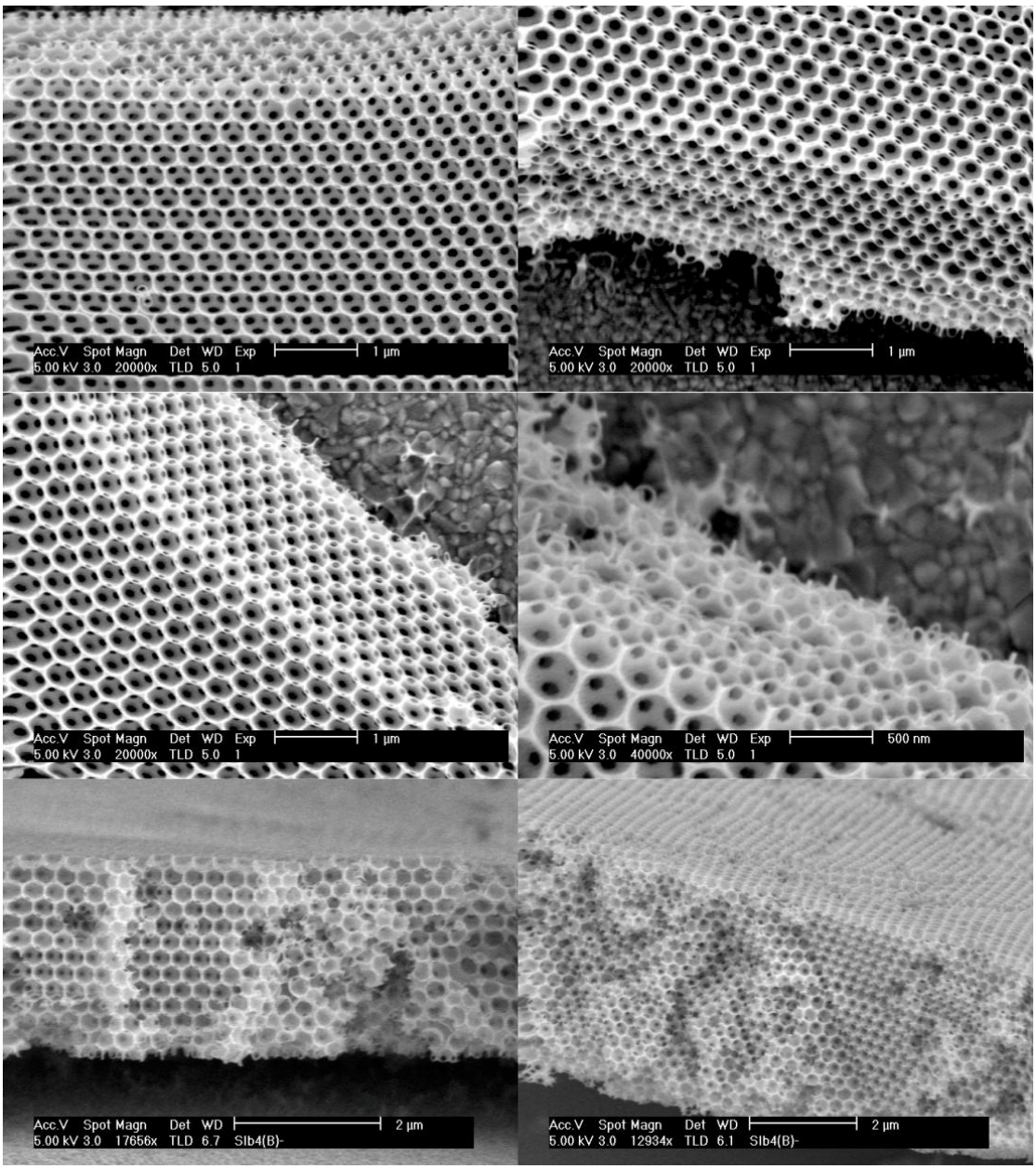

Figure 52: SEM images of mac-FTO films at the edge of islands and from cross-section (prepared by improved method).

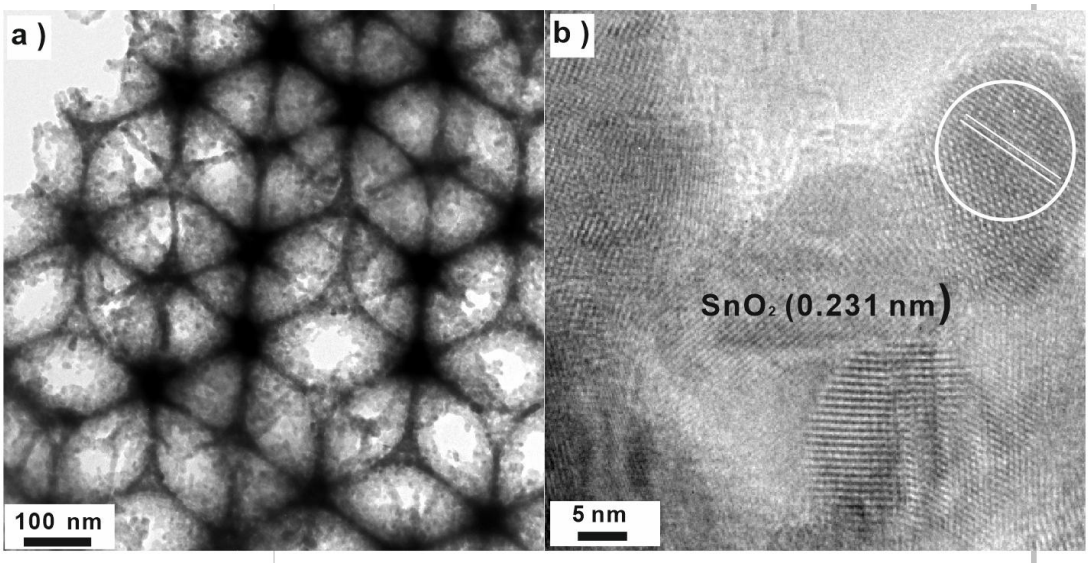

Figure 53: TEM images of mac-FTO electrode. a): FCC lattice structure of mac-FTO and b): lattice fringes of FTO nanoparticle.

As shown in Figure 53a by TEM imaging, the ordered FCC structure of mac-FTO was presented. In addition, the lattice fringes of tin oxide was measured to be 2.31 Å, corresponding to 111 crystal plane. (SnO_2 JCPDS 41-1445).

2.4.3: UV-vis transmission Spectroscopy

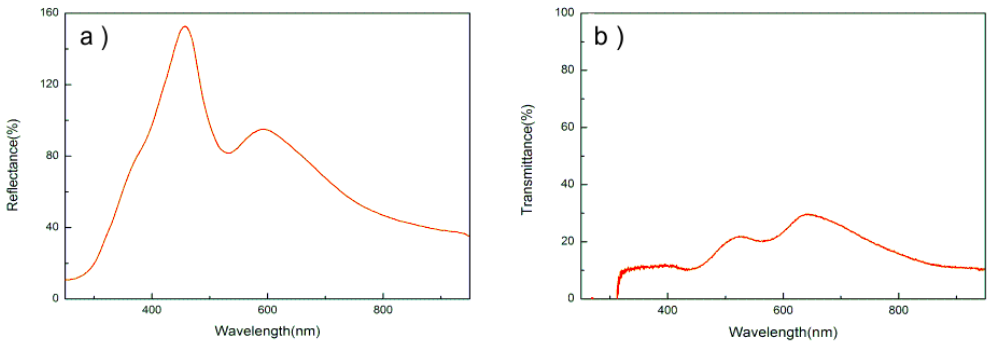

Figure 54: UV-vis spectra of a mac-FTO film with F/Sn atomic ratio 0.5 prepared by improved method under vacuum. a): reflectance, b): transmittance.

The high quality mac-FTO film achieved in this work exhibit excellent photonic properties, the high intensity of the photonic stop band centred at 615 nm (Figure 54a) indicates the mac-FTO film is homogeneous, highly ordered and with good coverage. Correspondingly, around 20 % transmittance in visible and UV light region was observed as shown in Figure 54b suggesting the light of wavelength in this range is effectively diffracted and scattered. The lack of transmission means that the photons will have a greater path length via diffraction and scattering thus improving the chance of absorption by a photocatalyst coated onto the 3DOM support. It is worth noting that the position reflectance peaks corresponds to the position of the transmission dips in spectra. This is the most extinguished photonic stop observed in mac-FTO or TO by far in comparison with previous literatures (ca. 52 % in reflectance, [21] over 40 % in transmission[125,133,161]). An example of UV-vis transmission spectra of macroporous SnO_2 in previous literature report is presented in Figure 55 for comparison.

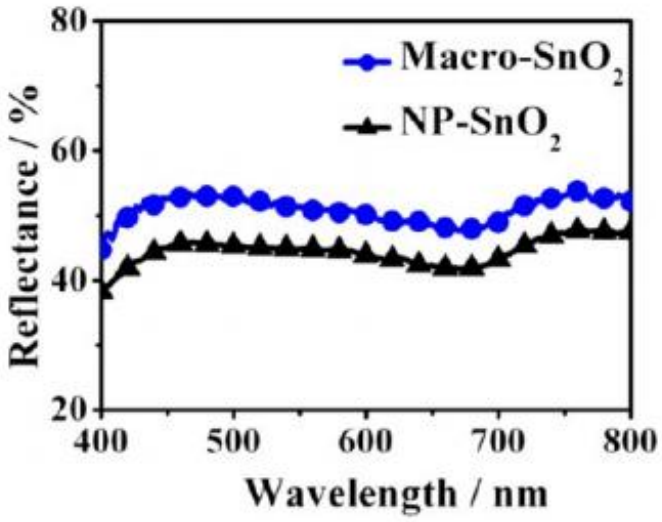

Figure 55: DRUVS spectra of nanoparticle SnO_2 film (NP-SnO_2) and macroporous SnO_2 film (Macro-SnO_2) in a previous literature report.[125]

2.4.4: Digital photographs

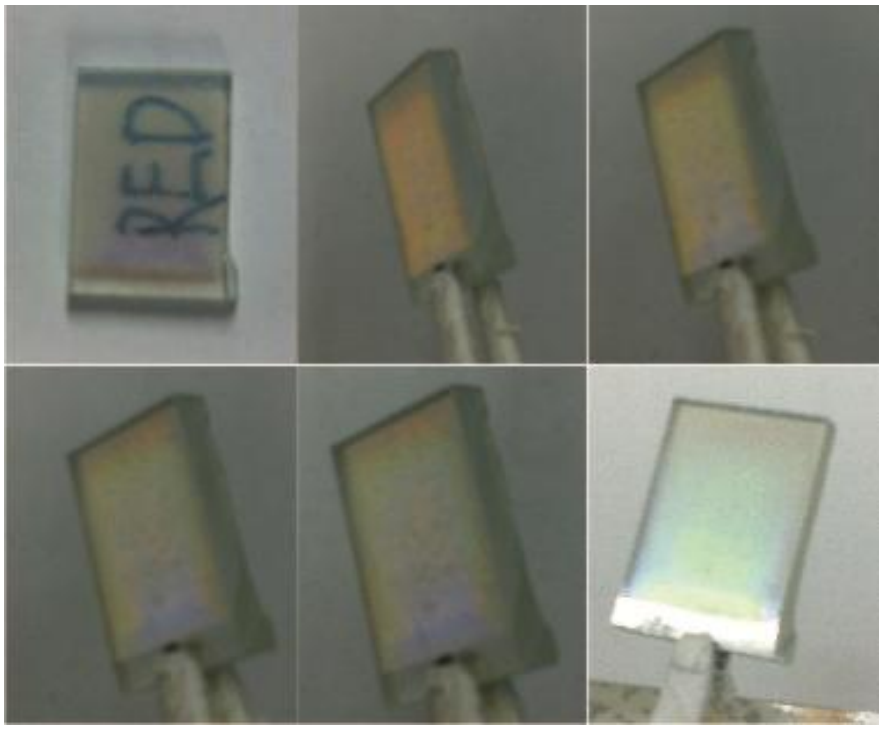

Figure 56: Digital photographs of mac-FTO electrode showing opalescence.

As shown in Figure 56, the mac-FTO film is transparent but exhibit various beautiful colours due to Bragg reflection when changing the observation angle. By eye, is the simplest and most straight forward way to evaluate the quality of a photonic crystal since only photonic crystals with high quality can exhibit these bright colours. Similar performance was also observed in highly ordered PS template film (Figure 29).

Figure 57b shows a broken piece of mac-FTO on commercial FTO glass after calcined at 800 ^{o}C for 2 h. Although the substrate is broken and melted, the mac-FTO film still show opalescence. Using FTO quartz substrate can prevent the mac-FTO electrode from breaking at high temperature (Figure 57c). Some defects were observed after high temperature calcination by SEM as shown Figure 57d,

however, the ordered macroporous structure still remained. Although defects could be introduced at high temperature, the mac-FTO films still exhibit potential usage in supporting materials which need to be synthesised at 800 ^{o}C through in-situ method.

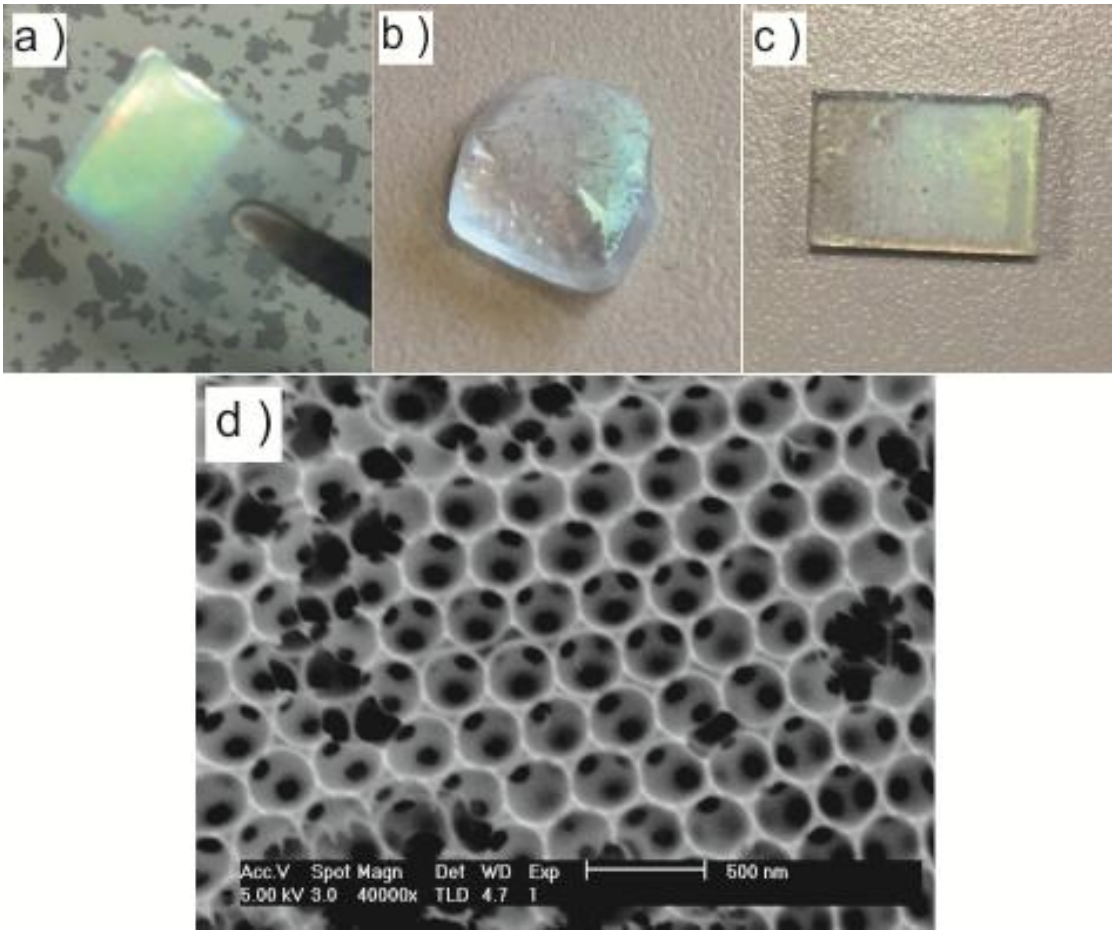

Figure 57: Digital photographs and SEM image of mac-FTO films. a): photograph of mac-FTO on commercial planar FTO glass calcined at 450 ^{o}C for 2 h; b): photograph of mac-FTO on commercial planar FTO glass calcined at 800 ^{o}C for 2 h; c): photograph of mac-FTO on lab made planar FTO quartz calcined at 800 ^{o}C for 2 h; d): SEM image of mac-FTO on lab made planar FTO quartz calcined at 800 ^{o}C for 2 h.

2.4.5: Electronic properties of mac-FTO film

Typically, the electrical properties of continuous films are determined via the four point probe van der Pauw method and Hall measurements.[136] However, for macroporous films on a continuous conductive support it is necessary to avoid direct probe contact with the support which would likely lead to data reflective of the electronic properties of the support and not the macroporous structure. Using traditional metal paint or low melting solid contacts we could not guarantee avoiding contact with the support and spring-loaded metal contacts damaged the porous structure. Therefore, partly because the final application is for photoelectrochemistry, electrochemical techniques were used to inform conductivity of the mac-FTO films.

In collaboration with Danielle Jowett (a fellow PhD student) electrochemical methods were used to estimate a surface roughness factor for the mac-FTO in comparison to planar FTO. When used as an electrode for the oxidation/reduction of ferrocene (Figure 58) the increase in the estimated geometric surface area is not reflected in a similar increase in current, which was also observed for other structured FTO electrodes. However, mac-FTO exhibits ca. 3 times greater current than planar electrodes and greater reversibility with the cathodic-anodic peak-to-peak difference $\Delta E_{1/2}$ of 100 and 450 mV, respectively.

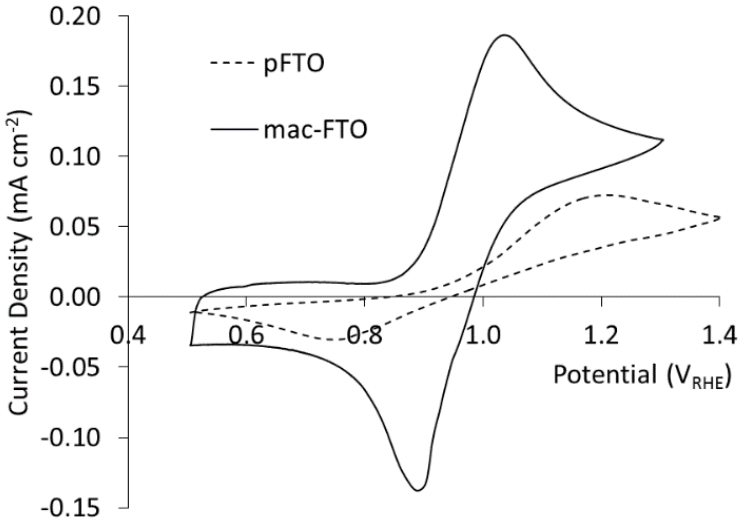

Figure 58: Cyclic voltammetry of ferrocene (1 mM) on planar FTO and mac-FTO film.

Electrochemical methods were also used to estimate a surface roughness factor by comparison of capacitance measurements of planar and mac-FTO films. These measurements are usually considered more accurate than comparison of measurements where current is passed because of factors that can affect electron transfer. For the planar FTO electrodes, regardless of the conditions used to make them, have similar peak currents when probed with ferrocene, which suggests that the surface area is broadly similar. If the capacitance of these electrodes is determined, then it can be used as a reference for the macroporous electrodes giving a roughness factor. The capacitance of planar FTO was found to be ~7 μF in all cases and this is now defined as a roughness factor of 1.

Figure 59 clearly shows that the capacitance of the mac-FTO electrode is much higher than that of the planar FTO electrode from the CV. The maximum roughness factor is observed for an electrode calcined at 450 °C, with a roughness factor of 12.

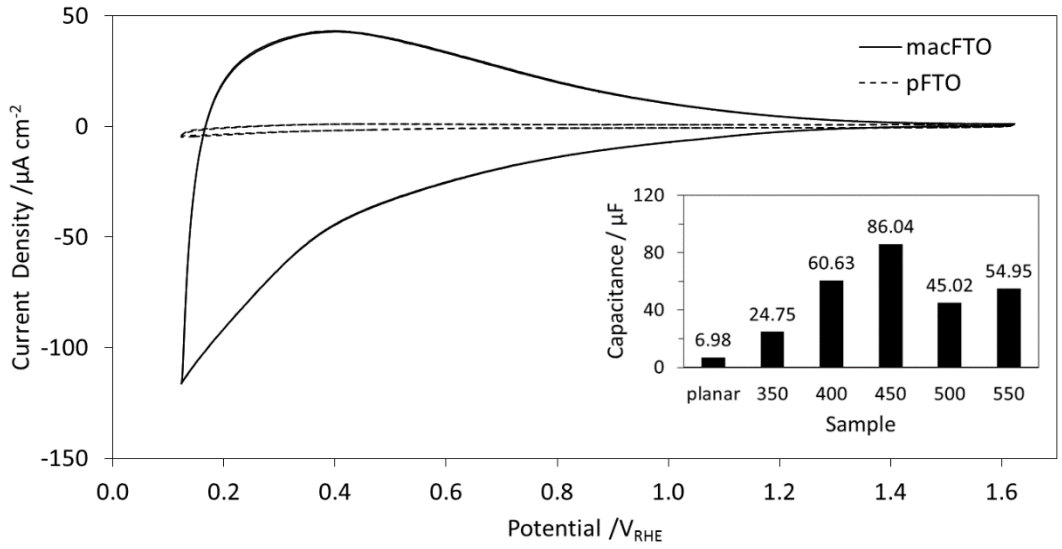

Figure 59: Capacitance of a mac-FTO electrode (Sn/F = 0.5, calcined at 450 °C), compared to the commercial planar FTO electrode and (inset) the capacitance of mac-FTO electrodes calcined at different temperatures (°C) compared to the planar FTO electrode.

In chapter 3, the mac-FTO film will be shown to support charge transport on excitation of a photoactive material supported on the mac-FTO.

2.4.6: Determination of fluorine content

The fluorine content of mac-FTO electrodes could not be determined directly by XPS due to the very low content. During synthesis the vast majority of the fluoride is lost as volatile by-products from calcination. In the literature there is no clear correlation between fluorine content and electronic properties and in most cases the F content is not determined. Knowledge of the fluorine content in planar FTO and mac-FTO films as a function of Sn/F ratio would provide insight into the comparability between planar FTO and mac-FTO films. For example it was unknown if calcination in the presence of the polystyrene template for mac-FTO altered the final F-content and if this is dependent on the initial Sn/F ratio. EDX and SSNMR

were used to investigate the F content of the mac-FTO-films. All FTO syntheses use large excess of fluoride because most is lost during calcination as HF and the solubility of fluoride in SnO_2 is inherently low. Potentially, a high concentration of carbonaceous material could lead to volatile CF species, thus reducing the F content further and compromising the conductivity of the film. The final F content is rarely determined because of the difficulty of fluorine analysis, particularly at low concentration.

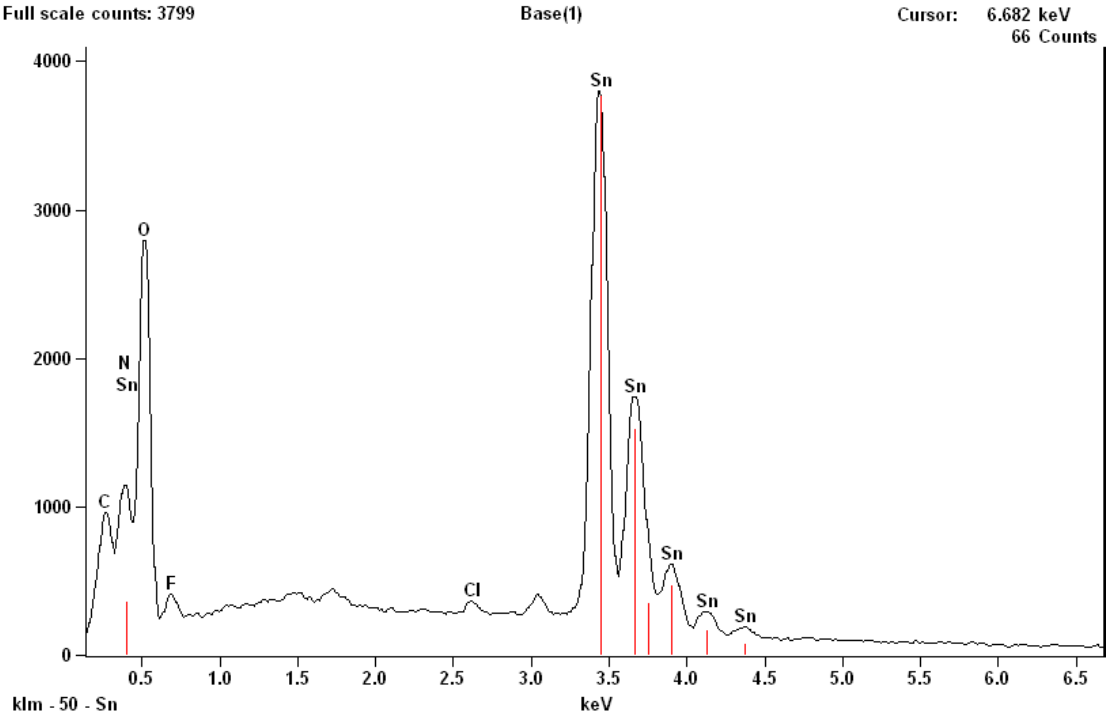

Figure 60: SEM/EDX elemental spectra of transparent highly ordered mac-FTO film.

Element Line	Norm. Wt.%	Atom %
C	3.80	13.23
N	4.59	13.70
O	17.59	45.95
F	0.57	1.25
Sn	73.45	25.86
Total	100.00	100.00

Table 3: SEM/EDX elemental analysis of transparent highly ordered mac-FTO film.

The results of EDX analysis are shown in Figure 60 and Table 3. The fluorine content was also quantified with ^{19}F solid state NMR (Figure 61) by Dr. Pedro Aguilar at the University of York, following the approach taken by Günne *et al*.[162] Powders of porous FTO samples were made using the same conditions to the mac-FTO electrodes to give sufficient material for NMR analysis. The fluorine content of the powders was lower than that of the precursor solution by about a factor of 100, yielding a fluorine content of around 0.005 (Sn:F) or 0.5 at. %. Typical values for Hall effects measurements in the literature give the number of F atoms on the order of 5 $x10^{20}$ cm^{-3} which is equivalent to ca. 3 at. %. It is not uncommon for numbers as low as 0.7 at. % to be reported, which is similar to the fluorine content found in this work.

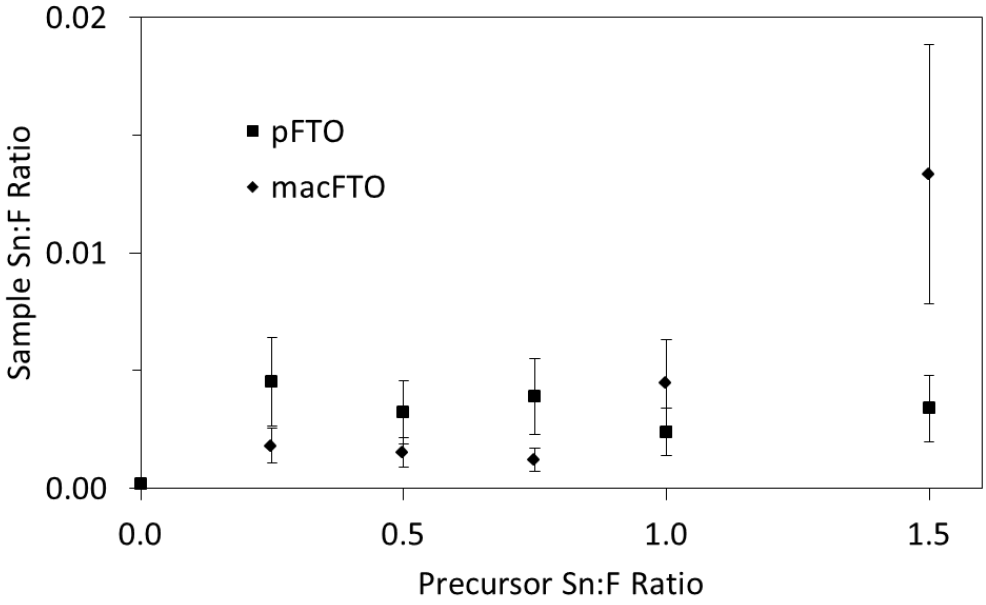

Figure 61: Solid state ^{19}F NMR results for templated (diamonds) and non-templated (squares) FTO powders.

The polystyrene template may also affect F content so powders were prepared without template which may be responsible for loss of C_xF_y volatiles on calcination. The quantity of fluorine was similar for both templated and non-templated powders and therefore the template does not significantly affect the doping.

The discrepancy between EDX and SSNMR is most likely due to the inaccuracy of fitting the F peaks in the EDX. Nevertheless the values are both within the expected range expected for FTO.

2.4.7: Mac-FTO film surface area calculation

The calculation below is regarding the mac-FTO as a perfect inverse opal structure with 100 % coverage on substrate. The aim is to estimate the theoretical surface area can be offered by a perfect mac-FTO film on a 1 cm^2 substrate.

- R (the radius of holes)=155 nm; r (the radius of windows) =25 nm;
- size of substrate = 10 mm×10 mm; film thickness = 7 μm
- fcc filling factor = 0.74

V_{total}: The combined volume of walls and voids in mac-FTO electrode

V_{hole}: The volume of a single hole in mac-FTO electrode

$V_{all\ holes}$: The sum volume of all the holes in mac-FTO electrode

N_{holes}: The number of holes in mac-FTO electrode

S_{hole}: The surface area of one hole in mac-FTO electrode

$S_{all\ holes}$: The total surface area of mac-FTO electrode, the area of windows (each hole was connected to 12 other holes and every single window was share by two holes) had been deducted from it.

V_{total}=10 mm×10 mm×10 μm = 0.7×10^{-3} cm^3

$V_{hole}=4/3(\pi R^3) = 1.56\times10^{-14}$ cm^3

$V_{all\ holes} = 0.74\times V_{total} = 0.52\times10^{-3}$ cm^3

$N_{holes} = V_{all\ holes}/V_{hole} = 3.33\times10^{10}$

$S_{hole} = 4\pi R^2-12/2(\pi r^2) = 3.1\times10^{-9}$ cm^2

$S_{all\ holes} = N_{holes} \times S_{hole} = 102.88\ cm^2$

2.5: Synthesis of hs-AZO film from PS template

Zinc oxide is an n-type semiconductor which has a 3.3 eV band gap with zincite structure and it is highly transparent in visible light region.[163] But the low conductivity of pure zinc oxide limits the applications of it as a good transparent conductor. However it was found that conductivity of zinc oxide films were highly improved when either nonstoichiometric or doped with atoms such fluorine, boron, aluminium, gallium, or indium.[164-167]

Well defined hollow sphere structure is quite interesting because it has plenty potential applications in fields like catalysis, protection of biologically active agents, carriers of pigments and drugs, etc.[168-174] Monodisperse metal oxide hollow spheres powder have been synthesized[175] but films of metal oxide hollow sphere have never been fabricated before. Transparent conductive materials such as ITO, FTO and ZnO have been widely studied for optical application as transparent electrodes,[134] and among these three metal oxides, ZnO is the one with lowest cost. ZnO is an attractive material for synthesis of optoelectronic devices due to its ease in doping with Si,[176] Ga[177] and Al[178] and nontoxic nature. The lowest resistance of aluminium doped zinc oxide is around $7 \times 10^{-4}\ \Omega\ cm^{-1}$ with a transmittance around 80% .[179] In this work, hollow sphere AZO was synthesized onto FTO conductive substrates, the hollow spheres film been achieved was close packed, homogeneous and almost crack free.

2.5.1: Method development for the synthesis of hs-AZO film

Since the vacuum infiltration exhibited a great performance to optimize the fabrication of mac-FTO films as discussed in Section 2.3.3, the initial intention was to prepared mac-AZO, however, it was found that infiltration was more efficient giving hollow spheres of AZO (hs-AZO).

The precursor solution of AZO was prepared according to a modified literature report.[179] $Zn(Ac)_2{\cdot}2H_2O$ (2g, 9 mmol) was first dissolved in 40 mL methanol, after sonication, and from 6 to 12mg (0.045 to 0.09 mmol) of $AlCl_3$ was then added to the $Zn(Ac)_2$ methanol solution. The PS template film (450 nm in diameter) on FTO slide was pre-soaked in methanol before being stood vertically and submerged in the AZO precursor solution in a glass vial and stored in a desiccator with a partial vacuum applied for 0.5 to 1.5 h. The slide was removed from the glass vial and then calcined immediately under air. The hs-AZO with great coverage and homogeneity was obtained when soaking the PS template film in AZO precursor solution (added with 8 mg of $AlCl_3$) for 1h under partial vacuum. The samples by SEM imaging below were all fabricated by the AZO precursor solution with $AlCl_3$ (8 mg, 0.06 mmol), which equals to 0.67 at. % of Al in AZO precursor solution. The reason for using this ratio will be explained in the next section.

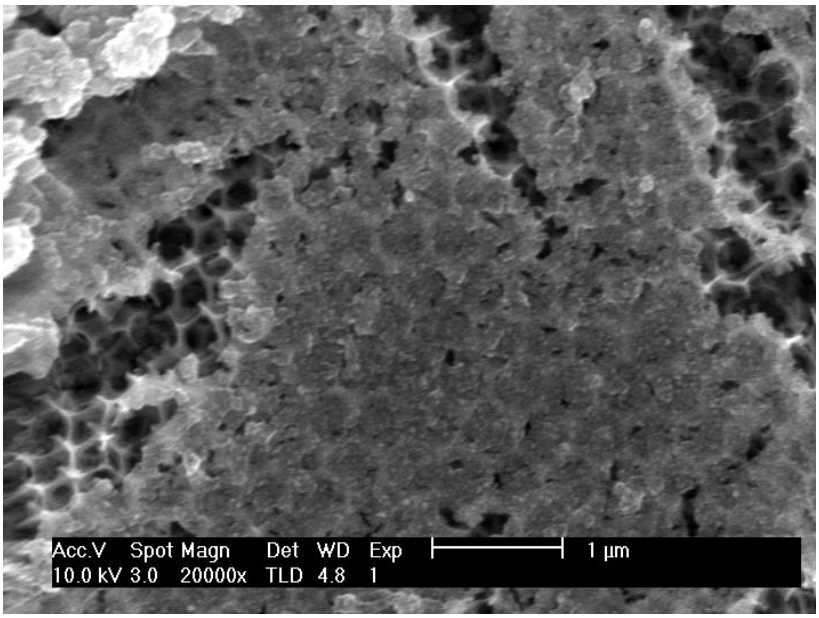

Figure 62: SEM image of structured AZO film obtained when soaking in precursor solution for 0.5 h under vacuum.

During the synthesis of structured AZO film, a morphology dependency on soaking time of PS template film in AZO precursor solution was observed by SEM imaging. As shown in Figure 62, a macroporous-like structure was obtained. However, the abundant material on the top of macroporous film suggests that the infiltration of AZO precursor is greater than that of FTO and with less contraction. After increasing the soaking time to 0.75 h, the hs-AZO film was obtained as shown in Figure 63. But the morphology of it is not homogeneous, complete and partially formed sphere (see below) were both observed by SEM.

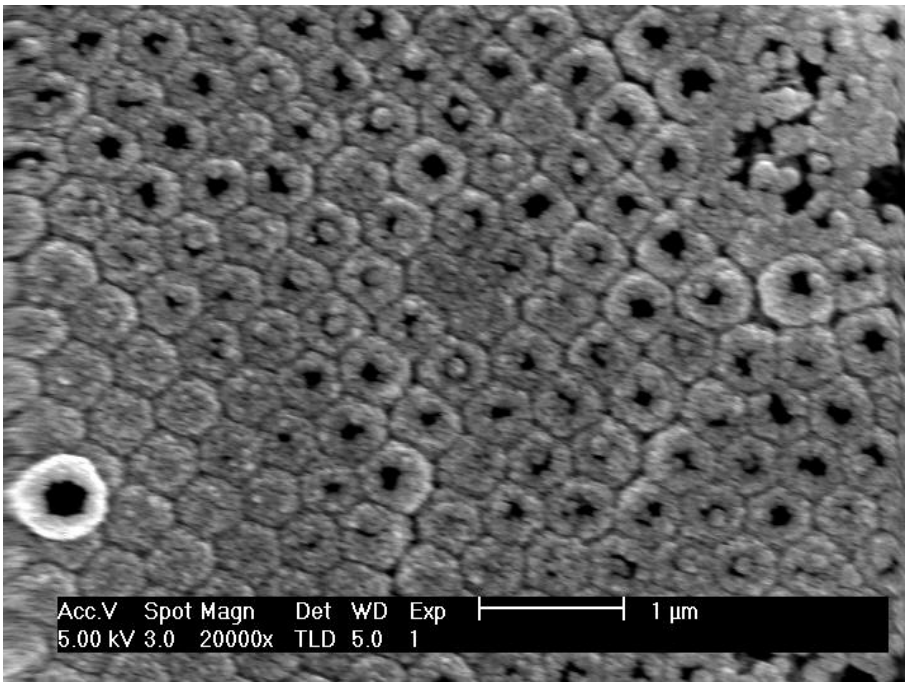

Figure 63: SEM image of structured AZO film obtained when soaking in precursor solution for 0.75 h under vacuum.

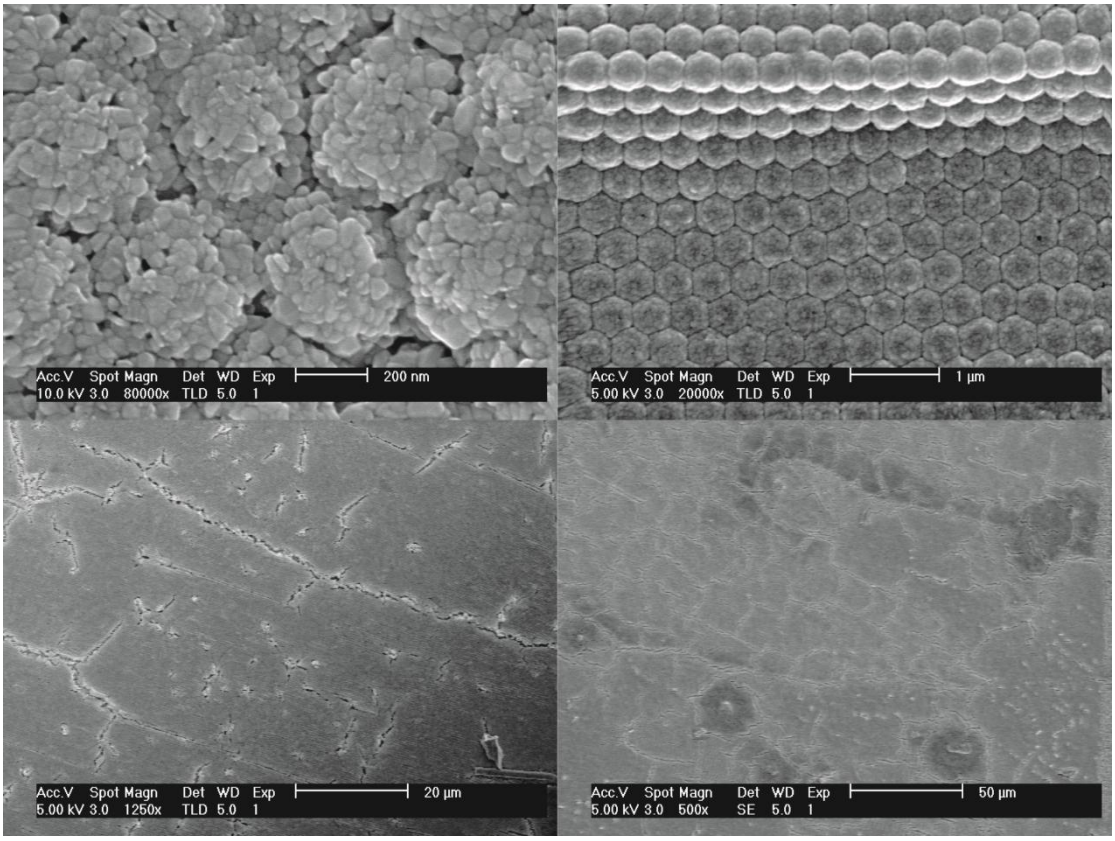

Figure 64: SEM images of hs-AZO film obtained when soaking in precursor solution for 1 h under vacuum.

As shown in Figure 64, the hollow spheres are around 390±5 nm of periodic order in fcc lattice and unlike the mac-FTO films, no uncovered area and almost no perpendicular cracks were observed even in a large region of 300 × 400 μm by SEM, suggesting a very low shrinkage of AZO during the calcination. The low shrinkage was also observed in synthesis of ZnO hollow sphere powder by PS sphere template in a literature report.[180]

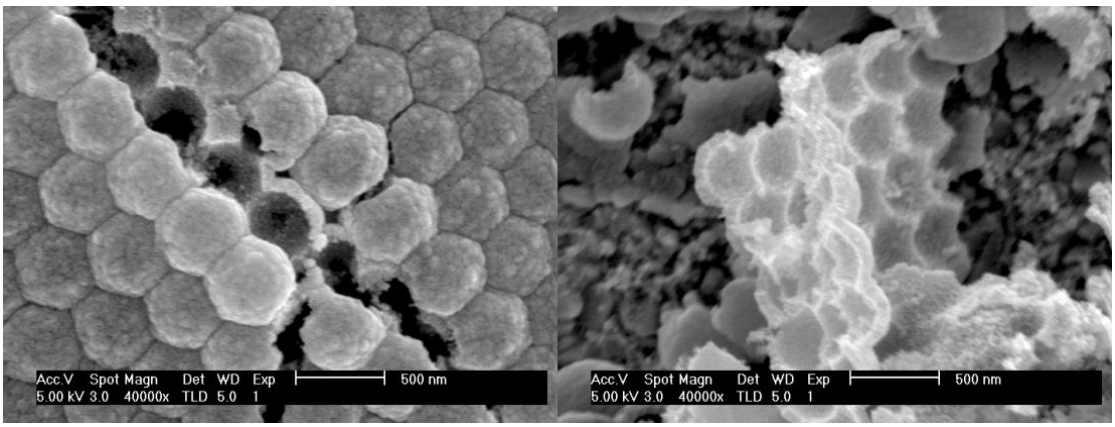

Figure 65: SEM images of hs-AZO pieces scraped off from hs-AZO film.

To study the internal morphology of hs-AZO films, the film was scraped with a knife and imaged by SEM as shown in Figure 65. The thickness of the shell is around 35 nm and the air sphere within the hs-AZO has a diameter around 365±5 nm. The macroporous ZnO powder[181] and hollow sphere ZnO powder[182] synthesised from polymer sphere templates generally exhibit a wall or shell thickness around 50±15 nm and ca. 30 nm respectively according to previous literature reports. The regions surrounded by the solid AZO shell represent the voids (air spheres) which were previously occupied by polystyrene spheres. Former contact points between neighbouring polystyrene spheres appear as windows between the air spheres. In addition, as shown in Figure 66 by SEM imaging, the hs-AZO is around 10 layers in thickness. Similarly to the mac-FTO film in last section, the ordered close-packed hollow sphere films are expected to exhibit photonic behaviour due to the regular modulation of the refractive index difference between AZO (refractive index = 1.9 to 1.95)[183] shells and air spheres.

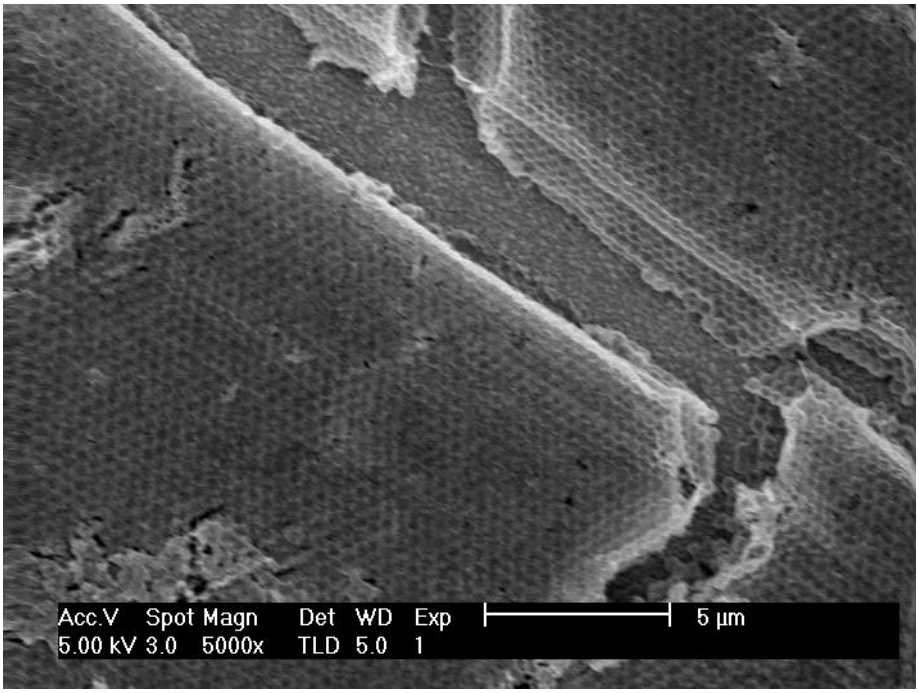

Figure 66: SEM image of edge of hs-AZO film showing the multiple layered hollow sphere structure of it.

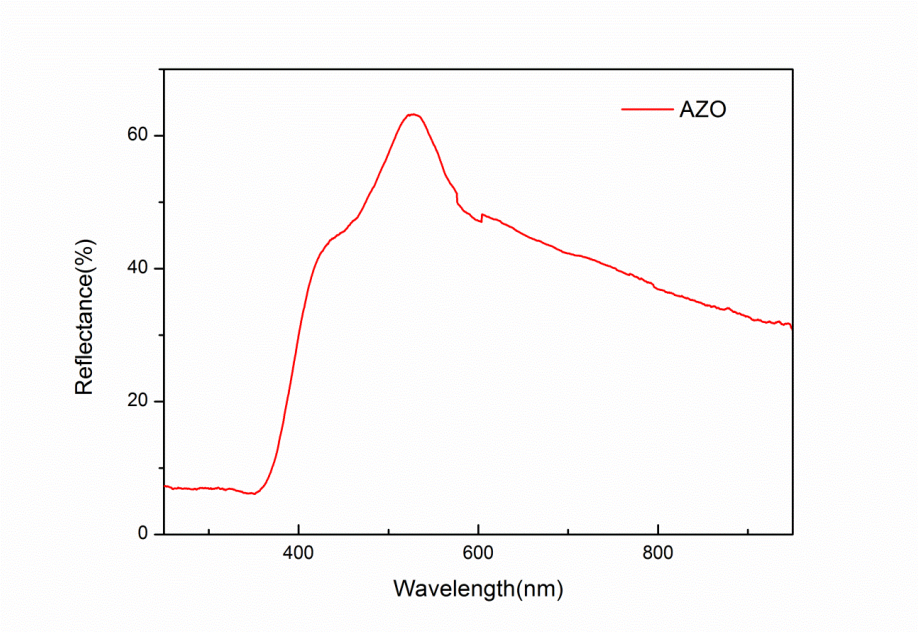

Figure 67: DRUVS spectra of hs-AZO film coated on planar FTO substrate.

Figure 67 shows an intensive and sharp photonic stop band of hs-AZO film centred at 520 nm suggesting good photonic properties due to the refractive index difference between AZO and air. The filling factor of hs-AZO film is calculated to be 7.1% which is lower than that of mac-FTO (ca. 18 %), this is because the shell of hs-AZO is consist of voids and AZO nanocrystals as observed in Figure 71b. The high intensity and sharpness also reflects a homogeneous and uniform structure of the sample with great coverage as discussed in Section 2.3.4.

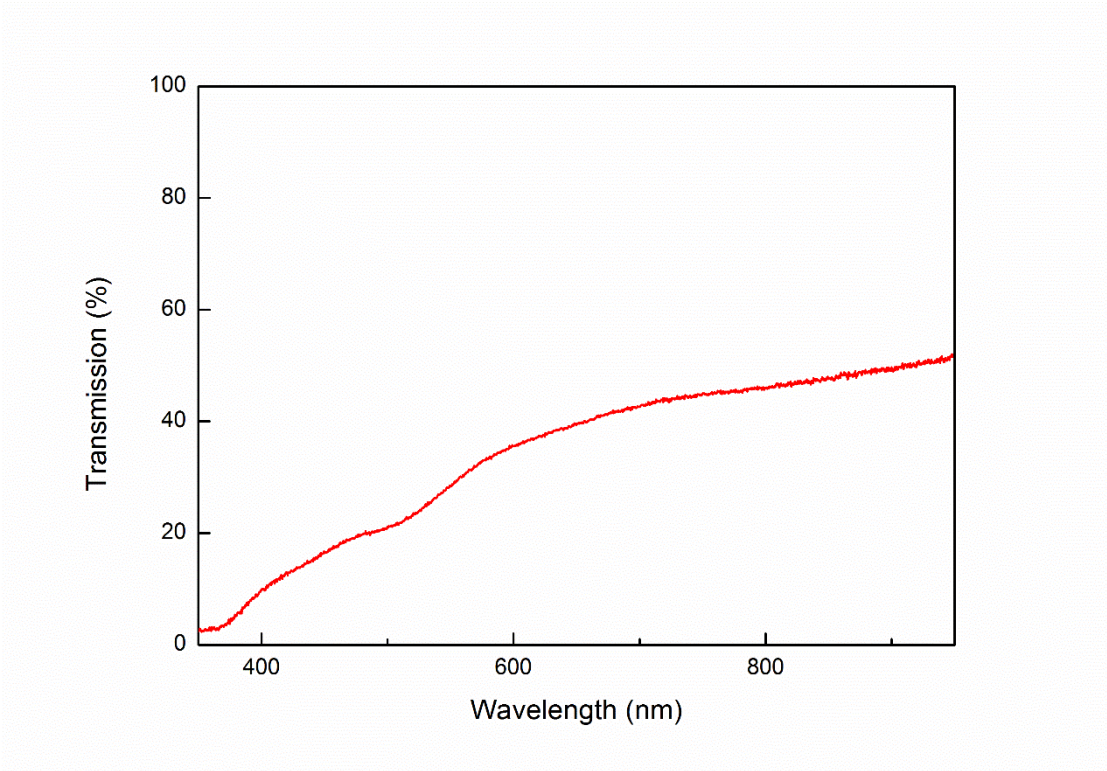

Figure 68: UV-vis transmission spectra of hs-AZO film.

In addition to the reflectance, transmittance below 30 % in light region shorter than 600 nm was observed as shown in Figure 68 suggesting the light of wavelength in this range is effectively diffracted and scattered. It is worth noting that the position reflectance peaks (Figure 67, 520 nm) can correspond to the position of the transmission dip in spectra (Figure 68, 520 nm)

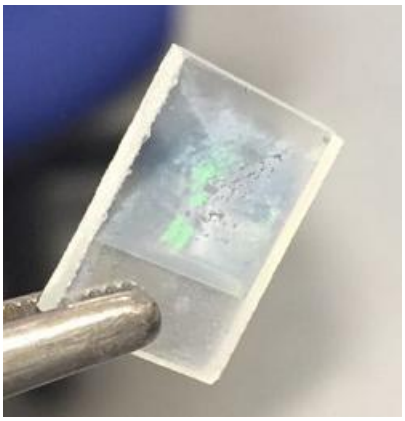

Figure 69: Digital photograph of an hs-AZO electrode showing opalescence.

Similarly to mac-FTO film, the hs-AZO film also behave opalescence as shown in Figure 69 by digital photograph. This optical property can be easily identified by eye, and the opalescence suggests a high quality photonic structure in micro-scale.

The PXRD spectra of the hs-AZO film is presented in Figure 70. The diffraction peaks of the hs-AZO shifted to higher angle by ca 0.5^{o} due to the aluminium doping. This shift was also observed in previous reports after doping Al in ZnO.[184]

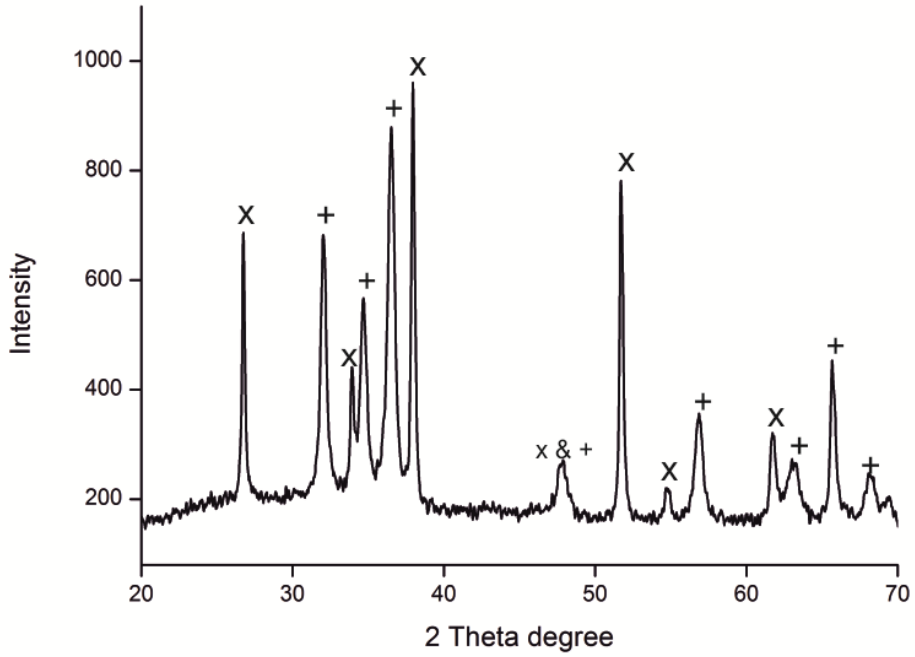

Figure 70: The powder-XRD of FTO substrate coated with hs-AZO film. + = ZnO, JCPDS 36-1451, x = SnO_2, JCPDS 41-1445. A silicon holder was used in this measurement.

As shown in Figure 71a, other nano-structured AZO such as the nanorod in the black circle was observed when the soaking time of PS template in AZO precursor solution was increased to 1.5 h. The potential loaded photocatalyst materials may not benefit from these extra nano-structured AZO, but it suggests that a hybrid nano-structured AZO can be easily synthesized. Besides, since the shell of hs-AZO consist of AZO crystal particles and holes around 10 nm as shown in the red circle in Figure 71b, it is theoretically possible for exchange of nanoparticles, electrolyte and solutions in and out the shell.

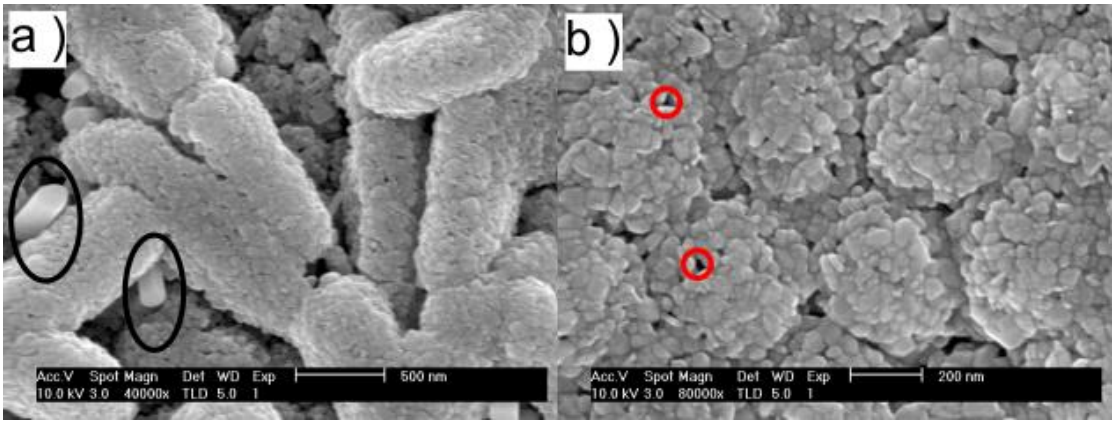

Figure 71: SEM images of hs-AZO electrodes. a): other nan-structured AZO on top of the hs-AZO film when increasing the soaking time to 1.5 h. b): holes on the shell of hs-AZO.

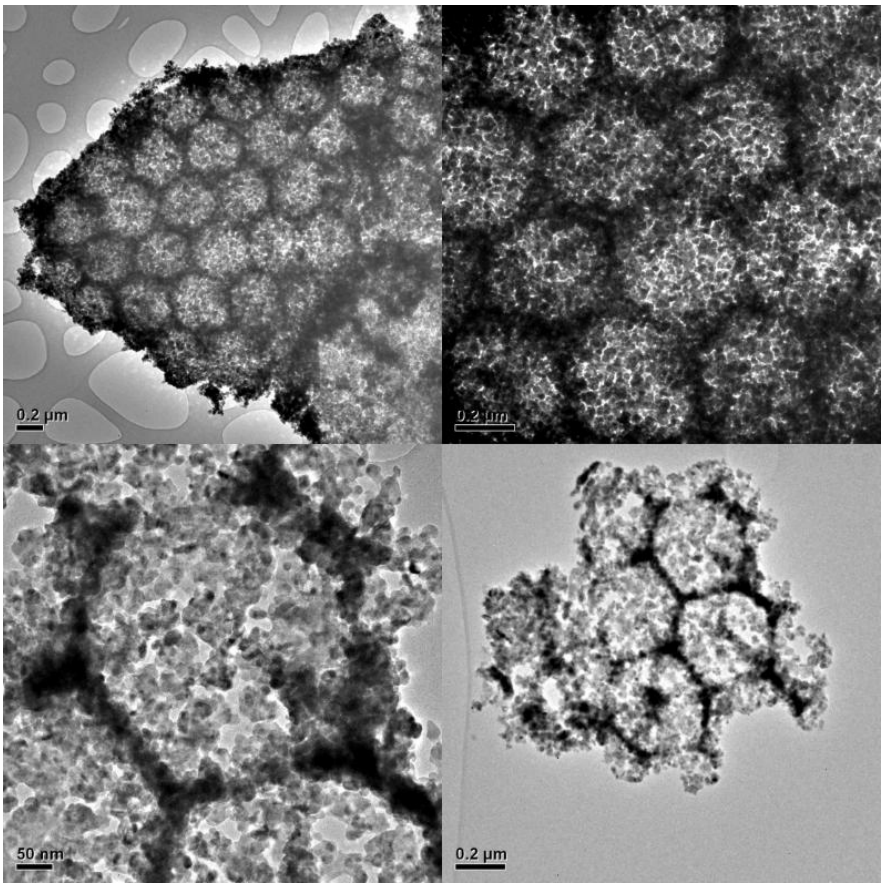

Figure 72: TEM images of hs-AZO scraped from a slide sample.

Here the TEM images of hs-AZO was taken by Dr. Robert Mitchell at the University of York. The hs-AZO film was also imaged by TEM as shown in Figure 72, the darker region is the solid shell of AZO crystal grains and the lighter region is the voids with the hs-AZO. The EDX spectra shown in Figure 73 exhibit a rough idea of the elemental composition and ratio of hs-AZO products. The aluminium found in the AZO products is ca. 0.72 at. % (subtracting the SnO_2 content in Table 4) is similar to the Al content in precursor. The Al content observed in hs-AZO film is lower than the Al ratio observed in AZO fibre (1.6 at.%)[185] and planar film (1.3 at.%)[186] products in literature report. This is because the viscosity of AZO precursor solution do not need to be considered when making AZO planar film and fibre, the influence of Al content in precursor will be discussed in the next section.

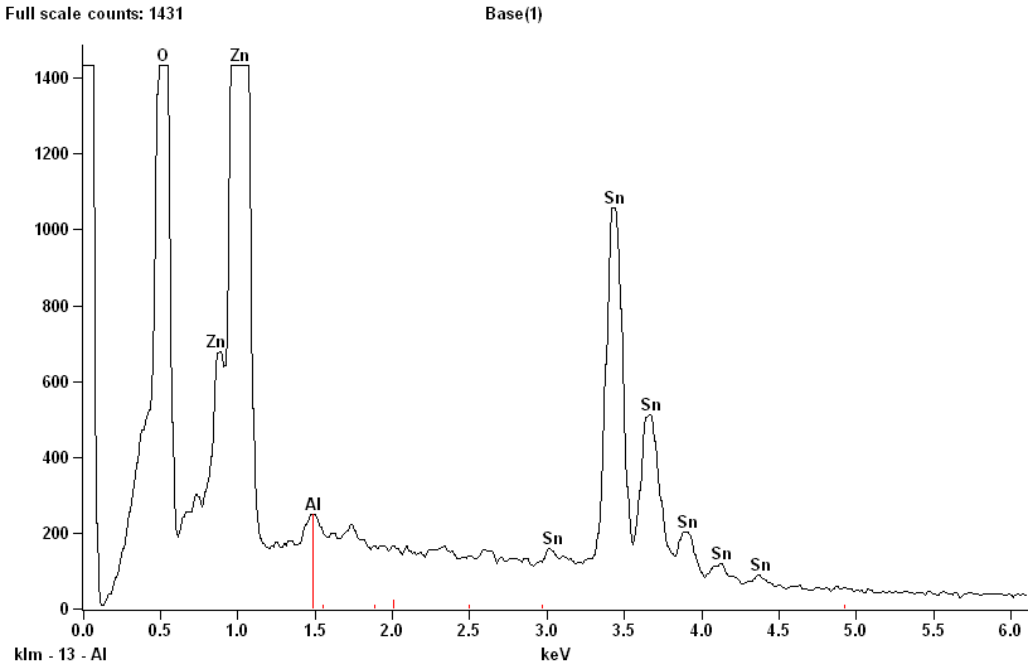

Figure 73: EDX spectra of hs-AZO film coated on FTO substrate.

Element Line	Norm. Wt.%	Atom %
O	19.74	55.76
Al	0.38	0.63
Zn	42.51	29.38
Sn	37.37	14.23
Total	100.00	100.00

Table 4: SEM/EDX elemental analysis of transparent highly ordered hs-AZO film.

2.5.2: Influence of Al doping level in AZO

The PS sphere template film infitrated by AZO precursor solution with various Al at. % (0.5, 0.67, 0.83 and 1.0 at. %) were prepared. After calcination, obtained products exhibit opalsence when the doping of aluminum in precursor solution is below 0.8 at. %. Alternatively, the samples prepared by AZO precursor solution with over 0.8 at.% exhibited no opalsence and poor coverage. In the pervious literature report, it was found that the aluminum doping level had little influence on the transmittance, and the lowest conductivity was generally obtained with a calcination temperature around 400 ^{o}C and a doping aluminium of 0.8 at.%.[184] According to another literature report, not only the conductivity of AZO have dependency on Al at. % (higher Al at. % tend to give greater conductivity), but also the solution viscosity will increase with higher Al doping level.[187] The high viscosity of the AZO precursor solution with more Al dopant may lead to quite difficult inftiltraion. Compromise had to be made to optimise both the photonic and electrical properties of hs-AZO film. The hs-AZO films prepared by precursors solution with 0.67 at. % of aluminum had presented good optical properties and morphology, and the electrical properties of it

will be discussed in Chapter 3 by photoelectrochemistry experiments with decoration of CdS.

2.6: Conclusion

Planar FTO films coated on borosilicate glass and quartz synthesised in this chapter exhibit low sheet resistance (7.6 Ω □) and high transmittance over 85 %, making them suitable substrates for supporting structured photonic crystals or photocatalysts. Polystyrene sphere template films with good optical and mechanical quality were deposited on these conductive substrates for preparing 3DOM TCOs.

The mac-FTO and hs-AZO films were fabricated on conductive planar FTO substrate from the high quality PS sphere template. These two structured TCO films could provide a three dimensionally structured platform for the decoration by various photocatalysts. In comparison to a planar electrode, the photonic properties and the enhanced surface area per geometric area exhibit potential to improve the efficiency of photocurrent generation. The mac-FTO films described here are approximately 7 μm thick and cover 80% of the geometric surface area, giving an estimated 15 fold increase in surface area determined by calculation and capacitance measurements. In addition, the mac-FTO films made by the improved method exhibits much better optical properties when compared with previous reports. The hs-AZO films described in this work are also exhibit a good optical properties and present almost 100 % coverage of geometric surface area. Furthermore, to the best of our knowledge, hollow sphere TCO films have never been synthesised before.

Chapter 3: Decoration of CdS photocatalyst in structured TCO film

3.1: Introduction

As discussed in Section 1.3, various photocatalysts were presented in previous literature reports for the formation of composite materials consisting of small particles or thin films loaded into a porous support. Among the various approaches for hydrogen production, photocatalytic water splitting using semiconductors has drawn much attention due to its potential applications on producing hydrogen directly from water under solar light irradiation.[188,189]

In terms of the photocatalyts, the most common and widely used material is TiO_2 and other doped TiO_2 materials.[56,190] TiO_2 acts as highly effective photocatalysts under UV light irradiation when it is loaded with suitable co-catalysts like Pt. The composition material TiO_2/Pt is suitable for hydrogen evolution, but it is not able to generate hydrogen without loading with co-catalysts due to the high recombination rates.[191] To obtain cheaper and effective photocatalytic devices, this section will focus on visible light driven photocatalysts without loading of noble metals, and their performance when coupled with photonic crystals. Since the ultraviolet light from solar spectra (4 to 6 %) reaches the earth's surface is lower when compared to visible light which accounts for 44 %, visible light driven photocatalysts should exhibit better overall efficiency. In terms of a visible light active photocatalyst for water splitting, their band gap energy must be between 1.23 eV (for water splitting the free energy of activation is 238 $kJmol^{-1}$, which equates to 1.23 eV and 976 nm) to 3.0 eV. Also, the band position of the photocatalyst materials is also a critical factor for water oxidation and reduction. For effective water reduction, the conduction band position should be more negative than the reduction potential of

protons and the valence band should be more positive than the oxidation potential of water.

Many semiconductor photocatalysts have been studied for hydrogen evolution from water under visible light irradiation. CdS is a n-type semiconductor, and photo-generated carriers in CdS have long diffusion length.[192] CdS has been widely used as a photoanode in photoelectrochemistry because of its properties and the band gap (2.3 eV)[193] corresponds well with the visible light spectrum and the conduction band position is more negative than the H_2O/H_2 reduction potential over a wide pH range (pH = 0 to 13).[28] For instance, CdS coupled TiO_2 colloids have been extensively studied in photoelectrochemistry and water splitting system,[194,195] CdS sensitized ZnO nanorods exhibit a photocurrent density of 4.3 mA cm^{-2},[196] and ITO glass coated with CdS thin film show a photocurrent of 3.51 mA cm^{-2}.[197] However, it should be noted that CdS based devices are prone to corrosion, but nonetheless is useful for proof of concept studies.

The photochemistry of CdS will be dependent on the synthesis method and many routes including organometallic precursors,[198,199] solution-liquid-solid,[200] microwave irradiation,[201] and one-pot synthesis[202] have been used in previous studies. In addition, high quality CdS and other Ⅱ-Ⅳ semiconductor nanocrystals have been synthesized by one-pot synthesis, providing tuneable optical properties by simply varying the concentration of ligands in the solution.[203]

Another common technique for the preparation of CdS is precipitation from aqueous solution of cadmium salt either by reacting with another aqueous solution of Na_2S or by applying H_2S gas.[193,204] This method can be used for synthesis of the CdS within the structured material by simply soaking the structured material into the aqueous precursor solutions separately, the precipitate will formed inside the structured materials. For instance, TiO_2 inverse opal films were immersed in a solution containing cadmium acetate dihydrate in ethanol for a certain time, dried, and the

inverse opal film was then dipped into a precursor solution containing sodium sulfide nonahydrate in methanol for a certain time. The precipitate of CdS in TiO_2 inverse opal films particles were therefore achieved.[102]

The obtained precipitation was then annealed to improve the crystallinity. However, it has been found that the CdS tend to photocorrode during photocatalytic reaction where the CdS itself is oxidized by the photogenerated holes.[205] Generally, a mixture of 0.25 M Na_2SO_3/Na_2S solution was applied as sacrificial agent to prevent the CdS from self-oxidization.

3.2: Chapter aims

The aim of this chapter is to investigate if structured TCO electrodes have advantage in supporting larger photocurrent per geometric surface area than planar TCOs electrodes, and if so, whether the conductivity, optical properties, and morphology are important.

In this chapter, the CdS nanoparticles were synthesized and deposited onto the mac-FTO electrode fabricated as described in Section 2.3.3. The aim here is to have isolated nanoparticles and show if the TCO can collect and transport charge to the external contact. Different methods and concentrations of the CdS nanoparticles dispersion were then used for the decoration to optimize the photoelectrochemistry performance of the nano-CdS/mac-FTO composition and maximize the photocurrent. In these systems a continuous film of CdS is present. The development of photocurrent generation in photoelectrochemistry will also be presented for CdS@mac-FTO and CdS@hs-AZO fabricated by a simple sequential coating method called SILAR (successive ionic layer adsorption and reaction).

Characterization of the CdS@mac-FTO and CdS@hs-AZO composites will be conducted by PXRD, TEM, SEM, EDX and photoelectrochemistry. The effect of loading on the structured photonic TCOs was also be studied by DRUVS.

3.3: Results and discussion

3.3.1: Synthesis of nan-CdS

According to a literature report,[203] a modified method was employed to make CdS nanoparticles (nan-CdS) for decoration of the photonic crystal films. CdO and oleic acid were added to octadecene and heated to 300 ˚C. Sulfur suspended in octadecene was then added to the hot mixture and held for 5 mins. The obtained yellow-orange nanoparticles were dissolved in toluene to give an absorbance of *ca*. 1.0 (10 mm path length) with the absorption maximum centred at ca. 500 nm as shown in Figure 74. The position of the absorption maximum is similar to CdS thin film photoelectrochemical solar cells reported previously.[206] This method has been used extensively in the group and gives nanoparticles of 2.84 ± 0.30 nm as judged by TEM. Additional imaging of the CdS nanoparticles will be shown on coating of the TCO supports below.

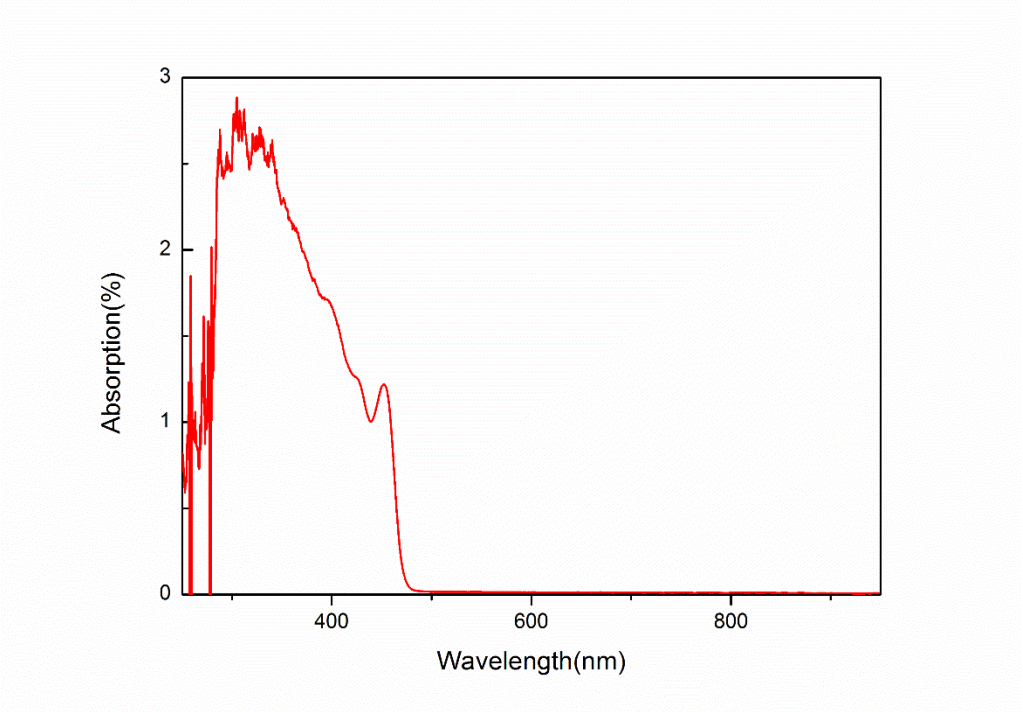

Figure 74: UV-vis absorption spectra of nan-CdS dispersed in toluene.

3.3.2: Mac-FTO films decorated with nan-CdS

For the decoration of mac-FTO films by CdS nanoparticles (nan-CdS), the nan-CdS dispersed in toluene which give an absorbance of 1.0 (10 mm path length) with the absorption maximum centred at ca. 500 nm was used as a standard dispersion solution.

The standard CdS dispersion solution assigned the normalized concentration of 1, was diluted by different amounts of toluene. Varied concentrations of the nan-CdS dispersion solution was employed for the decoration of mac-FTO electrodes to study the CdS loading dependency of mac-FTO electrodes.

The initial attempted method for deposition of CdS nanoparticles into mac-FTO electrodes was modified according to a previous literature report.[207] In this study, it was founded that the nanoparticle-nanoparticle interaction is greater than the nanoparticle-support interaction, therefore, the removal of solvent by calcination

leads to aggregation of the CdS nanoparticles. The interaction between nanoparticles and surface of metal oxide support materials were enhanced after adding oleic acid (OA). A similar method had been used for the infiltration of CdSe quantum dots dispersion into the voids of a SiO_2 sphere template powder. The SiO_2 template spheres were modified by stearyl alcohol and then soaked in a CdSe quantum dots dispersion with tri-n-octylphosphine oxide surface ligand. Interaction between the CdSe nanocrystals and the SiO_2 template spheres allowed for a good infiltration and the 3DOM CdSe was obtained after etching the silica by HF.[208]

The mac-FTO electrodes (15 $\times$ 10 $\times$ 2 mm) were initially treated (or not) by soaking in a hexane solution of oleic acid before being transferred to and set horizontally in a glass vial. The nan-CdS dispersion in toluene was then added into the glass vial and the electrode submerged for a period. The mac-FTO electrode was transferred to a furnace oven for heat treatment at 450 ^{o}C to remove the ligands and improve the interface between the CdS nanoparticles and mac-FTO. The mac-FTO pre-treated with OA exhibit a yellow colour after the calcination. No obvious colour change was observed from the sample without OA pre-treatment.

For all deposition attempts, the nano-CdS decorated mac-FTO electrodes were weighed before and after the deposition. In addition, the nan-CdS@mac-FTO electrodes were also weighed after calcination as a further check to confirm the quantity of CdS nanoparticles loaded.

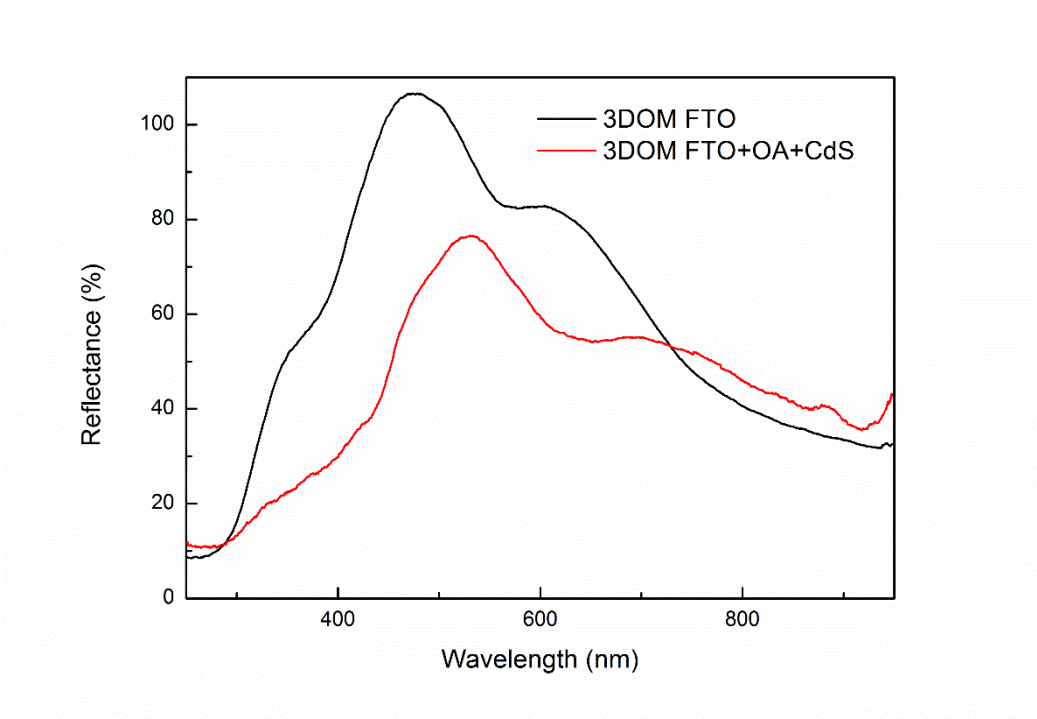

Figure 75: DRUVS reflectance spectra of mac-FTO film (black line) with stop band at 620 nm and mac-FTO film deposited with OA-CdS nanoparticles (red line) with stop band at 660 nm.

DRUVS was employed to analyse the effect of CdS loading on the stop band of the structured photonic material. Figure 75 shows the DRUVS reflectance spectra of a mac-FTO film before and after the deposition of oleic acid treated CdS nanoparticles. The concentration of CdS nanoparticle dispersion used is 0.5 and the sample was heated to 450 ^{o}C for 2 h to remove the ligands before the DRUVS measurement. As discussed in Section 1.12.3, the positions of photonic stop band of structured TCO films are generally defined by the Bragg-Snell equation (equation 8), with modifications, the photonic stop band of structured TCO films with decoration of photocatalyst materials can be defined by equation 9. Where λ_{new} is the stop band position of photocatalyst@structured-TCOs, n_p is the refractive index of loaded photocatalyst and φ_p is the filling factor of it. Alternatively, n is the refractive index of TCO and φ is the filling factor of it. In addition, n_0 and θ is the refractive index of void and incident light angle, respectively.

Equation 9: $\lambda_{new} = \frac{2d_{hkl}}{m}[\varphi n^2 + \varphi_p n_p^2 + (1 - \varphi - \varphi_p)n_0^2 - \sin^2\theta]^{1/2}$

The filling factor of the wall composite, φ_{total}, is defined by the following expression:

Equation 10: $\varphi_{total} = \varphi + \varphi_p$

An expression for φ_p was determined by subtraction of Bragg-Snell equation (Equation 8) from Equation 9 to give Equation 11:

Equation 11: $\varphi_p = \frac{3(\lambda_{new}^2 - \lambda^2)}{8D^2(n_p^2 - n_{0)}^2}$

A red shifted photonic stop (from 620 nm to 660 nm) band was observed in Figure 75 after the mac-FTO electrode deposited with OA stabilised CdS nanoparticles, hence a filling factor of φ_p = 3.69 % was calculated. This red shift can be predicted by Equation 9, since the addition of a volume of CdS nanoparticles (n_p = 2.53) with greater refractive index than that of air (1.00). It should be noted that the absorption edge of CdS is at ca. 500 nm, and the downward shift in DRUVS spectra at ca. 500 nm (Figure 75) after loading nan-CdS may be due to absorption of it.

In addition to the red shift in the photonic stop band position, a decrease of intensity of the photonic stop band was also observed, this may due to the imperfectly deposition of nan-CdS leading to diminished ordering of the photonic structure as whole.

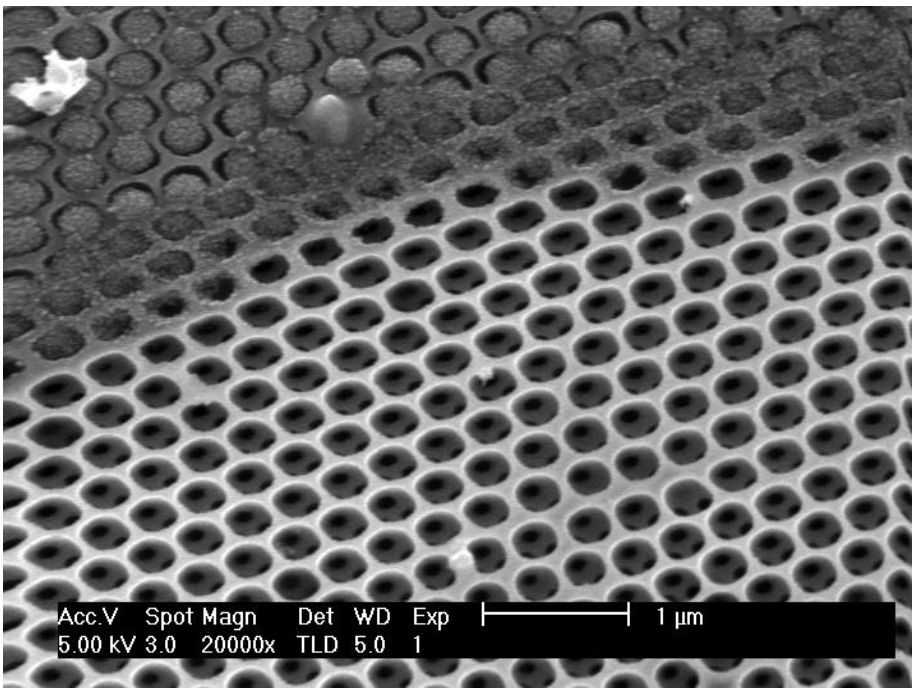

Figure 76: SEM image of mac-FTO film deposited with OA stabilised nan-CdS.

Figure 76 shows a typical area of the OA stabilised nan-CdS decorated mac-FTO electrode by SEM imaging. Although the CdS nanoparticles was successfully deposited on the mac-FTO film, the aggregation of CdS nanoparticles which lead to low photocatalytic activity was observed. The empty pores and the pores totally filled by CdS nanoparticles suggested a heterogeneous deposition and a diminished ordering of photonic structure which will lead to the reduction of photonic stop band intensity shown in DRUVS spectra. In addition to DRUVS, SEM EDX was also used to analyse the elemental compositions of OA stabilised nan-CdS/mac-FTO films. As shown in Figure 77 and table 5, the Cd content (1.59 at. %) observed in the OA stabilised nan-CdS/mac-FTO electrode by EDX is higher than the S content (0.85 at. %) because the CdS nanoparticles tend to be oxidized to CdO during the calcination under air, but these CdO will be transformed to CdS during the photoelectrochemsitry in presence of the Na_2S/Na_2SO_3 electrolyte.[28]

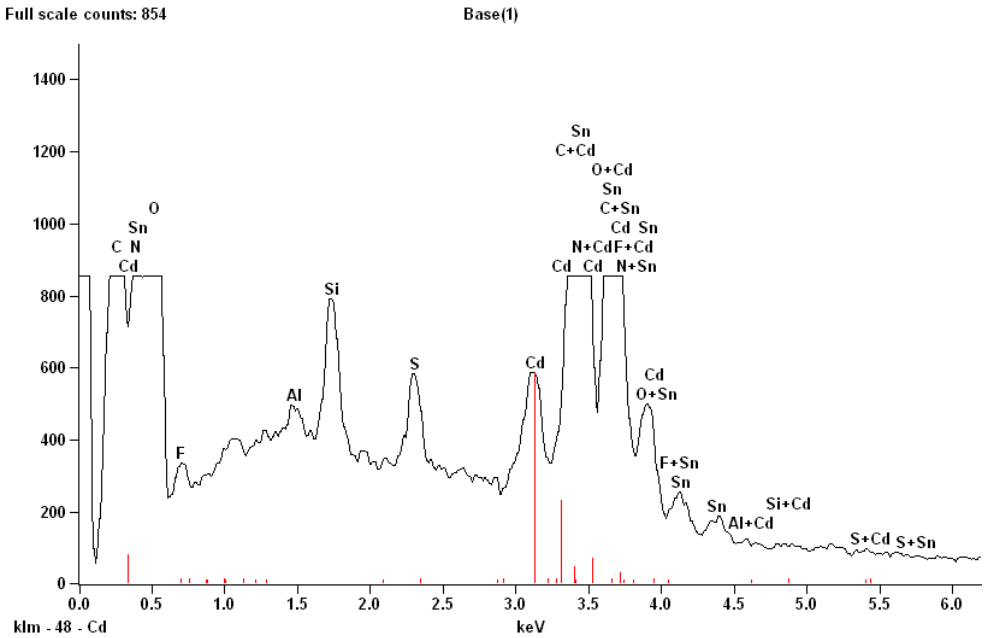

Figure 77: SEM EDX spectra of OA stabilized nan-CdS@mac-FTO electrode.

Element Line	Norm. Wt.%	Atom %
C	9.14	25.14
N	5.17	12.20
O	20.29	41.90
F	0.51	0.89
Al	0.16	0.20
Si	1.07	1.26
S	0.82	0.85
Cd	5.40	1.59
Sn	57.43	15.98
Total	100.00	100.00

Table 5: EDX elemental analysis of OA stabilised nan-CdS/mac-FTO electrode.

In terms of the deposition of CdS nanoparticles on mac-FTO film without pre-treated by oleic acid, it was observed that the weight of the mac-FTO only increased around 0.02 mg after the deposition of CdS nanoparticles and the calcination. The small weight increase suggest a poor infiltration of the CdS nanoparticle in the absence of oleic acid treatment and hence the photonic stop band of mac-FTO film was hardly changed after the deposition. Figure 78 shows the DRUVS spectra of mac-FTO film before and after the deposition of CdS nanoparticles by this method, the intensity of photonic stop band was slightly decreased and the band position was shifted only around 5 nm (from 620 to 625 nm) suggesting a filling factor of φ_p = 0.45 %. Similar photonic stop band change was observed in macroporous tin oxide electrode loaded with low content of CdS quantum dots which exhibit a photocurrent density of only 10 μA cm^{-2}.[161]

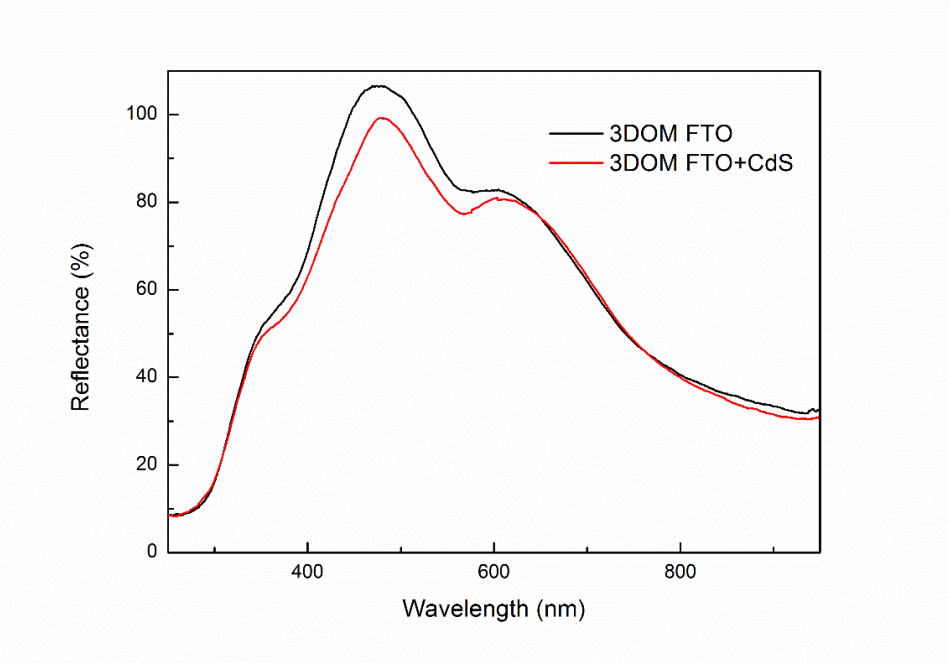

Figure 78: DRUVS reflectance spectra of mac-FTO film (black line) with stop band at 620 nm and nan-CdS@mac-FTO electrode without pre-treated by OA with stop band at 625 nm. (red line).

Figure 79 shows the SEM and TEM images of nan-CdS@mac-FTO electrode. Correspondingly to the low filling factor of φ_p = 0.45%, no obvious CdS nanoparticles were observed by SEM imaging, but the individual CdS nanoparticles were imaged by the TEM. The CdS nanoparticles are around 4 to 6 nm in diameter attaching homogeneously to the walls of mac-FTO as shown in Figure 79bc. The low Cd atomic content as shown in Figure 80 and Table 6 (0.54 at. %) by EDX can correspond to the electron microscopic results. The EDX elemental analysis is not quite accrue but it can give a rough idea of the nan-CdS loading.

By comparing the results of deposition of CdS nanoparticles on mac-FTO films with or without pre-treated by OA, a new approach must be employed to optimize both the loading level and the homogeneity.

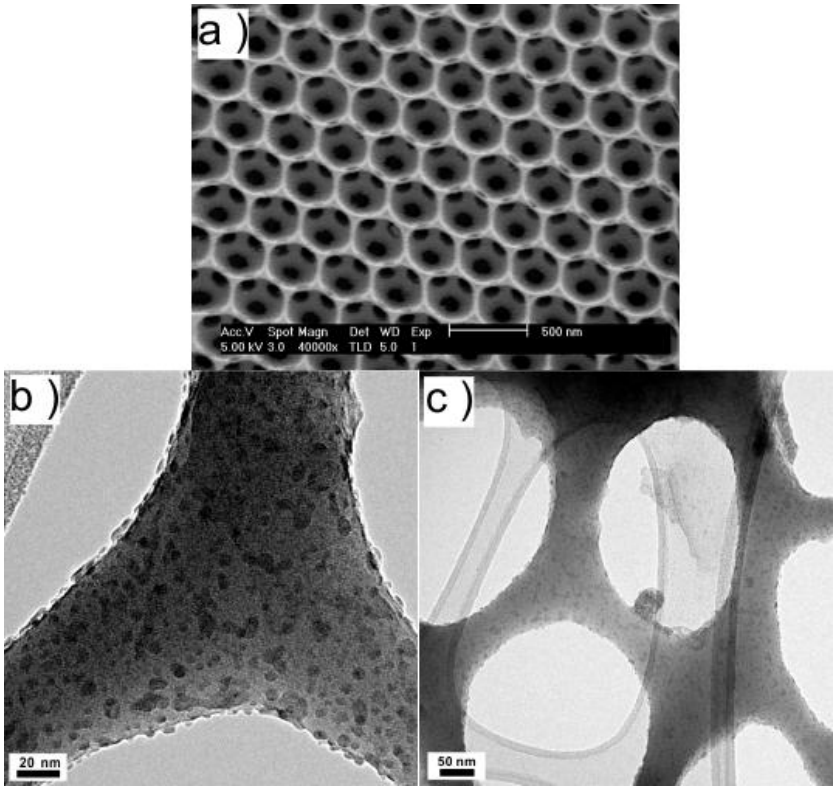

Figure 79: SEM and TEM images of nan-CdS@mac-FTO made without pre-treated by OA. a): SEM image; b) and c): TEM images.

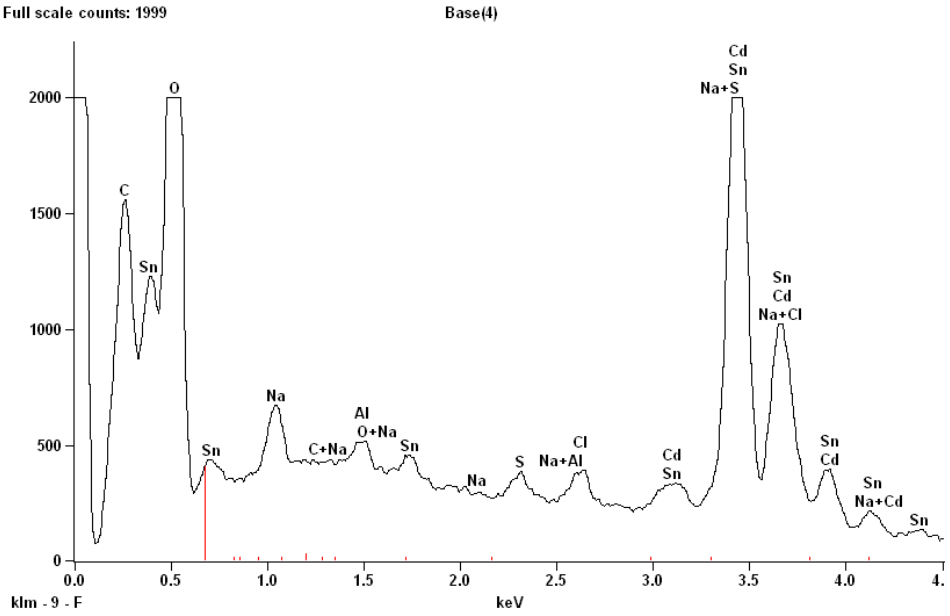

Figure 80: EDX spectra of nan-CdS@mac-FTO electrode without pre-treated by OA.

Element Line	Norm. Wt.%	Atom %
C	11.87	25.14
O	30.29	55.21
Na	0.78	0.99
Al	0.26	0.31
S	0.43	0.39
Cl	0.73	0.60
Cd	2.10	0.54
Sn	53.52	13.15
Total	100.00	100.00

Table 6: EDX elemental analysis of nan-CdS@mac-FTO electrode without pre-treated by OA

As mentioned above, the mac-FTO electrodes were weighed before deposition, after deposition and after calcination to estimate the loading and corrosion of CdS in mac-FTO films.

By comparing before deposition of independently prepared CdS nanoparticles and after calcination of the nan-CdS@mac-FTO composite, it was found that the weight of samples pre-coated with OA increased more after calcination (ca. 0.12 mg) in respect to those without OA (ca. 0.02 mg) pre-coating. This suggests that the OA can enhance the decoration of CdS nanoparticles onto 3DOM materials, even though aggregation and blockage of pores were induced at the same time. However, this aggregation and blockage of pores were not observed when loading CdS nanoparticles into 3DOM TCOs powders under the same conditions.[207] This may be because, the nanoparticles and the oleic acid can infiltrate into 3DOM TCOs powders from all directions. For the mac-FTO films in this work access from the top

of the film may lead to preferred deposition at the top most layers, leading to aggregation and blockage of pores as shown in Figure 76.

As shown in Table 7, the weight of mac-FTO increased ca. 0.36 mg after OA stabilised nan-CdS deposition, and a weight reduction (ca. 0.25 mg) was observed in these nan-CdS@mac-FTO samples after calcination since the OA was burned off during the heat treatment. The loading of nan-CdS (0.25) was slightly enhanced from 0.09 to 0.12 mg when more concentrated nan-CdS dispersion was used (0.5), but the loading was not improved when further increase the concentration of CdS dispersion to 0.75. No obvious weight change was measured after the deposition of nan-CdS for the samples without pre-treating of OA , this is because the low loading level of CdS nanoparticles (Table 8). In these tables, the concentration means the diluted nan-CdS dispersion mentioned above, mac-FTO means the weight of mac-FTO electrodes, after deposition means the weight of nan-CdS@mac-FTO electrode, weight increase means increasing weight of mac-FTO electrode after nan-CdS deposition, after calcination means the weight of nan-CdS@mac-FTO electrodes after calcination and loading means the final weight change between mac-FTO electrodes and nan-CdS@mac-FTO products.

Concentration	mac-FTO (mg)	After deposition (mg)	Weight increase (mg)	After calcination (mg)	Loading (mg)
0.25	823.81	824.05	0.34	823.90	0.09
0.5	801.02	801.35	0.33	801.14	0.12
0.75	804.72	805.11	0.39	804.84	0.12

Table 7: The weight of mac-FTO electrodes and OA stabilized nan-CdS@mac-FTO electrodes after different treatments.

Concentration	mac-FTO (mg)	After deposition (mg)	Weight increase (mg)	After calcination (mg)	Loading (mg)
0.25	800.25	800.28	0.03	800.27	0.02
0.5	816.73	816.75	0.02	816.75	0.02
0.75	809.41	809.43	0.02	809.43	0.02

Table 8: The weight of mac-FTO electrodes and nan-CdS/@mac-FTO electrodes without OA after different treatments.

3.3.3: Mac-FTO films decorated with CdS by SILAR method

To further improve the photocurrent generation of the CdS@mac-FTO composition, another approach was used to enhance decoration of CdS in mac-FTO films, because not only the amount of CdS photocatalyst loaded into the mac-FTO film but also the distribution and homogeneity are the key factors for the enhancement of photocurrent generation. In addition to the deposition of independently prepared CdS nanoparticles, a successive ionic layer adsorption and reaction (SILAR) route was employed. In a glass vial a mac-FTO electrode was stood vertically in a solution of $Cd(Ac)_2$ in ethanol for 1 min, and then dried under a stream of N_2. The electrode was then stood vertically in a second glass vial containing aqueous N_2S for 1 min, rinsed with distilled water and dried under a stream of N_2. This cycle was repeated from 1 to 10 times to form sufficient amount of CdS precipitation within the mac-FTO films. The electrode was finally heated under argon at 400 ^oC and the obtained CdS@mac-FTO electrodes exhibit an orange-yellow colour.

The varied repeat cycles in this work is for controlling the amount or density of CdS within the mac-FTO electrodes. DRUVS and SEM were employed to analyse the morphology of the CdS@mac-FTO electrodes treated with different dipping cycles. From here, the CdS decorated mac-FTO through SILAR method is defined as CdS(n)@mac-FTO, where n means the number of dipping cycles. The performance of the CdS@mac-FTO electrode, was studied using photoelectrochemistry under visible light irradiation.

DRUVS spectra shows the shifted stop bands (Figure 81) with varied loading cycles, and the SEM shows that below 8 cycles the thickness of the CdS film increases without significant blockage of the pores, whereas greater loading result in more significant blockage and surface coverage (Figure 87).

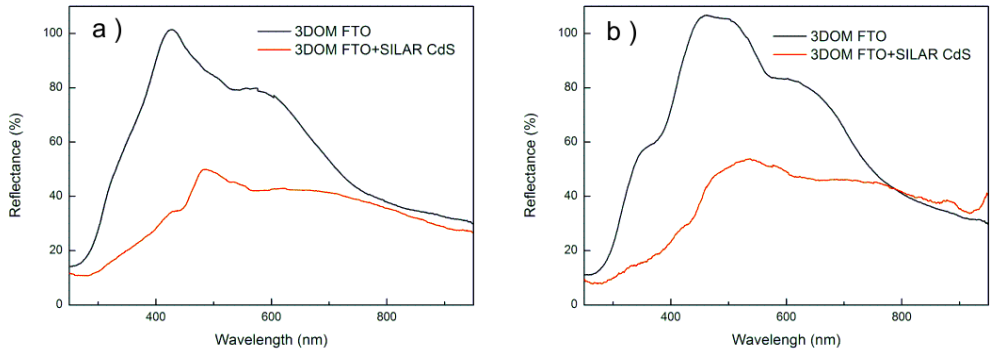

Figure 81: DRUVS reflectance spectra of CdS/mac-FTO electrodes fabricated by SILAR method. a): CdS(5)@mac-FTO made; b): CdS(6)@mac-FTO

Figure 81 shows DRUVS spectra of an example of the red shifted photonic stop bands of mac-FTO films after the decoration of CdS with different cycles. Similar to the red shifted stop band observed in the OA stabilised nan-CdS/mac-FTO electrodes, this red shift can be predicted by Equation 9. In addition to the red shift in photonic stop band position, a decrease of intensity of the photonic stop band was also observed, this may be due to the deposition of CdS films leading to diminished

ordering of the photonic structure. The CdS@mac-FTO electrode treated with 6 dipping cycles exhibited greater (ca. 36 nm) red shift of stop band position than that of 5 cycles (ca. 30 nm) in DRUVS spectra, because the greater wall thickness increase lead to a greater fill factor in terms of the Bragg-Snell equation. Correspondingly, the weight increase after the decoration of CdS by SILAR method is from 0.06 to 0.60 mg depending on the cycles of dipping. The filling factor of CdS in CdS(n)@mac-FTO electrode is estimated using Equation 9 as shown in Table 9. The calculation of filling factor suggests that the loading of CdS can be easily controlled by using different dipping cycles. No obvious stop band was observed from CdS(n)@mac-FTO with 9 and 10 dipping cycles since the overloading, but it can assume that these two samples have greater filling factor by SEM imaging (Figure 87).

Number of dipping cycles	Red-shift (nm)	hkl	ϕ (%)
1	10	111	0.89
2	16	111	1.37
3	22	111	1.93
4	25	111	2.24
5	30	111	2.71
6	36	111	3.22
7	43	111	3.94
8	50	111	4.58

Table 9: Filling factor of CdS in CdS(n)@mac-FTO electrodes.

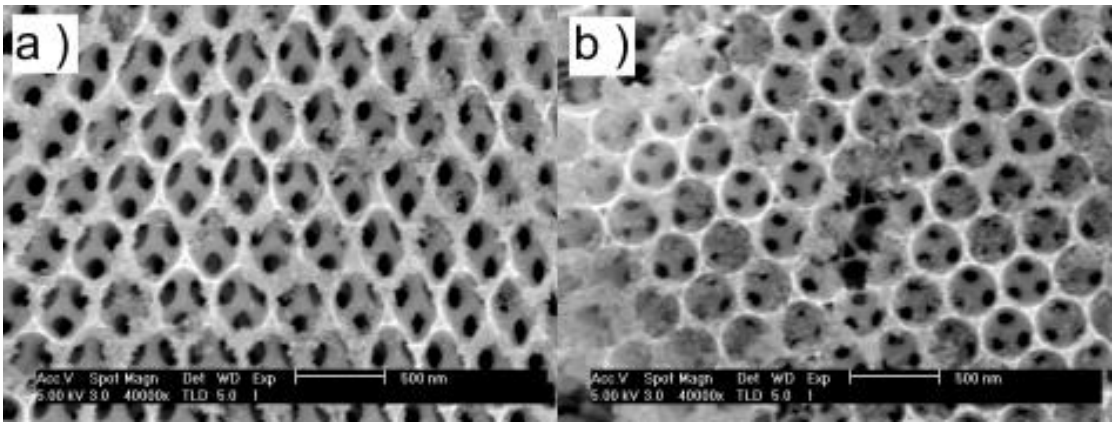

Figure 82: SEM images of CdS(n)@mac-FTO by SILAR method treated with different cycles. a): 3 cycles, b): 4 cycles.

As shown in Figure 82, the CdS nanoparticles attaching to the walls of mac-FTO films were observed by SEM imaging. The decoration of CdS on mac-FTO is homogeneous and no agglomerates or blockage of the pores were observed in the samples with 3 and 4 cycles suggesting the mac-FTO films can support more CdS nanoparticles by increasing the dipping cycles without diminishing the photonic structure too much. Greater loading of photocatalyst in structured materials can lead to greater light absorption and more photocurrent, but overloading of photocalalysts tend to increase the carrier path lengths, leading to a greater possibility for the recombination of electron/hole pairs. In addition, the over loaded materials can block the pores which will diminish the photonic structure of mac-FTO films and reduce the electrode/electrolyte interface area. Both of these effects will lead to a less efficient photocurrent generation. Therefore, the homogeneity and the loading level of photocatalyst nanoparticles must be optimised and controlling the number of dipping cycles is the simplest way. CdS(n)@mac-FTO electrodes treated with 1 to 10 dipping cycles were tested by photoelectrochemistry under visible light irradiation and it was found that the CdS@mac-FTO electrodes exhibit a photocurrent up to ca. 10 mA cm^{-2} with no bias vs. Ag/AgCl under visible light irradiation (> 420 nm).

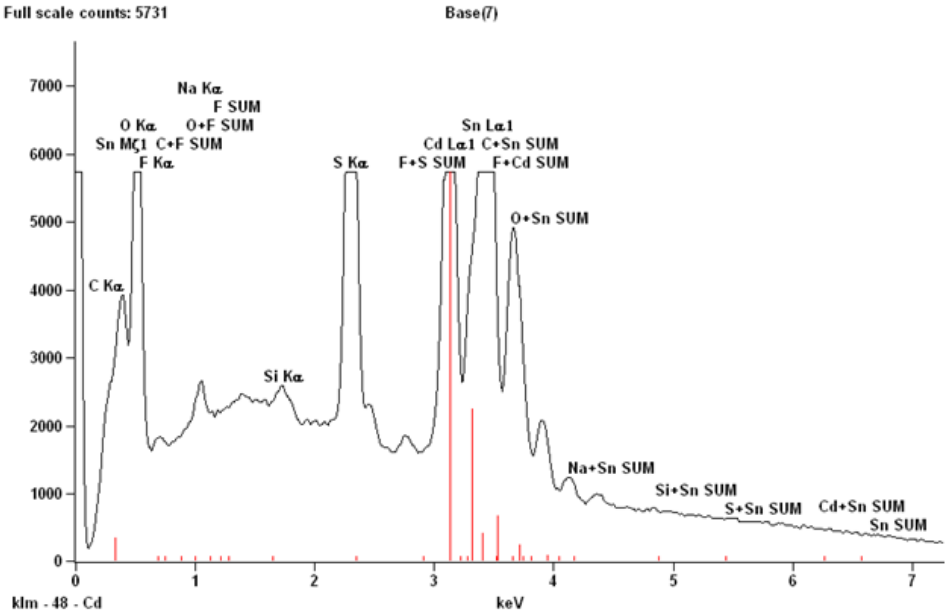

Figure 83: SEM EDX spectra of CdS(n)@mac-FTO fabricated by SILAR method with 8 dipping cycles.

Element Line	Norm. Wt.%	Atom %
C	4.86	17.95
O	15.99	44.33
Na	0.24	0.46
Si	0.33	0.52
S	6.74	9.32
Cd	26.65	10.52
Sn	45.20	16.89
Total	100.00	100.00

Table 10: SEM EDX elemental analysis of CdS(8)@mac-FTO electrode fabricated by SILAR method.

Figure 83 and Table 10 show an example SEM EDX analysis of the high loading level of CdS nanoparticle in mac-FTO (8 cycles, using the SILAR method). , The

atomic percent of Cd detected (10.52 at. %) is higher than that of independently prepared CdS nanoparticles deposition (1.59 at. %) in mac-FTO electrodes (with or without OA stabilizer) suggesting an increase in CdS deposition. The EDX also shows a Cd:S atomic ratio of ca. 1:1, because the calcination of CdS@mac-FTO by SILAR method was accomplished under argon hence no extra O^{2-} will be introduced into the CdS during the heat treatment.

Figure 84 shows the morphology of CdS(8)@mac-FTO by SILAR method imaged by SEM. The walls of the mac-FTO film were fully coated with the CdS nanoparticles in a conformal film. Extra dipping cycles will increase the thickness of the walls and the possibility of aggregation and blockage of the pores. Although the decoration of CdS in this sample (Figure 72) is relatively more homogeneous in respect to Figure 64, aggregations (white circle) and partially blocked pores (red circles) were observed by SEM imaging.

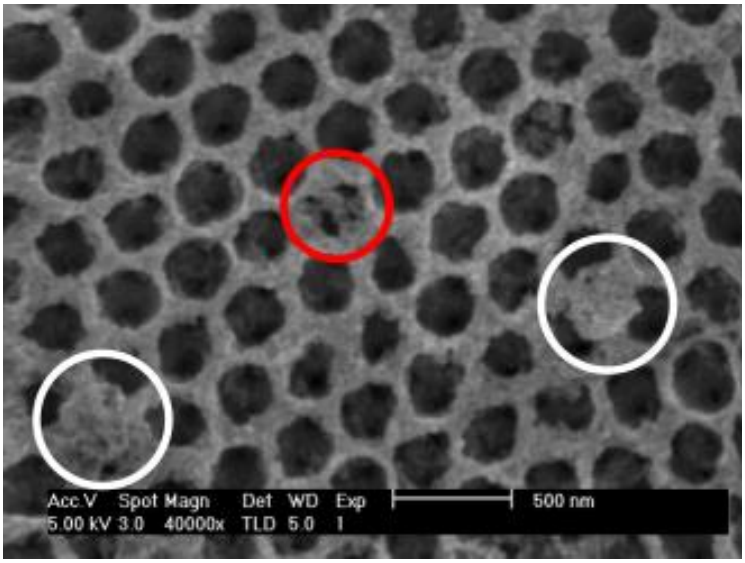

Figure 84: SEM image of CdS(8)@mac-FTO electrodes fabricated by SILAR method.

In addition, the decoration of CdS nanoparticles in mac-FTO film by SILAR method can not only enhanced the infiltration of photocatalyst to give a greater loading, but

also presented a more homogeneous decoration of the CdS nanoparticles in comparison with OA stabilized nan-CdS@mac-FTO electrode when similar weight of CdS nanoparticles was deposited (ca. 0.15 mg). CdS(2)@mac-FTO electrode exhibit a higher photocurrent density (～ 3.2 mA) than that of the OA stabilized nan-CdS@mac-FTO (ca. 0.8 mA) suggesting the homogeneity of the photocatalyst nanoparticles has a significant influence on the photocurrent generation of CdS@mac-FTO composite. More details about the photoelectrochemistry performance of these CdS@mac-FTO fabricated by various methods and conditions will be discussed in the next section.

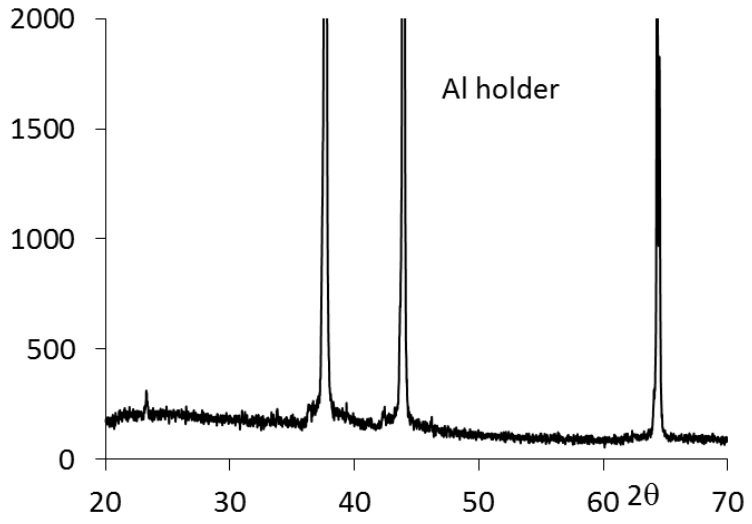

Figure 85: Diffractogram of blank aluminium holder used for surface electrode PXRD. JCPDS 04-0887.

The powder X-ray diffraction shows peaks attributable to the wurtzite polymorph of CdS, JCPDS number 65-3414. The same PXRD spectra was obtained from nan-CdS@mac-FTO samples and CdS(n)@mac-FTO samples with various dipping cycles. This is a common polymorph observed in previous CdS containing composites.[195,197]

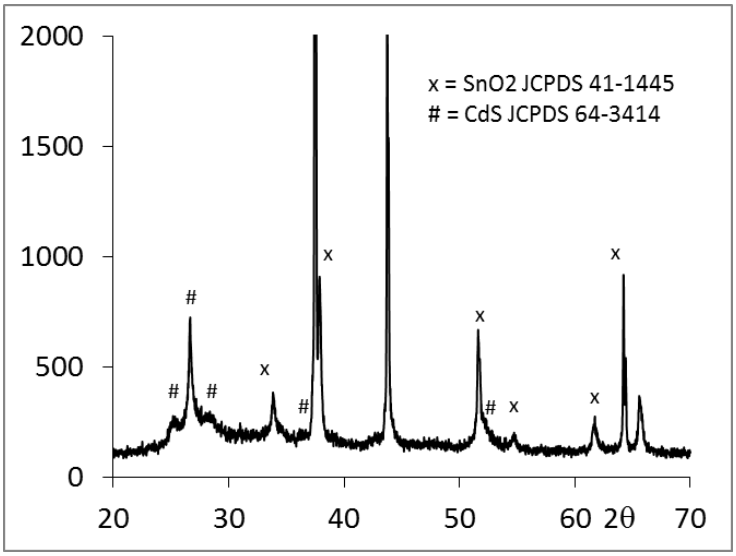

Figure 86: PXRD spectra of a CdS(8)@mac-FTO electrode made by SILAR method. Where x = SnO_2 JCPDS 41-1445, # = CdS JCPDS 65-3414.

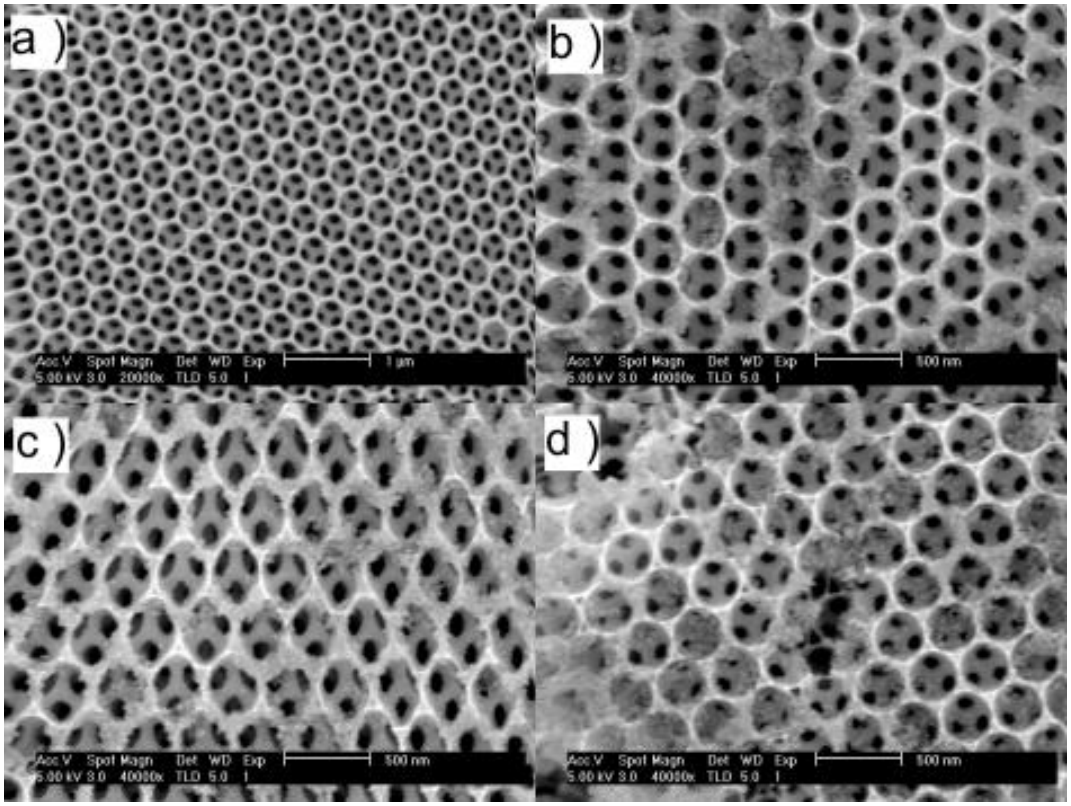

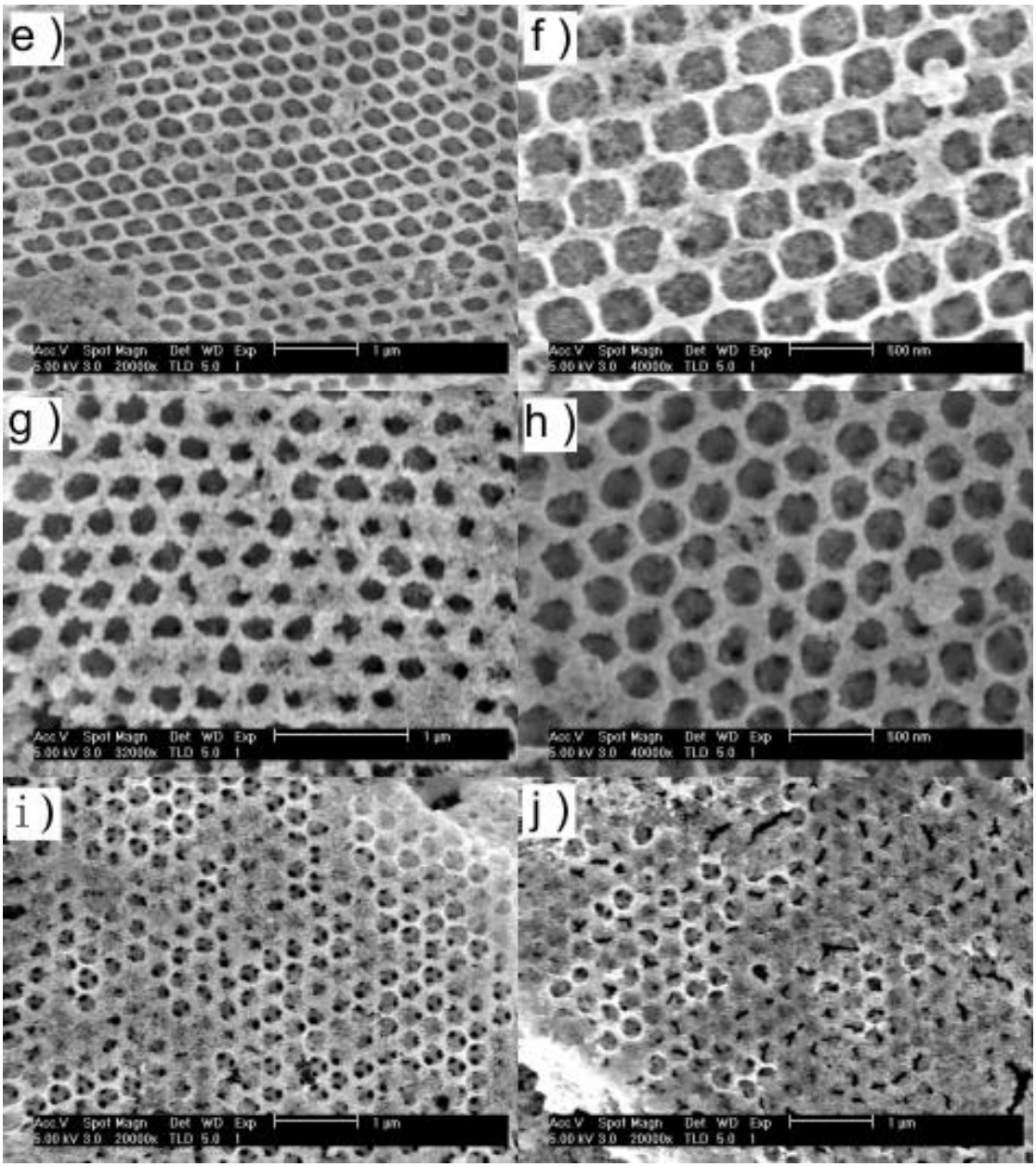

Figure 87: SEM images of CdS(n)@mac-FTO electrode with varied dipping cycles by SILAR method. a) – j): 1 to 10 dipping cycles.

Figure 87 shows the CdS(n)@mac-FTO electrodes fabricated by SILAR method, varied morphologies were observed by SEM imaging when the mac-FTO electrodes treated with different dipping cycles. No obvious CdS nanoparticles were observe as shown in Figure 87a suggesting an insufficient precursor material infiltration as 1 dipping cycle and a little weight increase (0.03 mg) was found by weighing before and after the deposition, but this nan-CdS@mac-FTO still exhibit a photocurrent

density around 0.72 mA cm^{-2} in photoelectrochmistry under visible light irradiation. The CdS nanoparticles can be observed by SEM imaging from 2 dipping cycles, Figure 87b shows that the highly ordered inverse opal structure is covered by a thin CdS layer and no evident aggregation and pore clogging were observed within 4 dipping cycles (Figure 87a-d). As the dipping cycles increasing, the CdS layer became denser (Figure 87e-j) and the aggregations of CdS nanoparticles were observed in all these samples. In terms of the CdS(n)@mac-FTO electrodes treated with 5 to 8 dipping cycles during the deposition, the aggregation of CdS only account for minority content for the overall morphology as shown in Figure 76e-h and no evidence of pore blockage was observed in these samples. After 8 dipping cycles, the aggregation of CdS became more and more common as observed by SEM imaging (Figure 87i-j) and the pore blockages were more evident in these samples, especially for the 10 dipping cycles as presented in Figure 87j. Although the mac-FTO films were loaded with more CdS photocatalysts by 9 and 10 dipping cycles as observed by SEM and weighing, they exhibit no further enhancement in photocurrent density compared with the 8 dipping cycle sample as detected by the photoelectrochemistry. Of course the high content of aggregation will lead to greater possibility for recombination which will reduce the photocurrent generation and limit the electrode/electrolyte interface.

Figure 88 shows the TEM images of CdS(n)@mac-FTO in various magnifications, Figure 88c was taken from an area of Figure 88b. The lattice fringes of the CdS and tin oxide, which were measured to be 2.45 Å and 2.31 Å, corresponding to (102) and (111) crystal plane of each, respectively. (CdS JCPDS 64-3414, SnO_2 JCPDS 41-1445). The aggregation of CdS was also observed by TEM imaging as shown in Figure 89 (white circle).

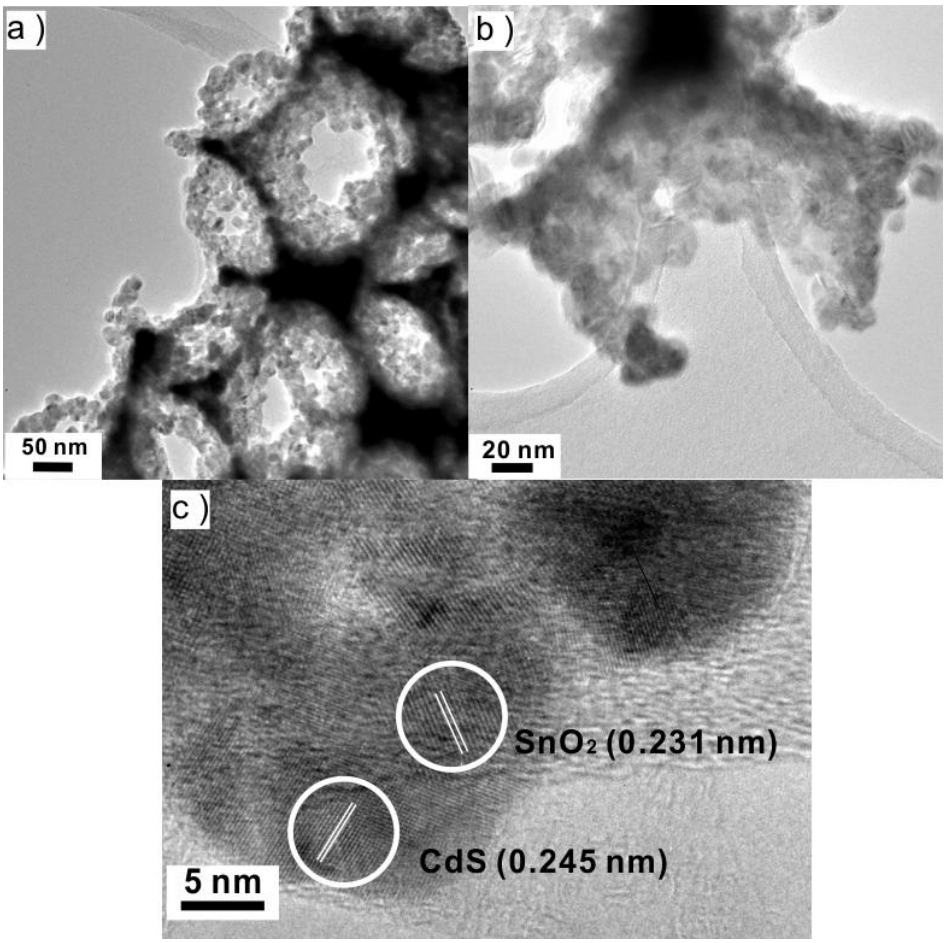

Figure 88: TEM image of the CdS@mac-FTO fabricated by SILAR method.

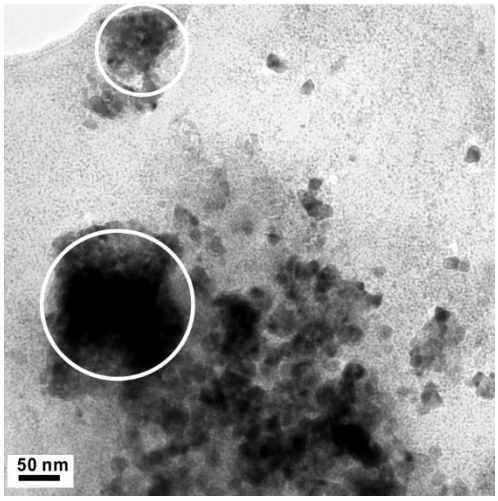

Figure 89: TEM of the CdS@mac-FTO fabricated by SILAR method. Aggregation of CdS nanoparticles (white circle)

The weight measurement was also employed to analyse the loading of CdS in CdS(n)@mac-FTO by SILAR method. Since no organic reagent was like OA was used in this case, no obvious weight change between after deposition and after calcination was observed.

Dipping cycle	mac-FTO (mg)	After deposition (mg)	After calcination (mg)	Loading (mg)
1	815.25	815.32	815.31	0.06
2	802.42	802.61	802.61	0.19
3	807.38	807.77	807.75	0.37
4	821.19	821.44	821.43	0.24
5	812.36	812.67	812.67	0.31
6	806.54	806.94	806.91	0.36
7	811.65	812.08	812.08	0.43
8	807.21	807.72	807.71	0.50
9	820.44	821.00	820.99	0.55
10	805.77	806.37	806.37	0.60

Table 11: The weight of mac-FTO electrodes and CdS(n)@mac-FTO electrodes fabricated by SILAR method after different treatments.

In terms of the CdS(n)@mac-FTO electrodes fabricated by SILAR method, the increase of weight after calcination as shown in Figure 90 enhanced steadily with the dipping cycles for the overall trend. There was no obvious weight change after calcination because no surface ligands such as OA are present. The planar FTO substrates were also weighted before and after the fabrication of mac-FTO films, the average weight increase is 3.2 mg which indicates the CdS in the optimising loaded

CdS(8)@mac-FTO electrode is around 15.6 wt. %. The loading of CdS in this work is greater than that of CdS@mac-SnO_2 (10 wt. %) in a previous literature report. [161]

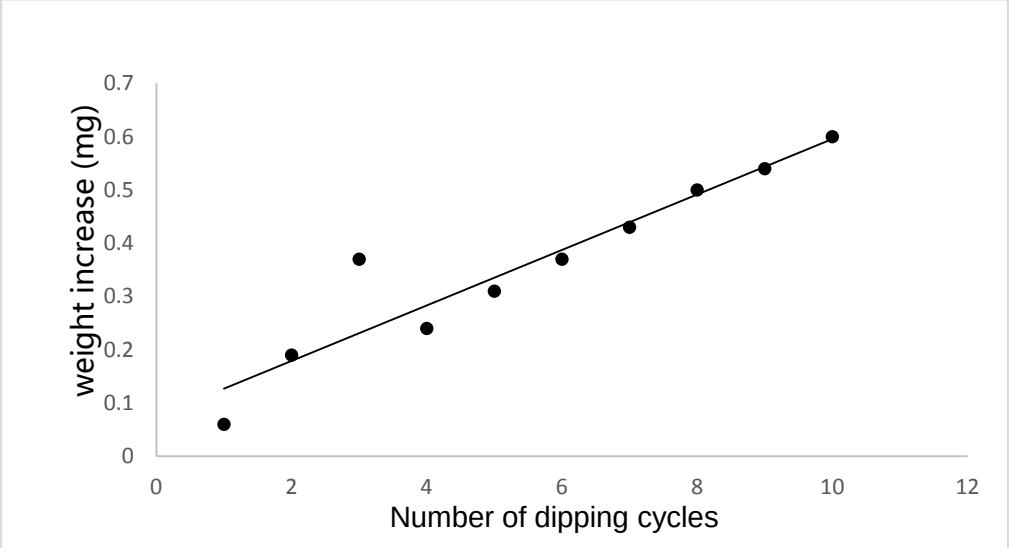

Figure 90: Weight increase of CdS(n)@mac-FTO electrodes with varied dipping cycles fabricated by SILAR method.

3.3.4: Photoelectrochemistry

Photoelectrochemistry tests were conducted in collaboration with Miss Danielle Jowett a fellow PhD student in the group.

The photoelectrochemical response of *nan*-CdS@mac-FTO and CdS(n)@mac-FTO were studied in an aqueous electrolyte of Na_2S (0.25 M)/Na_2SO_3 (0.35 M) at pH 11. Electrodes were illuminated with a Xe lamp through a 420 nm band pass filter with an irradiance of *ca*. 100 mW cm^{-2}, approximating to 1 sun.

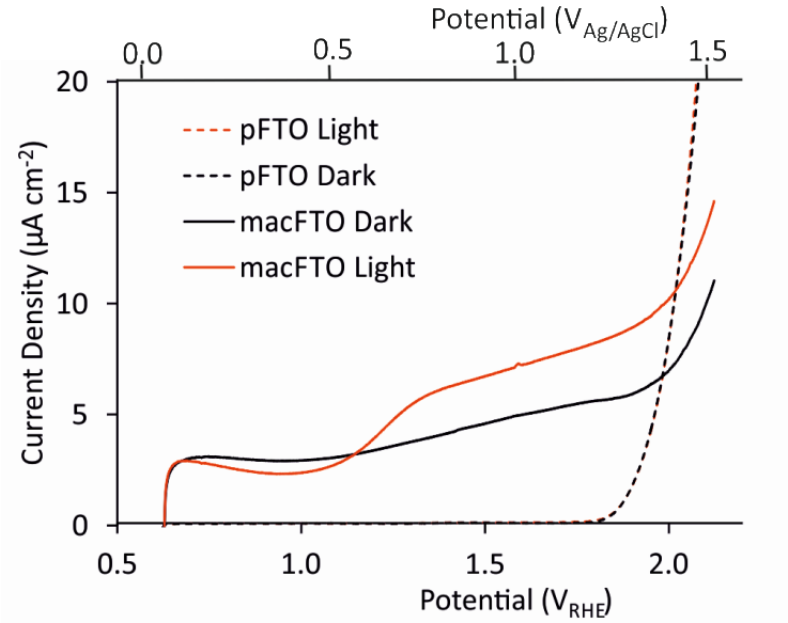

Figure 91: Cyclic voltammetry of planar FTO and mac-FTO in 0.1M $KCl_{(aq)}$ in the dark and under illumination with > 420 nm light (100 mW cm^{-2}).

On illumination no photocurrent is observed for planar FTO and the CV is superimposable with dark conditions as shown in Figure 91. For mac-FTO electrode, a small photocurrent (ca. 2 μA cm^{-2}) is observed above 1.2 V vs RHE (0.4 vs Ag/AgCl) which may be due to defects[195] in the mac-FTO nanoparticles, but the origin of the current is uncertain and is very small. To initially determine if mac-FTO supported charge carrier mobility, nan-CdS@mac-FTO (without OA) was compared to a planar FTO electrode coated with the same mass of nan-CdS and constant potential measurements were conducted at 0 V vs Ag/AgCl (0.8 V vs RHE) (Figure 92).

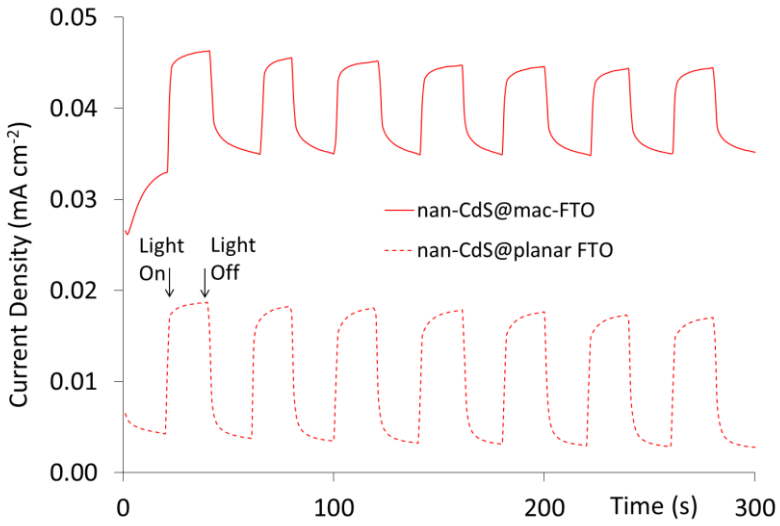

Figure 92: Light response of nan-CdS@planar FTO and nan-CdS@mac-FTO, illuminated with Xe lamp, >420 nm, 100 mW cm^{-2} 0 V vs Ag/AgCl (0.8 V vs RHE) Na_2S (0.25 M)/Na_2SO_3 (0.35 M) (aq).

The photoelectrochemistry below is focussed on the photocurrent generation of nan-CdS@mac-FTO under visible light irradiation with 0 V vs Ag/AgCl (0.8 V vs RHE). Similar light response (Figure 92) was observed for nan-CdS@mac-FTO and nan-CdS@planar FTO samples when a low mass of nan-CdS was used to ensure sub monolayer coverage. Both planar and mac-FTO electrodes give comparable current density of 10 - 15 μA cm^{-2} showing that charge collection occurs from nan-CdS dispersed on the mac-FTO structure and that mac-FTO provides a conduction pathway for extraction of photoelectrons. Repeated cycles show rapid response and reasonable stability over a few minutes.

In addition, it was also found that the current density increases significantly from 4 to 15 μA cm^{-2} (Figure 93) on calcination, presumably due to improved interfacial contact between nan-CdS and mac-FTO on removal of *nan*-CdS surface ligands.

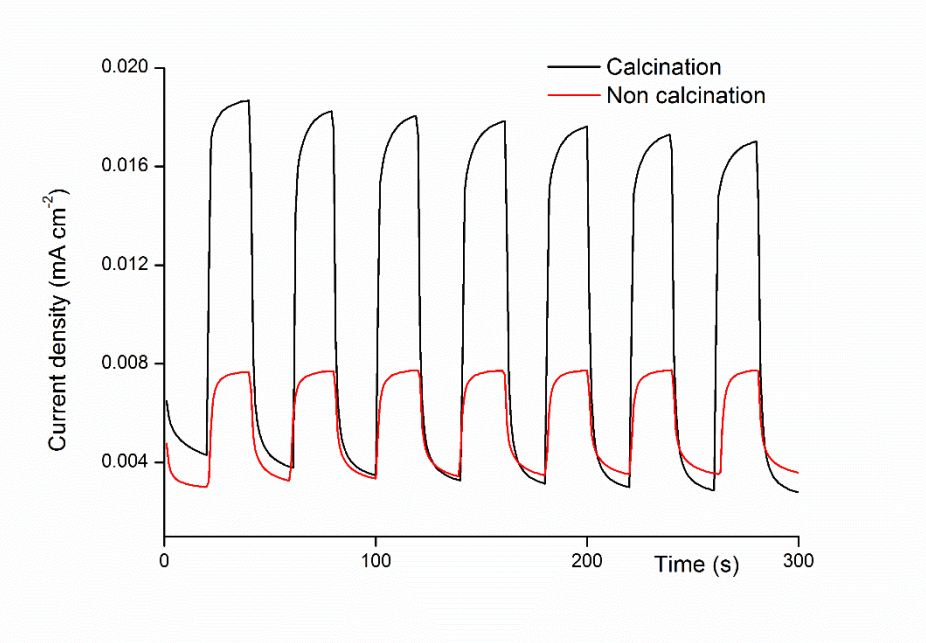

Figure 93: Light response of nan-CdS@mac-FTO (without OA) at 0 V vs Ag/AgCl, treated with (black line) or without (red line) calcination under air.

For the nan-CdS@mac-FTO stabilized by OA, the CdS nanoparticle dispersion with varied concentration were deposited into the mac-FTO films. A slight enhancement of the photocurrent density when more concentrated nan-CdS dispersion employed was observed in photoelectrochemistry as shown in Figure 94. The highest photocurrent density obtained under these conditions is ca. 0.58 mA cm^{-2}, which is greater than the light response of nan-CdS on TiO_2 nanorods ($\sim$0.1 mA cm^{-2}).[209] However, the photocurrent density did not significantly increase using more concentrated CdS dispersions, presumably due to the greater content aggregation and pore blockage.

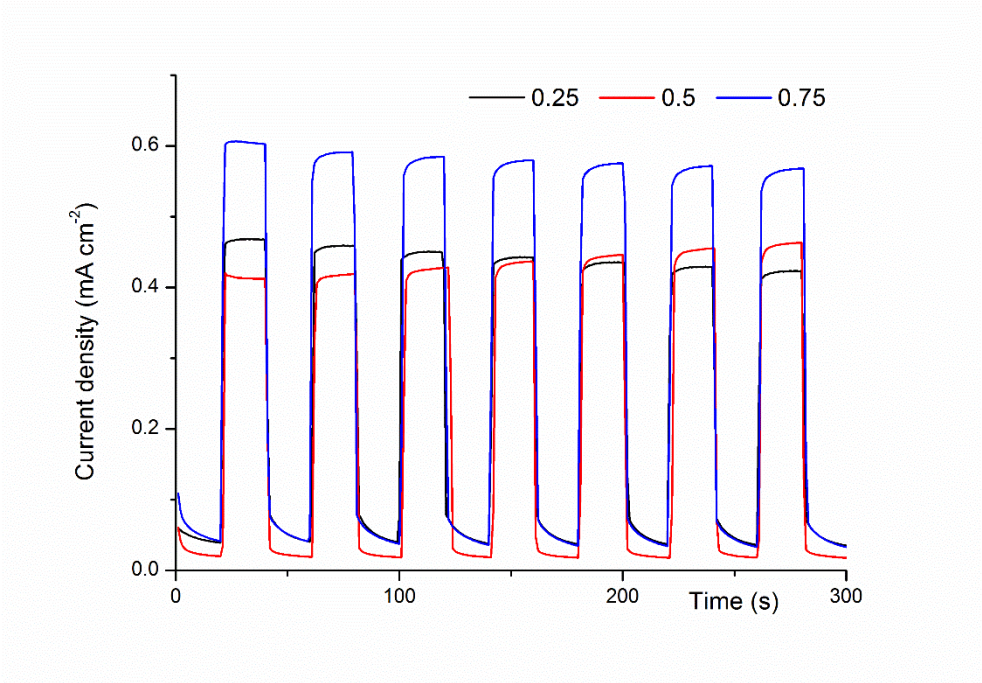

Figure 94: Light response of nan-CdS@mac-FTO stabilized by OA with varied nan-CdS dispersion concentration at 0 V vs Ag/AgCl.

The control of nan-CdS dispersion concentration was also tested on the nan-CdS@mac-FTO electrodes in absence of OA stabilizer, but no obvious improvement was observed by photoelectrochemistry in terms of the photocurrent generation. This result can correspond to the weight measurement of these samples (no obvious weight change when using varied nan-CdS dispersion concentration). Although a homogeneous coating of nan-CdS on mac-FTO was observed (TEM imaging, Figure 79), the poor infiltration of nan-CdS by this approach may limit the improvement of photocurrent generation. According to the weigh measurement data in the last section, the nan-CdS within mac-FTO electrode only account for below 1 wt. % and ca. 4 wt. % when pre-treated without or with OA stabilizer, respectively. This loading amount is lower than that of CdS@3DOM TCOs powder (ca. 10 wt. %)[207] when using the same method. However, the OA free nan-CdS@mac-FTO electrode exhibit relatively higher photocurrent (Figure 95) than that with OA, this presumably because aggregation and electron transfer being prevented in the presence of OA. And the photocurrent generation in OA free nan-CdS@mac-FTO

were not affected by concentration of nan-CdS dispersion, this can correspond to the weight measurement in Table 8. Since the poor interaction between nan-CdS and mac-FTO, more concentrated nan-CdS dispersion will not improve the loading.

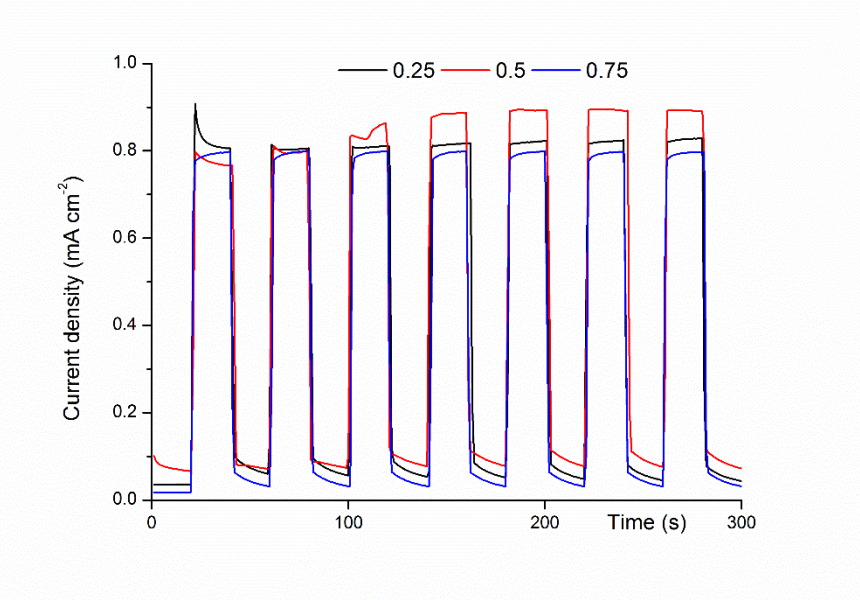

Figure 95: Light response of nan-CdS@mac-FTO without OA fabricated by varied nan-CdS dispersion concentration at 0 V vs Ag/AgCl.

In terms of these nan-CdS@mac-FTO, the electrodes were normally soaked into the electrolyte one hour before the photoelectrochemistry measurement. This is to ensure that the CdO formed during the calcination under air will be transformed to CdS before the PEC tests. The CdO phase was always found when annealing the CdS under air, as it is formed by the oxygen incorporation to the CdS film surface due to the presence of oxygen.[210] It was found that the photocurrent density increased with a decreasing rate and a stable current density was obtained after 1 h as shown in Figure 96, presumably due to the formation of CdS.

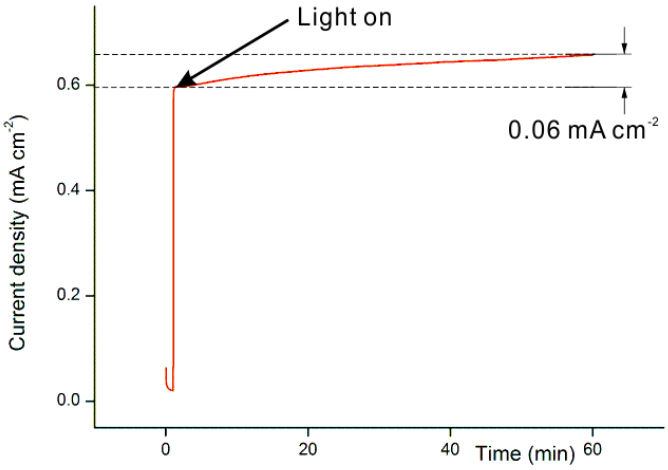

Figure 96: Photocurrent generation by nan-CdS@mac-FTO under light irradiation immediately after calcination at 0 V vs Ag/AgCl.

For the CdS(n)@mac-FTO photoelectrodes fabricated by the SILAR method, the dipping cycle dependency of photocurrent generation was observed by photoelectrochemistry. CdS(n)@mac-FTO show greater photocurrents due to the increased loading of CdS on mac-FTO. Successive deposition cycles give increasing photocurrent which maximises at about 8 - 10 cycles (Figure 97) due to macropore filling and surface coverage. In addition, it was found that the photocurrent generation of CdS@planar FTO increase with the thickness of CdS and maximized at certain thickness, according to a previous literature report,[211] therefore too many dipping cycles may lead to negative influence on the photocurrent. There is some variability between electrodes, which is attributed to the imperfection of mac-FTO fabrication and heterogeneous CdS coverage. Maximum photocurrents of up to ca. 10 mA cm^{-2} (Figure 98a) are observed at 0 V vs Ag/AgCl (0.8 V vs RHE).

In comparison to the CdS on other structured electrodes, the observed photocurrent is much higher than mac-TiO_2 films sensitized by CdS (ca. 5.0 mA cm^{-2})[102,212] CdS@planar-FTO (0.846 mA cm^{-2})[213] and the nan-CdS@mac-SnO (10 μA cm^{-2})[161]

under visible light irradiation at 0 V vs. Ag/AgCl.[214] Alternatively, in respect to the mac-FO film decorated with other photocatalysts fabricated by SILAR method, this result is also higher than TiO_2@mac-FTO (4.67 mA cm^{-2}),[215] TiO_2@mac-FTO (ca. 6.6 mA cm^{-2})[134] under full wavelength irradiation.

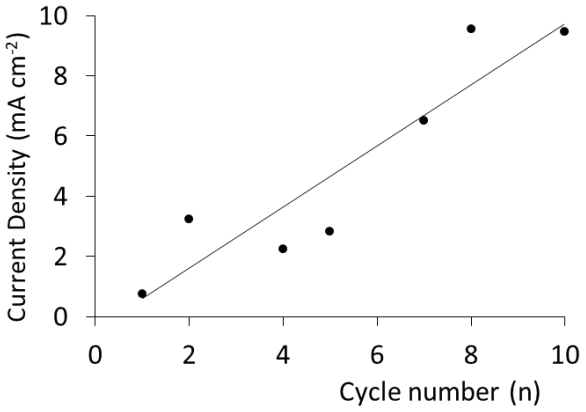

Figure 97. Current density of CdS(n)@mac-FTO as a function of deposition cycle (n) at 0 V vs Ag/AgCl.

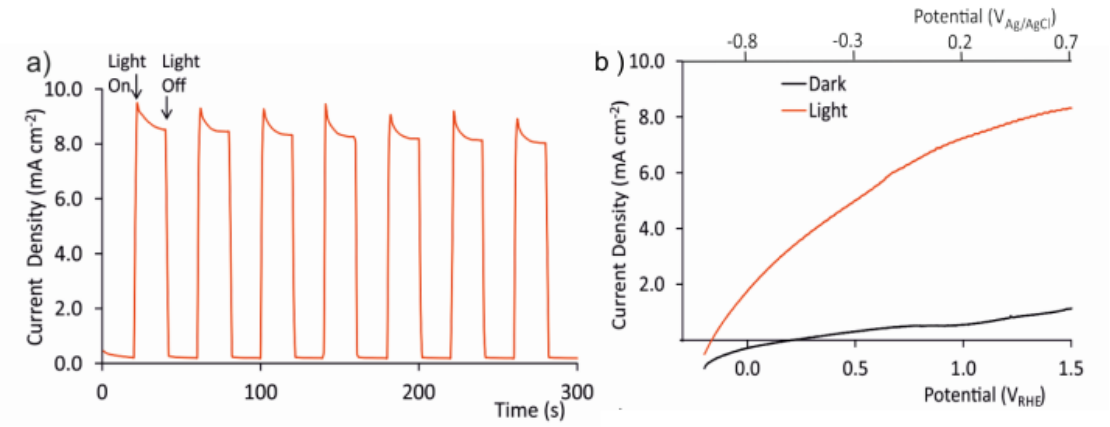

Figure 98: a): Light response of CdS(8)@macr-FTO at 0 V vs Ag/AgCl; b): linear sweep voltammogram CdS(8)@mac-FTO under dark and illuminated conditions.

Linear sweep voltammetry under dark and illuminated conditions (Figure 98b) shows the onset of photocurrent at ca. -1 V vs Ag/AgCl (-0.2 V vs RHE) which is

similar to CdS coated onto other electrodes.[216] In addition, a chronoamperometry (over 2 h) measurement under visible light irradiation was employed to study the stability of CdS(5)@mac-FTO fabricated by SILAR method. Figure 99 shows an example of CdS(5)@mac-FTO, the current density reduced under light irradiation with a decreasing rate, the starting high reducing rate may be due to the poorly attached CdS and the steadily decrease afterwards is due to the decrease of the concentration of the sulfite ion and the change in pH of the electrolyte solution near the electrode.[28] Similar stability of CdS@FTO was also observed in a previous study.[217] Furthermore, SEM imaging of CdS@mac-FTO (Figure 100) and no obvious change was observed suggesting the electrode is stable in PEC experiments. The photograph of CdS(8)@mac-FTO electrode is also shown in Figure 110 (inset), depending on the number of dipping cycles, the colour of CdS(n)mac-FTO electrode can change from pale-yellow to orange, and no colour change can be observed by eye before and after PEC measurement.

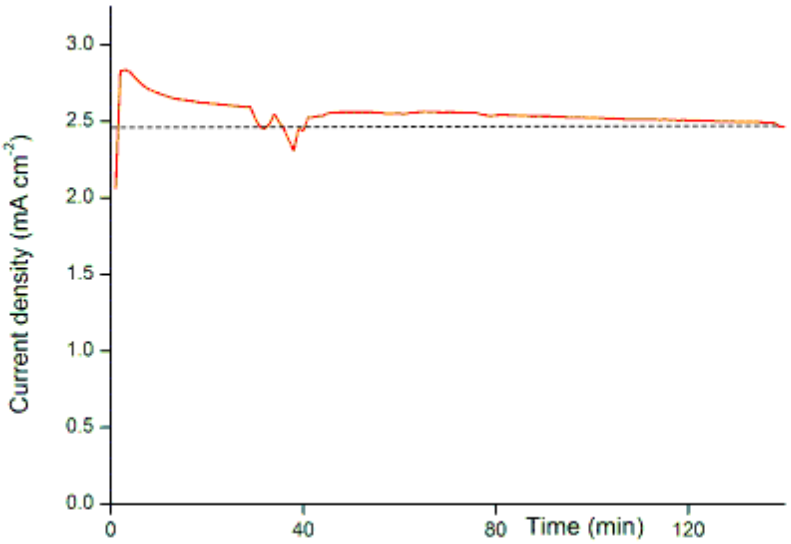

Figure 99: Photocurrent generation by CdS(5)@mac-FTO under long time light irradiation at 0 V vs Ag/AgCl.

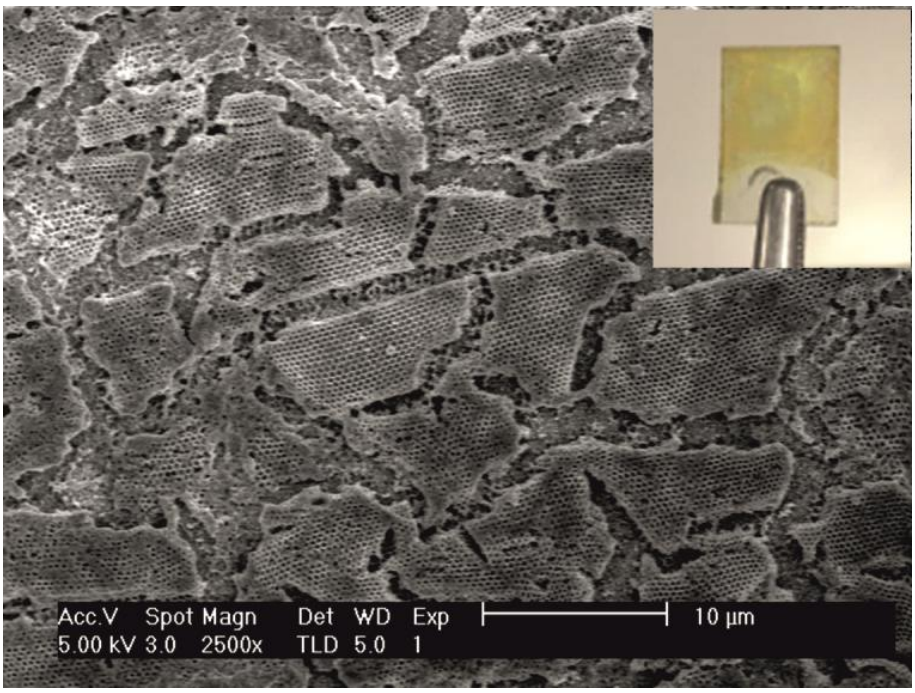

Figure 100: SEM image and digital photograph (inset) of CdS(8)@mac-FTO electrode after PEC measurement.

3.3.5: IPCE measurements

Finally, the IPCE (incident photon-to-electron conversion efficiency) could also be determined for CdS(8)@mac-FTO electrodes compared to CdS@planar FTO electrode with 8 cycles of CdS deposition (Figure 101).

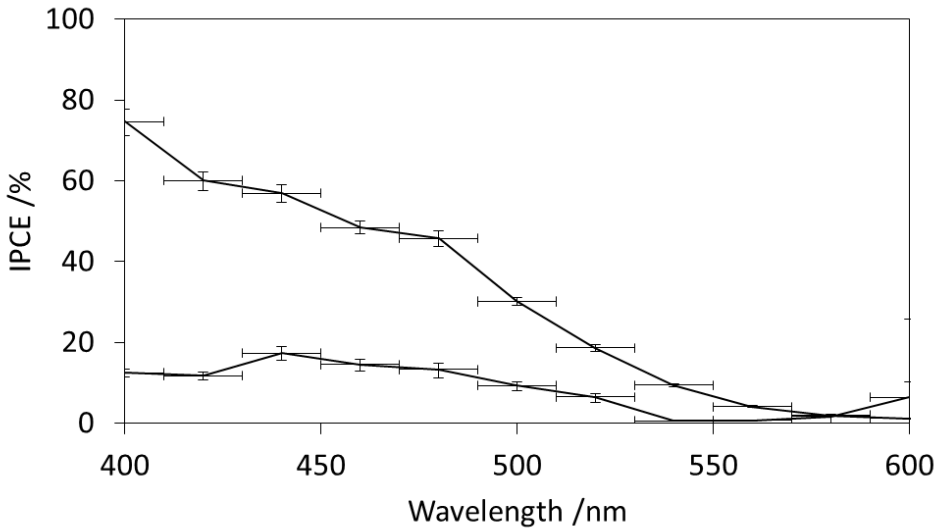

Figure 101: IPCE of CdS(8)@mac-FTO and CdS@planar FTO with 8 cycles.

CdS@planar FTO has a IPCE of ca. 15% at 400 - 500 nm, which then drops off to <1% at higher wavelengths of > 500 nm, consistent with the absorption profile of CdS(8)@mac-FTO has a much higher IPCE, of ca. 50% (45 to 60%) from 400 to 500 m. Again this drops off to < 2% at higher wavelengths of > 500 nm. This is consistent with reports of the IPCE for CdS electrodes in the literature. [218,219]

The IPCE was difficult to measure as the electrode very rapidly loses photocurrent density due to degradation of the CdS. This is apparent in the IPCE profile as a slope in the 400 – 450 nm region where the IPCE should be relatively stable as CdS absorbs broadly here.

3.4: Hs-AZO films decorated with CdS by SILAR method

As mentioned in Chapter 2, hollow sphere materials have many applications, but in this section only the performance of hs-AZO films as support for CdS photocatalyst was focused on. Since the successful CdS deposition on mac-FTO by SILAR method, the same approach was employed for the decoration of hs-AZO.

Similarly, hs-AZO electrode was stood vertically in a glass vial with solution of $Cd(Ac)_2$ in ethanol (50 mM) for 1 min and then dried under a stream of N_2. The electrode was then stood vertically in a second glass vial containing an aqueous N_2S (50 mM) for 1 min, rinsed with distilled water and dried under a stream of N_2. The process was repeated for 3 - 6 times to optimize the photoelectrochemistry performance. The electrode was finally heated under argon at 400 ^oC and an orange electrode was obtained. The CdS@hs-AZO was characterized by DRUVS, PXRD, EDX, SEM, TEM and photoelectrochemistry.

As shown in Figure 102, a red shift of ca. 35 nm was observed after loading the hs-AZO electrode with CdS by 5 SILAR cycles. A filling factor of CdS φ_p = 1.98 % was calculated by Equation 11. The filling factor of CdS on hs-AZO is lower than that on mac-FTO (ca. 3 % with same dipping cycles) due to the morphology of mac-FTO is easier for infiltration.

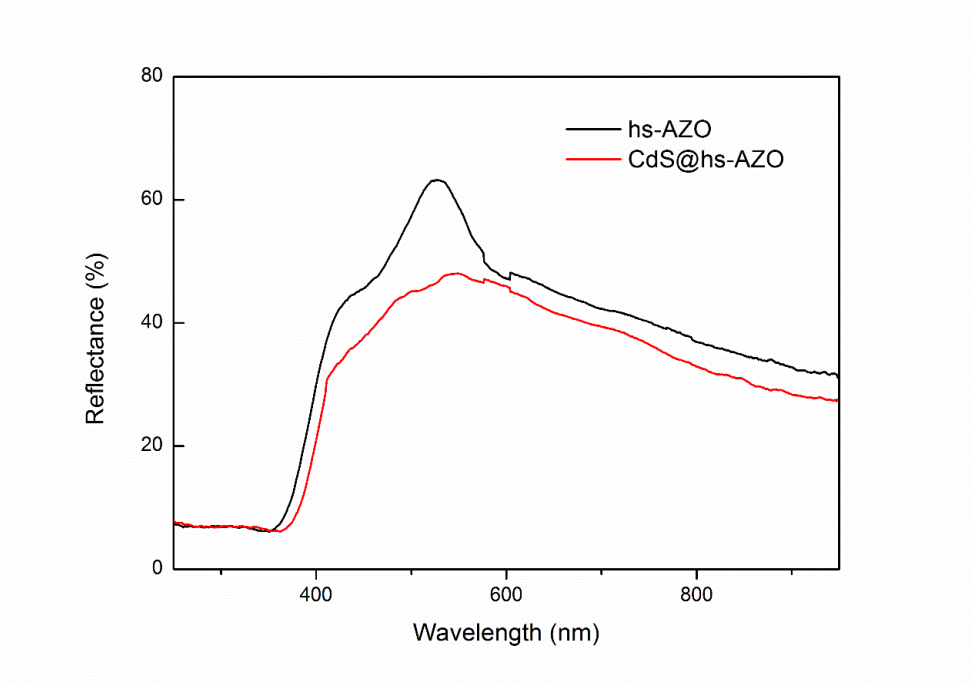

Figure 102: DRUVS spectra of hs-AZO electrode (black line) and CdS@hs-AZO electrode (red line).

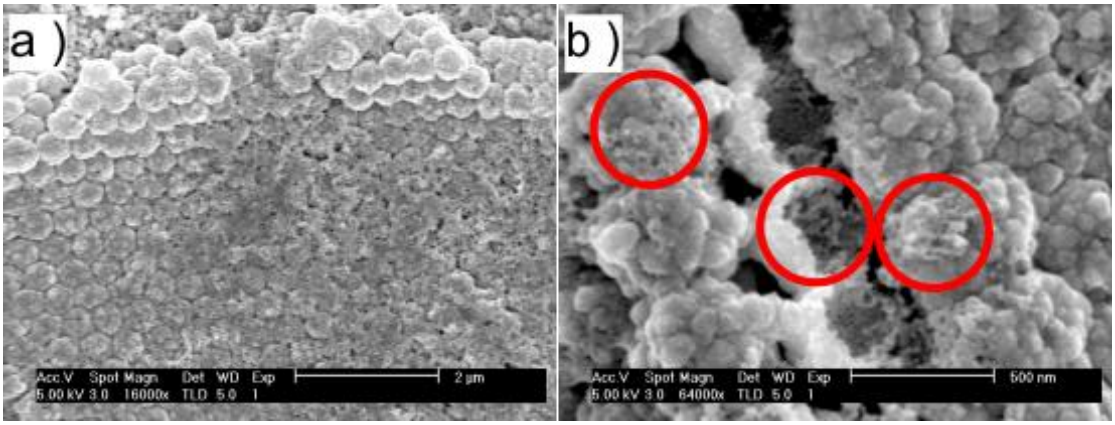

Figure 103: SEM images of CdS(5)@hs-AZO. Red circles (CdS loading)

As shown in Figure 103, the CdS was observed on the hs-AZO film by SEM imaging. Unlike CdS@mac-FTO, the CdS deposited on hs-AZO is more like a film and the coating is homogenous, most area was covered by the dense CdS film (Figure 103a) but neither the SEM nor TEM can confirm whether the CdS had infiltrated into the hollow shell of AZO. Figure 103b present the cracks of the hollow shells coated with

CdS (red circle). The TEM imaging and PXRD spectra of CdS@hs-AZO was presented in Figure 104 and Figure 105, respectively. Both suggest that zincite structure ZnO crystals were formed after the calcination, this zincite ZnO crystal structure was commonly seen in previous literature reports.

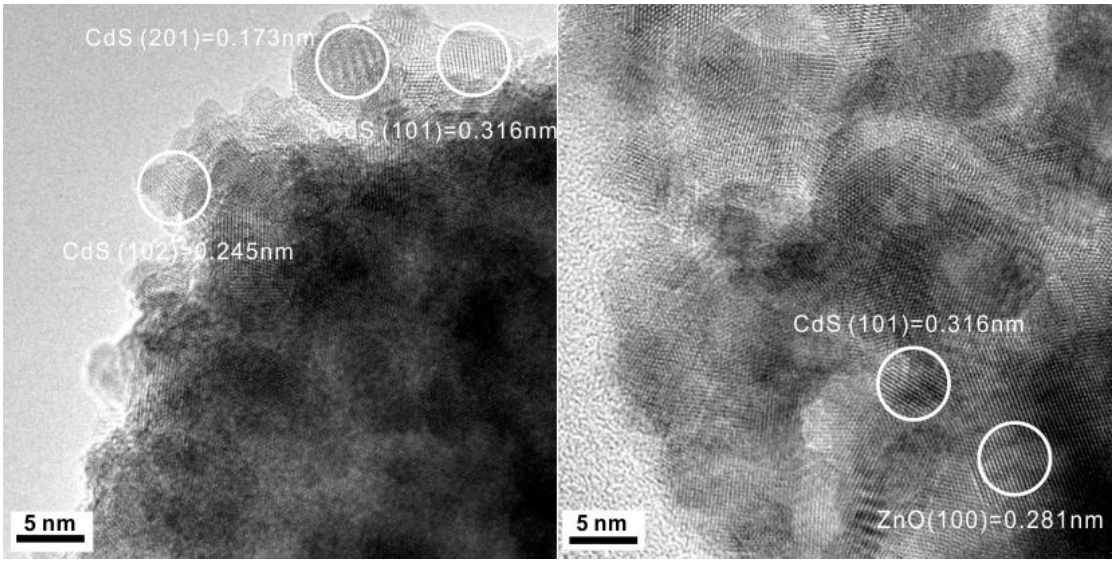

Figure 104: TEM images of CdS(n)@hs-AZO . ZnO JCPDS 36-1451; CdS JCPDS 65-3414

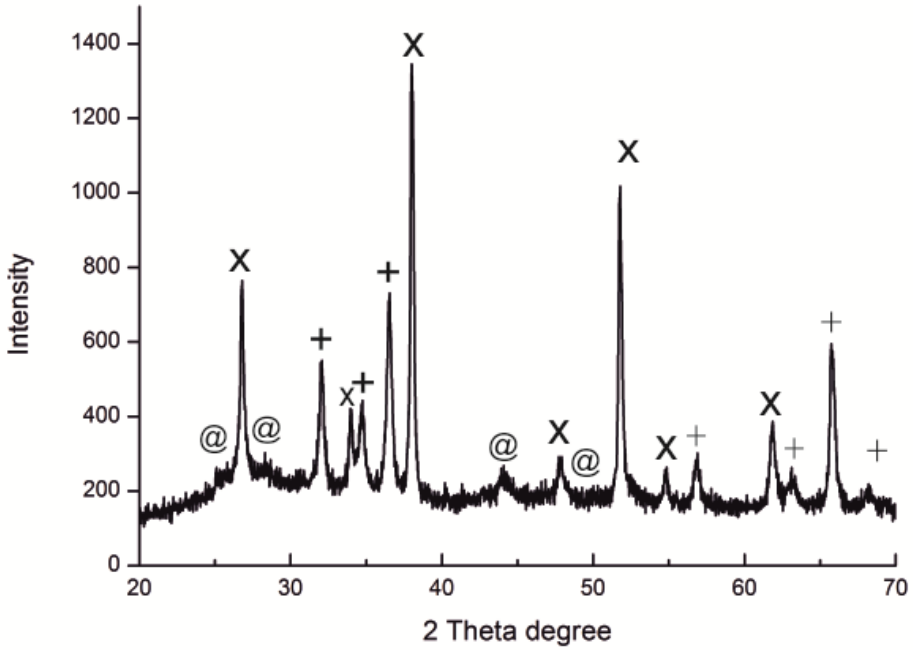

Figure 105: PXRD spectra of hs-AZO electrode with deposited CdS. A silicon holder was used for the measurement. x = SnO_2 JCPDS 41-1445, + = ZnO JCPDS 36-1451, @ = CdS JCPDS 65-3414

In addition, TEM EDX was also employed to confirm the CdS loading on the hs-AZO films. The obvious Cd and S peaks were observed as shown in Figure 106b. But since sample for TEM was scraped from a CdS@hs-AZO film electrode and followed by grounding and dispersing in methanol, the real CdS content should be greater than that of the TEM sample.

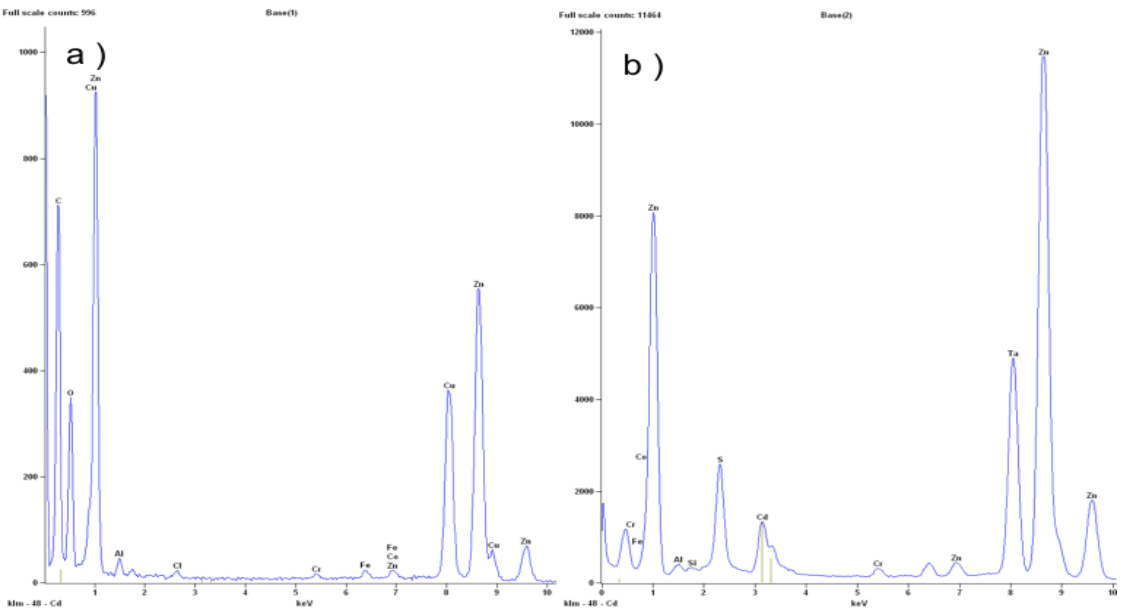

Figure 106: TEM EDX spectra of a): hs-AZO; b): CdS@hs-AZO.

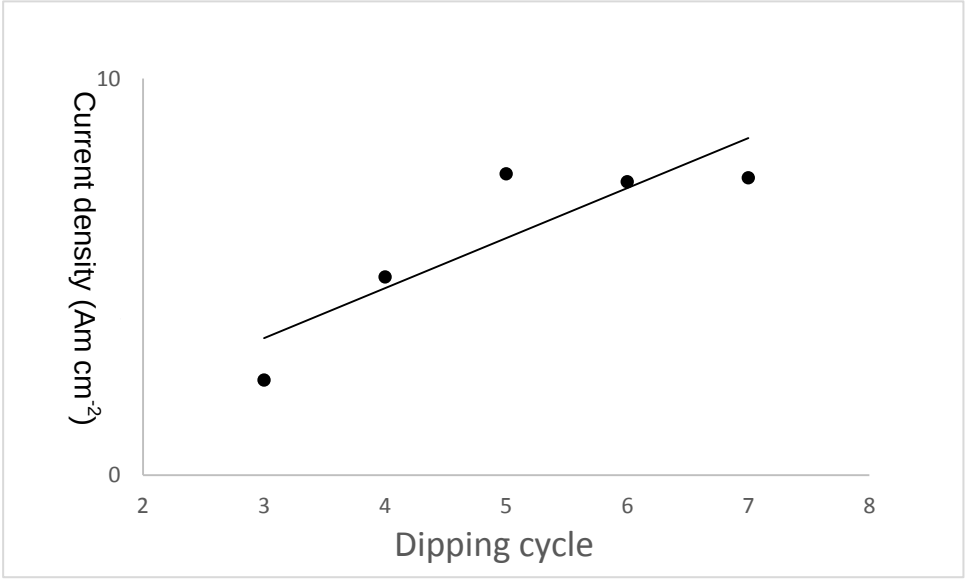

Figure 107: Current density of CdS(n)@hs-AZO as a function of deposition cycle (n) at 0 V vs Ag/AgCl

For the CdS(n)@hs-AZO fabricated by SILAR method, CdS(n)@hs-AZO show greater photocurrents due to the increased loading of CdS on hs-AZO (Figure 107). Successive deposition cycles give increasing photocurrent which maximises at about 5 - 7 cycles due to surface coverage and the thickness of CdS film as discussed in the CdS@mac-FTO case.

Linear sweep voltammetry under dark and illuminated conditions (Figure 108b) shows the onset of photocurrent at ca. -1.2 V vs Ag/AgCl (-0.4 V vs RHE) and the maximum photocurrent density of ca. 7.8 mA cm^{-2} obtained in CdS(5)@hs-AZO (Figure 108a) which is higher than the photocurrent density of CdS@nanocone-AZO (4.23 mA cm^{-2}) fabricated by the same SILAR method[220] and that of CdS@nanocable-AZO (4.74 mA cm^{-2}).[221]

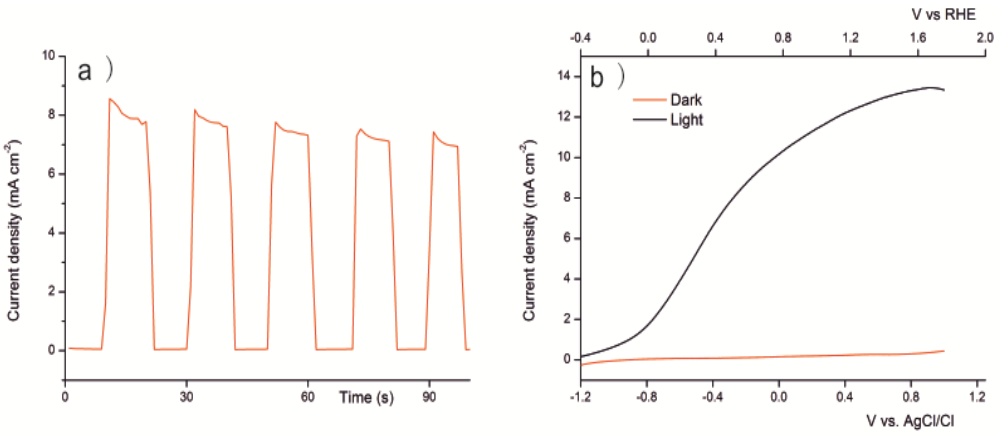

Figure 108: a): Light response of CdS(5)@hs-AZO at 0 V vs Ag/AgCl; b): linear sweep voltamogram CdS(5)@hs-AZO under dark and illuminated conditions

Furthermore, a slightly decreasing photocurrent density of CdS@hs-AZO electrode was observed by chronoamperometry suggesting similar stability to CdS@mac-FTO. Figure 109 shows an example of the CdS(4)@hs-AZO electrode, the current density reduced around 10% after 10 minutes and current density recovered when repeating the tests for multiple times. This is due to the sulfite ions concentration

and pH nearby the CdS recovered between each runs as discussed in the CdS(n)@mac-FTO case.

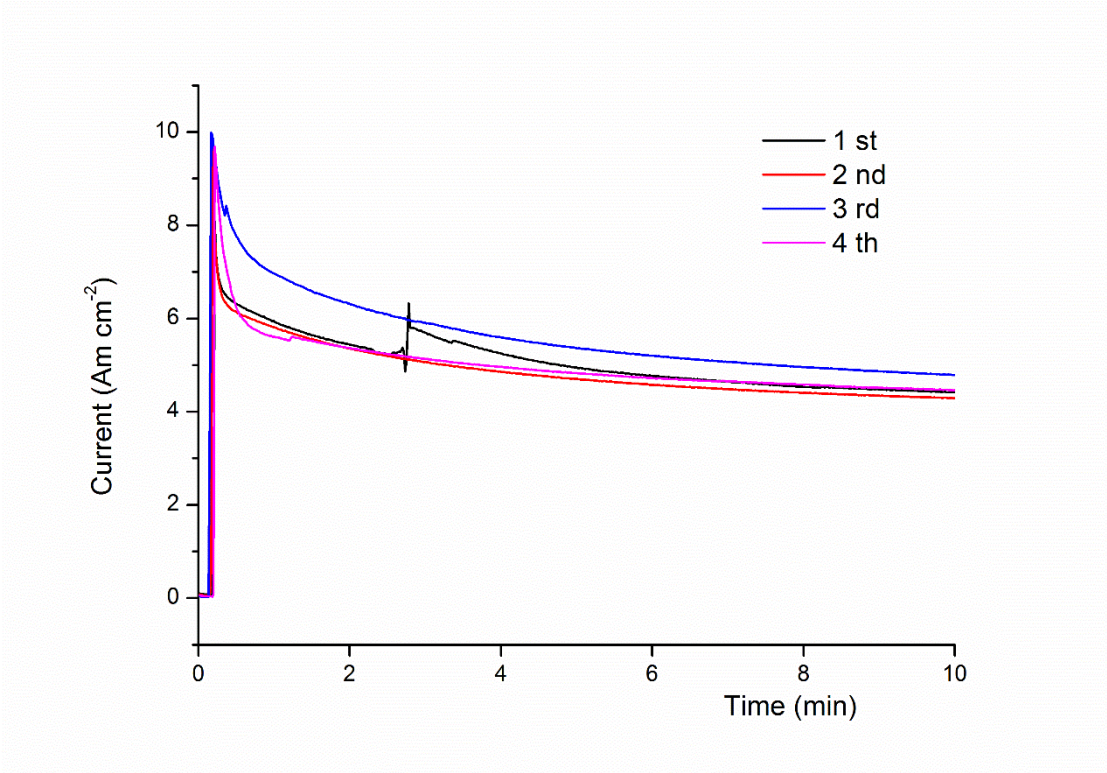

Figure 109: Photocurrent generation by one CdS@hs-AZO electrode in different runs under long time light irradiation at 0 V vs Ag/AgCl.

3.5: Conclusion

A method was developed for deposition of nan-CdS and CdS onto structured TCOs electrodes as relatively homogeneous conformal coating. The CdS nanoparticles and CdS precursor for SILAR method used was readily synthesized according to previous literature reports. The deposition of nan-CdS was optimized through variation of the dispersion solution and pre-treatment of the mac-FTO support. Pre-soaking the mac-FTO electrodes in OA, followed by deposition of nan-CdS dispersion was found to enhance the loading but decrease the homogeneity.

Alternatively, the mac-FTO without OA stabilizer exhibits a homogenous coating but poor infiltration of the CdS nanoparticles. During the calcination, the ligands were burned off from the nan-CdS@mac-FTO and an enhancement of photocurrent generation was observed.

For improvement, decoration of CdS onto mac-FTO and hs-AZO through the SILAR method was optimized by controlling the dipping cycles in CdS precursor solutions and the loading of the CdS is tuneable. The homogeneity of the nanoparticles coating was evidenced by electron microscopy and no significant aggregation was observed when using suitable dipping cycles. The shifted stop band position of mac-FTO electrodes were observed by DRUVS which is dependent on the loading level of CdS. The CdS loading was confirmed by EDX analysis and weighing the sample before and after the deposition. The amount of loading CdS in mac-FTO was significantly improved with high homogeneity. Therefore, a high photocurrent density up to 10 mA cm^{-2} was obtained under visible light irradiation at 0V vs. Ag/AgCl, proving the advantages of the nan-structured TCOs for supporting high photocurrent generation per geometric area. This result is higher than CdS coupled with other nano-structured or planar TCOs electrodes. Furthermore, the CdS@mac-FTO electrodes under visible light irradiation exhibit greater performance than that of the most common TiO_2@mac-FTO electrodes under full wavelength light irradiation or the CdS@mac-TiO_2 under visible light in the presence of sacrificial reagent. [102,134,212-215]

In terms of the future work of mac-FTO, the gas evolution of the CdS@mac-FTO and mac-FTO decorated with sacrificial reagent free photocatalysts may be worth trying to get the best use of photonic mac-FTO electrodes.

The CdS@hs-AZO was optimized and characterized by the similar techniques of CdS@mac-FTO, the highest photocurrent density obtained is up to 7.8 mA cm^{-2} which is greater than that of CdS deposited on other nano-structured AZO

electrodes in previous literature report. [220,221] Due to the special morphology of hs-AZO, only CdS films were observed by SEM imaging, whether the internal hollow sphere was filled with CdS is not certain. Since the shell of hs-AZO consist of AZO crystal particles and holes around 10 nm as shown in the red circle of Figure 71 (chapter 2), it is theoretically possible for the infiltration of CdS precursor solution and electrolyte. In this work, the hs-AZO was only studied as a support for CdS photocatalysts, but it should have more applications in other fields due to its interesting morphology.

In summary, the high quality structured TCO electrodes including mac-FTO and hs-AZO synthesised in Chapter 2 are decorated with CdS. It is evidenced by series of experiments in this chapter that both the mac-FTO and hs-AZO electrodes can support photocurrent. In addition, the structured TCO electrodes here are not just a scaffold to offer active surface sites for continuous photocatalyst film in previous literature work,[131] but can support photocurrent for isolated nanoparticles and discontinuous photocatalyst films.

Chapter 4: Synthesis and deposition of other photocatalysts on mac-FTO film

4.1: Introduction

In this chapter, visible light driven photocatalysts: carbon nitride and iron oxide were used for the decoration of mac-FTO electrodes aiming to improve the photocurrent generation of these photoactive materials in the absence of sacrificial reagent.

Carbon nitrides (C_3N_4) are a class of polymeric metal free materials consisting mainly of carbon and nitrogen. They are cheap and can be easily synthesized by polymerization of cyanamide, dicyanamide or melamine.[222] The band gap energy (2.6 to 2.9 eV) of C_3N_4 and its valence band and conduction band position are sufficient to do water splitting reaction,[223] but commonly have very low efficiency. This is because of the inefficiency in separating and transporting charges for chemical reaction due to the unavoidable disordered structure or defects of C_3N_4 and rapid charge recombination.[224] Recently, carbon nitrides have attracted great attention in the materials science field owing to their potential applications in catalysis,[222,225] fuel cells[226,227] and batteries.[228] In addition, layered C_3N_4 has been used as a photocatalyst for water splitting and organic pollutant degradation.[229,230] To improve the photocatalytic activity of carbon nitrides, the graphitic carbon nitride (g-C_3N_4) has been synthesized with morphologies that have greater surface area although the activity does not always scale with surface area. For studying the photoelectrochemistry performance, g-C_3N_4 has been loaded on planar FTO film and exhibited a photocurrent density around 6 μA cm^{-2} (at 0.4 V vs. Ag/AgCl in 0.2 M Na_2SO_4, under visible light) according to previous literature report.[231] As mentioned in chapter 1, the photonic crystals can suppress the recombination of electron/hole

pairs and supply great surface area, therefore photocatalytic activity of C_3N_4 can be potentially improved within the photonic crystal support. Since no attempts had been reported for coating the mac-FTO films with C_3N_4, in terms of the C_3N_4 study in this chapter, the aim is to fabricate C_3N_4@mac-FTO atempting an improvement of photocurrent generation in comparison with the C_3N_4@planar-FTO in previous studies.

Iron oxide (hematite) has unique properties for application in photoelectrochemistry reactions due to its chemical stability, nontoxicity, abundance, low cost and small band gap energy (ca. 2.1 eV).[232] However, although oxidation of water to dioxygen is possible, the position of the conduction band is too positive to reduce water to hydrogen directly, therefore an external bias voltage is generally applied to overcome this.[233] For oxidation, despite recent efforts,[234-236] no photocurrent density over 1 mA cm^{-2} (from a theoretical 12.3 mA cm^{-2}) was achieved from iron oxide anodes at a bias voltage of 1.23 V vs. RHE under visible light irradiation in 0.1 M NaOH. This is because the slow kinetics of water oxidation by valence band holes and rapid recombination of excited carriers.[237]

4.2: Chapter aims

The aim of this chapter is to study the generality of mac-FTO electrode as a support for various visible light driven photocatalysts, and to find a new way for improving the photocatalytic activity of C_3N_4. The methods and conditions will be investigated to optimize the decoration of photocatalyst material (C_3N_4 and Fe_2O_3) on mac-FTO electrodes. In addition, the photoelectrochemistry was employed to confirm if the mac-FTO electrodes can support the photocurrent of different photocatalysts with varied morphologies (in comparison with the CdS decoration in chapter 3) in the absence of sacrificial reagent.

4.3: Result and discussion

4.3.1: Synthesis of carbon nitride on mac-FTO film

In previous studies, the most common approach for the synthesis of C_3N_4 involves thermal condensation of nitrogen- and carbon-rich monomers such as cyanamide, dicyanamide or melamine.[222] Most products of these approaches are bulk C_3N_4, while for photoelectrochemical applications a direct and continuous C_3N_4 layer is preferred.[238]

For the initial attempts, a modified literature method was used.[224] Melamine was mixed with a eutectic salt (LiCl : KCl : NaCl = 0.7:1:1 weight ratio) in a 1:15 by weight ratio. The mixture was finely ground in a mortar. The resulting mixture was then transferred into an alumina boat, after that, mac-FTO electrode was immersed into the mixture and heated to 500 ^{o}C under air. After it was cooled to room temperature, a yellow electrode was obtained. The yellow electrode was rinsed with deionized water for 2 times to get rid of the poorly attached material and salts. The morphology of the C_3N_4@mac-FTO film was examined by SEM imaging as shown in Figure 110. Bulk C_3N_4 was observed on top of the mac-FTO film suggesting a poor decoration of C_3N_4 on mac-FTO film or significant overloading. Poor penetration may be because the molten melamine has a poor interaction with the FTO leading to insufficient infiltration into the photonic FTO crystal. Unsurprisingly, this C_3N_4@mac-FTO electrode exhibited a poor photocurrent density ($\sim$3.5 μA cm^{-2}).

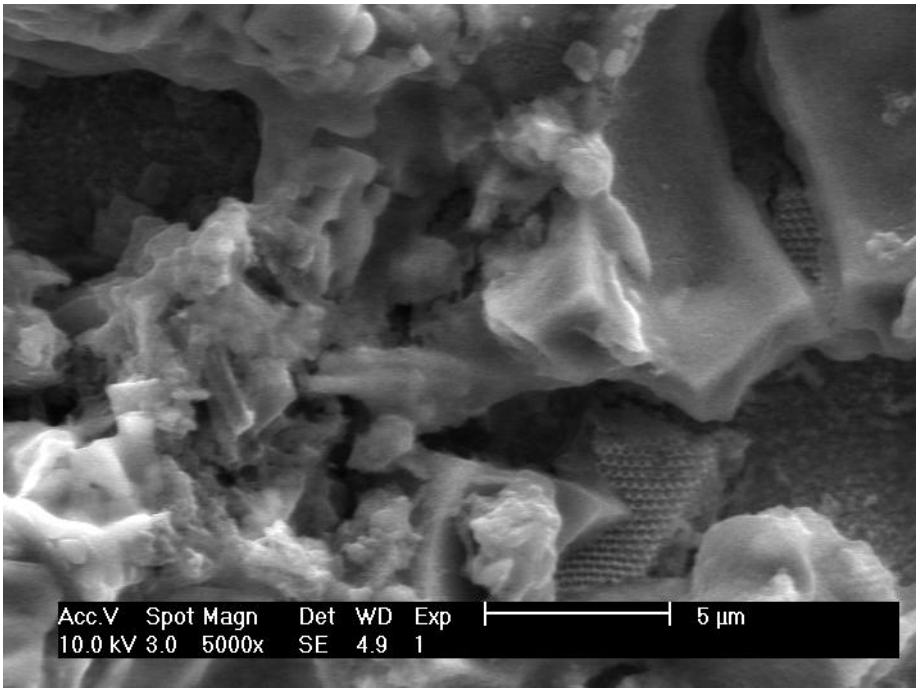

Figure 110: SEM image of C_3N_4@mac-FTO electrode fabricated by immerse mac-FTO in melamine precursor.

According to a literature report for fabrication of C_3N_4 films,[239] a modified method was used for decoration of mac-FTO electrodes by cyanamide precursor. Firstly cyanamide was dissolved in HCl and ethanol and the pH was adjusted to 2 with HCl. 200 uL of the solution was then added to the top of mac-FTO electrode and calcined at 500 ^{o}C under argon. By eye, the obtained electrode appears to have no obvious colour, like bare planar FTO. As shown in Figure 111, a C_3N_4 film on top of the mac-FTO was observed, and unusual scroll type structures, and it was not possible to determine if the mac-FTO is coated homogeneously underneath. Potentially, the molten cyanamide is too viscous to infiltrate the pores of mac-FTO films.

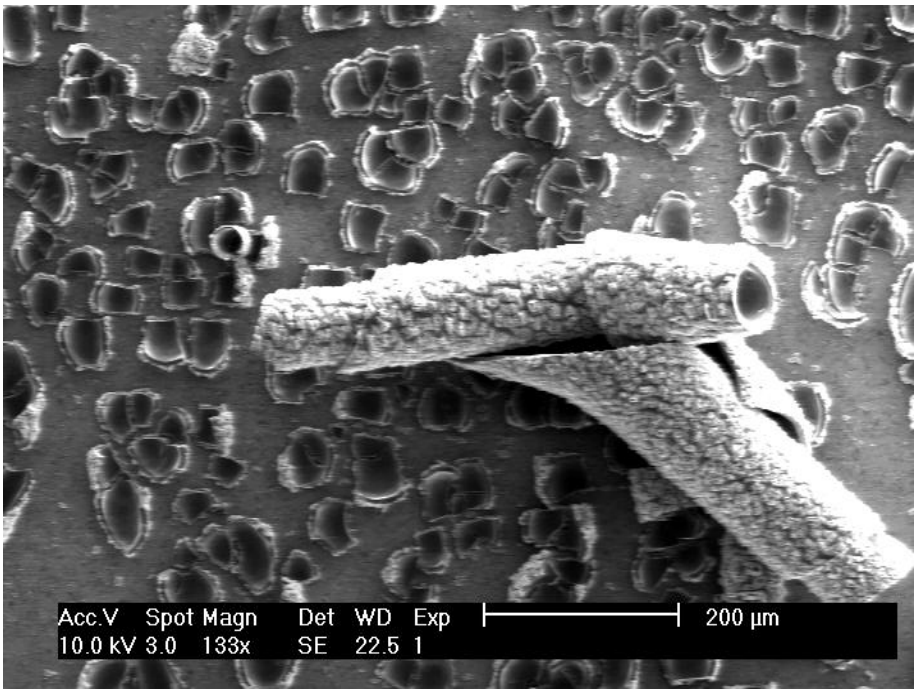

Figure 111: SEM image of C_3N_4@mac-FTO electrode fabricated by immerse mac-FTO in cyanamide precursor.

To improve the decoration by C_3N, the powder precursor complexes was transformed to liquid state before direct thermal condensation into C_3N_4 solid films. A liquid-based growth of carbon nitride layers[240] was modified for the fabrication of C_3N_4@mac-FTO electrodes. Cyanuric acid was mixed with 2,4-diamino-6-phenyl-1,3,4-trizanie and the powder was transferred into 10 mL DI water with shaking, and dried at 60 ^oC overnight. Various amounts (5, 10 and 20 mg) of the powder mixture precursor were put evenly onto mac-FTO electrodes. The mac-FTO electrodes with powder precursor was set horizontally in a crucible totally covered with aluminium foil and heated to 550 ^oC under argon. After cooling, yellow-brown electrodes were obtained.

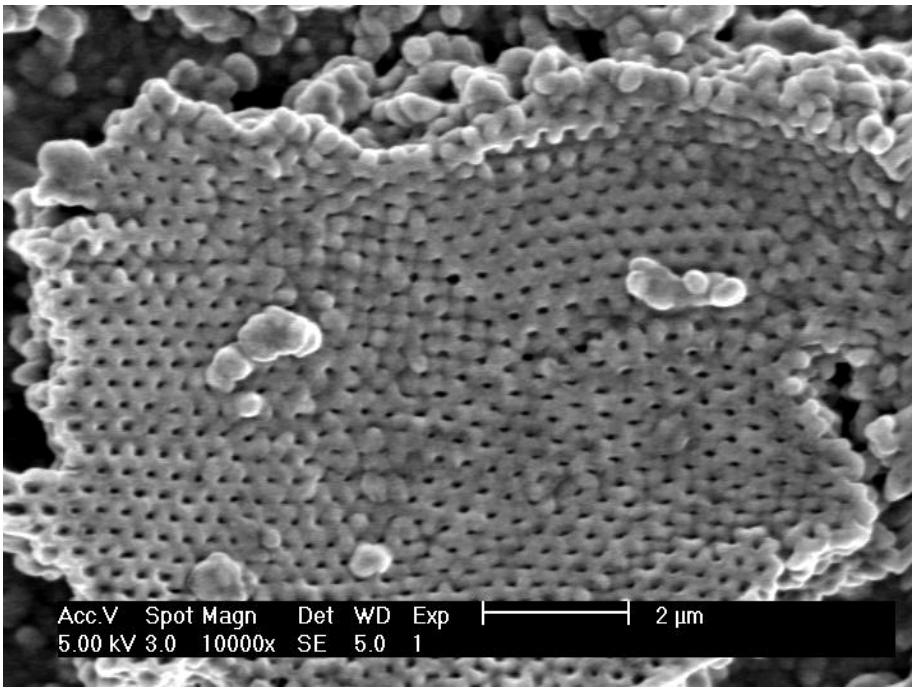

Figure 112: SEM image of mac-FTO electrode loaded with 20 mg of C_3N_4 powder mixture precursor.

The mac-FTO electrode was homogeneously decorated with C_3N_4 as shown in Figure 112, suggesting the C_3N_4 precursor can easily infiltrate the mac-FTO electrode, presumably due to the lower viscosity of the C_3N_4 precursor during the calcination process. In addition, even though the C_3N_4 coating is quite thick (ca. 130 nm), no C_3N_4 large films covering the top of the mac-FTO electrode is observed which blocks the pores (compared to the morphology shown in Figure 111. This may be because the C_3N_4 precursor in this approach has high surface wettability when coupling with FTO. According to a previous literature study,[241] C_3N_4 grown on a planar FTO substrate exhibited a film 20 times thicker than that on a planar TiO_2 substrate under same conditions due to the difference in surface wettability.

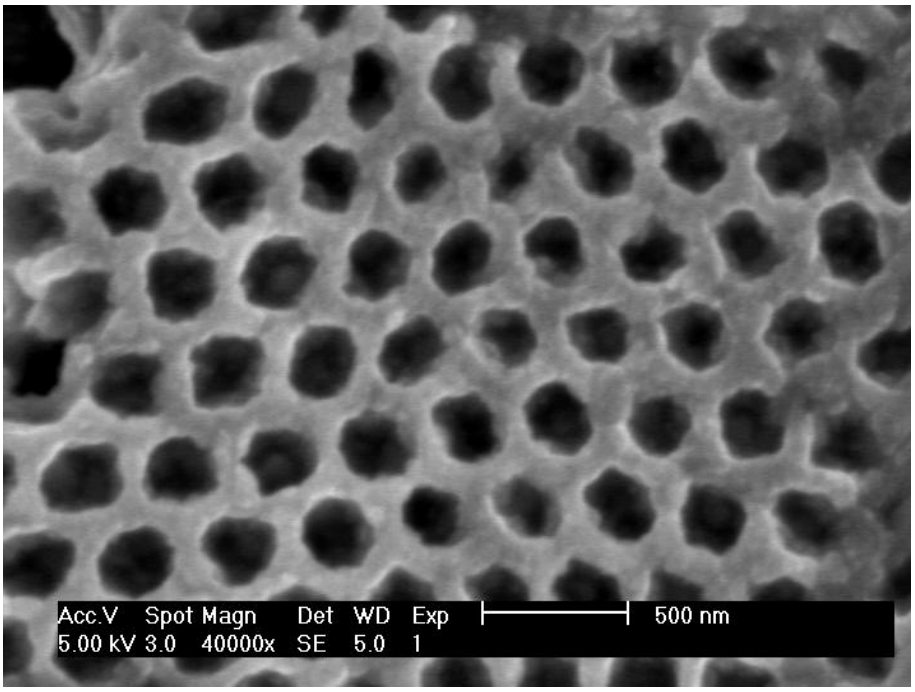

Figure 113: SEM image of mac-FTO electrode loaded with 10 mg of C_3N_4 mixture powder precursor.

As discussed in chapter 1, the long path way for photogenerated electrons will lead to low efficiency due to the recombination of electron/hole pairs in the defects of photocatalysts film. The thickness of coated C_3N_4 films were controlled by varying the amount of powder precursor, by reducing the powder precursor (to 10 mg), thinner C_3N_4 film (ca. 30 nm) decorated on mac-FTO electrode was obtained as shown in Figure 113. The C_3N_4 films were coated on the skeleton of mac-FTO film homogeneously and no blocked pores were observed by SEM imaging. It is worth noting that, the C_3N_4 films were bound to the mac-FTO electrodes strongly by this approach, the morphology as shown in Figure 112 and Figure 113 remained after a sonication in DI water for 1 h. In addition, on further reduction (5 mg) of the powder mixture precursor, thin C_3N_4 film on mac-FTO was obtained as shown in Figure 114. This sample exhibits low photocurrent (below 1 μA cm^{-2}) suggesting an insufficient decoration of photocatalyst.

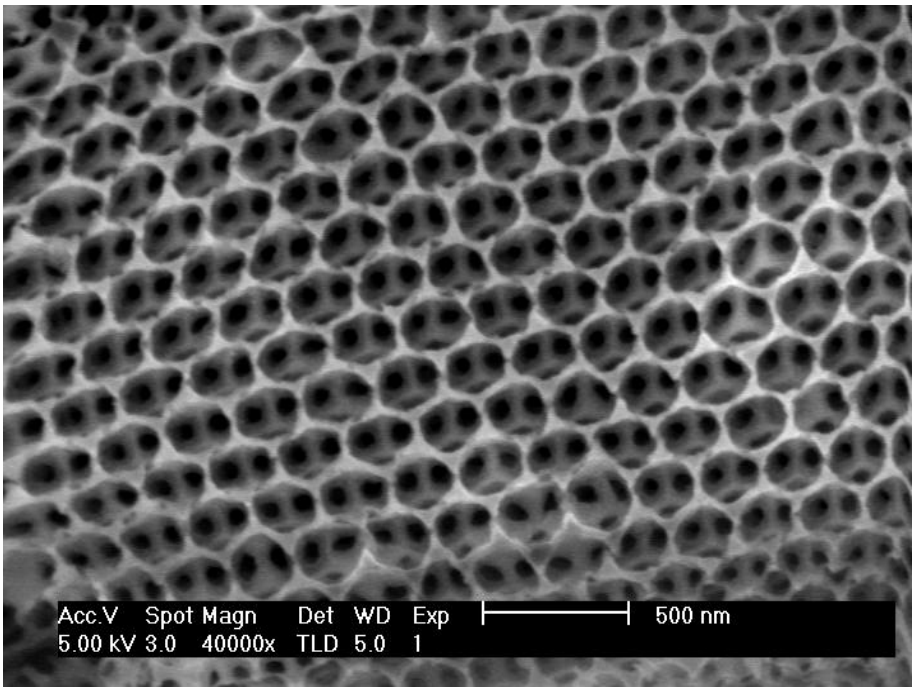

Figure 114: SEM image of mac-FTO electrode loaded with 5 mg of C_3N_4 mixture powder precursor.

Furthermore, the DRUVS spectra are presented in Figure 115 to study the light absorption of C_3N_4. The absorption edge of C_3N_4 is around 440 nm in visible light region which is similar to that observed in previous literature report[241] suggesting the photogenerated electrons should occur under visible light.

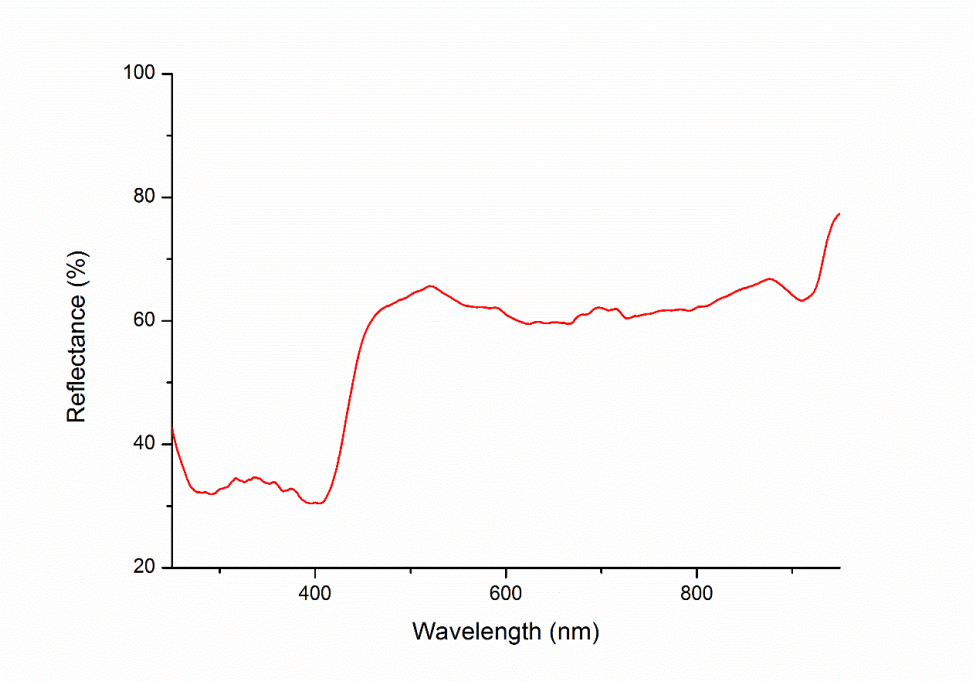

Figure 115: DRUVS spectra of C_3N_4 synthesized by liquid-based growth of carbon nitride layers.

As shown in Figure 116, the IR spectrum of C_3N_4 shows bands which correspond to that of previous literature report.[242] The C_3N_4 powder used for IR measurement was fabricated on planar-FTO in the same batch with C_3N_4@mac-FTO electrodes. The C_3N_4 powder was scratched from the planar-FTO substrate by a sharp blade. Characteristic features are the sharp peak at 810 cm^{-1} due to a breathing mode of heptazine rings and peaks at ca.1500 cm^{-1} due to C=N stretches. In addition, the elemental analysis of C_3N_4@mac-FTO electrode was carried out by EDX as shown in Figure 117 and Table 12. The atomic content of C and N in the terminal product is 10.121 % and 14.084 %, respectively. The C/N ratio is around 0.72 and it can correspond to a compound of $C_{2.87}N_4$ which is close to C_3N_4. Since the C/N ratio in bulk C_3N_4 observed by elemental analysis in previous report is 0.67 to 0.70 due to the incomplete condensation of precursor materials,[239] the C/N ratio obtained in this work is closer to the ideal value (0.75). In addition, since the most intense diffraction peak of C_3N_4 (27.2°)[242] overlaps with the SnO_2 (110) JCPDS 41-1445 peak at 27.0°

or the C_3N_4 was not highly crystallised, it is not convenient to analyse the C_3N_4@mac-FTO by PXRD.

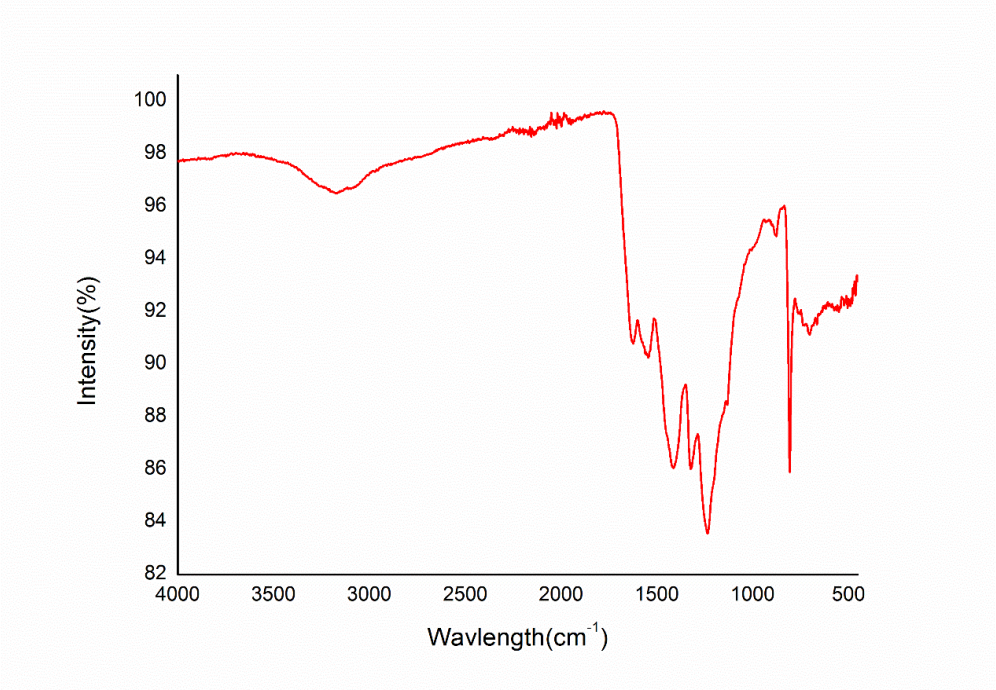

Figure 116: IR spectrum of C_3N_4 synthesized by above method.

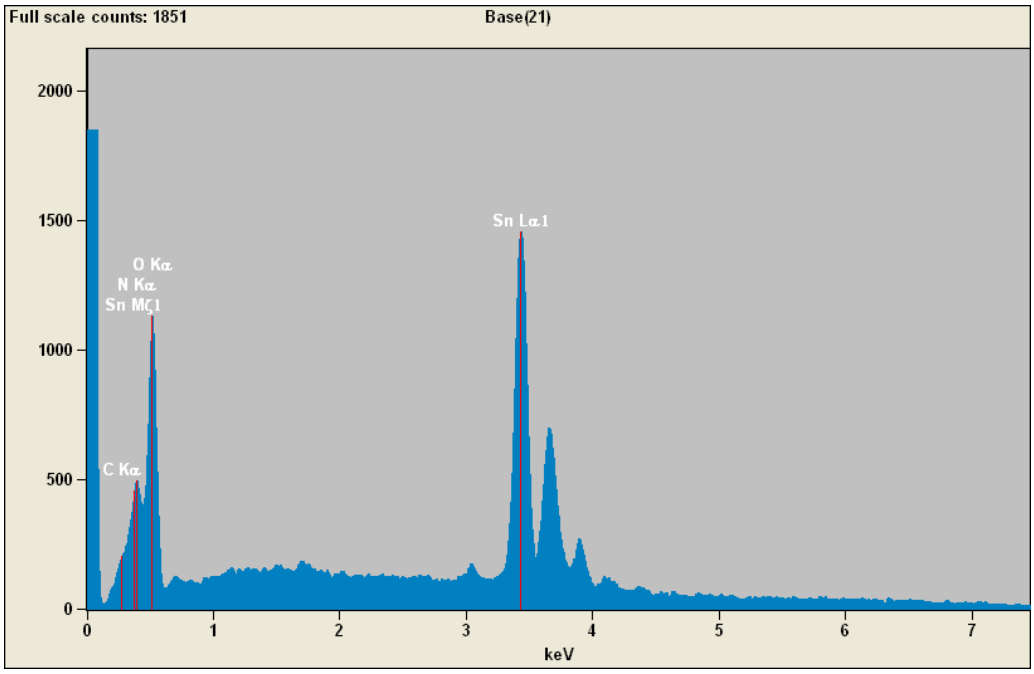

Figure 117: SEM EDX spectrum of C_3N_4(10mg)@mac-FTO electrode.

Element Line	Norm. Wt.%	Atom %
C	3.123	10.121
N	5.068	14.084
O	21.702	52.802
Sn	70.107	22.993
Total	100.00	100.00

Table 12: EDX elemental analysis of C_3N_4(10 mg)@mac-FTO electrode.

The DRUVS reflectance spectrum of C_3N_4@mac-FTO electrodes fabricated with varied amounts (5, 10 and 20 mg) of powder precursor is shown in Figure 118. A red shift (ca. 5 nm) was observed in C_3N_4(5 mg)@mac-FTO electrode, this is because the loading of C_3N_4 (refractive index = 1.6 to 1.8)[243] leads to an increase of n_{ave} (average refractive index of wall and photocatalysts materials), therefore a red shift should occur and according to Equation 9, filling factor φ_p = 1.53 % and 7.79 % was calculated when using 5 mg and 10 mg precursor, respectively. The sample with 20 mg precursor shows no stop band due to the overloading.

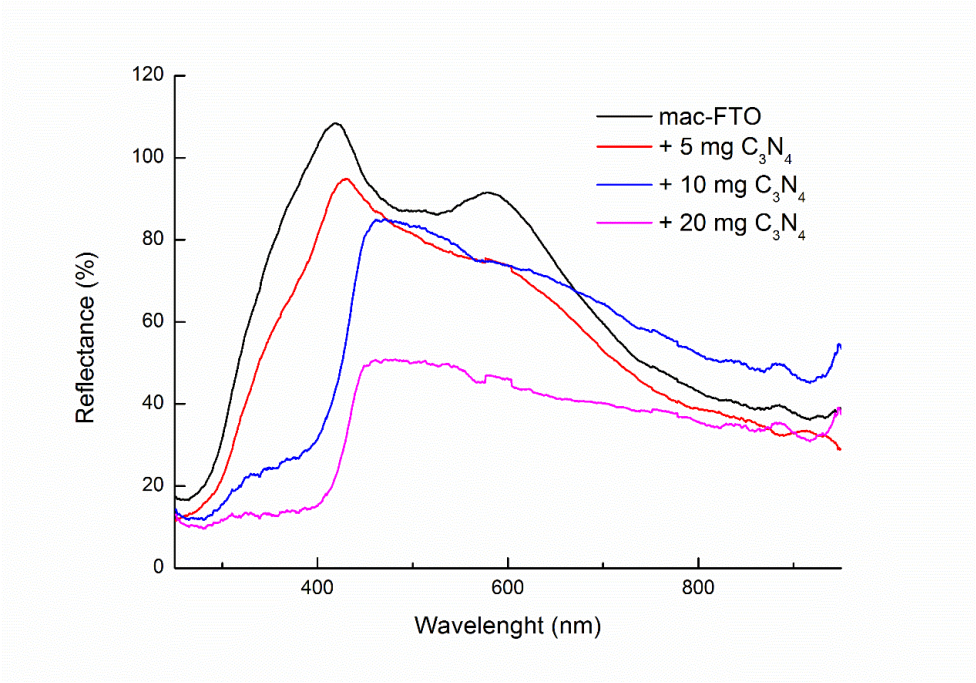

Figure 118: DRUVS spectrum of C_3N_4@mac-FTO electrodes fabricated with varied amount (5, 10 and 20 mg) powder precursor.

In terms of the photoelectrochemistry performance, for the comparison of the C_3N_4@mac-FTO with film or shaped C_3N_4 on planar conductive substrate, the photoelectrochemistry experiments used conditions according to a previous literature report about C_3N_4@planar-FTO.[231] Based on this, the transient photocurrent was measured from C_3N_4@mac-FTO electrodes at 0.4 V vs. Ag/AgCl in 0.2 M Na_2SO_4 under visible light irradiation ($\lambda > 420$ nm). As shown in Figure 119, the C_3N_4(10mg)@mac-FTO electrode present a photocurrent whose photoresponse is quite reversible. There is a degradation of photocurrent density observed which was commonly found from the photoresponse measurement in literature reports. The greatest photocurrent density (ca. 30 μA cm^{-2}) was observed from C_3N_4(10mg)@mac-FTO electrode, the C_3N_4(5 mg)@mac-FTO and C_3N_4 (20mg)@mac-FTO electrode exhibited photocurrent density around 1 μA cm^{-2} and 4 μA cm^{-2}, respectively. Due to the greater surface area and presumably the photonic properties of mac-FTO support, the C_3N_4 (10mg)@mac-FTO electrode in this work

exhibits a higher photocurrent density (ca. 30 μA cm^{-2}) than C_3N_4@planar-FTO electrode (6 μA cm^{-2})[231], C_3N_4 nanoplates (3.1 μA cm^{-2}) and C_3N_4 nanorods (5.9 μA cm^{-2})[244] in previous literature reports under the same photoelectrochemistry conditions.

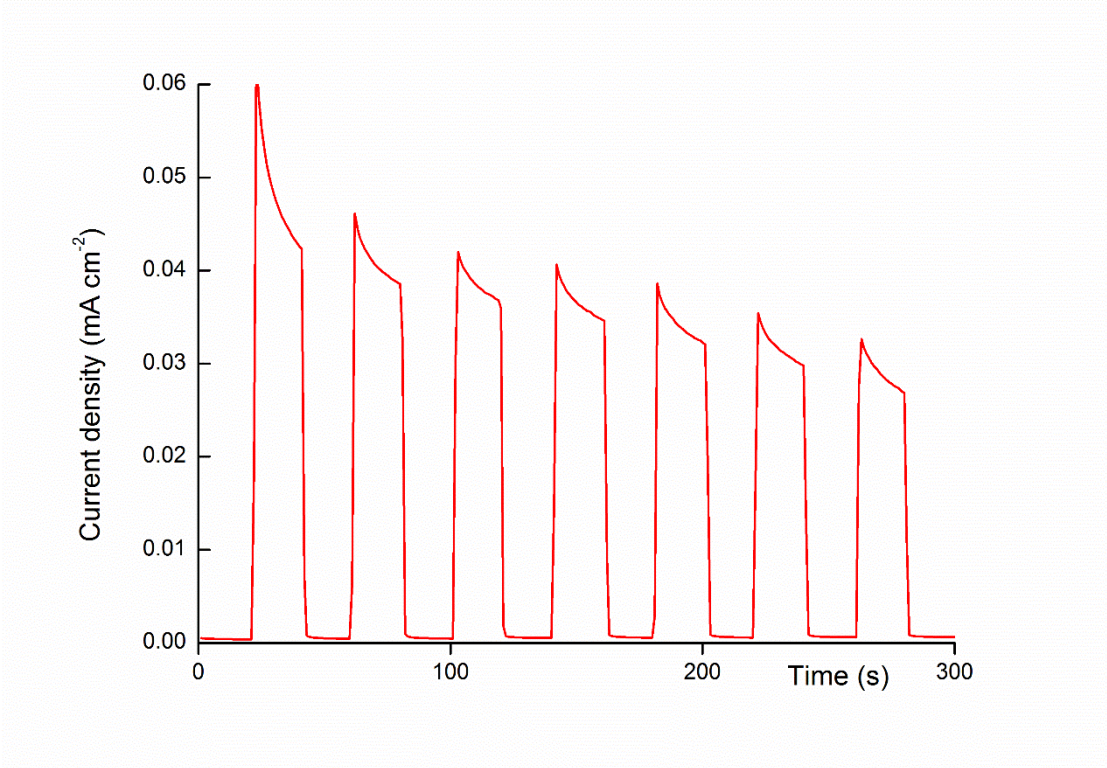

Figure 119: Transient photocurrent generation from C_3N_4 (10mg)@mac-FTO electrode at 0.4 V vs. Ag/AgCl in 0.2 M Na_2SO_4 under visible light (λ > 420 nm).

4.3.2: Synthesis of iron oxide (Fe_2O_3) on mac-FTO film

Spin coating, spray coating and chemical vapour deposition were attempted for the decoration of iron oxide onto mac-FTO electrode. However, only the CVD method exhibited homogeneous decoration. In this method, the iron oxide precursor solution was prepared according to a previous literature report.[235] $FeCl_3$ was dissolved in 10 mL ethanol, the mac-FTO electrodes was set horizontally in 3 mL of the precursor

solution in a glass vial under varied conditions and evaporation at 70 ^{o}C for 3 h gives the best morphology of Fe_2O_3@mac-FTO (Figure 107) after the calcination. The calcination was at 600 ^{o}C and a red electrode was obtained.

As shown in Figure 120 by SEM imaging, the iron oxide nanocrystals were decorated on the skeleton of mac-FTO homogeneously and uniformly. The size of iron oxide nanocrystal is around 60 nm.

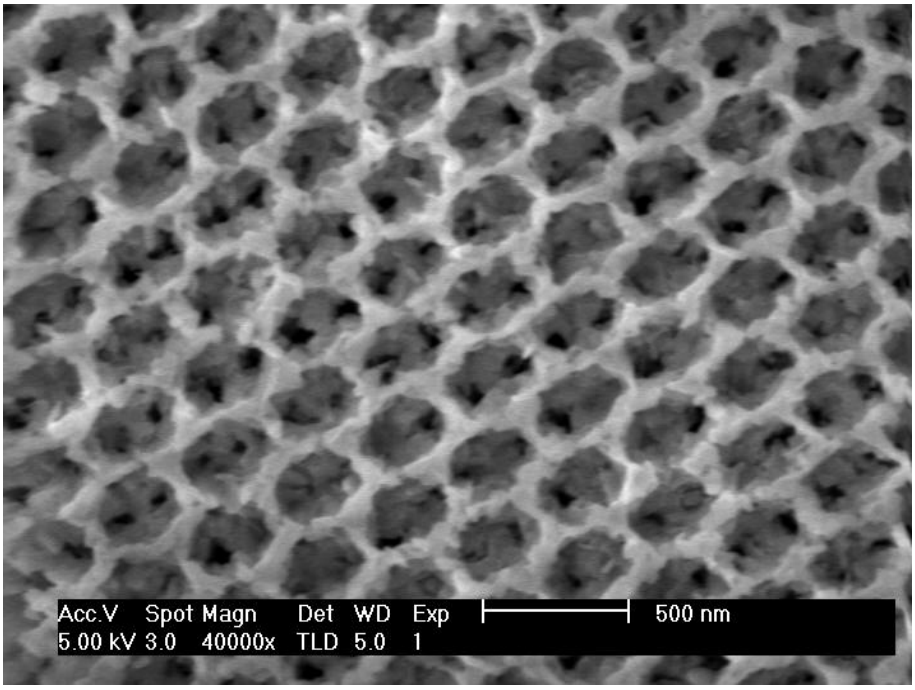

Figure 120: SEM image of Fe_2O_3@mac-FTO electrode by CVD method at 70 ^{o}C for 3 h.

In addition, DRUVS spectra of Fe_2O_3@mac-FTO is shown in Figure 121. A red shift (ca. 45 nm) of stop band position was observed after loading the Fe_2O_3 onto mac-FTO electrode suggesting a φ_d of ca. 7.91 % according to Equation 9.

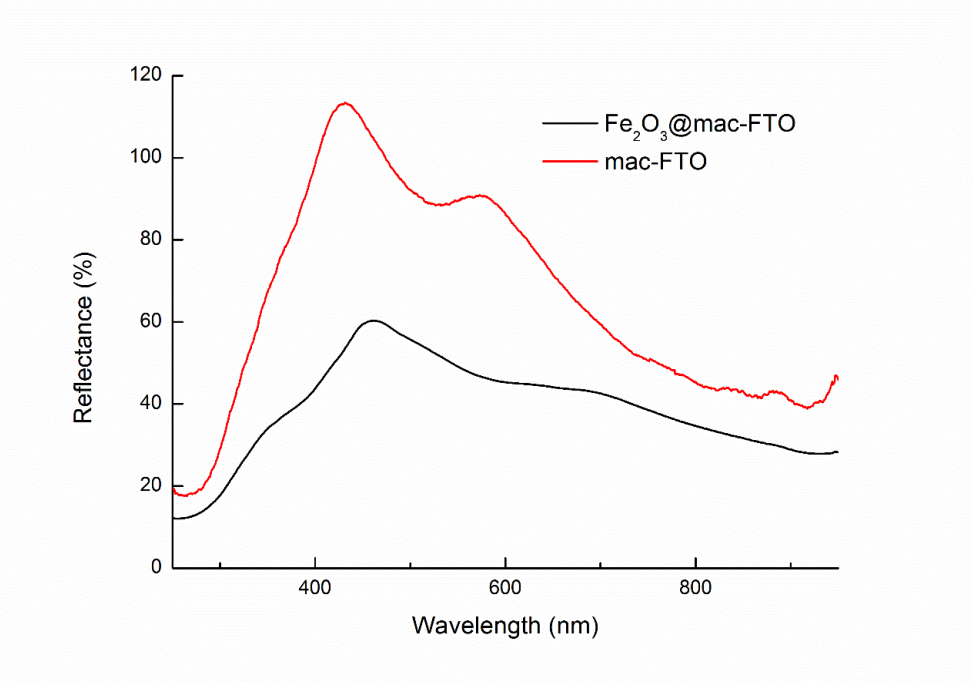

Figure 121: DRUVS spectrum of mac-FTO and Fe_2O_3@mac-FTO electrodes.

Photoelectrochemistry was used to compare the iron oxide on different structured FTO electrodes. Transient photocurrent generation from iron oxide on planar- and mac-FTO electrodes was measured as shown in Figure 122. The mac-FTO electrode exhibit enhancement (0.42 mA cm^{-2}) comparing with the planar FTO (0.07 mA cm^{-2}) when loading iron oxide using the same method. However, using other methods structured Fe_2O_3 anodes on planar FTO can be prepared which gives current density up to ca. 0.7 mA cm^{-2}. [235]

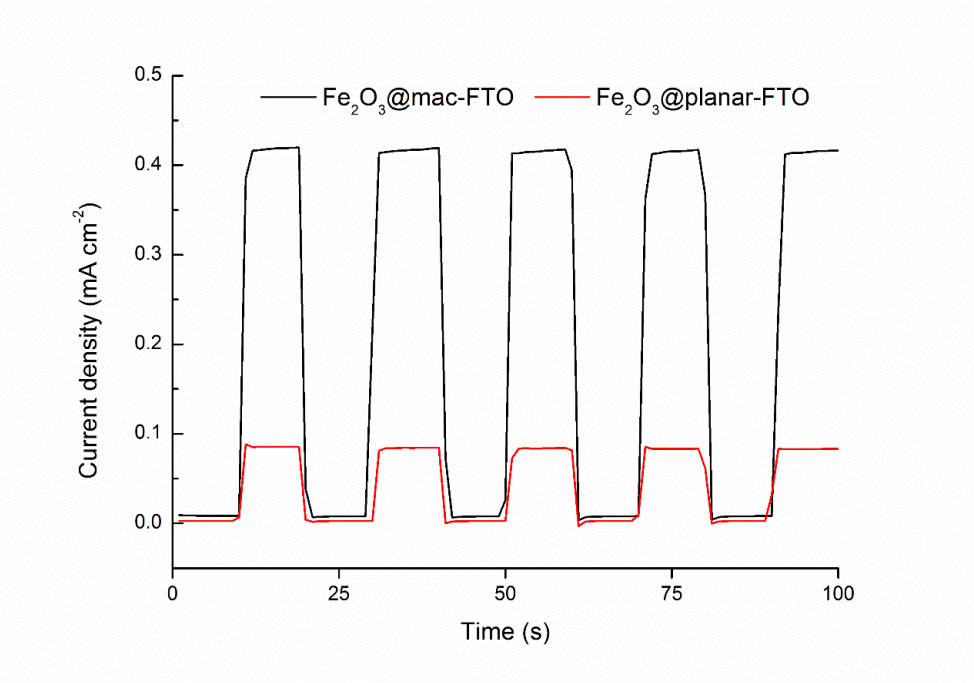

Figure 122: Transient photocurrent generation from Fe_2O_3@mac-FTO and Fe_2O_3@planar-FTO electrodes at 0.2 V vs. Ag/AgCl in 0.1 M NaOH under visible light (λ > 420 nm).

The PXRD patterns of iron oxide decorated mac-FTO and pure mac-FTO electrodes are shown in Figure 123. In both patterns the SnO_2 matching JCPDS file 41-1445 were observed. The Fe_2O_3 matching JCPDS file 01-089-7147 was only observed when the calcination of mac-FTO electrode infiltrated with iron oxide precursor is over 600 ^oC.

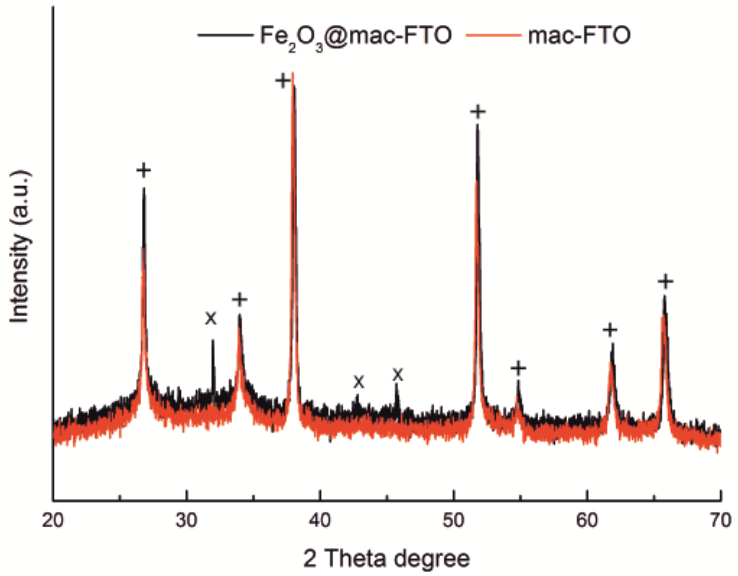

Figure 123: Powder XRD pattern of mac-FTO electrode (red line) and Fe_2O_3@mac-FTO electrode (black line). + = SnO_2, JCPDS 41-1445; x = Fe_2O_3, JCPDS 01-089-7047.

The coverage of Fe_2O_3 is sensitive to the synthesis conditions. For example, when the deposition was conducted at 50 ^oC overnight (in comparison to 70 ^oC for 3 h), sheet-like structures appear on the surface of mac-FTO as shown by SEM in Figure 124. This sample exhibits a lower photocurrent density of 0.27 $mAcm^{-2}$ (compared to 0.42 mA cm^{-2}).

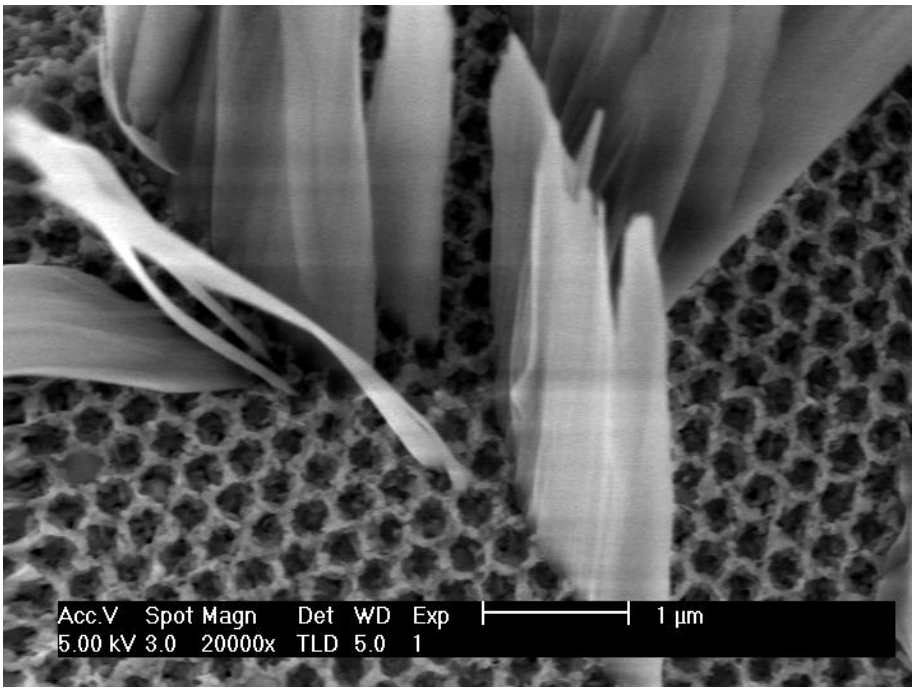

Figure 124: SEM image of Fe_2O_3@mac-FTO electrode using lower evaporation temperature and longer time

4.4: Conclusion

In this chapter, visible light driven photocatalysts C_3N_4 and Fe_2O_3 were synthesized on mac-FTO. By developing the methodology, homogeneously decoration of both the photocatalysts on mac-FTO electrodes was obtained. In addition, the C_3N_4 loading can be easily controlled by adding varied amount of precursor powder on to the mac-FTO electrodes. Photoelectrochemistry shows both C_3N_4@mac-FTO and Fe_2O_3@mac-FTO exhibit photoresponse in the absence of a sacrificial reagent suggesting the mac-FTO electrode can be widely used for supporting photocurrent of various photocatalysts. Furthermore, the C_3N_4@mac-FTO exhibit higher photocurrent density than C_3N_4@planar-FTO electrode introduced in previous literature report suggesting an advantage of mac-FTO in supporting photocurrent. In

the last, the generality of decorated mac-FTO film is extended to non-metal materials, further enhancing its versatility.

In terms of the further work, doped C_3N_4 and Fe_2O_3 are worth trying to improve the photochemistry performance of C_3N_4@mac-FTO and Fe_2O_3@mac-FTO. Because the phosphorus doped C_3N_4[238] and Ti (IV) or Al (III) doped Fe_2O_3[235] have exhibited an enhancement in photocurrent generation on planar FTO when compare with the pure materials. Furthermore, the gas evolution of these composites should also be measured.

4.5: Summary and future direction

The aims of this project were to develop a method to synthesise structured TCO electrodes with high electrical conductivity and optical properties, and investigate their application to support photoelectrochemical applications; specifically to optimize photocurrent per illuminated geometric surface area. For the study of these applications, methods were developed to homogeneously decorate photoactive materials including metal oxide and chalcogenide, and organic semiconductors in structured TCO supports that would optimise light collection and charge carrier extraction. Photoelectrochemical applications have been demonstrated, showing the advantages of utilising structured TCO films to increase the photocurrent per illuminated geometric area under approximately 1 sun. The improved synthesis of mac-FTO and new hs-AZO films was shown to produce homogeneous multiple layered (10 to 15 layers) films with coverage around 80 % and 100 %, respectively. These structured TCO films exhibit high surface area and better quality optical properties when compared with previous reports.

Several methods were investigated for the decoration of the structured TCO films and the SILAR method was demonstrated to produce conformal CdS@mac-FTO electrodes, where the loading of CdS can be easily controlled. The generality of this method was extended to make CdS@hs-AZO electrodes. The optimized decoration of CdS exhibits photocurrent over 9 mA cm^{-2} and 7.5 mA cm^{-2} for CdS@mac-FTO and CdS@hs-AZO, respectively, the highest reported for any comparable photoelectrodes. The photoelectrochemistry and electrochemistry characterizations suggest that the structured TCO films are conductive and do support high photocurrent. By the synthesis of C_3N_4@mac-FTO and Fe_2O_3@mac-FTO, it was proved that mac-FTO films can be decorated with multiple kinds of photocatalysts, even including non-metal materials. Although each material requires a unique synthesis and coating conditions each method is based on simple wet chemistry. This is in contrast to structured photoelectrodes of photoactive materials (e.g. ordered nanorod and nanotube arrays) that require complex fabrication methods and sophisticated apparatus such as atomic layer deposition. For example, C_3N_4@mac-FTO exhibits a photocurrent around 30 μA cm^{-2} which is much higher than various structured C_3N_4 reported in previous works (below 10 μA cm^{-2}).

As a proof of concept, this work represents the first example of improvement of photocurrent generation by using conductive mac-FTO and hs-AZO films, and show enhancement when compared with other structured transparent oxides including SnO_2 and TiO_2. In addition, the successful synthesis of hs-AZO film is the first example of making hollow sphere TCO films, and offers a simple way to fabricate structured AZO film with different morphologies (from macroporous to hollow sphere).

As discussed in the previous chapters, the effect of the photonic stop band overlapping with the absorption edge of the photoactive materials could be investigated as further work. In parallel to the research describe here, Danielle Jowett has investigated the photonic effects of mac-FTO and shown that there is an

angular dependence on photocurrent, however this needs to be investigated for a range of photoactive materials and for hs-AZO. Photoelectrochemistry is often limited by surface catalysis and surface charge recombination. To improve the photocurrent further, the addition of a co-catalyst material to reduce surface e^-/h^+ recombination and increase catalysis could also be investigated. Other photoactive materials include metal nitrides and oxynitrides such as GaN/ZnO and TaON which could be formed using the quartz FTO substrates which can withstand the high temperatures required to synthesise these materials. No previous work has been reported for structured TCO films coated with metal nitrides. In addition, due to the unique structure of hs-AZO film, it is worth trying in the further to enhance the infiltration of nano materials into the shells, and determine if electrochemistry is occurring within the inner volume of the spheres.

Chapter 5: Experimental

5.1: Chemical used

Ammonium fluoride (NH_4F, 98 %), Cadmium oxide (CdO 99.99 %), Cyanamide (CH_2N_2, 99%), Cyanuric acid ($C_3H_3N_3O_3$, 98%), 2,4-diamino-6-phenyl-1,3,5-triazine ($C_9H_9N_5$, 97%), Sulfuric acid (H_2SO_4, ≥95%), Hydrogen peroxide (H_2O_2, 30%), Iron (III) chloride ($FeCl_3$, 97 %), Lithium chloride (LiCl, 99 %), Oleic acid ($C_{18}H_{34}O_2$, 99 %), 1-octadecene (C18H36, 90 %), Potassium chloride (KCl, 99 %), Potassium persulfate ($K_2S_2O_8$, 99 %), Tetraethyl-orthosilicate ($Si(OC_2H_5)_4$, 99 %), Sodium chloride (NaCl, ≥ 99 %), Sodium sulfite (Na_2SO_3, 98 %), Sodium sulfide nonahydrate ($Na_2S{\cdot}9H_2O$, 98 %), Styrene (C_8H_8, 99 %), Sulphur (S, reagent grade), Tetraethyl-orthosilicate ($Si(OC_2H_5)_4$, 99 %) ,Tin (IV) chloride pentahydrate ($SnO_2{\cdot}5H_2O$, 98 %) and Zinc acetate dehydrate ($Zn(CH_3O_2H)_2{\cdot}H_20$, 98%) were purchased from Sigma Aldrich and used as received.

Sheets of fluorine doped tin oxide coated glass were purchased from Sigma Aldrich (7 Ω/sq, 30 x 30 cm), and cut into 1 x 1.5 cm slides. Before use, slides were soaked in piranha solution and then sonicated in acetone to remove surface contaminants.

Holey carbon films on 400 mesh copper grids for mounting TEM samples, and short pin aluminium stubs (0.5 inch) and 12 mm LEIT adhesive carbon tabs for SEM sample preparation were purchased from Agar Scientific.

Where water been mentioned in any synthesis process, it refers to deionized water.

5.2: Techniques

5.2.1 Powder X-ray Diffraction (PXRD)

Wide angle PXRD patterns were recorded on a Bruker-AXS D8 Advance instrument with Lynx eye detector, using Cu Kα radiation (1.54 Å) with a 1 mm slit on the source and 2.5 mm detector slit. Data was collected from 10 – 70 ° 2θ, with 0.02 ° step size and a scan speed of 0.1 seconds per step. As shown in Figure 125, sample slides were set horizontally into a special designed aluminium sample holder which can just fit the size of sample (2×10×15 mm).

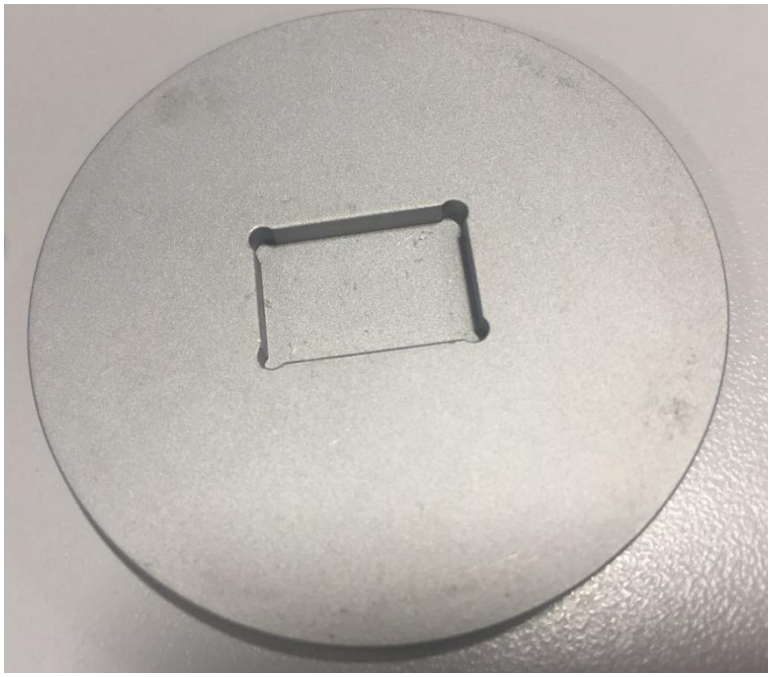

Figure 125: Aluminum holder for PXRD measurement of sample slides.

5.2.2: Scanning Electron Microscopy

SEM images were obtained using an FEI Sirion scanning electron microscope. Prior to imaging, samples were supported on an aluminium stub with an adhesive carbon tab and sputter coated with a 10 nm layer of carbon using an Agar auto carbon coater. For 3DOM materials, the periodicity and wall thicknesses of the structures were analysed by > 20 independent measurements from SEM images.

Energy Dispersive Analysis of X-rays (EDX) was performed using an attached EDAX Phoenix X-ray spectrometer. Scans were recorded at 10 kV accelerating voltage for 1 minute, over regions 50 μm by 35 μm in size. Elemental analyses of samples were averaged over at least 10 of these measurements.

5.2.3: Transmission Electron Microscopy

TEM images and electron diffraction patterns were obtained using a JEOL 2011 transmission electron microscope operated at 200 kV accelerating voltage. Dark field imaging and HAADF STEM imaging/EDX mapping were performed at the University of Leeds on a Tecnai TF20 FEGTEM operated at 200 kV**.** CCD images were extracted using Gatan Digital Micrograph software. Particle size distributions of nanoparticles were evaluated by averaging the diameter of >100 particles from TEM images.

Prior to analysis, solid samples for TEM imaging were ground in methanol and sonicated for 15 minutes to disperse. One drop of the dispersion was deposited onto 3 mm holey carbon coated copper grids and allowed to dry in air. FTO film samples were scraped off the slide, then ground in methanol/sonicated as above. For ligand stabilised nanoparticle dispersions in organic solvents, TEM samples were prepared by evaporation of a single drop of diluted solution onto a holey carbon copper grid.

5.2.4: UV-vis absorption, transmission and reflection spectroscopy

UV-Visible absorption, transmission and reflectance spectra were recorded on an Ocean Optics HR2000+ High Resolution Spectrometer with DH-2000-BAL Deuterium/Helium light source (200 – 1100 nm). An R400-7-UV-Vis reflection probe was used to record diffuse reflectance spectra. Powder samples were deposited as a flat layer between two pyrex or quartz slides and placed beneath the reflection probe. Spectra were recorded using Spectra Suite software from an average of 10 scans, an integration time of 20 seconds and box car smoothing width of 20 nm. Solution UV-Visible absorption spectra were recorded with the same light source, in quartz cuvettes using a solution cell.

5.2.5: Infra-Red spectroscopy

Attenuated total reflectance infra-red spectra were recorded on a Perkin Elmer Spectrum Two FT-IR spectrometer with UATR single reflection diamond accessory. Powdered materials were deposited on the diamond surface. The

pressure arm was tightened onto the sample until the force gauge displayed 100 N.

5.2.6: Solid state Nuclear Magnetic Resonance (SSNMR)

^{19}F spectra were acquired using a rotor synchronised (v_{rot} = 10 kHz, one rotor-period) Hahn-echo experiment, using 90- and 180-degree pulse lengths of 2.5 and 5 μs, respectively. PEEK (polyether ether ketone) inserts were utilized to centre the sample within the rotor, ensuring the whole of the sample was within the active region of the detection coil. All ^{19}F chemical shifts are reported relative to $CFCl_3$ and were referenced using solid sodium fluoride (δ_{iso} = -104.2 ppm) as an external secondary reference.

Calcium fluoride dilute with sodium chloride was used as a calibrant (fluorine content 6.9 x 10^{-7} to 3.2 x 10^{-5} moles), and required 16-200 co-added scans, with a 300 s delay between scans to avoid saturation, to generate spectra. FTO samples required 160-320 co-added scans, with a 20 s pulse delay.

Hahn-echo experiments with inter-pulse delays of one to seven rotor periods (total evolution times of 200 to 1400 μs) were acquired to determine the spin-spin relaxation time constant T_2 of calcium fluoride and one sample of FTO in order to correct for signal intensity loss during the Hahn-echo evolution periods. It is assumed that the T_2 is very similar for all FTO samples.

The quality factor (Q) of the impendence-matched probe circuitry was measured using a Wavetek Benchmark 1150 spectrum analyser for all samples as a measure of the intrinsic sensibility of the probe in order to calculate the necessary 90 and 180-degree pulses for each sample and correct measured absolute integrals in analogy to the PULCON method.[245]

5.2.7: IPCE measurements

IPCE measurements were done in a quartz cell with a reference electrode of Ag/AgCl (3 M NaCl) and a counter electrode of Pt wire (20 mm long by 0.25 mm diameter). Samples were illuminated with monochromated light with a slit width of 20 nm. The lamp power was measured using an International Light Technologies 1400-A Radiometer Photometer. The cell window was as close to the sample as feasible possible to ensure as little light scattering as possible.

5.3: Synthetic methods

5.3.1: Coating of planar FTO film on transparent substrate

The following procedure was used to clean the glass before the coating of FTO film.

The glass slide (2 x 10 x 15 mm) was soaked in a beaker containing tap water (100 mL) and sonicated for 30 min and then transferred to DI water (100 mL) and

sonicated for a further 30 min. Then the slide was dried under a flow of nitrogen at room temperature. The slide was then soaked for 2 h in a mixture (100 mL) of sulfuric acid (≥95 %) and hydrogen peroxide (30 %) of volume ratio 3:1 before washed with ethanol and finally dried under a flow of nitrogen. The slides were used immediately after cleaning.

An FTO precursor solution was prepared according to a modified literature method.[133] $SnCl_4 \cdot 5H_2O$ (1.4 g, 4 mmol)) was sonicated in ethanol (40 mL ,0.4M) until dissolved and then saturated (45 g in 100 mL under standard conditions) NH_4F aqueous solution (0.12 to 0.72 g, 0.1 to 0.6 mmol), was added, and the resulting mixture was sonicated about 1 h until optically clear and a colourless solution was achieved.[133]

Three methods were attempted to achieve highly conductive FTO film with relatively high transmittance, and the precursors being used in all these three methods were prepared as mentioned above.

Drop coating:

50 uL of FTO precursor solution was simply spread onto the glass slide repetitively (2, 5 and 10 drops). The drop of precursor solution spread naturally and the next drop was added onto the substrate after the solution evaporated in the fume hood. The sample was then transferred to a furnace and heated to 450 ^oC with a heat ramp of 1 $^oC\ min^{-1}$ and held for 2 h.

Spin coating:

Different amounts of FTO precursor solution (500 uL, 250 uL and 100 uL) was put onto the microscopic slide using a Gilson pipette and the spin coater was set at

3300 rpm. The coated film was obtained after a few seconds and then heated to 450 ^{o}C with a heat ramp rate of 1 ^{o}C min^{-1} and held for 2 h, transparent products with pale yellow colour were obtained after the heat treatment.

Spray pyrolysis:

Air brush: The glass or quartz slide was put on a hotplate heated to 510 ^{o}C for 15 min to get a stable surface temperature before coating. The surface temperature of the slide top was 430 ^{o}C measured by a thermocouple. The airbrush was filled with 3 mL of FTO precursor solution with various F/Sn atomic ratio (0.25 to 1.5) and the distance between the air brush and the target is 13 cm. The hot transparent slide was sprayed every 10 seconds and was sprayed 5 seconds each time to retain the surface temperature at 430 ^{o}C. The precursor solution was boiled and evaporated immediately when in contact with the hot transparent slide. This procedure was repeated for several time until all the 3 mL FTO precursor was used up. The hotplate was then turned off until the slide cooled down to room temperature. After cool, the slide was transferred to a furnace of for heat treatment at 450 to 850 ^{o}C for 2 h with a heat ramp rate of 1 ^{o}C min^{-1}.

Aerosol Assisted Deposition (AAD): The glass or quartz slide on a hotplate at 510 ^{o}C was heated for 15 min to obtain a stable surface temperature of 430 ^{o}C, which was measured by a thermocouple. The FTO precursor solution (5 mL) with various F/Sn atomic ratio (0.25 to 1.5) was placed in a nebulizer. The aerosol was delivered to the heated slide via a flexible plastic pipe (2 cm of diameter, 35 cm of length) which was held in place by a home-made raster (Figure 126). The distance between the pipe and transparent slide was adjusted to 13 cm to obtain the best coating. An aerosol of FTO precursor was vaporised on the heated slide giving an increasingly shiny surface. The coating process was run for 5 to 13 min to optimize the transmittance and the conductivity of the coated film. The spray operation was

temporarily stopped and resumed after the surface temperature of the glass substrate returned to 430 ^{o}C. The average interval between the spray was around 10 s. The hotplate was then turned off until the slide cooled down to room temperature. After cool, the slide was transferred to a furnace of for heat treatment at 450 to 850 ^{o}C for 2 h with a heat ramp rate of 1 ^{o}C min^{-1}.

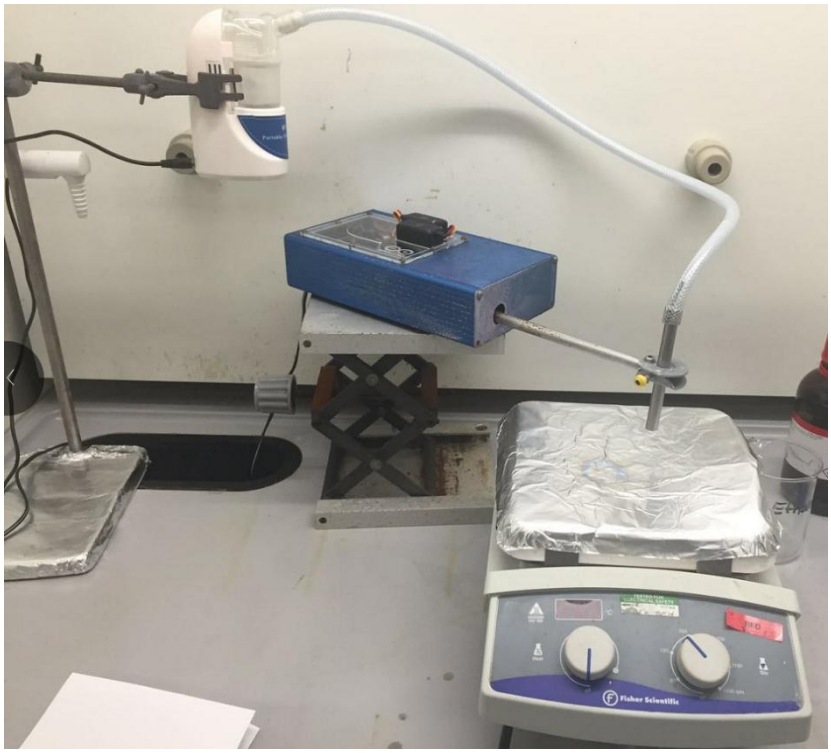

Figure 126: Setup of aerosol assisted deposition for synthesis of planar FTO films.

5.3.2: Synthesis of polystyrene spheres

Polystyrene spheres of diameter 450 ± 10 nm was synthesized through emulsifier free emulsion polymerization using a reported method.[124] As shown in Figure 127, a three necked round bottom flask (2L) was connected with reflux condenser, overhead motorised stirrer, temperature controller (this neck was also being used

for addition of reagents). Before the reaction, styrene (140 mL, 1.218 mol) was washed for 4 times with NaOH (0.1 M, 140 mL) and another 4 times with water (140 mL) in a new funnel to get rid of inhibitors. Inhibitor free styrene (129 mL, 1.122 mol) was obtained after washing, the weight loss is due to the removal of inhibitor. $K_2S_2O_8$ (0.442 g, 1.635 mmol) was dissolved in 66 mL water with sonication for 20 min for further use in this reaction. 1133 mL of water was put into the round flask and it was heated to 70 ^oC with a constant stir speed at 245 rpm under flowing nitrogen gas. The inhibitor free styrene was then added into the flask and the $K_2S_2O_8$ solution was added into this mixture after 30 min.

This reaction was allowed to proceed for 28 h until milky colloid dispersion was achieved. The polymer dispersion was cooled down to room temperature, and then filtered by glass wool to get rid of the polymer agglomerates.

Polystyrene spheres of diameter from 300 to 600 nm were synthesised through a modified method by Robert Mitchell.[246] The temperature and constant stir speed were controlled to achieve the polystyrene spheres of certain diameter. The polystyrene sphere of diameter of 350 nm being used in this thesis was a stock dispersion made by Robert Mitchell.

Figure 127: The setup for the synthesis of polystyrene sphere.

5.3.3: Fabrication of porous FTO powder

The polystyrene sphere dispersion was centrifuged for 2 h, 4000 rpm, and the supernatant fluid decanted to leave a white solid of polystyrene spheres. The polystyrene spheres were transferred to an oven at 60 ^{o}C overnight until a white brittle solid was obtained. Around 4 g of PS sphere was achieved from 50 m L colloid dispersion after drying.

Based on a reported method,[247,248] 1 g of the dry polystyrene spheres were grounded using mortar to a fine white powder, the powder was then put into a glass sinter funnel (porosity 3, 16-40 μm) with a piece of filter paper on. This powder was soaked with ethanol for 30 min and then dried under vacuum on the sinter.

Similar to the FTO precursor solution prepared for the synthesis of planar FTO films, the more concentrated FTO precursor solution was prepared from $SnCl_4 \cdot 5H_2O$ (1.4 g, 4 mmol)) sonicated in ethanol (20 mL, 0.2M) until dissolved and then saturated (45 g in 100 mL under standard conditions) NH_4F solution (0.12 to 0.72 g, 1 to 6 mmol) was added to give various F/Sn atomic ratios (0.25 to 1.5), and the result mixture was sonicated about 1 h until optically clear and colourless solution was achieved. 5 mL of FTO precursor was added to the 1 g of polystyrene powder, the impregnation was achieved after soaking overnight. The sample was then heated to 450 ^oC for 2 h with a ramp rate of $1^oC\ min^{-1}$ to remove polystyrene sphere template. About 70 mg opalescent porous FTO powder was obtained.

5.3.4: Deposition of highly ordered polystyrene film on FTO glass

Highly ordered polystyrene sphere films were deposited on FTO coated substrate (glass or quartz) by an original method. The FTO substrate slide (2 x 10 x 15 mm) was soaked in tap water (100 mL) and sonicated for 30 min and then transferred to DI water (100 mL) and sonicated for a further 30 min. Then the slide was dried under a flow of nitrogen at room temperature. The slide was then soaked for 2 h in 100 mL Piranha solution (a mixture of sulfuric acid and hydrogen peroxide in a volume ratio 3:1) before washing with acetone and finally dried under a flow of nitrogen ready for use.

The solvent for preparing polystyrene suspension is a mixture of water and ethanol (8:82 volume ratio), 1, 1.2 and 2.0 mL of stock polystyrene spheres (350 or 450 nm of diameter, synthesized as described in section 5.3.2) was add into 90 mL of the mixture of water/ethanol solvent. This suspension was used for deposition of highly order PS film immediately after sonication for 1 h. The Piranha treated FTO slide was stood vertically against the wall in a 5 mL glass vial, and polystyrene sphere suspension (3.5 mL) was added just above the top of the vertical slide. The solvent was evaporated at a temperature from 40 to 70^{o}C over 8 h to 3 days in a furnace oven. The best sample was obtained by evaporation at 60 ^{o}C for 15 h with PS suspension of 1.2 mL stock PS in 90 mL water/ethanol solvent. The slide was removed until around 5 mm height of polystyrene suspension remained. It is worth noting that the deposition of PS film is very sensitive to the volume of oven. In this work, serval ovens were employed for the evaporation process, only the furnace oven (15 x 18 x 25 cm) which has smallest volume gave highly quality PS films. The FTO slide (10 x 15 mm) with 10 x 10 mm opalescent, uniform polystyrene film was removed by a pair of tweezers, and an area (5 x 10 mm) was cleaned carefully by acetone for electrical contact. Under these conditions, highly ordered close packed polystyrene film of 8 to 10 μm in thickness (corresponding to 15 to 20 layers of polystyrene spheres) were achieved.

5.3.5: Synthesis of mac-FTO film from PS template film

Similar to the FTO precursor solution prepared for the synthesis of porous FTO powder, the FTO precursor solution was prepared from $SnCl_4 \cdot 5H_2O$ (1.4 g, 4 mmol)) sonicated in ethanol (20 mL, 0.2M) until dissolved and then saturated (45 g in 100 mL under standard conditions) NH_4F solution (0.12 to 0.72 g, 1 to 6 mmol) was added to give various F/Sn atomic ratios (0.25 to 1.5), and the result mixture was sonicated about 1 h until optically clear and colourless solution was achieved. The

FTO precursor solution was used immediately after preparation to avoid formation of particles from oxidized $SnCl_4$ blocking infiltration of precursor. For all the experiments in this section, the FTO precursor solution with various F/Sn atomic ratio (0.25 to1.5) was attempted.

Dropwise infiltration:

The PS template film was set horizontally, and a total amount of FTO precursor solution (50, 100 and 150 µL) was homogeneously spread on the PS photonic template films. 50 µL of FTO precursor solution infiltrated the PS photonic films through the voids among polystyrene sphere by capillary force. The FTO infiltrated samples were then dried at room temperature for 10 min, and the films were then heat to 100 ^{o}C to remove any residual solvent. This process was repeated for 1 or 2 more times intend to obtain a sufficient filling of the voids by FTO precursor. The resulting samples were then heated to 450 ^{o}C. This heating program is optimised from a heating temperature from 350 to 550 ^{o}C.

Modified Soaking infiltration:

A PS template film was pre-soaked in ethanol for 30 min horizontally before being stood vertically and submerged in the FTO precursor solution (3.5 mL) in a glass vial for another 30 min in a vacuum desiccator, in this period a partial vacuum was applied or not applied. The wet slide was removed from the glass vial and fresh stock FTO precursor solution (0, 20 µL and 40 µL) was carefully dropped onto the wet film with a Gilson pipette. The FTO infiltrated slides were then transferred to a furnace oven immediately for calcination at 450 ^{o}C for 2 h with a heat ramp of 1 ^{o}C min^{-1} under air. An opalescence slide sample was obtained after the calcination. Using the FTO precursor solution (F/Sn atomic ratio = 0.5), the best mac-FTO film was obtained by vacuum infiltration with 20 µL refilled. For the thermal stability study,

the obtained mac-FTO film was then heated to 550 to 850 ^{o}C for 2 h with a heat ramp of 1 ^{o}C min^{-1} under air.

5.3.6: Synthesis of hs-AZO film from PS template film

Hs-AZO film was synthesised using a similar method for the synthesis of mac-FTO film. For preparing the AZO precursor solution, $Zn(Ac)_2{\cdot}2H_2O$ (2 g, 9.1 mmol) was first dissolved in methanol (40 mL) and sonicated around 15 min until a clear solution was achieved. To this solution $AlCl_3$ (6 to 12 mg, 0.045 to 0.09 mmol) was then added and the solution sonicated for 1 h, AZO precursor solution with Al content from ca. 0.5 to 1.0 at. % was obtained. The precursor solution was used immediately.

PS template film was pre-soaked in methanol for 30 min before being stood vertically and submerged in the AZO precursor solution (3.5 mL) in a glass vial and stored in a desiccator with a partial vacuum being applied for 0.5 to 1.5 h. The soaked PS film was removed from the glass vial and then calcined immediately at 450 ^{o}C for 2 h with a heat ramp rate of 1 ^{o}C min^{-1} under air. The best hs-AZO film was obtained when soaking the PS template film in AZO precursor solution (0.67 at. % of Al) for 1 h under partial vacuum.

5.3.7: Synthesis of nan-CdS

The synthesis of CdS nanoparticles was based on a literature method.[249] CdO (12.80 mg, 0.1 mmol) and oleic acid (0.847 g, 3 mmol) were added to 1-octadecene (3.1398 g, 12.4 mmol) and heated to 300 ˚C. Sulfur (1.69 mg, 0.52 mmol) suspended in octadecene (2.0 g, 7.9 mmol) was then added to the hot mixture and held for 5 mins. To quench the reaction, the solution was cooled in an ice bath to 20

^{o}C. When cool, toluene (4 mL) was added and the solution made up to 50 mL with ethanol giving a brown precipitate. This suspension was centrifuged at 4400 rpm for 30 mins before being decanted and washed twice more with ethanol (40 mL) to give 26.7 mg of a yellow-orange powder. The nanoparticles were dissolved in toluene (ca. 50 mL) to give an absorbance of 1.0 (10 mm path length) at the absorption maximum centred at ca. 500 nm.

5.3.8: Decoration of nan-CdS on mac-FTO film

The nan-CdS dispersed in toluene which give an absorbance of 1.0 (10 mm path length) with the absorption maximum centred at ca. 500 nm was used as a standard dispersion solution (as concentration of 1.0). The standard nan-CdS dispersion (3 mL) was diluted by 9, 3 and 1 mL toluene to give nan-CdS dispersion of concentration of 0.25, 0.5 and 0.75, respectively. Varied concentrations of the nan-CdS dispersion solution was employed for the decoration of mac-FTO electrodes to study the CdS loading dependency of mac-FTO electrodes.

The mac-FTO electrode (15 $\times$ 10 $\times$ 2 mm) were initially treated (or not) by soaking in a hexane solution of oleic acid for 30 minutes before being transferred to and set horizontally in a glass vial (5 mL) in oil bath at 65 ^{o}C. The nan-CdS dispersion in toluene (4 mL) was then added into the glass vial and the mac-FTO electrode submerged for 90 min. The mac-FTO electrode was transferred to a furnace oven for a heat treatment at 450 ^{o}C for 2 h with a heat ramp rate of 2 ^{o}C min^{-1} to remove the ligands and improve the interface between the CdS nanoparticles and mac-FTO. The mac-FTO pre-treated with OA exhibit a yellow colour after the calcination. No obvious colour change was observed from the sample without OA pre-treatment.

5.3.9: Decoration of CdS on mac-FTO film by SILAR method

According to a literature report,[102] a modified SILAR method was used for the decoration of CdS on mac-FTO film. In a glass vial a mac-FTO electrode was stood vertically in a solution of 3 mL $Cd(Ac)_2$ in ethanol (50 mM) for 1 min, and then dried under a stream of N_2. The electrode was then stood vertically in a second glass vial containing 3 mL aqueous Na_2S solution (50 mM) for 1 min, rinsed with distilled water and dried under a stream of N_2. This cycle was repeated from 1 to 10 times. The electrode was finally heated under argon at 400 ^oC held for 30 min using a ramp rate of 1 $^oC\ min^{-1}$ and the obtained CdS(n)@mac-FTO electrodes exhibit an orange-yellow colour. Using 8 dipping cycles, the best sample was obtained.

5.3.10: Decoration of CdS on hs-AZO film by SILAR method

In a glass vial a hs-AZO electrode was stood vertically in a solution of 3 mL $Cd(Ac)_2$ in ethanol (50 mM) for 1 min, and then dried under a stream of N_2. The electrode was then stood vertically in a second glass vial containing 3 mL aqueous Na_2S solution (50 mM) for 1 min, rinsed with distilled water and dried under a stream of N_2. This dipping cycle was repeated from 3 to 7 times. The electrode was finally heated under argon at 400 ^oC held for 30 min using a ramp rate of 1 $^oC\ min^{-1}$. The obtained CdS(n)@hs-AZO electrodes exhibit an orange-yellow colour. Using 5 dipping cycles, the best sample was obtained.

5.3.11: Decoration of C_3N_4 on mac-FTO film

Three methods were used for the synthesis of C_3N_4@mac-FTO film.

- A modified literature method was used.[224] Melamine was mixed with a eutectic salt (LiCl : KCl : NaCl = 0.7:1:1 weight ratio) in a 1:15 by weight ratio. The mixture was finely ground in a mortar. The resulting mixture (2 g) was then transferred into an alumina boat, after that, mac-FTO electrode was immersed into the mixture and heated to 500 ^{o}C for 1 h with a heat ramp rate of 1 ^{o}C min^{-1} under air. After it was cooled to room temperature, a yellow electrode was obtained. The yellow electrode was rinsed with deionized water for 2 times to get rid of the poorly attached material and salts.

- According to a literature report,[239] cyanamide (0.3 g, 7.1 mmol) was dissolved in 0.01 M HCl (4 g) and ethanol (4 g) and the pH was adjusted to 2 with 1 M HCl. The mixture was stirred for 30 min, 200 uL of the solution was then added to the top of mac-FTO electrode and calcined at 500 ^{o}C for 1 h with a heat ramp rate of 1 ^{o}C min^{-1} under argon. By eye, the obtained electrode appears no obvious colour, like bare planar FTO.

- A liquid-based growth of carbon nitride layers[240] was modified for the synthesis of C_3N_4@mac-FTO electrode. Cyanuric acid (0.65 g, 0.05 mol) was mixed with 2,4-diamino-6-phenyl-1,3,4-trizanie (0.95 g, 0.05 mol) and the powder mixture was transferred into 10 mL DI water with shaking, and dried at 60 ^{o}C overnight. Various amounts (5, 10 and 20 mg) of the powder mixture precursor were put evenly onto mac-FTO electrodes. The mac-FTO electrodes with powder precursor was set horizontally in a crucible totally covered with aluminium foil

and heated to 550 ^{o}C for 4 h with a heat ramp rate of 2 ^{o}C min^{-1} under argon. After cooling, yellow-brown electrode were obtained.

The best C_3N_4@mac-FTO sample was obtained using liquid-based growth with 10 mg loading of powder mixture precursor.

5.3.12: Decoration of Fe_2O_3 on mac-FTO film

Fe_2O_3 precursor solution was prepared according to a previous literature report,[235] $FeCl_3$ (0.162 g, 1 mmol) was dissolved in 10 mL ethanol, the mac-FTO electrodes was set horizontally in 3 mL of the precursor solution in a glass vial in oil bath under evaporation at 50 to 70 ^{o}C for 1 h to overnight. The calcination was at 600 ^{o}C for 2 h with a heat ramp rate of 2 ^{o}C min^{-1} and a red electrode was obtained. Conditions of evaporation at 70 ^{o}C for 3 h give the best morphology of Fe_2O_3@mac-FTO film.

Abbreviations

3DOM ─ Three Dimensional Ordered Macroporous

AAD ─ Aerosol Assisted Chemical Vapour Deposition

Ac ─ Acetate

ALD ─ Atomic Layer Deposition

ATO ─ Antimony Doped Tin Oxide

AZO ─ Aluminium Doped Tin Oxide

CB ─ Conduction Band

CCP ─ Cubic Close Packed

CdS(n)@hs-AZO ─ hs-AZO film decorated with CdS by SILAR method with n dipping cycles

CdS(n)@mac-FTO ─ mac-FTO film decorated with CdS by SILAR method with n dipping cycles

CV ─ Cyclic Voltammetry

CVD ─ Chemical Vapour Deposition

DRUVS ─ Diffuse Reflectance UV-Visible Spectroscopy

DSSC ─ Dye Sensitive Solar Cell

EDX ─ Energy Dispersive X-ray Analysis

FCC ─ Face Centred Cubic

FTO ─ Fluorine Doped Tin Oxide

HS ─ Hollow Sphere

IO ─ Inverse Opal

IPCE ─ Incident Photon to Current Conversion Efficiency

IQE ─ Internal Quantum Efficiency

IR ─ Infra Red

ITO ─ Indium Doped Tin Oxide

IPCC ─ Intergovernmental Panel on Climate Change

Macroporous ─ > 50 nm

Mesoporous ─ 2 to 50 nm

Microporous ─ < 2 nm

Nan-CdS ─ CdS nanoparticles

Nan-CdS@mac-FTO ─ mac-FTO decorated with CdS nanoparticles

NHE ─ Normal Hydrogen Electrode

NP ─ Nanoparticles

OA ─ Oleic Acid

P25 ─ 80 : 20 mixture of Anatase : Rutile TiO_2

PC ─ Photonic Crystal

PEC ─ Photoelectrochemistry

PMMA ─ Poly (methyl methacrylate)

PS ─ Polystyrene

PXRD ─ Powder X-ray Diffraction

QD ─ Quantum Dot

QE ─ Quantum Efficiency

QY ─ Quantum Yield

RHE ─ Reversible Hydrogen Electrode

SEM ─ Scanning Electron Microscopy

SILAR ─ Successive Ionic Layer Adsorption and Reaction

SPR ─ Surface Plasmon Resonance

SSNMR ─ Solid State Nuclear Magnetic Resonance

TCO ─ Transparent Conductive Oxide

TEM ─ Transmission Electron Microscopy

UV ─ Ultraviolet Light

UV-vis ─ Ultraviolet and Visible light

VB ─ Valence Band

List of references

(1) Linsebigler, A. L.; Lu, G. Q.; Yates, J. T. *Chem. Rev.* **1995**, *95*, 735.

(2) Liang, Y.; Li, Y.; Wang, H.; Zhou, J.; Wang, J.; Regier, T.; Dai, H. *Nat Mater* **2011**, *10*, 780.

(3) Robel, I.; Subramanian, V.; Kuno, M.; Kamat, P. V. *J. Am. Chem. Soc.* **2006**, *128*, 2385.

(4) Tian, Y.; Tatsuma, T. *J. Am. Chem. Soc.* **2005**, *127*, 7632.

(5) Zhong, D. K.; Cornuz, M.; Sivula, K.; Grätzel, M.; Gamelin, D. R. *Energy. Environ. Sci.* **2011**, *4*, 1759.

(6) Hasanzadeh, M.; Bahrami, A.; Alizadeh, M.; Shadjou, N. *RSC Adv.* **2013**, *3*, 24237.

(7) Blankenship, R. E.; Tiede, D. M.; Barber, J.; Brudvig, G. W.; Fleming, G.; Ghirardi, M.; Gunner, M. R.; Junge, W.; Kramer, D. M.; Melis, A.; Moore, T. A.; Moser, C. C.; Nocera, D. G.; Nozik, A. J.; Ort, D. R.; Parson, W. W.; Prince, R. C.; Sayre, R. T. *Science* **2011**, *332*, 805.

(8) Roy, S. C.; Varghese, O. K.; Paulose, M.; Grimes, C. A. *ACS nano* **2010**, *4*, 1259.

(9) Energy, U. S. D. o. *Energy Information Administration* **2008**.

(10) Izumi, Y. *Coord. Chem. Rev.* **2013**, *257*, 171.

(11) Fujishima, A. H., K *Nature* **1972**, *238*, 37.

(12) Kudo, A.; Miseki, Y. *Chem. Soc. Rev.* **2009**, *38*, 253.

(13) Maeda, K. *J. Photoch. Photobio. C* **2011**, *12*, 237.

(14) Tsuji, I.; Kato, H.; Kudo, A. *Angew. Chem.* **2005**, *117*, 3631.

(15) Sayama, K.; Arakawa, H. *J. Phys. Chem.* **1993**, *97*, 531.

(16) Yui, T.; Kan, A.; Saitoh, C.; Koike, K.; Ibusuki, T.; Ishitani, O. *ACS Appl Mater Interfaces* **2011**, *3*, 2594.

(17) Irie, H.; Miura, S.; Kamiya, K.; Hashimoto, K. *Chem. Phys. Lett.* **2008**, *457*, 202.

(18) Zhao, Z.; Fan, J.; Xie, M.; Wang, Z. *J. Clean. Prod.* **2009**, *17*, 1025.

(19) Kisch, H. *Angew. Chem. Int. Ed. Engl.* **2013**, *52*, 812.

(20) Fu, Q. *Radiation (solar)*; Academic Press, 2003.

(21) Gueymard, C. A. *Solar Energy* **2001**, *71*, 325.

(22) Shimodaira, Y.; Kato, H.; Kobayashi, H.; Kudo, A. *J. Phys. Chem. B* **2006**, *110*, 17790.

(23) Yao, W.; Ye, J. *Chem. Phys. Lett.* **2008**, *450*, 370.

(24) Kato, H.; Kudo, A. *J. Phys. Chem. B* **2002**, *106*, 5029.

(25) Niishiro, R.; Kato, H.; Kudo, A. *PCCP* **2005**, *7*, 2241.

(26) Qin, H.-L.; Gu, G.-B.; Liu, S. *Mater. Chem. Phys.* **2008**, *112*, 346.

(27) Serpone, N.; Pelizzetti, E. *Wiley, New York* **1989**.

(28) Jeon, K.; Youn, H.; Kim, S.; Shin, S.; Yang, M. *Nanoscale Res Lett* **2012**, *7*, 253.

(29) Wu, Y.; Ceder, G. *J. Phys. Chem. C* **2013**, *117*, 24710.

(30) Kato, H.; Asakura, K.; Kudo, A. *J. Am. Chem. Soc.* **2003**, *125*, 3082.

(31) Wang, D. F.; Tang, J. W.; Zou, Z. G.; Ye, J. H. *Chem. Mater.* **2005**, *17*, 5177.

(32) Abe, R.; Takami, H.; Murakami, N.; Ohtani, B. *J. Am. Chem. Soc.* **2008**, *130*, 7780.

(33) Kudo, A.; Domen, K.; Maruya, K.; Onishi, T. *Chem. Phys. Lett.* **1987**, *133*, 517.

(34) Sayama, K.; Arakawa, H. *J. Photochem. Photobiol. A: Chem.* **1996**, *94*, 67.

(35) Takahara, Y.; Kondo, J. N.; Takata, T.; Lu, D. L.; Domen, K. *Chem. Mater.* **2001**, *13*, 1194.

(36) Lu, D. L.; Hitoki, G.; Katou, E.; Kondo, J. N.; Hara, M.; Domen, K. *Chem. Mater.* **2004**, *16*, 1603.

(37) Takata, T.; Hitoki, G.; Kondo, J. N.; Hara, M.; Kobayashi, H.; Domen, K. *Res. Chem. Intermed.* **2007**, *33*, 13.

(38) Maeda, K.; Domen, K. *J. Phys. Chem. C* **2007**, *111*, 7851.

(39) Ishii, T.; Kato, H.; Kudo, A. *J. Photochem. Photobiol. A: Chem.* **2004**, *163*, 181.

(40)Maeda, K.; Takata, T.; Hara, M.; Saito, N.; Inoue, Y.; Kobayashi, H.; Domen, K. *J. Am. Chem. Soc.* **2005**, *127*, 8286.

(41) Maeda, K.; Teramura, K.; Takata, T.; Hara, M.; Saito, N.; Toda, K.; Inoue, Y.; Kobayashi, H.; Domen, K. *J. Phys. Chem. B* **2005**, *109*, 20504.

(42) Matsumura, M.; Saho, Y.; Tsubomura, H. *J. Phys. Chem.* **1983**, *87*, 3807.

(43) Reber, J. F.; Rusek, M. *J. Phys. Chem.* **1986**, *90*, 824.

(44) Xing, C.; Zhang, Y.; Yan, W.; Guo, L. *Int. J. Hydrogen Energy* **2006**, *31*, 2018.

(45) Serpone, N. *J. Photochem. Photobiol. A: Chem.* **1997**, *104*, 1.

(46) Gómez, M.; Rodríguez, J.; Tingry, S.; Hagfeldt, A.; Lindquist, S. E.; Granqvist, C. G. *Sol. Energy Mater. Sol. Cells* **1999**, *59*, 277.

(47) Kawai, T.; Sakata, T. *J. Chem. Soc. Chem. Commun.* **1980**, 694.

(48) Villa, K.; Domènech, X.; García-Pérez, U. M.; Peral, J. *Catal. Lett.* **2015**, *146*, 100.

(49) Kawai, T.; Sakata, T. *Chem. Lett.* **1981**, 81.

(50) Ren, W. J.; Ai, Z. H.; Jia, F. L.; Zhang, L. Z.; Fan, X. X.; Zou, Z. G. *Appl Catal B-Environ* **2007**, *69*, 138.

(51) Zhang, H.; Lv, X. J.; Li, Y. M.; Wang, Y.; Li, J. H. *ACS nano* **2010**, *4*, 380.

(52) Kudo, A.; Kato, H. *Chem. Phys. Lett.* **2000**, *331*, 373.

(53) Kato, H.; Okutomi, H.; Kudo, A.; Iwase, A.; Kato, H.; Okutomi, H.; Kudo, A. *Chem. Lett.* **2004**, *33*, 1260.

(54) Yamakata, A.; Ishibashi, T.; Kato, H.; Kudo, A.; Onishi, H. *J. Phys. Chem. B* **2003**, *107*, 14383.

(55) Bard, A. J. *J. Phys. Chem.* **1982**, *86*, 172.

(56) Domen, K.; Naito, S.; Soma, M.; Onishi, T.; Tamaru, K. *J. Chem. Soc. Chem. Commun.* **1980**, 543.

(57) Domen, K.; Kudo, A.; Onishi, T.; Kosugi, N.; Kuroda, H. *J. Phys. Chem.* **1986**, *90*, 292.

(58) Ishikawa, A.; Takata, T.; Kondo, J. N.; Hara, M.; Kobayashi, H.; Domen, K. *J. Am. Chem. Soc.* **2002**, *124*, 13547.

(59) Kelzenberg, M. D.; Boettcher, S. W.; Petykiewicz, J. A.; Turner-Evans, D. B.; Putnam, M. C.; Warren, E. L.; Spurgeon, J. M.; Briggs, R. M.; Lewis, N. S.; Atwater, H. A. *Nat Mater* **2010**, *9*, 239.

(60) Zhang, X.; Chen, Y. L.; Liu, R. S.; Tsai, D. P. *Rep. Prog. Phys.* **2013**, *76*, 046401.

(61) Buldum, A.; Ciraci, S.; Fong, C. Y. *J. Phys. Condens. Matter.* **2000**, *12*, 3349.

(62) Sakoda, K. *Opt. Express* **1999**, *4*, 167.

(63) Wang, F.; Subbaiyan, N. K.; Wang, Q.; Rochford, C.; Xu, G.; Lu, R.; Elliot, A.; D'Souza, F.; Hui, R.; Wu, J. *ACS Appl Mater Interfaces* **2012**, *4*, 1565.

(64) Hwang, D. K.; Lee, B.; Kim, D. H. *RSC Adv.* **2013**, *3*, 3017.

(65) Yablonovitch, E. *Phys. Rev. Lett.* **1987**, *58*, 2059.

(66) John, S. *Phys. Rev. Lett.* **1987**, *58*, 2486.

(67) Yablonovitch, E. *J. Opt. Soc. Am. B: Opt. Phys.* **1993**, *10*, 283.

(68) Russell, P. S. J. *Nature* **1996**, *381*, 290.

(69) Kosaka, H.; Kawashima, T.; Tomita, A.; Notomi, M.; Tamamura, T.; Sato, T.; Kawakami, S. *Phys. Rev. B* **1998**, *58*, 10096.

(70) Aloshyna, M.; Sivakumar, S.; Venkataramanan, M.; Brolo, A. G.; van Veggel, F. C. J. M. *J. Phys. Chem. C* **2007**, *111*, 4047.

(71) Gevaux, D. G.; Bennett, A. J.; Stevenson, R. M.; Shields, A. J.; Atkinson, P.; Griffiths, J.; Anderson, D.; Jones, G. A. C.; Ritchie, D. A. *Appl. Phys. Lett.* **2006**, *88*, 131101.

(72) Li, L.-M.; Zhang, Z.-Q. *Phys. Rev. B* **1998**, *58*, 9587.

(73) Baba, T.; Mori, D. *J. Phys. D: Appl. Phys.* **2007**, *40*, 2659.

(74) Imhof, A.; Vos, W. L.; Sprik, R.; Lagendijk, A. *Phys. Rev. Lett.* **1999**, *83*, 2942.

(75) Chen, J. I. L.; von Freymann, G.; Choi, S. Y.; Kitaev, V.; Ozin, G. A. *Adv. Mater.* **2006**, *18*, 1915.

(76) Okawachi, Y.; Bigelow, M. S.; Sharping, J. E.; Zhu, Z.; Schweinsberg, A.; Gauthier, D. J.; Boyd, R. W.; Gaeta, A. L. *Phys. Rev. Lett.* **2005**, *94*, 153902.

(77) Chen, J. I.; Loso, E.; Ebrahim, N.; Ozin, G. A. *J. Am. Chem. Soc.* **2008**, *130*, 5420.

(78) Rick C. Schroden, M. A.-D., Christopher F. Blanford, and Andreas Stein *Chem. Mater* **2002**, *14*, 11.

(79) McLachlan, M. A.; Johnson, N. P.; Rue, R. M. D. L.; McComb, D. W. *J. Mater. Chem.* **2004**, *14*, 144.

(80) Liu, X.; Zhang, Y.; Ge, D.; Zhao, J.; Li, Y.; Endres, F. *Phys. Chem. Chem. Phys.* **2012**, *14*, 5100.

(81) Zhang, Y.-Q.; Wang, J.-X.; Ji, Z.-Y.; Hu, W.-P.; Jiang, L.; Song, Y.-L.; Zhu, D.-B. *J. Mater. Chem.* **2007**, *17*, 90.

(82) Goldenberg, L. M.; Wagner, J.; Stumpe, J.; Paulke, B.-R.; Görnitz, E. *Langmuir* **2002**, *18*, 3319.

(83) Míguez, H.; Blanco, A.; Meseguer, F.; López, C.; Yates, H. M.; Pemble, M. E.; Fornés, V.; Mifsud, A. *Phys. Rev. B* **1999**, *59*, 1563.

(84) Gugliermetti, F.; Bisegna, F. *Build. Environ.* **2003**, *38*, 479.

(85) Frenzer, G.; Maier, W. F. *Annu. Rev. Mater. Res.* **2006**, *36*, 281.

(86) Fang, G.; Li, D.; Yao, B.-L. *Vacuum* **2002**, *68*, 363.

(87) Moholkar, A. V.; Pawar, S. M.; Rajpure, K. Y.; Bhosale, C. H.; Kim, J. H. *Appl. Surf. Sci.* **2009**, *255*, 9358.

(88) Alam, M. J.; Cameron, D. C. *Surf. Coat. Technol.* **2001**, *142-144*, 776.

(89) Tetreault, N.; Arsenault, E.; Heiniger, L. P.; Soheilnia, N.; Brillet, J.; Moehl, T.; Zakeeruddin, S.; Ozin, G. A.; Gratzel, M. *Nano Lett.* **2011**, *11*, 4579.

(90) Stein, A.; Li, F.; Denny, N. R. *Chem. Mater.* **2008**, *20*, 649.

(91) Sato, S.; White, J. M. *Chem. Phys. Lett.* **1980**, *72*, 83.

(92) Kato, H.; Kudo, A. *J. Phys. Chem. B* **2001**, *105*, 4285.

(93) Yuan, Y. P.; Zheng, J.; Zhang, X. L.; Li, Z. S.; Yu, T.; Ye, J. H.; Zou, Z. G. *Solid State Ionics* **2008**, *178*, 1711.

(94) Ikeda, S.; Hara, M.; Kondo, J. N.; Domen, K.; Takahashi, H.; Okubo, T.; Kakihana, M. *Chem. Mater.* **1998**, *10*, 72.

(95) Tomita, K.; Petrykin, V.; Kobayashi, M.; Shiro, M.; Yoshimura, M.; Kakihana, M. *Angew. Chem. Int. Ed. Engl.* **2006**, *45*, 2378.

(96) Becker, M. A.; Radich, J. G.; Bunker, B. A.; Kamat, P. V. *J Phys Chem Lett* **2014**, *5*, 1575.

(97) Amalraj, A. S.; Senguttuvan, G. *J. Mater. Sci. Mater. El.* **2014**, *25*, 2035.

(98) VanderHyde, C. A.; Sartale, S. D.; Patil, J. M.; Ghoderao, K. P.; Sawant, J. P.; Kale, R. B. *Solid State Sci* **2015**, *48*, 186.

(99) Chen, S.; Shen, S.; Liu, G.; Qi, Y.; Zhang, F.; Li, C. *Angew. Chem. Int. Ed. Engl.* **2015**, *54*, 3047.

(100) Zhao, Y.; Yang, B.; Xu, J.; Fu, Z.; Wu, M.; Li, F. *Thin Solid Films* **2012**, *520*, 3515.

(101) Zhang, X.; Liu, Y.; Lee, S.-T.; Yang, S.; Kang, Z. *Energy. Environ. Sci.* **2014**, *7*, 1409.

(102) Cheng, C.; Karuturi, S. K.; Liu, L.; Liu, J.; Li, H.; Su, L. T.; Tok, A. I.; Fan, H. J. *Small* **2012**, *8*, 37.

(103) Motohiro, T.; Yamadera, H.; Taga, Y. *Rev. Sci. Instrum.* **1989**, *60*, 2657.

(104) Martinu, L.; Poitras, D. *J. Vac. Sci. Technol A* **2000**, *18*, 2619.

(105) Premalal, E. V. A.; Dematage, N.; Kaneko, S.; Konno, A. *Electrochemistry* **2012**, *80*, 624.

(106) Peulon, S.; Lincot, D. *Adv. Mater.* **1996**, *8*, 166.

(107) Cable, R. E.; Schaak, R. E. *Chem. Mater.* **2007**, *19*, 4098.

(108) Granqvist, C. G. *Sol. Energy Mater. Sol. Cells* **2007**, *91*, 1529.

(109) Granqvist, C. G. *Pergamon, Oxford, UK* **1991**, *Chapter 5*, 106.

(110) Ellmer, K. *Nature Photonics* **2012**, *6*, 809.

(111) Ellmer, K.; Mientus, R. *Thin Solid Films* **2008**, *516*, 4620.

(112) Hamberg, I.; Granqvist, C. G. *J. Appl. Phys.* **1986**, *60*, R123.

(113) Chi, Y.-j.; Fu, H.-g.; Qi, L.-h.; Shi, K.-y.; Zhang, H.-b.; Yu, H.-t. *J. Photochem. Photobiol. A: Chem.* **2008**, *195*, 357.

(114) Alam, M. J.; Cameron, D. C. *Thin Solid Films* **2000**, *377*, 455.

(115) Sima, C.; Grigoriu, C.; Antohe, S. *Thin Solid Films* **2010**, *519*, 595.

(116) Kim, H.; Gilmore, C. M.; Horwitz, J. S.; Piqué, A.; Murata, H.; Kushto, G. P.; Schlaf, R.; Kafafi, Z. H.; Chrisey, D. B. *Appl. Phys. Lett.* **2000**, *76*, 259.

(117) Wang, H.; Liu, Y.; Li, M.; Huang, H.; Zhong, M.; Shen, H. *Appl. Phys. A* **2009**, *97*, 25.

(118) Koo, H. J.; Kim, Y. J.; Lee, Y. H.; Lee, W. I.; Kim, K.; Park, N. G. *Adv. Mater.* **2008**, *20*, 195.

(119) Colodrero, S.; Mihi, A.; Häggman, L.; Ocaña, M.; Boschloo, G.; Hagfeldt, A.; Míguez, H. *Adv. Mater.* **2009**, *21*, 764.

(120) Heiniger, L. P.; O'Brien, P. G.; Soheilnia, N.; Yang, Y.; Kherani, N. P.; Gratzel, M.; Ozin, G. A.; Tetreault, N. *Adv. Mater.* **2013**, *25*, 5734.

(121) Guo, M.; Xie, K.; Lin, J.; Yong, Z.; Yip, C. T.; Zhou, L.; Wang, Y.; Huang, H. *Energy. Environ. Sci.* **2012**, *5*, 9881.

(122) Matsushita, S.; Suavet, O.; Hashiba, H. *Electrochim. Acta* **2010**, *55*, 2398.

(123) Lin, S. Y.; Fleming, J. G.; Hetherington, D. L.; Smith, B. K.; Biswas, R.; Ho, K. M.; Sigalas, M. M.; Zubrzycki, W.; Kurtz, S. R.; Bur, J. *Nature* **1998**, *394*, 251.

(124) Holland, B. T.; Blanford, C. F.; Do, T.; Stein, A. *Chem. Mater.* **1999**, *11*, 795.

(125) Li, K. N.; Wang, Y. F.; Xu, Y. F.; Chen, H. Y.; Su, C. Y.; Kuang, D. B. *ACS Appl Mater Interfaces* **2013**, *5*, 5105.

(126) McLachlan, M. A.; Rahman, H.; Illy, B.; McComb, D. W.; Ryan, M. P. *Mater. Chem. Phys.* **2011**, *129*, 343.

(127) Kőrösi, L.; Papp, S.; Beke, S.; Pécz, B.; Horváth, R.; Petrik, P.; Agócs, E.; Dékány, I. *Appl. Phys. A* **2012**, *107*, 385.

(128) Lee, K.-T.; Lu, S.-Y. *J. Mater. Chem.* **2012**, *22*, 16259.

(129) Müller, V.; Rasp, M.; Štefanić, G.; Ba, J.; Günther, S.; Rathousky, J.; Niederberger, M.; Fattakhova-Rohlfing, D. *Chem. Mater.* **2009**, *21*, 5229.

(130) Arsenault, E.; Soheilnia, N.; Ozin, G. A. *ACS nano* **2011**, *5*, 2984.

(131) Moir, J.; Soheilnia, N.; O'Brien, P.; Jelle, A.; Grozea, C. M.; Faulkner, D.; Helander, M. G.; Ozin, G. A. *ACS nano* **2013**, *7*, 4261.

(132) Zhang, L.; Reisner, E.; Baumberg, J. J. *Energy. Environ. Sci.* **2014**, *7*, 1402.

(133) Yang, Z.; Gao, S.; Li, W.; Vlasko-Vlasov, V.; Welp, U.; Kwok, W. K.; Xu, T. *ACS Appl Mater Interfaces* **2011**, *3*, 1101.

(134) Yuan, S.; Huang, H.; Wang, Z.; Zhao, Y.; Shi, L.; Cai, C.; Li, D. *J. Photochem. Photobiol. A: Chem.* **2013**, *259*, 10.

(135) Shanthi, S.; Subramanian, C.; Ramasamy, P. *Mat Sci Eng B-Solid* **1999**, *57*, 127.

(136) Yamashita, M.; Agu, M. *Jpn. J. Appl. Phys.* **1984**, *23*, 1499.

(137) Thangaraju, B. *Thin Solid Films* **2002**, *402*, 71.

(138) Elangovan, E.; Ramamurthi, K. *Thin Solid Films* **2005**, *476*, 231.

(139) Sanon, G.; Rup, R.; Mansingh, A. *Phys. Status Solidi A* **1991**, *128*, 109.

(140) Elangovan, E.; Singh, M. P.; Ramamurthi, K. *Mat Sci Eng B-Solid* **2004**, *113*, 143.

(141) Fukano, T. *Sol. Energy Mater. Sol. Cells* **2004**.

(142) J. Ba, D. F. R., Armin Feldhoff *Chem. Mater* **2006**, *18*, 7.

(143) Martínez, A. I.; Huerta, L.; León, J. M. O. R. d.; Acosta, D.; Malik, O.; Aguilar, M. *J. Phys. D: Appl. Phys.* **2006**, *39*, 5091.

(144) Kawashima, T.; Ezure, T.; Okada, K.; Matsui, H.; Goto, K.; Tanabe, N. *J. Photochem. Photobiol. A: Chem.* **2004**, *164*, 199.

(145) Shanthi, E.; Banerjee, A.; Chopra, K. L. *Thin Solid Films* **1982**, *88*, 93.

(146) Senthilkumar, V.; Vickraman, P.; Ravikumar, R. *J. Sol-Gel Sci. Technol.* **2009**, *53*, 316.

(147) Chen, M. F.; Lin, K. M.; Ho, Y. S. *Mater Sci Eng B-Adv* **2011**, *176*, 127.

(148) Neser, S.; Bechinger, C.; Leiderer, P.; Palberg, T. *Phys. Rev. Lett.* **1997**, *79*, 2348.

(149) Dimitrov, A. S.; Nagayama, K. *Langmuir* **1996**, *12*, 1303.

(150) Meng, Q. B.; Gu, Z. Z.; Sato, O.; Fujishima, A. *Appl. Phys. Lett.* **2000**, *77*, 4313.

(151) Park, S. H.; Xia, Y. *Langmuir* **1999**, *15*, 266.

(152) Xie, H.; Li, Y. Z.; Jin, S. F.; Han, J. J.; Zhao, X. J. *J. Phys. Chem. C* **2010**, *114*, 9706.

(153) Chen, X. Q.; Li, Z. S.; Ye, J. H.; Zou, Z. G. *Chem. Mater.* **2010**, *22*, 3583.

(154) Sadakane, M.; Takahashi, C.; Kato, N.; Ogihara, H.; Nodasaka, Y.; Doi, Y.; Hinatsu, Y.; Ueda, W. *Bull. Chem. Soc. Jpn.* **2007**, *80*, 677.

(155) Stein, A. *Microporous Mesoporous Mater.* **2001**, *44*, 227.

(156) Yan, H. W.; Blanford, C. F.; Holland, B. T.; Smyrl, W. H.; Stein, A. *Chem. Mater.* **2000**, *12*, 1134.

(157) Wijnhoven, J. E. *Science* **1998**, *281*, 802.

(158) Laligant, Y.; Calage, Y.; Heger, G.; Pannetier, J.; Ferey, G. *J. Solid State Chem.* **1989**, *78*, 66.

(159) Hsu, R.; Maslen, E. N.; duBoulay, D.; Ishizawa, N. *Acta Crystallogr. B* **1997**, *53*, 420.

(160) Bisht, H.; Eun, H. T.; Mehrtens, A.; Aegerter, M. A. *Thin Solid Films* **1999**, *351*, 109.

(161) Guo, S.; Li, D.; Zhang, Y.; Zhang, Y.; Zhou, X. *Electrochim. Acta* **2014**, *121*, 352.

(162) Avadhut, Y. S.; Weber, J.; Hammarberg, E.; Feldmann, C.; Schellenberg, I.; Pöttgen, R.; Schmedt auf der Günne, J. *Chem. Mater.* **2011**, *23*, 1526.

(163) Hu, J.; Gordon, R. G. *J. Appl. Phys.* **1992**, *71*, 880.

(164) Jin, Z. C.; Hamberg, I.; Granqvist, C. G. *J. Appl. Phys.* **1988**, *64*, 5117.

(165) Aktaruzzaman, A. F.; Sharma, G. L.; Malhotra, L. K. *Thin Solid Films* **1991**, *198*, 67.

(166) Hu, J.; Gordon, R. G. *Solar Cells* **1991**, *30*, 437.

(167) Kamalasanan, M. N.; Chandra, S. *Thin Solid Films* **1996**, *288*, 112.

(168) Caruso, F.; Caruso, R. A.; Mohwald, H. *Science* **1998**, *282*, 1111.

(169) Jiang, P.; Bertone, J. F.; Colvin, V. L. *Science* **2001**, *291*, 453.

(170) Kim, S. W.; Kim, M.; Lee, W. Y.; Hyeon, T. *J Am. Chem. Soc.* **2002**, *124*, 7642.

(171) Xu, X.; Asher, S. A. *J Am Chem Soc* **2004**, *126*, 7940.

(172) Wang, Y. L.; Cai, L.; Xia, Y. N. *Adv. Mater.* **2005**, *17*, 473.

(173) Qian, H.; Lin, G.; Zhang, Y.; Gunawan, P.; Xu, R. *Nanotechnology* **2007**, *18*, 355602.

(174) Niu, D.; Ma, Z.; Li, Y.; Shi, J. *J Am Chem Soc* **2010**, *132*, 15144.

(175) Deng, Z. W.; Chen, M.; Gu, G. X.; Wu, L. M. *J Phys. Chem. B* **2008**, *112*, 16.

(176) Minami, T.; Sato, H.; Nanto, H.; Takata, S. *Jpn J Appl Phys 2* **1986**, *25*, L776.

(177) Choi, B. H.; Im, H. B.; Song, J. S.; Yoon, K. H. *Thin Solid Films* **1990**, *193*, 712.

(178) Kim, K. H.; Park, K. C.; Ma, D. Y. *J. Appl. Phys.* **1997**, *81*, 7764.

(179) Tang, W.; Cameron, D. C. *Thin Solid Films* **1994**, *238*, 83.

(180) Deng, Z.; Chen, M.; Gu, G.; Wu, L. *J. Phys. Chem. B* **2008**, *112*, 16.

(181) Yan, H.; Blanford, C. F.; Holland, B. T.; Smyrl, W. H.; Stein, A. *Chem. Mater.* **2000**, *12*, 1134.

(182) Zhang, J.; Wang, S.; Wang, Y.; Xu, M.; Xia, H.; Zhang, S.; Huang, W.; Guo, X.; Wu, S. *Sensors Actuators B: Chem.* **2009**, *139*, 411.

(183) Verma, A.; Khan, F.; Kumar, D.; Kar, M.; Chakravarty, B. C.; Singh, S. N.; Husain, M. *Thin Solid Films* **2010**, *518*, 2649.

(184) Tang, W.; Cameron, D. C. *Thin Solid Films* **1994**, *238*, 83.

(185) Cheng, S. L.; Liao, S. Y.; Syu, J. H. *Ceram. Int.* **2016**, *42*, 5271.

(186) Jiang, X.; Wong, F. L.; Fung, M. K.; Lee, S. T. *Appl. Phys. Lett.* **2003**, *83*, 1875.

(187) Lin, D.; Pan, W.; Wu, H. *J. Am. Ceram. Soc.* **2007**, *90*, 71.

(188) Zou, Z.; Ye, J.; Sayama, K.; Arakawa, H. *Nature* **2001**, *414*, 625.

(189) Hitoki, G.; Takata, T.; Kondo, J. N.; Hara, M.; Kobayashi, H.; Domen, K. *Chem. Commun.* **2002**, 1698.

(190) Domen, K.; Naito, S.; Onishi, T.; Tamaru, K. *Chem. Phys. Lett.* **1982**, *92*, 433.

(191) Galińska, A.; Walendziewski, J. *Energy & Fuels* **2005**, *19*, 1143.

(192) Trindade, T.; O'Brien, P.; Pickett, N. L. *Chem. Mater.* **2001**, *13*, 3843.

(193) Jing, D.; Guo, L. *J. Phys. Chem. B* **2006**, *110*, 11139.

(194) Gopidas, K. R.; Bohorquez, M.; Kamat, P. V. *J. Phys. Chem.* **1990**, *94*, 6435.

(195) Peter, L. M.; Riley, D. J.; Tull, E. J.; Wijayantha, K. G. U. *Chem. Commun.* **2002**, 1030.

(196) Lee, W.; Min, S. K.; Dhas, V.; Ogale, S. B.; Han, S.-H. *Electrochem. Commun.* **2009**, *11*, 103.

(197) Jia, H.; Hu, Y.; Tang, Y.; Zhang, L. *Electrochem. Commun.* **2006**, *8*, 1381.

(198) Murray, C. B.; Norris, D. J.; Bawendi, M. G. *J. Am. Chem. Soc.* **1993**, *115*, 8706.

(199) Manna, L.; Scher, E. C.; Alivisatos, A. P. *J. Am. Chem. Soc.* **2000**, *122*, 12700.

(200) Grebinski, J. W.; Hull, K. L.; Zhang, J.; Kosel, T. H.; Kuno, M. *Chem. Mater.* **2004**, *16*, 5260.

(201) Zhu, J.; Palchik, O.; Chen, S.; Gedanken, A. *J. Phys. Chem. B* **2000**, *104*, 7344.

(202) Li, N.; Zhang, X. L.; Chen, S. T.; Hou, X. M.; Liu, Y.; Zhai, X. M. *Mater Sci Eng B-Adv* **2011**, *176*, 688.

(203) Yu, W. W.; Peng, X. *Angew. Chem. Int. Ed. Engl.* **2002**, *41*, 2368.

(204) Sathish, M.; Viswanathan, B.; Viswanath, R. *Int. J. Hydrogen Energy* **2006**, *31*, 891.

(205) Meissner, D.; Memming, R.; Kastening, B. *J. Phys. Chem.* **1988**, *92*, 3476.

(206) Tiwari, S.; Tiwari, S. *Sol. Energy Mater. Sol. Cells* **2006**, *90*, 1621.

(207) Mitchell, R.; Brydson, R.; Douthwaite, R. E. *Phys. Chem. Chem. Phys.* **2015**, *17*, 493.

(208) Vlasov, Y. A.; Yao, N.; Norris, D. J. *Adv. Mater.* **1999**, *11*, 165.

(209) Xie, K.; Wu, Z.; Wang, M.; Yu, J.; Gong, C.; Sun, L.; Lin, C. *Electrochem. Commun.* **2016**, *63*, 56.

(210) Islam, M. A.; Haque, F.; Rahman, K. S.; Dhar, N.; Hossain, M. S.; Sulaiman, Y.; Amin, N. *Optik* **2015**, *126*, 3177.

(211) Kumarage, W. G. C.; Wijesundera, R. P.; Seneviratne, V. A.; Jayalath, C. P.; Dassanayake, B. S. *J. Phys. D: Appl. Phys.* **2016**, *49*, 095109.

(212) Cho, C.-Y.; Lee, J.; Lee, D. C.; Moon, J. H. *Electrochim. Acta* **2015**, *166*, 350.

(213) Khot, K. V.; Mali, S. S.; Kharade, R. R.; Mane, R. M.; Patil, P. S.; Hong, C. K.; Kim, J. H.; Heo, J.; Bhosale, P. N. *J. Mater. Sci. Mater. El.* **2014**, *25*, 5606.

(214) Cho, C.-Y.; Lee, S.; Lee, J.; Lee, D. C.; Moon, J. H. *J. Mater. Chem. A* **2014**, *2*, 17568.

(215) Gun, Y.; Song, G. Y.; Quy, V. H.; Heo, J.; Lee, H.; Ahn, K. S.; Kang, S. H. *ACS Appl Mater Interfaces* **2015**, *7*, 20292.

(216) Kozytskiy, A. V.; Stroyuk, O. L.; Breslavskiy, A. Y.; Kuchmy, S. Y.; Skorik, N. A.; Moskalyuk, V. O. *Theor. Exp. Chem.* **2013**, *49*, 213.

(217) Zyoud, A.; Saadeddin, I.; Khurduj, S.; Mari'e, M. m.; Hawash, Z. M.; Faroun, M. I.; Campet, G.; Park, D.; Hilal, H. S. *J. Electroanal. Chem.* **2013**, *707*, 117.

(218) Ogermann, D.; Wilke, T.; Klienermanns, K. *Open Jouranl of Physical Chemistry* **2012**, *2*, 47.

(219) Ching-Fa, C.; Shih-Yi, L.; Yuh-Lang, L. *Nanotechnology* **2010**, *21*, 025202.

(220) Liu, H.; Zhang, G.; Yin, J.; Liang, J.; Sun, W.; Shen, Z. *Mater. Res. Bull.* **2015**, *61*, 492.

(221) Deng, J.; Wang, M.; Liu, J.; Song, X.; Yang, Z. *J. Colloid Interface Sci.* **2014**, *418*, 277.

(222) Thomas, A.; Fischer, A.; Goettmann, F.; Antonietti, M.; Müller, J.-O.; Schlögl, R.; Carlsson, J. M. *J. Mater. Chem.* **2008**, *18*, 4893.

(223) Montigaud, H.; Tanguy, B.; Demazeau, G.; Alves, I.; Courjault, S. *J. Mater. Sci.* **2000**, *35*, 2547.

(224) Gao, H.; Yan, S.; Wang, J.; Huang, Y. A.; Wang, P.; Li, Z.; Zou, Z. *Phys. Chem. Chem. Phys.* **2013**, *15*, 18077.

(225) Wang, Y.; Wang, X.; Antonietti, M. *Angew. Chem. Int. Ed. Engl.* **2012**, *51*, 68.

(226) Liu, Q.; Zhang, J. *Langmuir* **2013**, *29*, 3821.

(227) Zheng, Y.; Jiao, Y.; Jaroniec, M.; Jin, Y.; Qiao, S. Z. *Small* **2012**, *8*, 3550.

(228) Wu, M.; Wang, Q.; Sun, Q.; Jena, P. *J. Phys. Chem. C* **2013**, *117*, 6055.

(229) Yan, S. C.; Li, Z. S.; Zou, Z. G. *Langmuir* **2009**, *25*, 10397.

(230) Yan, S. C.; Li, Z. S.; Zou, Z. G. *Langmuir* **2010**, *26*, 3894.

(231) Zhang, G.; Zhang, J.; Zhang, M.; Wang, X. *J. Mater. Chem.* **2012**, *22*, 8083.

(232) Gratzel, M. *Nature* **2001**, *414*, 338.

(233) Duret, A.; Gratzel, M. *J. Phys. Chem. B* **2005**, *109*, 17184.

(234) Khan, S. U. M.; Akikusa, J. *J. Phys. Chem. B* **1999**, *103*, 7184.

(235) Jorand Sartoretti, C.; Ulmann, M.; Alexander, B. D.; Augustynski, J.; Weidenkaff, A. *Chem. Phys. Lett.* **2003**, *376*, 194.

(236) Bjoerksten, U.; Moser, J.; Graetzel, M. *Chem. Mater.* **1994**, *6*, 858.

(237) Dare-Edwards, M. P.; Goodenough, J. B.; Hamnett, A.; Trevellick, P. R. *J. Chem. Soc., Faraday Trans. 1* **1983**, *79*, 2027.

(238) Zhang, Y.; Mori, T.; Ye, J.; Antonietti, M. *J. Am. Chem. Soc.* **2010**, *132*, 6294.

(239) Kailasam, K.; Epping, J. D.; Thomas, A.; Losse, S.; Junge, H. *Energy. Environ. Sci.* **2011**, *4*, 4668.

(240) Ishida, Y.; Chabanne, L.; Antonietti, M.; Shalom, M. *Langmuir* **2014**, *30*, 447.

(241) Xu, J.; Brenner, T. J.; Chabanne, L.; Neher, D.; Antonietti, M.; Shalom, M. *J. Am. Chem. Soc.* **2014**, *136*, 13486.

(242) Li, X.-H.; Zhang, J.; Chen, X.; Fischer, A.; Thomas, A.; Antonietti, M.; Wang, X. *Chem. Mater.* **2011**, *23*, 4344.

(243) Jelinek, M.; Kulisch, W.; Delplancke-Ogletree, M. P.; Lancok, J.; Jastrabik, L.; Chvostova, D.; Popov, C.; Bulir, J. *Appl Phys a-Mater* **2001**, *73*, 167.

(244) Bai, X.; Wang, L.; Zong, R.; Zhu, Y. *J. Phys. Chem. C* **2013**, *117*, 9952.

(245) Wider, G.; Dreier, L. *J. Am. Chem. Soc.* **2006**, *128*, 2571.

(246) Mitchell, R.; Brydson, R.; Douthwaite, R. E. *Nanoscale* **2014**, *6*, 4043.

(247) Schroden, R. C.; Al-Daous, M.; Blanford, C. F.; Stein, A. *Chem. Mater.* **2002**, *14*, 3305.

(248) Sadakane, M.; Kato, R.; Murayama, T.; Ueda, W. *J. Solid State Chem.* **2011**, *184*, 2299.

(249) Yu, W. W.; Peng, X. G. *Angew. Chem. Int. Ed.* **2002**, *41*, 2368.